Spring 1-1-2012

Sea Ice Topography Profiling using Laser Altimetry from Small Unmanned Aircraft Systems

Roger Ian Crocker
University of Colorado at Boulder, riancrocker@gmail.com

Sea Ice Topography Profiling using Laser Altimetry from Small Unmanned Aircraft Systems

by

Roger Ian Crocker

B.S., University of Colorado, 2004

M.S., University of Colorado, 2007

A dissertation submitted to the

Faculty of the Graduate School of the

University of Colorado in partial fulfillment

of the requirements for the degree of

Doctor of Philosophy

Department of Aerospace Engineering Sciences

2012

This thesis entitled:
Sea Ice Topography Profiling using Laser Altimetry from Small Unmanned Aircraft Systems
written by Roger Ian Crocker
has been approved for the Department of Aerospace Engineering Sciences

James A. Maslanik

William J. Emery

Ute C. Herzfeld

Scott E. Palo

Dennis M. Akos

Date

The final copy of this dissertation has been examined by the signatories, and we find that both the content and the form meet acceptable presentation standards of scholarly work in the above mentioned discipline.

Crocker, Roger Ian (Ph.D., Aerospace Engineering Sciences)

Sea Ice Topography Profiling using Laser Altimetry from Small Unmanned Aircraft Systems

Thesis directed by Research Professor James A. Maslanik

Arctic sea ice is undergoing a dramatic transition from a perennial ice pack with a high prevalence of old multiyear ice, to a predominantly seasonal ice pack comprised primarily of young first-year and second-year ice. This transition has brought about changes in the sea ice thickness and topography characteristics, which will further affect the evolution and survivability of the ice pack. The varying ice conditions have substantial implications for commercial operations, international affairs, regional and global climate, our ability to model climate dynamics, and the livelihood of Arctic inhabitants. A number of satellite and airborne missions are dedicated to monitoring sea ice, but they are limited by their spatial and temporal resolution and coverage. Given the fast rate of sea ice change and its pervasive implications, enhanced observational capabilities are needed to augment the current strategies.

The CU Laser Profilometer and Imaging System (CULPIS) is designed specifically for collecting fine-resolution elevation data and imagery from small unmanned aircraft systems (UAS), and has a great potential to compliment ongoing missions. This altimeter system has been integrated into four different UAS, and has been deployed during Arctic and Antarctic science campaigns. The CULPIS elevation measurement accuracy is shown to be 95±25 cm, and is limited primarily by GPS positioning error (50±25 cm), aircraft attitude determination error (<20 cm), and sensor misalignment error (<20 cm). The relative error is considerably smaller over short flight distances, and the measurement precision is shown to be <10 cm over a distance of 200 m. Given its fine precision, the CULPIS is well suited for measuring sea ice topography, and observed ridge height and ridge separation distributions are found to agree with theoretical distributions to within 5%. Simulations demonstrate the inability of course-resolution measurements to accurately represent the theoretical distributions, with differences up to 30%. Future efforts should focus on reducing the total measurement error to <20 cm to make the CULPIS suitable for detecting ice sheet elevation change.

Dedication

To my family.

$\infty\heartsuit\infty$

Acknowledgements

Thank you:

Jim Maslanik, Bill Emery, Ute Herzfeld, Scott Palo, Dennis Akos, Dan Baldwin, Charles Fowler, Dax Matthews, John Adler, Greg Walker, Bob Stone, Rune Storvold, John Burkhart, Thorston Markus, Mark Tschudi, Tej Dhakal, Matt Edwards, Nick Gliszinski, Francis von Kaas Bemis, Family, National Oceanic and Atmospheric Administration (NOAA), Cooperative Institute for Research in Environmental Sciences (CIRES), Advanced Ceramics Research (ACR), Manta UAS crew, Ilulissat, Kangerlussuaq International Science Support (KISS), National Aeronautics and Space Administration (NASA), SIERRA UAS crew, Ny-Ålesund, Kings Bay, Norwegian Polar Institute, UNAVCO, National Science Foundation (NSF), Aerosonde, Hood Technologies, American Aerospace Engineering, Research Council of Norway, Coordinated Investigation of Climate-Cryosphere Interactions (CICCI) participants, Andøya Rocket Range, European Space Agency (ESA), International Association for Mathematical Geosciences (IAMG), American Geophysical Union (AGU), Research and Engineering Center for Unmanned Vehicles (RECUV), NASA Graduate Student Researchers Program (GSRP), Colorado Center for Astrodynamics Research (CCAR), Department of Aerospace Engineering Sciences, University of Colorado at Boulder.

Contents

Chapter

Tables

Table

Figures

Figure

Chapter 1

Overview

1.1 Scientific Rationale

Arctic sea ice areal extent, its physical properties, and its variability and distribution across the Arctic Ocean have long been recognized to have a considerable impact on geophysical and social dynamics (e.g. [5, 7, 10, 79, 106, 119–121]). The ice pack plays a major role in governing the heat and momentum exchange between the atmosphere and ocean, thereby affecting weather and climate. Seasonally and annually changing ice conditions impact shipping routes, resource exploration operations, and wildlife habitat, which in turn influence the commerce, culture, and wellbeing of Arctic peoples and their communities. In order to better understand, monitor, and predict the nature of sea ice and its interactions within the Earth system, substantial effort has gone into observing and modeling its various characteristics and their evolution.

The morphology[1] of Arctic sea ice is continually evolving under the the influence of oceanic and atmospheric conditions. In general, two phenomena act to alter the thickness and topography[2] of sea ice. Thermodynamic processes are responsible for mass changes at the upper and lower boundary of the ice, and mechanical processes, resulting from nonuniform motion of the ice, cause the formation of leads and pressure ridges [113]. As described by Ketchum[61], the sea ice surface topography is one of the basic criteria for visually identifying the stages of ice development or ice age. Very early stages of ice development generally have smooth, level surfaces with only minor pressure ice formations, such as rafted ice. Later stages of ice development, during the first year's growth, maintain a generally level surface, but have frequent, more

[1] Morphology refers herein to thickness and topography.
[2] Topography refers herein to roughness and ridging.

prominent pressure ice formations, such as ridges and rubble fields. Due to summer melting and deformation, multiyear sea ice two or more years old has an undulating or gradual rolling surface characterized by rounded hummocks, which are typically weathered ridges and rubble, and melt pond depressions. Second year ice is generally hard to distinguish from first year ice, but the hummocks and melt pond topography becomes more pronounced with each melt cycle.

Early scientific studies of Arctic sea ice morphology conducted in the late 1950s and early 1960s utilized *in situ* measurements collected at drifting ice stations (e.g. station Alpha, 1957-1958 [101]) and remotely sensed measurements collected via upward looking submarine sonar (e.g. U.S. Navy operations, 1960 [49]) to investigate ice thickness, roughness, and ridging characteristics [49, 119, 121]. These measurements were, however, limited in their spatial and temporal extent. By the mid 1960s, various remote sensor systems were being flown on aircraft to evaluate their usefulness for mapping and measuring sea ice conditions and features, and by the late 1960s airborne laser altimetry was being utilized to measure sea ice freeboard and topography [61]. It was recognized that the various stages of ice development could be identified through interpretation of the laser topography data, and that determination of the areal coverage of ridged ice was critical for documenting the ice mass interannual variability [51].

The initial efforts to model sea ice morphology were, in part, prompted by the relatively large collection of observations provided by remote sensing systems, which offered a broader view of the ice conditions and a statistical means to tune and validate the models. The theoretical efforts were based on an understanding that the motion and resulting deformation of the ice pack produces characteristic pressure ridge features, and that these features contain much of the gravitational and potential energy of the ice pack in their mass and in their frictional interactions with the wind and water [113]. Hibler et al.[50] developed theories to describe the spatial distribution of ridge heights and ridge separations, and Parmerter and Coon[97] developed a kinematic model to describe the formation of pressure ridges. Hibler[47] and Thorndike et al.[113] built upon this work and developed theories to model dynamic and thermodynamic changes in ice thickness due to melting and freezing and the rearrangement of ice to form leads and pressure ridges. These theories laid the framework for current sea ice models and indicated that the parameters of primary importance are the ice extent, the areas of open water and very thin ice, and the ice thickness and roughness [113].

Through the 1980s, the prevalence of airborne and sonar remote sensing observations of sea ice continued to increase (e.g. [18, 127]), and were complimented by the development of airborne and satellite microwave imaging and radar altimetry systems (e.g. [102, 124]). Satellite imagery, in particular, made it possible to study the synoptic temporal and spatial variability of the ice pack. Dual-polarized multispectral microwave radiance data provided the necessary radiometric information for obtaining both the ice concentration[3] and the fraction of sea ice cover that is first-year and multiyear ice. These data showed large interannual variations in the ice extent, ice concentration, and distribution of multiyear ice [14].

By the late 1990s, the body of observations that had been collected over the years suggested that the Arctic sea ice composition had begun to transform and thin. Submarine sonar data showed a significant decline in the mean ice draft[4] between 1976 and 1996 by approximately 43% across much of the central and eastern Arctic Ocean [104, 123, 125, 126]. Satellite microwave data revealed a reduction of about 6% in the areal extent of the perennial ice pack between 1979 to 1989 [86], and reduction of about 14% in the area of multiyear ice in winter during the period from 1978 to 1998 [59]. These data also indicated a strong correlation between the area of multiyear ice and the thickness of the perennial ice pack. It was speculated that if this apparent transformation were to continue, it may lead to a markedly different ice regime in the Arctic, altering heat and mass exchanges as well as ocean stratification.

In light of the dramatic changes that were beginning to unfold in the Arctic, further effort went into advancing modeling and observational capabilities. Numerical methods for describing ice thickness distribution in sea ice models were improved (e.g. [82]), and satellite radar and laser altimeter sensors specifically suited for collecting sea ice thickness measurements were launched (e.g. ERS-1, 1991; ERS-2, 1995; Envisat, 2002; ICESat, 2003). Observations from these satellites revealed high-frequency interannual variability in mean sea ice thickness dominated by the length of the summer melt period [77], and an overall decline in the thickness and volume of the ice pack explained by a decrease in the multiyear ice coverage [76]. With the combination of synoptic imagery and altimetry data, it became possible to explore relationships between sea ice microwave brightness temperature (BT) signatures and topography features. There was shown to be a strong correlation between ice age and thickness [75, 88], and that topography impacts the

[3] Sea ice concentration is the fractional area that is covered by ice within a given region, the remaining area is open water.
[4] Ice draft is the measurement of the ice depth below the waterline and serves as a proxy for total ice thickness.

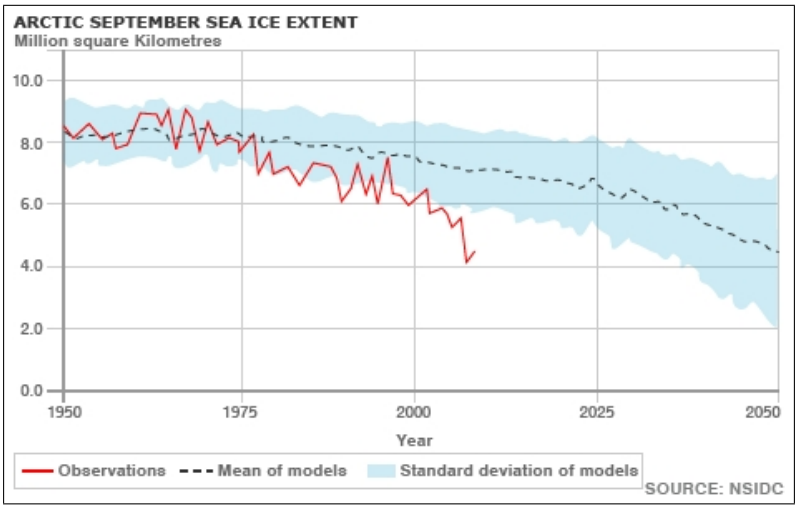

Figure 1.1: The September Arctic ice extent as observed in satellite imagery, and the mean and standard deviation of ice extent as forecast by various climate models. The observed ice extent is declining faster than the models projections, and the most recent observations fall well outside the model standard deviations. Image from the National Snow and Ice Data Center (NSIDC).

observed microwave emissivity, which may translate into overestimates of ice concentrations [87].

One of the more striking changes in the Arctic ice pack in recent years is the dramatic reduction in summertime ice extent. Climate change simulations forecast a shift to a seasonal ice cover, but the loss of ice extent in summer appears to be happening up to 30 years ahead of the projections [111]. As illustrated by Figure 1.1, the latest observations indicate that the September ice extent is well outside of the model standard deviations. Ice coverage in summer 2007 reached a record minimum, with the ice extent being 42% less than in the 1980s [88]. The earlier-than-predicted decline in ice extent was, in part, the result of relatively unusual ocean-atmosphere interdynamics stimulated by climate warming [84, 88, 94], and also by inexact representations of sea ice dynamics [54, 103] and underestimates of the greenhouse gas response in climate models [111, 112].

Not only has there been an abrupt reduction of the summertime sea ice extent, but there is a trend toward an overall younger ice cover; not simply in terms of a change from perennial to first-year ice, but a shift toward much younger and thinner ice within the remaining perennial ice pack [30, 88]. As was previously alluded to, sea ice age is an important parameter that represents the state and evolution of the ice pack, and indicates the longer-term climactic conditions within the Arctic [115]. The ice age record shows that

the fraction of total ice extent composed of multiyear ice in March has decreased from about 75% in the mid-1980s to 45% in 2011, and the proportion of the oldest ice (5+ years old) declined from about 50% of the multiyear ice pack to 10% in 2011 [85]. Correspondingly, in 2007, 58% of the remaining multiyear ice consisted of relatively young 2- and 3-year-old ice, compared to 35% in the mid-1980s [88].

The dramatic change in Arctic sea ice age between March 1990 and March 2010 is shown in Figure 1.2. In 1990, multiyear ice 5+ years old is present throughout the western Arctic Ocean, whereas in 2010, the oldest multiyear ice is confined to a narrow strip along the northern Alaskan coast and Canadian Archipelago. While the overall ice extent during March has not drastically changed, the pack is now composed primarily of young first-year and second-year ice.

The change in ice age distribution implies two fundamental shifts over the last 30 years. First, the ice pack has transitioned from a substantially perennial pack to a seasonal pack [95]. Second, the remaining multiyear ice is much younger and thinner than in the past [85, 88]. Given how fast these changes have occurred, uncertainty remains on the current and continuing loss of ice mass and its redistribution within the Arctic Ocean (e.g. [4, 56, 72, 76, 104]), on the longer-term survivability of the ice (e.g. [71, 85, 88]), and on the ability to simulate these changes using climate models (e.g. [55, 80, 111]).

In addition to changes in ice extent, age, and thickness, the overall ridging and roughness characteristics can be expected to change if the ice pack is undergoing a fundamental shift in its composition. It has been shown that the decrease in ice thickness is dominated by a replacement of ridged ice by undeformed ice [103]. Deformation processes, such as ridging, rafting, and rubble formation, offer means of accumulating ice mass. Additionally, changes in ice topography affect dynamical and thermodynamical processes, which will affect the momentum and heat exchange between the ice, atmosphere, and ocean. For example surface topography and snow accumulation affect the surface albedo, and thus the melt process [22, 100, 116]. These complex interactions, and the degree to which they might act as positive or negative feedbacks that could accelerate or mitigate the decline in the ice cover, are not well understood.

The extensive changes occurring in the Arctic sea ice conditions suggest that the Arctic system is approaching a point where a return to more-stable, mid-20$^{\text{th}}$ century ice conditions is increasingly unlikely, and where abrupt, dramatic changes in ice cover may become the norm [80, 88]. However, a slight recovery

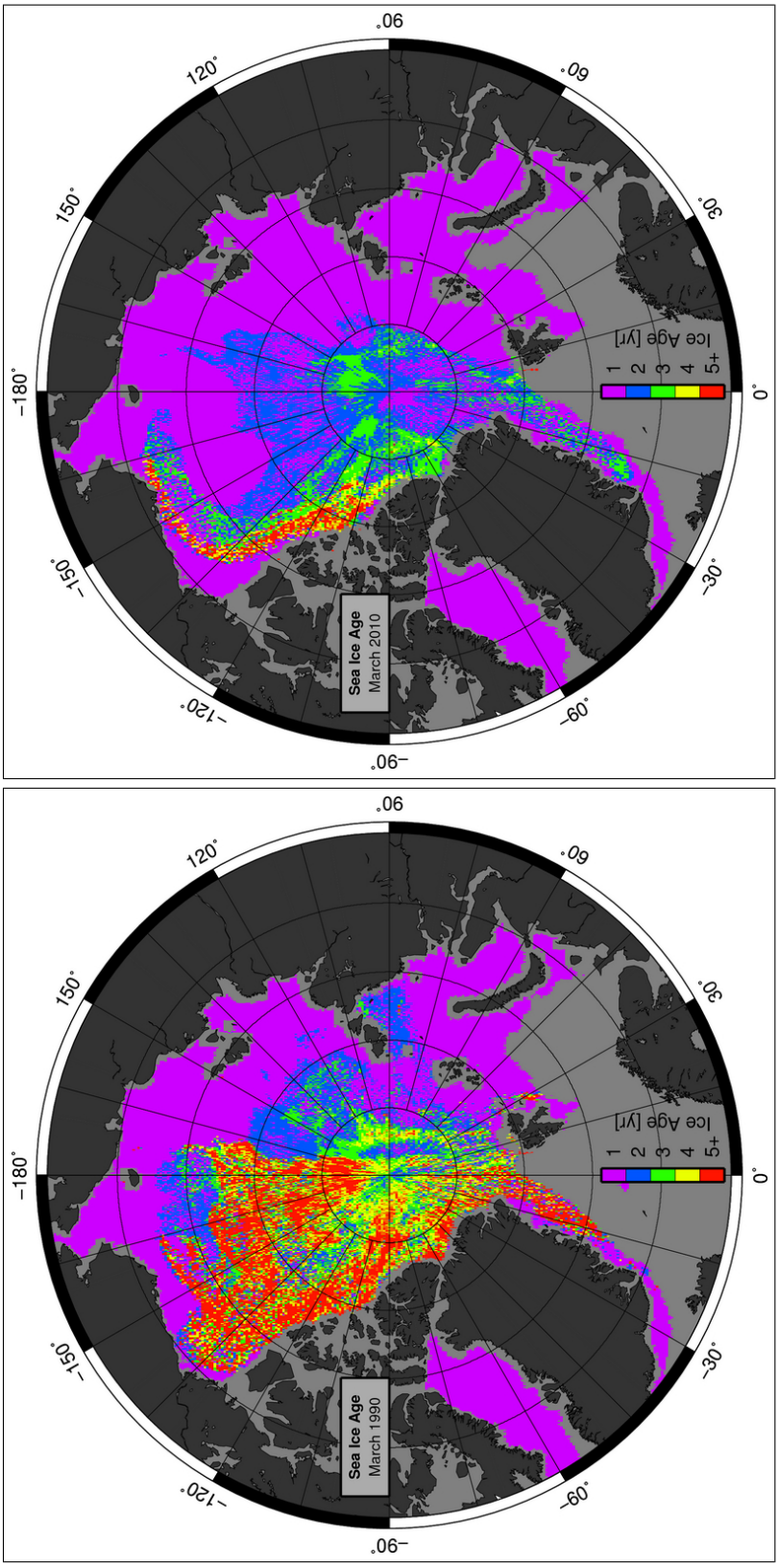

Figure 1.2: Arctic sea ice age in March 1990 and March 2010. In 2010, a dramatic reduction of the oldest ice is apparent throughout the central Arctic Basin, and the oldest ice is confined to a narrow strip along the Canadian Archipelago and northern Alaskan Coast. The ice age data was provided by Dr. Charles Fowler [30].

in multiyear ice extent seen in March 2011 relative to the extreme reductions in 2007 and 2008, and the continued aging of this ice through multiple melt seasons, may suggest that the Arctic has not passed a point beyond which it no longer supports perennial ice cover [85].

The degree to which ice morphology and associated feedback interactions are accurately treated within climate models will affect our ability to predict Arctic and global change. Evidence suggests that ice dynamics are more predictable for a thicker ice pack than for a thinner ice pack [55]. Furthermore, variations in the prevalence of deformed and ridged ice have an impact on simulations of the ice cover redistribution, summer melt-out, and end-of-summer areal extent [55]. Historically-based observational relationships used in statistical regression models may have less relevance in future, or even possibly present, ice regimes [55, 109]. Improved treatments of sea ice surface topography information through more extensive observational capabilities and updated model parameterizations have considerable potential benefit for better understanding ice dynamics and simulating its evolution [4, 54, 109]. Steiner[109] has demonstrated that a roughness parameter can be incorporated into sea ice models through the atmosphere-ice drag coefficient to provide a more realistic representation of the boundary layer processes. However, further observational data are needed to optimize and continually update the empirical parameterizations given the changing roughness conditions.

Routine collections of Arctic sea ice topography data are currently provided by airborne and satellite operations, such as the National Aeronautics and Space Administration (NASA) IceBridge airborne program and the European Space Agency (ESA) CryoSat-2 satellite mission. The launch of the NASA ICESat-2 satellite in 2016 will further these collection efforts; however, there remains an overall shortage of widespread, fine-resolution sea ice topography observations (e.g. [109]). In light of the breadth of issues related to climate warming and its relation to changing Arctic sea ice conditions, the overlying motivation for this research is based on the presumption that laser altimetry data collected using small unmanned aircraft systems (UAS) can be utilized to enhance our understanding of the current sea ice conditions, and to improve our ability to simulate its future evolution.

1.2 Airborne Laser Altimetry

The use of light detection and ranging (LIDAR) for airborne mapping of surface topography and elevation has a rich history that has been driven by technological advancements and geophysical applications. In the most basic sense, airborne LIDAR mapping systems have two major components: a laser altimeter and a positioning system. The laser altimeter measures the distance, or range, from the aircraft to a reflecting surface, and the positioning system measures the location and orientation of the aircraft such that the laser range data can be related to the surface elevation. Brock et al.[12] provides a comprehensive overview of the governing equations and methods affiliated with airborne laser altimetry.

As reviewed by Link et al.[81], in the mid-1960s lasers were being placed on aircraft to examine their potential for terrain and bathymetric mapping. These first systems utilized a variety of lasers and positioning systems, but they were primarily profiling systems whose measurement accuracy was limited by the horizontal and vertical positioning capabilities. Over time, improved sensors, processing techniques, and positioning methods led to the development of numerous profiling and scanning systems, which in turn broadened their scientific application. In order to highlight the historical context of this dissertation research, the remainder of this section discusses the progression of airborne laser altimetry as applied toward measuring Arctic sea ice characteristics, and presents important topics which are relevant throughout this work.

In 1962, the Naval Oceanographic Office (NAVOCEANO) mounted a major sea ice surveillance program, termed Project Birdseye, for the collection of data concerning the various ice features and conditions in the Arctic [61]. Information on the distribution, frequency, and size of water openings, ice ridges, stages of ice development, and other variables were needed to support the Naval ice prediction services. The early years of Project Birdseye were largely dependent on visual observation; hence data collection was strongly restricted by poor weather, extended periods of Arctic darkness, and the inherent human limitations for objectively and quantitatively estimating magnitudes of ice surface features.

In 1964, in order to overcome the weaknesses inherent in visual observations, NAVOCEANO began conducting airborne experiments over the Arctic pack ice to test and evaluate the usefulness of various remote sensor systems for mapping and measuring sea ice conditions and features. Then, in April 1968, a

Spectra-Physics Geodolite 3A Laser Profiler was flown onboard a Lockheed NC-121K aircraft to collect sea ice topography data north of Barrow, AK [61]. In addition to the laser range data, barometric pressure data were collected to measure aircraft altitude variations, and visible photographs were collected to aid with ice feature characterization and laser topography interpretation. Based on available literature, this is one of the first, if not the very first effort to utilize airborne laser altimetry for examining Arctic sea ice characteristics.

Some of the primary objectives of the initial NAVOCEANO efforts were to determine the usefulness of laser altimetry for identifying and measuring sea ice ridges, ice freeboard, water openings, and to distinguish profile signatures of first-year and multiyear ice. It was found that identifying the surface roughness characteristics using the laser terrain profile and visible imagery indeed made it possible to interpret the basic stages of ice development and to distinguish between first-year and multiyear ice [49]; however, useful estimates of ice freeboard were not possible because the aircraft altitude resolution was limited to 1.6 ft by the capabilities of the barometric pressure sensor, which was not sufficient for measurements of freeboard. Additionally, it was noted that the ability to measure the true ice surface height, and thus the total ice thickness and mass, was contingent upon knowing the snow cover depth [61].

In light of the aforementioned limitations, studies in the early 1970's focused on estimating and removing aircraft altitude variability from the ice elevation profiles, and placed emphasis on evaluating roughness and ridging characteristics that are not dependent on direct measurements of freeboard or highly-accurate knowledge of snow depth. In particular, Hibler[48] developed an automated method for estimating aircraft altitude variations from laser profiles by fitting a curve to minimum elevation points located on either side of pressure ridges. It had been shown that these minimum elevations are depressed slightly below water level, and thus serve as a relatively consistent reference surface and a close estimation of the local water level [128]. The smoothed minimum elevation curve can then be subtracted from the native laser profile to yield approximate freeboard topography elevations relatively free of aircraft altitude variations, which are in turn used to identify the locations of pressure ridge peaks. Hibler et al.[50] then derived theoretical models to describe ridge height and ridge separation distributions, and used the laser ridge peak observations to validate the theory. Hibler[47] built upon this work to develop a dynamic and thermodynamic sea ice model.

Subsequent work continued to further describe and classify ridge properties in the western Arctic

Basin. It was shown that pressure ridges are not randomly oriented, but rather prevalent wind and sea conditions favor certain orientations for ridge formation [49, 91]. Additionally, a ridging intensity parameter was defined in order to characterize the number and mean height of ridges over a given distance, which gave an estimate of the volume of deformed ice per unit distance [51]. It was shown that the theoretical ridge height and separation models were related to the ridge intensity and ice deformation, and thus have important implications for ice dynamics and mass balance. Distinct regions of different ridging intensity were identified, and the ridging intensity within these regions was found to vary annually. It was suggested that annual ridging variations may affect ice production and the overall ice mass balance on longer times scales. Accordingly, studies began to investigate the spatial and temporal variability of roughness and ridging distribution in the Arctic Ocean and peripheral seas (e.g [10, 117]).

By the mid-1970s the potential for airborne laser altimetry to be an effective and valuable method for measuring surface topography had been realized, and efforts grew to improve the measurement quality and broaden its application. During this time, NASA developed the Airborne Oceanographic Lidar (AOL), which had both profiling and experimental scanning capabilities, and was used for a variety of purposes, including lake and river basin mapping and for estimating vegetation biomass (e.g. [65, 67, 92]). The sea ice community began to assess the ability of airborne laser altimetry for measuring total ice thickness to expand upon thickness measurements provided by submarine sonar in order to obtain better estimates of the Arctic ice mass balance. The AOL was used to derive relationships between ice freeboard and ice draft using coincident laser profile data and submarine sonar data. It was found that the ice freeboard distribution probability density function (PDF) can be converted to an ice draft PDF by applying a simple coordinate transformation based on the measured mean freeboard and mean draft, and thus the ice thickness distribution can be derived from the surface topography measurement alone (e.g. [18, 127]). A strong relationship was also found to exist between ridge sail (i.e. the portion of the ridge above water) and ridge keel (i.e. the portion of the ridge below water) shapes and densities [114].

The advent of the Global Positioning System (GPS) offered a new method for determining the horizontal and vertical position of airborne laser altimetry systems, and in the mid-1980s NASA began conducting experiments to determine the positioning accuracy that could be achieved using kinematic, dual-frequency,

carrier phase, differential GPS (dGPS) processing techniques. It was found that close-baseline ($\lesssim$30 km) dGPS could provide 1-2 cm vertical precision and 10-25 cm vertical accuracy [66], which was an improvement over previous positioning methods. From that point forward GPS has been a standard component of airborne altimeter systems.

The use of airborne laser altimetry in the Arctic continued to broaden in the 1990s, and by the end of the decade there were dozens of commercial systems available and firms providing operational services [6]. During this time NASA developed the scanning Airborne Topographic Mapper (ATM) altimeter system, and continued to put considerable effort into assessing and minimizing the measurement error sources. A major component of this effort was further improving and refining GPS processing techniques. Eventually they were able to achieve an elevation measurement accuracy of 10-20 cm over long-baseline distances of several hundreds of kilometers (e.g. [68–70]). Spurred by the increased measurement performance offered by GPS and the ATM, NASA focused heavily on monitoring elevation changes of the Greenland ice sheet, and found that large sections of the southern and peripheral regions were thinning (e.g. [63, 64]).

With the rise of satellite radar and laser microwave altimetry through the 1990s and 2000s (e.g. ERS-1, ERS-2, Envisat, ICESat), and their use for measuring sea ice freeboard and thickness (e.g. [75, 77]), airborne laser altimetry was employed as a means to calibrate and validate the satellite observations (e.g. [19, 27, 31]). Following the failure of ICESat in 2009, NASA launched the IceBridge program in order to span the observational gap between ICESat and ICESat-2, which is set for launch in 2016. IceBridge is a major airborne campaign with annual deployments in the Arctic and Antarctic whose primary purpose is to continue the sea ice and ice sheet elevation data record between the ICESat satellite missions. Two laser altimeters being flown during this project are the ATM and NASA's Laser Vegetation Imaging Sensor (LVIS) [8], and they provide the scientific community with the most frequent and readily available airborne laser altimetry measurements of Arctic sea ice [62].

Despite the relative frequency of IceBridge flights and campaigns conducted by other institutions (e.g. [32, 34, 57], fine-resolution airborne laser altimetry data collections over Arctic sea ice continue to be spatially and temporally limited due to budget and weather constraints, and aircraft, sensor, and personnel availability. Broad-scale measurements of polar sea ice provided by satellite altimetry are also currently limited due to

the recent failure of Envisat in 2012 and the aforementioned gap between ICESat and ICESat-2. Presently, CryoSat-2 is the only satellite altimeter providing polar ice elevation measurements. Additionally, current sea ice research is heavily focused on assessing total ice thickness, and little attention is given to monitoring ice roughness and ridging distributions and variability. In light of the dramatic changes occurring in the Arctic, it is evident that there exists a need to increase the overall observational capabilities at high latitudes, and to collect fine-resolution data to monitor changes in ice topography which can be used to augment, calibrate, and validate the lower-resolution satellite data.

In recent years, technical advancements promoting sensor miniaturization and reduced cost have favored the development of new instrument payloads that are small, light, and inexpensive. These payloads are particularly suitable for use on small UAS, which have become more readily available to the scientific community and show great potential for geophysical research. UAS offer flexible payload integration options and often have less logistical requirements than manned research aircraft. They have the ability to operate in harsh environments, they have high maneuverability, and they can fly for long distances at low altitude. As such, they are well suited for collecting fine-resolution data in polar regions over a range of space and time scales.

The need for increased observational capabilities in the Arctic has been recognized by international organizations such as the Arctic Observing Network (AON), which is envisioned as a system of atmospheric, land-based, and ocean-based environmental monitoring capabilities that will significantly advance our observations of Arctic environmental conditions. In 2009 the AON identified four immediate needs of their sea ice observations component:

(1) A coordinated investigation to improve remote measurements of sea ice thickness and snow depth.

(2) Sustained sea ice mass balance measurements.

(3) Development of a portable, air-deployable, “disposable” energy balance station.

(4) Sustained observations of the energy balance of the atmosphere-ice-ocean boundary layer.

While airborne laser altimetry is not directly relevant to all of these needs, it is relevant for items

(1) and (2), and UAS in general could be equipped with various instrumentation to help address all four items. In addition to scientific applications, there is also a need for near-real-time observations of sea ice roughness, ridging and rubble distributions to foster safe shipping and offshore exploration activities in the Arctic. Groups such as the Arctic Monitoring and Assessment Programme (AMAP) have recognized the potential for UAS to help achieve the needs outlined by AON and the commercial industry, and they have created a UAS expert group to promote their use for Arctic environmental monitoring.

The first cryospheric studies to utilize UAS were conducted from 1999 to 2004 by Drs. Judy Curry and James Maslanik from the University of Colorado at Boulder (CU) who instrumented the AAI Corporation Aerosonde® UAS to collect basic meteorological measurements and sea ice photography north of Point Barrow, AK [23, 58]. Dr. Maslanik quickly recognized the potential for UAS laser altimetry, and began developing a system suitable for use on small UAS. These efforts culminated in the form of the CU Laser Profilometer and Imaging System (CULPIS), which was first used operationally in 2008 to collect topography measurements of the Greenland ice sheet, and then again in 2009 to measure sea ice freeboard and roughness in Fram Strait [21]. Assessing the capabilities of the CULPIS for ice sheet and sea ice surface profiling is one of the primary goals of this doctoral research.

1.3 Objectives and Approach

The Arctic ice pack is undergoing dramatic changes which have considerable impact on climate and commerce. Observations of ice freeboard (i.e. thickness) and ridging characteristics, and their distribution and variability throughout the Arctic Ocean, are crucial for estimating the ice mass balance and predicting the long-term survivability and conditions of the sea ice. Ice ridging characteristics, such as ridge height and ridge separation, also impact commercial shipping routes and offshore operations. The work presented here is motivated by the premise that the newly-developed, relatively inexpensive, and light-weight CULPIS laser altimeter system can be deployed on small UAS to measure fundamental topographic properties of Arctic sea ice, which will compliment and enhance the current observational capabilities, thereby improving our ability to monitor and predict sea ice conditions, evolution, and climate change.

The CULPIS was designed specifically to be integrated into relatively small UAS, and to provide fine-

resolution surface topography data and imagery. In general, this research focuses on assessing the capabilities of the CULPIS for measuring sea ice freeboard, roughness, and ridging. Attention is also given to assessing its abilities for measuring ice sheet elevation change, although that is not the primary application discussed herein. The research hypotheses and objectives are outlined below.

The motivating hypotheses of this research assert that:

(1) A relatively inexpensive laser altimeter system can be flown on UAS over broad regions in polar environments to collect fine-resolution surface elevation data which are pertinent for assessing the state of polar ice conditions, and which have sufficient quality to meet the requirements of the scientific community.

   (a) The CULPIS can measure sea ice freeboard and topography with a precision less than 10 cm.

   (b) The CULPIS can measure sea ice freeboard, ridge height, and ridge separation distributions.

   (c) The CULPIS can measure ice sheet elevation with an accuracy less than 20 cm.

   (d) The CULPIS can collect coincident elevation and imagery data to aid in their interpretation.

In accordance with these hypotheses, the primary objectives of this research are:

(1) Discuss the CULPIS sensors and their integration.

(2) Discuss the characteristics of the UAS in which the CULPIS has been integrated.

(3) Discuss the UAS campaigns in which the CULPIS has been flown.

(4) Establish the CULPIS elevation measurement accuracy and precision error magnitudes.

   (a) Review the results of prior error analysis efforts.

   (b) Establish the measurement error affiliated with each sensor: Laser, IMU, GPS.

   (c) Establish the errors affiliated with the UAS integration: sensor offsets and misalignments.

   (d) Establish the integrated, operational performance of the CULPIS.

   (e) Establish the deployment operations and processing steps required to achieve high-quality data.

(5) Compute geophysical parameters of interest from CULPIS data.

   (a) Discuss considerations for measuring sea ice freeboard and topography, and ice sheet elevation.

   (b) Present exemplary measurements collected during the UAS campaigns.

   (c) Compute sea ice freeboard and roughness measurements.

   (d) Identify sea ice ridges in the CULPIS profile data.

   (e) Compute sea ice ridge height and ridge separation distributions.

   (f) Compare observed ridge distributions to theoretical distributions for validation.

(6) Demonstrate the necessity of fine-resolution data for accurately measuring ridge distributions.

   (a) Simulate topography measurements collected with larger altimeter footprints.

   (b) Compute simulated ridge height and ridge separation distributions.

   (c) Compare simulated ridge distributions to true distributions and establish the difference error.

(7) Provide recommendations for improvements and future operations.

This work will make use of data acquired by the CULPIS during two UAS campaigns, the MUlti-Sensor Cryospheric Observation eXperiment (MUSCOX) and the Characterization of Arctic Sea Ice Experiment (CASIE). During MUSCOX the CULPIS was flown out of Ilulissat, Greenland and collected surface topography data and imagery over the Greenland ice sheet. During CASIE the CULPIS was flown out of Ny-Ålesund, Svalbard to collect surface topography data and imagery of sea ice in Fram Strait.

The general research approach combines instrument error analysis, sensor deployment over land and sea ice, data quality assessment, and extraction of geophysical conditions. Considerable emphasis is placed on evaluating the overall quality of the CULPIS data, and quantifying error sources. To obtain the most accurate surface elevation measurements, the aircraft must be accurately positioned and the laser measurement footprint must be geolocated to account for changes in aircraft attitude. The ability to accurately position the aircraft using dGPS processing, and the ability to profile a known reference surface, will be assessed using ground-based and flight-based data. These comparisons will focus on quantifying the CULPIS

sensor and system measurement error, and identifying considerations for measuring ice sheet elevation and sea ice freeboard and ridging. Observed sea ice ridge height and ridge separation distributions are compared to theoretical distributions to validate the CULPIS measurements, and to describe the 2009 summertime ice conditions in Fram Strait. The degree to which the observed ridge distributions change for larger laser footprints is also investigated.

The beginning of Chapter 1 presented the overarching scientific rational that sets the foundation and provides motivation for this research. The goal is not to directly investigate these topics, but rather it is to present a new observational method for collecting data, which will enhance our ability to address these topics in the future. Chapter 2 presents the CULPIS sensor specifications, Chapter 3 presents the UAS in which the CULPIS has been integrated, and Chapter 4 presents the campaigns in which the CULPIS has been flown. Chapter 5 is the CULPIS error analysis. It begins by reviewing the past error analysis efforts, then describes the individual error sources for each sensor, and finishes with evaluations of the full-system operational measurement error. The geophysical analysis presented in Chapter 6 is focused on extracting information on sea ice topography features and their distributions. The results and recommendations are summarized in Chapter 7. A considerable amount of information is also presented in the appendices, which should not be overlooked. Due to the relatively broad focus of this research, the appendices were used as a means to organize the diverse topics and present ancillary information while maintaining a clear focus in the main body of the text.

Chapter 2

The CU Laser Profilometer and Imaging System (CULPIS)

2.1 CULPIS Overview

The performance of the CULPIS is intended to meet the fundamental objectives that the system be capable of measuring changes in ice sheet surface elevation with an accuracy of <20 cm, and changes in sea ice topography with a precision of <10 cm. This is similar to the level of performance provided by the NASA ATM, LVIS, and the ICESat Geoscience Laser Altimeter System (GLAS) (see Table 5.1), which are well established laser altimeter systems [53, 66, 68, 70, 132]. In order to achieve the desired performance, the system measures aircraft position and attitude in order to account for aircraft roll, pitch, and vertical movement. Additionally, the CULPIS is designed specifically to be integrated into relatively small UAS and to collect fine-resolution surface topography and imagery in polar environments. Small UAS of the low altitude, long endurance (LALE) category typically provide a total payload capacity of 3-6 kg allocated to a volume of ~4000 cm^3, and a power availability of 18W [communication with Dr. James Maslanik].

Small UAS are particularly well suited for polar applications since they can operate with relatively minimal logistical requirements in conditions that would be risky for manned aircraft, such as sustained flight at low altitude above ground level, over open ocean, and in marginal weather. However, there are, of course, inherent risks associated with deploying newly developed technologies in challenging environmental conditions. While considerable effort is taken to reduce the risks associated with UAS missions in polar regions, it is important to recognize the fact that there is always the possibility of crashing or losing an aircraft during a campaign. Given the remote deployment locations, repairs in the field may be difficult or

impossible. In an ideal situation with sufficient funding and preparation time, multiple aircraft and payloads are available during campaigns to provide backup and redundancy for all systems.

To achieve the operational intentions, and to address the considerations mentioned above, the CULPIS package is designed to be relatively inexpensive, easy to reproduce and assemble, small in size and mass, and robust. These capabilities make it feasible to be integrated on a variety of aircraft, and to be utilized for flights-of-opportunity, which may offer limited preparation time. As will be shown, the system satisfies the mass, volume, and power constraints imposed by small LALE-class UAS (less than 6 kg, 4000 cm^3, and 18W), and the configuration of the components is somewhat flexible, such that the system can accommodate differing payload bay spatial orientations. The system is also able to operating in harsh polar environments, including temperatures below $-30\,^\circ$ C [communication with Dr. James Maslanik]. The CULPIS itself does not employ any methods or technologies to mitigate icing or other adverse weather conditions; however, the UAS generally have instrumentation and operational procedures that are used to address these issues, as discussed further in Chapter 3.

The CULPIS components are described in Section 2.2 and Appendix B, and the system architecture is described in Section 2.3. To date, the CULPIS has been integrated into four different UAS. These integration efforts and the aircraft characteristics are discussed in Chapter 3. The system's performance is assessed in Chapter 5 with respect to its ability to accurately and precisely resolve surface elevation. Readers are referred to Smith[107] and Edwards[25] for additional information on the component and system characteristics, functionality, and performance. Two additional cryospheric observational packages derived from the CULPIS, the CULPIS-X and the moulin probe, are presented in Appendix D. These systems will not be used for this research, but they illustrate the versatility of the CULPIS design and application.

2.2 CULPIS Sensor Suite

The CULPIS is a profiling (non-scanning) laser altimeter and imaging system that is composed primarily of relatively inexpensive, commercial off-the-shelf (COTS) components. As purchased, these COTS components have differing power requirements and data rates, and cannot be synchronized in time. Instrument synchronization is critical in order to facilitate laser range corrections and to take full advantage of the

complimentary altimetry and imagery datasets.

To alleviate the issues associated with COTS components, a custom power regulation printed circuit board (PCB) was designed to convert a single input power source to the voltages required by the various instruments, and a custom command and data handling (C&DH) PCB was developed to control the instruments and timestamp and log the measurement data [25]. The ability to power all the sensors from a single power supply, and the self-contained data logging capabilities, drastically simplify aircraft integration efforts. In this manner, the CULPIS does not need to interface with the autopilot hardware or software, and only requires one power source, either supplied by batteries or the aircraft.

The CULPIS altimetry sensor consists of a single-beam, nadir-pointing Laser Technology, Inc. Universal Laser System (ULS) rangefinder that is used to measure the distance from the aircraft to the ground surface, a NovAtel, Inc. Superstar II (SSII) GPS module that provides aircraft position, and a Microstrain, Inc. 3DM-GX1 inertial measurement unit (IMU) that provides aircraft attitude information. The imaging system consists of an Aiptek A-HD+ 1080P high-definition video camera, and a Canon PowerShot G10 still camera, both of which are used to provide imagery that are coincident with the altimetry data and can serve as a visual reference for the elevation measurements.

The CULPIS components are shown in Figure 2.1, and their power, mass, volume, and cost specifications are listed in Table 2.1. Additional specifications are provided in Appendix B. In overview, the CULPIS is a 12W system that draws 1A at 12V. It has a mass and volume of approximately 1.7 kg and 2560 cm^3, and the hardware costs roughly $5100 United States Dollars (USD)[1] . The system collects surface topography measurements at 400 Hz, which corresponds to a 7.5 cm along-track sample spacing when flown at 30 m/s, and it has a 30 cm footprint when flown at 100 m above ground level (AGL). The laser range and IMU angular measurement errors are 2 cm and 1°, respectively. The CULPIS measurement errors are further discussed in detail in Chapter 5.

[1] CULPIS costs are based on USD prices in spring 2010.

Table 2.1: CULPIS component specifications. See Appendix B for additional information.

Component	Current [mA]	Voltage [V]	Power [W]	Mass [g]	Volume [cm^3]	Cost [USD]
ULS laser rangefinder	200	12	2.4	660	1081	1800
3DM-GX1 IMU	65	9	0.6	75	146	1500
SSII GPS receiver (10 Hz)	180	5	0.9	35	62	350
Antcom L1 GPS antenna	35	5	0.2	184	112	260
Canon G10 still camera	220	7.4	1.6	425	385	490
URBI Still camera controller	80	5	0.4	12	26	125
Aiptek 1080P HD video camera	600	5	3.0	170	315	125
C&DH & power PCBs	170	12	2.0	140	431	450
Total	1000	12	12	1701	2559	5100

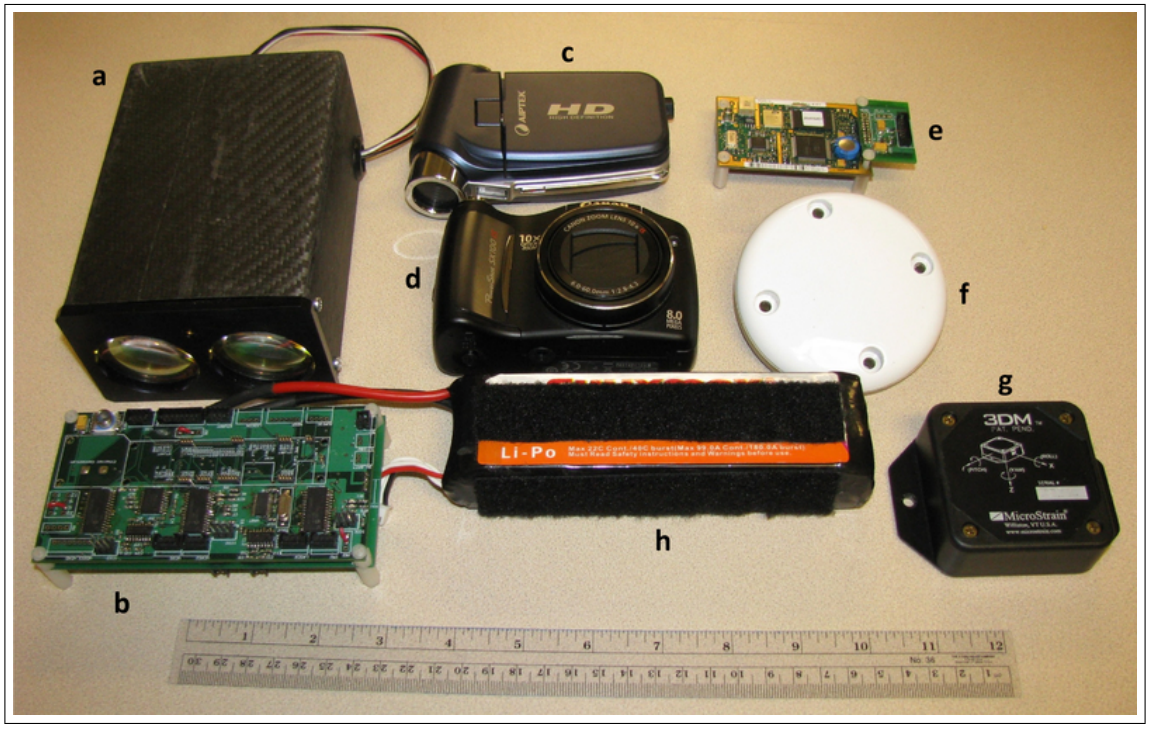

Figure 2.1: The primary components of the CULPIS: (a) laser unit, (b) C&DH and power regulation PCBs, (c) digital video camera, (d) digital still camera, (e) GPS receiver, (f) GPS antenna, (g) IMU, (h) power supply (battery as shown, or aircraft generated power).

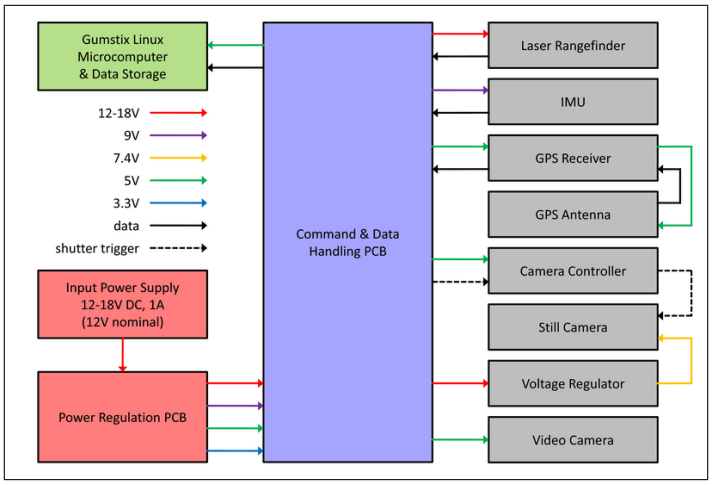

Figure 2.2: The CULPIS sensor integration architecture depicting the voltage distribution, data transfer, and camera shutter trigger signal. The system's power components (shown in red) regulate the input power and supply the C&DH PCB (shown in blue) with the voltages required by the various instruments. The C&DH PCB powers and operates the peripheral instrumentation (shown in gray), timestamps the measurements, and sends the data to the Gumstix (shown in green) for storage on a microSD card.

2.3 CULPIS Sensor Integration

The nominal CULPIS sensor integration architecture is shown schematically in Figure 2.2. A single input power source supplies 12-18V DC and 1A to the power regulation PCB, which then down-converts the voltage, and in turn, supplies the unregulated input voltage (12V nominal), 9V, 5V, and 3.3V to the C&DH PCB. The voltage down-conversion performed by the power regulation PCB has a power efficiency of 93%. The input power is provided by batteries or the aircraft generator, depending on the UAS being used.

The C&DH PCB serves as the interface between all the sensors. It supplies the unregulated input voltage, 9V, and 5V to the laser, IMU, and GPS receiver, and stamps their measurement data with GPS time. The timestamped data is then sent to the Gumsitx microcomputer where it is logged on a microSD card. The altimeter system components (laser, GPS, IMU) have a cumulative data rate of 37 MB/h, which facilitates 27 hours of continual operation when using a 1 GB storage card.

The C&DH PCB achieves accurate measurement timing by integrating the GPS receiver with a 32 kHz real-time clock. The GPS provides a standard reference time accurate to within one second, and the real-time clock provides microsecond-level precision. The process of collecting the instrument measurements and time stamping the data introduces a latency of 5 clock cycles, and as such, the timing of each measurement

is accurate to within 200 μs [25].

The C&DH PCB powers the video camera and the URBI camera controller with 5V, and supplies the unregulated input voltage to an adjustable voltage regulator, which then powers the still camera with 7.4V. The C&DH system also sends a voltage pulse to the URBI, which then triggers the still camera shutter to take a picture. The time at which the voltage pulse is generated is recorded on the Gumstix microSD card such that the time of each still image is known, and the images can be easily paired with the coincident GPS (for geolocation) and topography data. The time delay between consecutive shutter-trigger voltage pulses can be adjusted so pictures can be taken at any time interval. Additionally, it is possible to adjust the delay between powering on the URBI-controlled camera and the time at which the first picture is taken in order to save memory storage space by avoiding collecting unwanted imagery while the aircraft is still on the ground or is in transit to the study region of interest.

To achieve continual ground coverage from the still camera imagery, consecutive photos need to overlap. Equation (2.1) specifies the still camera shutter trigger timing separation, t, that is required to obtain a desired overlap percentage, O, between consecutive photos. The derivation of this equation is presented in Appendix C, along with Figure C.1, which illustrates the important camera timing parameters.

$$\boxed{t = \frac{[100 - O]\left[2H \tan\left(\frac{FOV}{2}\right)\right]}{V}} \tag{2.1}$$

where...

t = still camera shutter trigger timing separation

O = consecutive photo overlap percentage, [1-100%]

H = height above ground surface

FOV = camera along-track field-of-view

V = aircraft speed

There are several features of the cameras that are worth noting. The still images and video files are stored on the camera's SD cards, not on the Gumstix microSD card. A 32 GB SD card (one in the still camera and one in the video camera) can record ~10.6 hours of video data and ~12 hours of still photos

with 5 second separation (see Appendix B for camera data rate specifications). The still and video cameras must be manually turned on by pressing their power buttons prior to flight, and video recording must be manually engaged. The video camera can be modified by wiring external switches to the power and record circuitry, and these can then be mounted in convenient locations on the UAS for easy access. Re-engineering of the cameras for fully autonomous operation is potentially feasible, but was not carried out in keeping with the goal of minimizing cost and complexity.

The video data is not timestamped by the C&DH PCB, but the elapsed time is embedded in the video file. A simple, yet effective method for timestamping the video data is to hold a GPS receiver that displays the time-of-day in front of the camera, and the elapsed video time can then be related to the true time-of-day. Additionally, the CULPIS components should be mounted in a way that provides access to the camera's power and record buttons and the SD card ports, which is a non-trivial task given the space limitations of small UAS. Finally, the still and video imagery is only roughly geolocated by associating the image time with the UAS GPS location, and the imagery is not orthorectified. For our purposes it serves mainly as a visual reference for the topographic and ancillary payload measurements. These issues highlight the primary limitations of COTS components that require attention during aircraft integration and mission operations. With knowledgeable insight it is possible to mitigate these limitations and the constraints inherent to small UAS.

Chapter 3

Unmanned Aircraft Systems (UAS)

3.1 UAS Overview

The CULPIS has been integrated into four UAS platforms to date; the BAE Systems[1] Manta, the NASA Science Instrumentation Environmental Remote Research Aircraft (SIERRA), the AAI Corporation Aerosonde®, and the Insitu, Inc. ScanEagle. Table 3.1 provides general characteristics of these aircraft and their payload capabilities, and Figure 3.1 shows the aircraft and their payload instrumentation. It is common for the CULPIS to be integrated with supporting instrumentation to fully exploit the payload mass and volume capabilities, and to provide coincident, complementary measurements. Further discussion of these UAS and their operational use is provided below and in Sections 3.2 through 3.5.

The UAS discussed here all have differing characteristics and capabilities making them suitable for various applications; however, they are all able to be packaged in crates for shipping, making it feasible to transport them to virtually any location reasonably accessible by land, sea, or air. Once on site, they are all monitored and controlled by a ground control station (GCS) pilot-operator. The GCS communicates with the UAS via radio link when the aircraft is at close-range and in line-of-sight, and via Iridium[2] satellite link when down-range beyond line-of-sight. GPS waypoint coordinates are used to establish the UAS flight paths, and these can be modified in real-time to address unexpected situations that may be encountered during flight (e.g. poor weather, longer- or shorter-than-predicted flight endurance, changes in observational region-of-interest). Typically UAS operations require between 3-8 personnel, consisting of GCS pilot-operators,

[1] BAE Systems acquired Advanced Ceramics Research, Inc. in 2009
[2] Iridium Communications, Inc.: http://www.iridium.com/default.aspx

Table 3.1: Specifications and payload capabilities of the UAS in which the CULPIS has been integrated.

	Platform				Payload		
UAS	Wingspan [m]	Speed [m/s]	Endurance [h]	Range [km]	Capacity [kg]	Dimensions [cm]	Volume [cm^3]
Manta	2.5	21	6	453	6	38 x 25 x 13	12350
SIERRA	6.1	28	11	1108	45	55 x 40 x 40	88000
Aerosonde	3.4	26	20	1872	5	38 x 15 x 17	9690
ScanEagle	3.1	25	20	1800	3	23 x 18⌀	5853

Figure 3.1: The UAS in which the CULPIS has been integrated (left panels) and their associated payloads (right panels). The campaigns in which they have been involved are listed in blue. Some of the CULPIS components and ancillary sensors are not visible within the images.

R/C pilots, mechanics, payload specialists, and scientists.

On-board meteorological sensors, ancillary satellite data, and weather station measurements are generally used to detect potential icing conditions (freezing temperatures with high humidity), and these areas are avoided during flight whenever possible. Additionally, these UAS are typically equipped with heated pitot-static tubes and carburetors or fuel injection to prevent incorrect air speed measurements from being sent to the autopilot feedback control system, and to avoid engine failure. In calm atmospheric conditions they have been found to fly relatively straight and level with a slow back-and-forth rolling motion and a slight oscillation in the vertical position. It is relevant to note that the SIERRA, Aerosonde, and ScanEagle use engine-driven generators to supply power to the payloads, and as such, the payload power is limited by fuel consumption. At the time of writing, the Manta provides battery power, such that the payload operational duration is limited by its power draw and the battery capacity.

3.2 Manta UAS

The BAE Systems Manta UAS [98, 99] has a relatively short endurance (6 hours), but has a slow cruise speed (21 m/s) that promotes fine along-track spatial sampling of the surface topography. For its small size (2.5 m wingspan) it has considerable payload mass (6 kg) and volume (12,350 cm^3) capacity. The payload bay is fairly wide with a large hatch that facilitates easy installation and convenient access to the instrumentation. The Manta UAS flight control is managed by the Cloud Cap Technology[3] Piccolo autopilot, which includes inertial and GPS sensors and data-link radio. It supports beyond line-of-sight operations using Iridium satellite communications, during which time the autopilot telemetry is data is transmitted once every three seconds.

In 2008 the CULPIS was installed in the Manta and flown out of Ilulissat, Greenland to map glacier surface topography as part of the MUSCOX campaign sponsored by the National Oceanic and Atmospheric Administration (NOAA). Since the CULPIS is used to measure surface elevations based on the GPS altitude and laser range, it is important to know the relative vertical offset between these instruments. Following the CULPIS integration into the Manta, the GPS antenna was measured to be 15 cm above the laser

[3] Cloud Cap Technology: http://www.cloudcaptech.com/

sensor face. A pyrometer and a Resonon, Inc.[4] 60-band hyperspectral camera were in flown in addition to the CULPIS payload to provide ancillary surface temperature data and spectral imagery. These data are somewhat peripheral to the CULPIS, and as such, are not discussed further. However, exemplary hyperspectral imagery collected during MUSCOX is presented in Appendix E to illustrate the nature of these data. Extensive operational flight testing of the Manta and the CULPIS payload was carried out at BAE Systems in Tuscon, AZ to ensure proper functionality during the deployment. Additional information on the MUSCOX campaign is provided in Section 4.1.

3.3 SIERRA UAS

The NASA SIERRA UAS [26] is relatively large (6.1 m wingspan) UAS and can support a considerable payload (45 kg) with medium endurance (11 hours). The payload bay is a detachable nose-cone, which promotes accessibility and flexibility. Similar to the Manta UAS, the SIERRA UAS utilizes the Cloud Cap Technology Piccolo autopilot for flight control. Additionally, it was instrumented with a Systron Doner Inertial[5] C-Migit tactical-grade IMU, which measured aircraft attitude at 10 Hz with an accuracy of 0.06°.

In 2009 the CULPIS was installed in the SIERRA for the purpose of measuring sea ice topography in Fram Strait as part of the NASA CASIE campaign based out of Ny-Ålesund, Svalbard [89]. Due to the large payload capacity of the SIERRA, two ULS laser units and two still cameras were installed for the CASIE deployment. One laser was pointed nadir and the other was pointed 15° starboard of nadir. This combination acts as a pseudo-swath laser altimeter to provide cross-track topography measurements. As described in Appendix F, testing was carried out to evaluate potential interference between these two laser units. This testing identified the interference "signature" and assured that the data collected during CASIE was not compromised. The dual still cameras provide redundancy, make it possible to collect stereo pair imagery, and assure continuous photo coverage while flying at low altitude. Following the CULPIS integration into the SIERRA, the GPS antenna was measured to be 41 cm above the laser sensor heads.

An array of complimentary instrumentation was installed on the SIERRA during CASIE, including a pair of pyrometers, nadir- and zenith-viewing spectrometers, meteorological sensors, and a side-viewing

[4] Resonon, Inc.: http://www.resonon.com/
[5] Systron Doner Inertial: http://www.systron.com/

Artemis, Inc.[6] microASAR C-band (∼5.4 GHz) VV-polarization synthetic aperture radar (SAR) [24, 129]. To assist in the interpretation of the microASAR imagery, the CULPIS video camera was mounted with a view angle of 45° off nadir to align with the SAR swath location. Extensive operational flight testing of the SIERRA and the CULPIS payload was carried out at Crow's Landing airfield in California to ensure proper functionality during the CASIE deployment. More information on the CASIE campaign is provided in Section 4.2.

3.4 Aerosonde UAS

The AAI Corporation Aerosonde UAS has a long endurance (20 hours), but can only support a relatively small payload (5 kg). The Aerosonde is a well proven system with a long heritage of polar operations [13, 23, 58]. In 2009 the CULPIS was installed in the Aerosonde to map sea ice topography and wave height in Terra Nova Bay (TNB), Antarctica as part of the National Science Foundation (NSF) TNB UAS project [13]. For this deployment the CULPIS altimeter instrumentation was installed (laser, GPS, IMU), but the cameras were not because the Aerosonde was equipped with an independent imaging system. Further description of the TNB campaign is provided in Section 4.3.

3.5 ScanEagle UAS

As part of a collaborative effort, the CULPIS was installed in the University of Alaska's Insitu, Inc. ScanEagle UAS. The ScanEagle has a long endurance (20 hours), but can only support a relatively small payload (3 kg). The tight confines of the cylindrical payload bay make for challenging installation and difficult access to the camera data cards; however, the aircraft is modular and the payload bay is a removable section, which provides unique flexibility. The ScanEagle is launched with a pneumatic catapult and is recovered by flying into and catching on a hanging tether-line cable system. Without the need for a runway or smooth surface for take-off or landing, it possible to operate the ScanEagle from virtually any location, including large ship decks. Integration of the CULPIS into the ScanEagle payload bay was carried out with assistance from CU students working for the Research and Engineering Center for Unmanned Vehicles (RECUV). Special

[6] Artemis, Inc.: http://www.artemisinc.net/

thanks is extended to Josh Casserino and Eric Hall for their contribution to that effort. The ScanEagle CULPIS package has not yet been used operationally, but it has undergone extensive testing, as described in Appendix G, to ensure its ability to withstand the 8+ G launch acceleration force. This payload is fully functional and currently available for scientific investigations.

Chapter 4

Unmanned Aircraft Campaigns

4.1 Multi-Sensor Cryospheric Observation Experiment 2008 (MUSCOX)

The CULPIS, along with a supporting array of instrumentation, was integrated into two Manta UAS for the NOAA-sponsored MUSCOX campaign carried out in July 2008. The MUSCOX project was the first time UAS were used in Greenland for scientific purposes, and the primary goal was determination of the changing volumes of surpraglacial melt water lakes through the fusion of disparate datasets from in situ, airborne, and satellite sensors [1]. Furthermore, the project was a pilot study to demonstrate that fine-resolution, scientific-quality ice surface topography data and imagery can be collected with the CULPIS flown on UAS.

The MUSCOX study area and the flight tracks for the five science mission flights over the ice sheet are shown in Figure 4.1. The black box indicates the flight domain approved by the Danish Civil Aviation Administration. Data collection efforts were focused in the vicinity of three supraglacial melt lakes, which are the black features visible in the Moderate Resolution Imaging Spectroradiometer (MODIS) satellite image. A detailed view of the flight tracks within the study region is shown in the bottom panel of Figure 4.1. Adjacent tracks are spaced approximately 500 m apart. The science flights typically lasted 3-4 hours and covered 250-400 km per flight. By the end of the campaign, roughly 10 hours had been spent within the study region collecting ice sheet observations.

The Manta UAS and the CU personnel who were on deployment in Ilulissat, Greenland during the MUSCOX campaign are shown in Figure 4.2. This picture provides a sense of scale for the size of the Manta

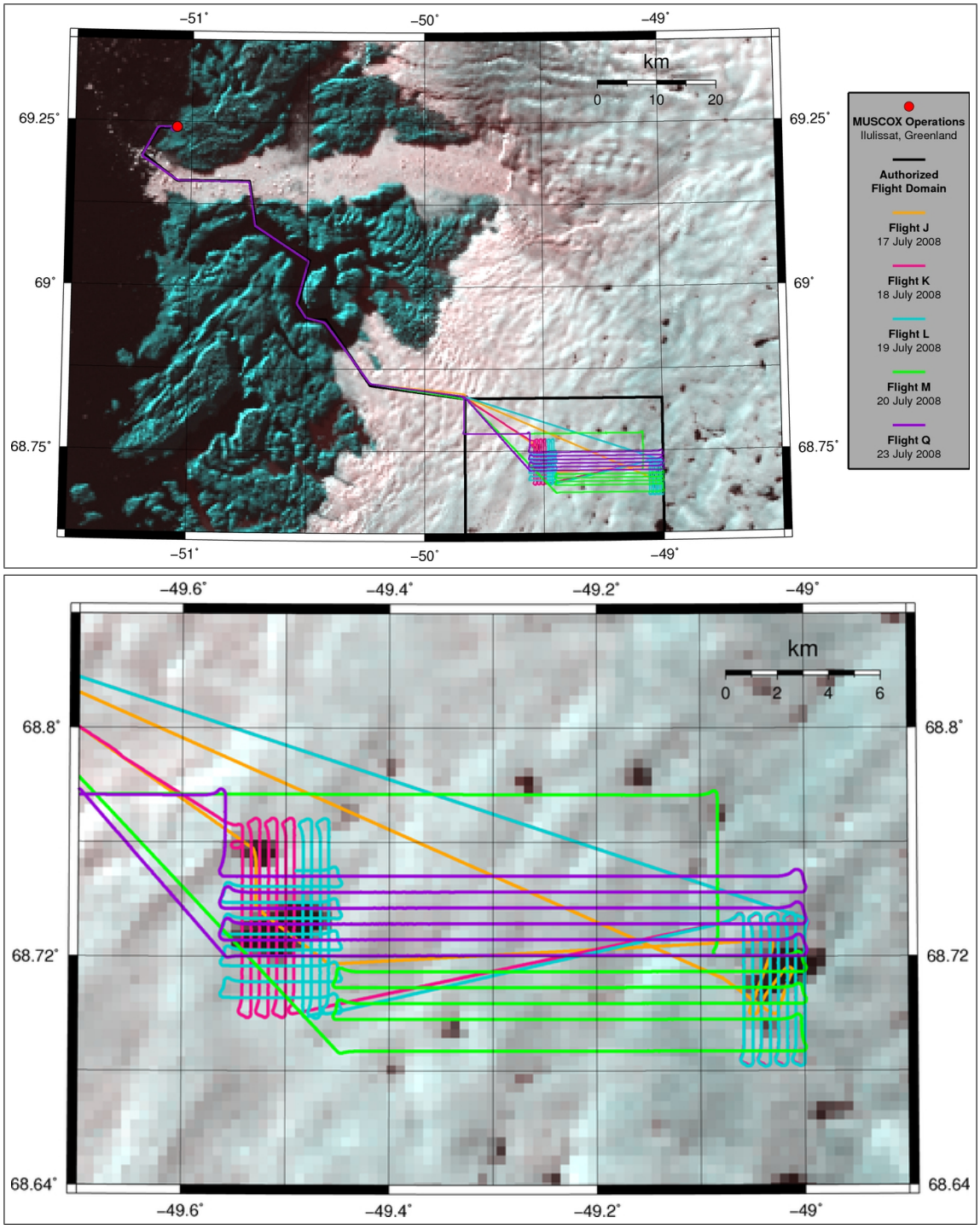

Figure 4.1: The top panel shows the full MUSCOX flight domain and flight tracks. The deployment was based out of Ilulissat, Greenland, and the domain was authorized by the Danish air traffic authorities. Jakobshavn Isbræ and the Ilulissat Icefjord are discernible toward the top of the image. The bottom panel is a closeup view of the scientific study region, which was focused around the vicinity of several supraglacial melt lakes. The background image in both panels is a false-color MODIS scene collected on 8 July 2008. Flights A-I, N, O, and P were operational checkout flights and are not shown here.

Figure 4.2: The Manta UAS and the CU personnel in Ilulissat, Greenland during the MUSCOX campaign. From left to right, James Maslanik, R. Ian Crocker, and John Adler.

UAS and depicts the general environmental surroundings in the vicinity of the Ilulissat airport.

As discussed by Adler[1], supraglacial melt lakes form on the Greenland ice sheet during the summer months and drain rapidly throughout the melt season as the ice sheet slowly shits and cracks. However, melt lake dynamics and the significance of their drainages for enhancing the ice sheet flow are not well understood. As such, it is important to quantify the melt lake water volume since their drainage via crevasses or moulins enables the injection of water directly into the ice sheet, which may contribute to basal lubrication. Accordingly, one of the goals of MUSCOX was to generate a fine-resolution digital elevation model (DEM) of the ice sheet surface in order to measure the areal extent, volume, and potential drainage routes of supraglacial melt lakes. The DEM generated from CULPIS data is presented as Figure L.1 on page 174, and serves as an example of the CULPIS utility for ice sheet topography mapping. Adler[1] used the CULPIS data, and a suite of ancillary measurements, to further study the ice sheet melt dynamics. For the purposes of this research, the MUSCOX CULPIS data are used primarily for assessing the quality of the laser altimetry measurements and for qualitatively demonstrating the system's utility for making ice sheet observations.

4.2 Characterization of Arctic Sea Ice Experiment 2009 (CASIE)

In July 2009 the CULPIS was flown onboard the SIERRA UAS to map sea ice topography in Fram Strait off the coast of Svalbard during the NASA-sponsored CASIE project [89]. A suite of supporting instrumentation was also flown, including nadir- and zenith-pointing spectrometers, a pair of pyrometers, the microASAR [24, 129], and meteorological sensors, taking advantage of the large payload capacity of the aircraft. Operations were based out of Ny-Ålesund, Svalbard, and the flight tracks for the six science mission flights are shown in Figure 4.3. The black triangle indicates the flight domain approved by the Norwegian Civil Aviation Administration. The science flights typically lasted 6-11 hours and covered 500-1100 km per flight. Unfortunately, the CULPIS altimetry data were not recorded during flight 10, likely due to a poor connection of the data storage card. By the end of the campaign more than 24 hours had been spent flying over more than 2500 km of sea ice. Science mission flights occurred in late July, toward the end of the melt season. The sea ice appeared to have minimal snow cover and extensive melting.

The SIERRA UAS and the NASA and CU personnel who were on deployment in Ny-Ålesund, Svalbard during the CASIE campaign are shown in Figure 4.4. This picture provides a sense of scale for the size of the SIERRA UAS and depicts the general environmental surroundings in the vicinity of the Ny-Ålesund airport.

The broad, overarching intention of CASIE was to leverage the suite of measurements, along with ancillary satellite data, to examine sea ice morphology, determine how ice roughness and thickness vary as a function of ice type and ice age, and improve our understanding of how the ice physical properties are expressed in remotely-sensed data [89]. This is similar in premise to a study discussed by Comiso et al.[18] in which multisensor intercomparisons were used to investigate relationships between the sensor measurements in terms of ice cover characteristics to assess the potential utility of using a combination of two or more sensors, and to determine the extent to which geophysical ice parameters derived from one sensor can be verified with the aid of other sensors. Conducted in the mid-1980s, that study was motivated by the fact that numerous measurements (e.g. microwave BT, SAR backscatter, radar and laser altimetry) were beginning to be collected from satellites (e.g. ERS-1, EOS) and aircraft (e.g. NASA P-3A). If the performance of

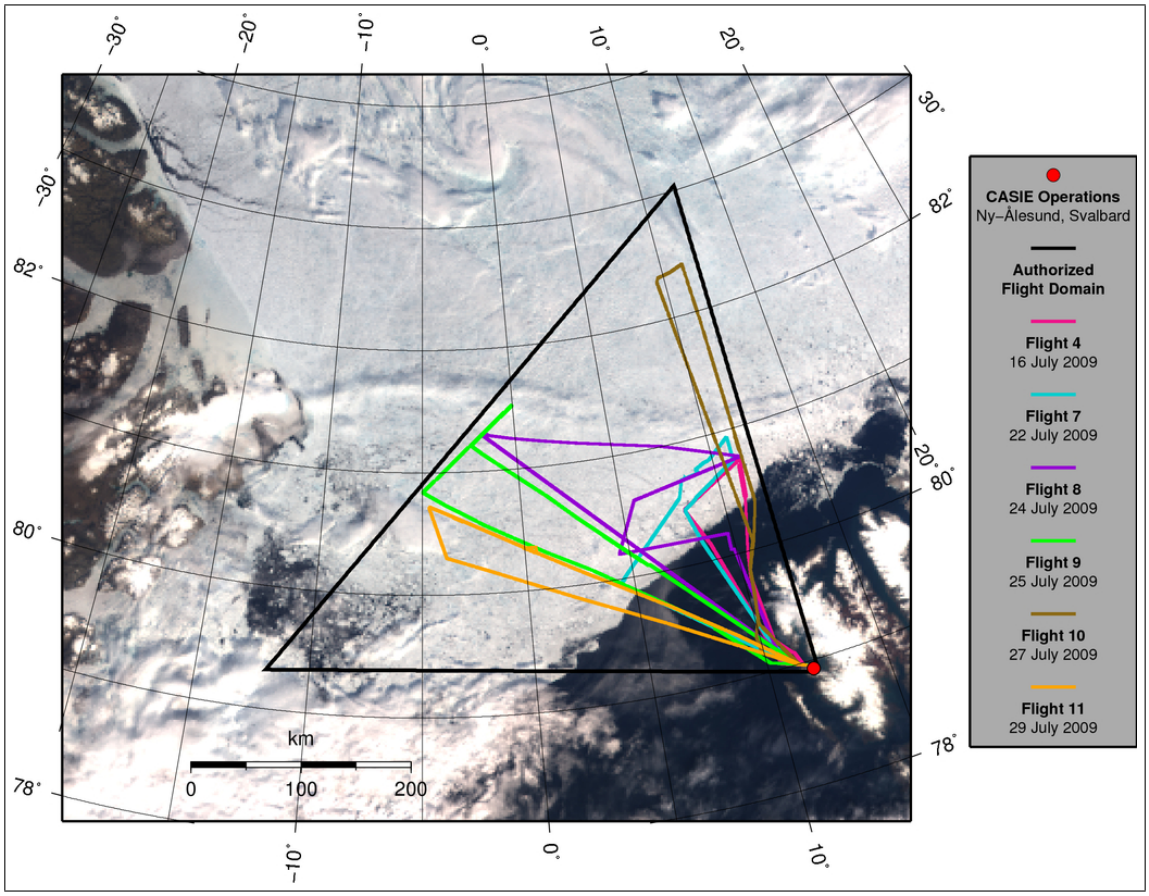

Figure 4.3: The CASIE study region and the science mission flight tracks. Data collection efforts were restricted to the flight domain authorized by Norwegian air traffic authorities. The deployment was based out of Ny-Ålesund, Svalbard. The background image is a true-color MODIS scene collected on 24 July 2009. The dark-colored northeastern coast of Greenland is visible toward the top left. The white sea ice pack and dark blue open ocean are clearly evident, and the snow-covered island of Spitsbergen, Svalbard is located toward the bottom right. Flights 1-6 were operational checkout flights and are not presented here.

Figure 4.4: The SIERRA UAS and the NASA and CU personnel in Ny-Ålesund, Svalbard during the CASIE campaign.

the sensors and the interrelation of their measurements could be validated in terms of their inferred ice parameters (e.g. ice extent, ice age, ice thickness, ice concentration), then their value for monitoring of global sea ice would be greatly enhanced.

The CASIE project aims to accomplish a similar task, but it is focused on assessing new sensors and technologies affiliated with UAS operations to determine their data quality and their utility for complimenting and augmenting satellite measurements of sea ice conditions. As discussed by Tucker et al.[118] and illustrated by Figure 4.5, ice discharging through Fram Strait can originate in essentially any part of the Arctic Basin. Floes that form in the western Arctic arrive at the strait via the Transpolar Drift and may include a relatively large percentage of multiyear ice, while ice from the Laptev and Kara seas can take a more direct approach to the strait and should include a larger percentage of younger ice. Thus the ice transiting Fram Strait could have originated in any number of different areas within the Arctic Basin. This suggests that if ice properties are strongly influenced by area of origin, or the environmental conditions they experience, then a large variation in properties might be observed in the Fram Strait. For these reasons, Fram Strait was chosen as the CASIE study region. The research presented herein focuses on the analysis of the CULPIS altimetry data, but the full multisensor dataset collected during CASIE has not been exploited and provides considerable potential for further analysis.

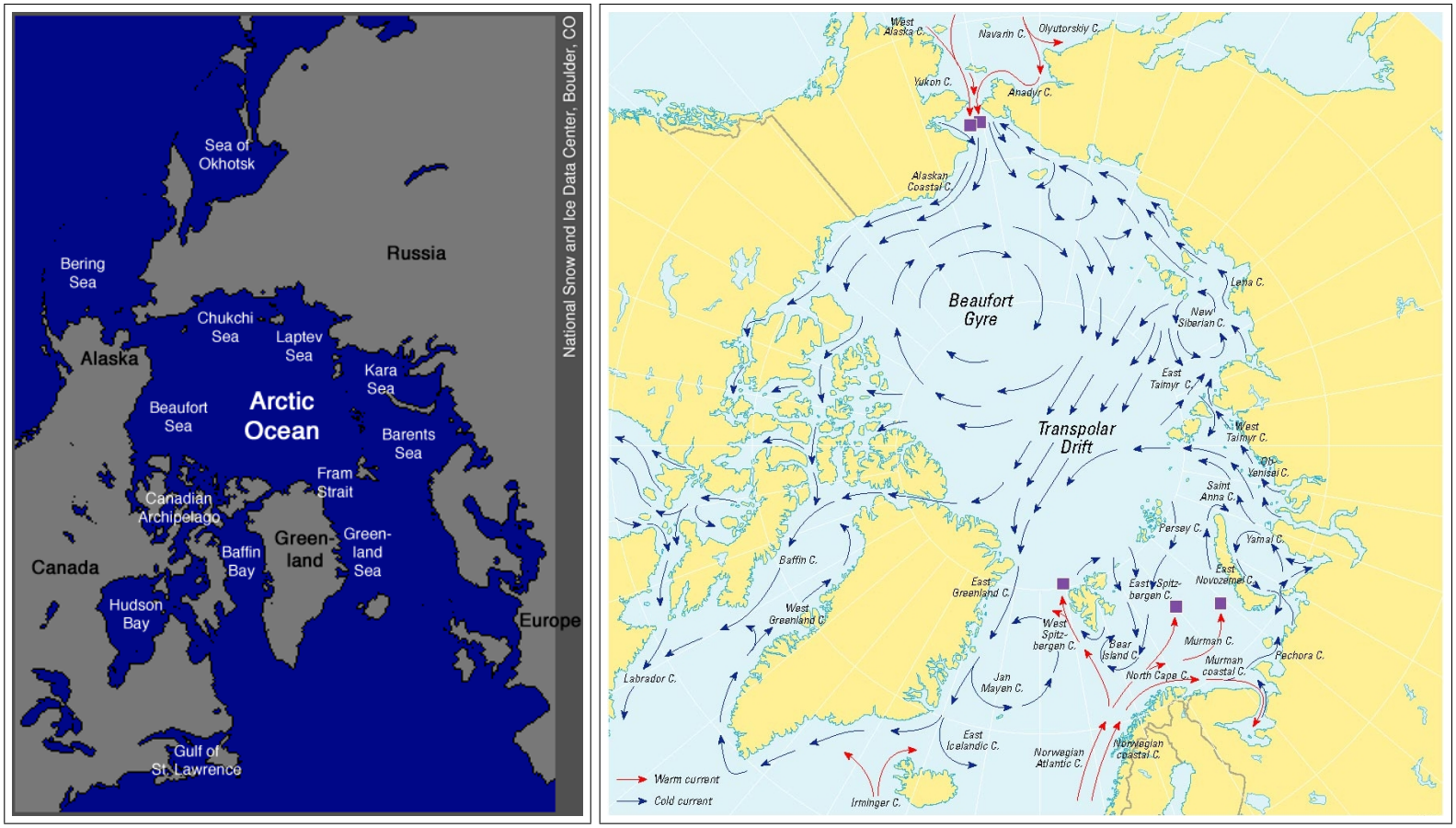

Figure 4.5: The seas of the Arctic Ocean and the ocean circulation. Ice exported through Fram Strait may have originated nearly anywhere within the Arctic Basin. The image at left is courtesy of NSIDC, and the image at right is courtesy of AMAP Assessment Report: Arctic Pollution Issues, 1998.

4.3 Terra Nova Bay 2009 (TNB)

In September and October 2009 the CULPIS laser altimeter instrumentation was flown onboard the Aerosonde UAS to map sea ice topography and wave heights in the Southern Ocean between McMurdo and TNB, Antarctica as part of the NSF-sponsored TNB UAS project. The Aerosonde was launched and operated from the Pegasus ice runway near McMurdo. The primary objective of this campaign was to make wintertime observations of the atmosphere, open ocean, and sea ice surface to investigate the boundary layer evolution of the katabatic winds propagating over the polynya in TNB. Flight conditions were especially challenging, with temperatures below -30°C, winds in excess of 15 m/s, and flight times up to 17 hours [13]. The TNB project is not a primary focus of this article, but it is mentioned here to illustrate the capabilities of UAS and the CULPIS to collect science data in harsh conditions over broad ranges.

Chapter 5

CULPIS Error Analysis

5.1 Error Analysis Overview

The primary objective of this chapter is to assess the CULPIS measurement capabilities for the purpose of glacier and sea ice surface profiling. Previous investigations carried out by Smith[107] and Edwards[25] utilized laboratory bench-testing and model simulations during the instrument design phase in order to quantify the theoretical surface measurement performance. The work presented here builds upon those efforts, but focuses on characterizing the fully-integrated CULPIS operational performance using data collected in the field during the MUSCOX and CASIE projects. These are the first two campaigns in which the CULPIS was deployed operationally to collect scientific topography data of ice sheets and sea ice. Evaluating the measurement performance using data collected during campaign operations is a logical and essential exercise to follow the previous laboratory and model testing as it will capture variable GPS errors dependent upon the time and geographic location of deployment, and will illuminate practical issues associated with the aircraft integration, the flight conditions, and the surface target of interest.

The assessment of airborne laser altimetry measurement capabilities is a fairly involved process which has a long and continually ongoing history of activities. The main objective of these efforts is to understand the sampling characteristics and error sources of the altimeter system, evaluate how those impact the surface elevation measurements, and then identify the resulting implications for geophysical analysis. With the development of new technologies and the with the growth of airborne laser altimetry applications, performance assessments are routinely conducted to evaluate the measurement quality. As GPS became readily available

Table 5.1: The nominal sampling characteristics and measurement accuracy for select NASA laser altimeter systems. The ATM and LVIS are airborne systems and ICESat is a satellite system.

Laser Altimeter System	AGL Flight Altitude [m]	Beam Divergence [mrad]	Footprint Diameter [cm]	Spatial Sampling [m]	Vertical Accuracy [cm]	Reference
ATM	800	2.1	85	400 m wide swath	<20	[68, 70, 105]
LVIS	10,000	2	2000	2 km wide swath	<20	[8, 52, 53]
ICESat	600,000	60 e^{-3}	7000	170 m along-track	<15	[11, 73, 132]

during 1980s, NASA began evaluating dGPS positioning capabilities for use with it's AOL altimeter system [66]. For several years following the development of their ATM system they placed considerable effort toward evaluating its capabilities for detecting ice sheet elevation change and beach erosion, and for calibrating and validating ICESat measurements (e.g. [68–70, 105, 131]). Similar assessments were also carried out for the LVIS system to evaluate its ability to measure forest canopy structure and estimate biomass [8, 52, 53].

The sampling characteristics and measurement accuracy of three NASA altimeter systems are shown in Table 5.1. These systems represent the typical performance capabilities which are available to the scientific community, and they serve as reference relative to which the CULPIS will be evaluated. More specifically, the NASA IceBridge science team has defined baseline performance requirements for measuring ice sheet and sea ice elevation, which are adopted as the goal performance for CULPIS. They specify that ice sheets should be measured with a vertical accuracy of 20 cm or better, and sea ice surface elevations should be measured with a shot-to-shot precision less than 10 cm with a footprint diameter less than 1 m spaced less than 3 m apart[1] .

The performance of the ATM and LVIS airborne systems have been determined through a number of methods. To begin, the instrument locations and alignments within the aircraft are very accurately measured during integration (location accuracy of 1 mm, angular alignment accuracy of 0.01° [70]). Then, the aircraft trajectory, attitude, and position are determined using highly accurate IMU angle measurements (accuracy of 0.02° [70]) and dGPS altitude measurements (accuracy of ∼10 cm [70]). The importance of these measurements will become more evident throughout this chapter. Finally, the operational system performance is evaluated by collecting repeat measurements over surveyed "ground truth" reference surfaces,

[1] IceBridge measurement requirements available at the science team webpage: http://bprc.osu.edu/rsl/IST/

such as airport runways (e.g. [68, 70]), ice sheets (e.g. [68, 70]), beach coastline (e.g. [69, 105]), and open ocean (e.g. [131]). Achieving the full breadth of these efforts is beyond the scope of this research, but these past studies are used as a guide and a reference for the CULPIS performance assessment.

The coordinate frames and sensor measurements associated with airborne laser altimetry are shown in Figure 5.1. The relative alignment and offsets of these frames are directly relevant for deriving surface elevation and assessing the error in these elevations. The inertial reference frames affiliated with the earth ellipsoid (e), local sea level (sl), and the aircraft vehicle (v) are offset in the vertical direction, but assumed to be aligned horizontally over the relatively short distance between the laser measurement point (m) and the vehicle nadir point on the surface. The laser, IMU, and GPS frames are fixed within the aircraft body (b) frame, but are offset and possibly misaligned with one another and with the inertial frames. Uncertain knowledge of these offsets and alignments is the source of error in airborne laser altimetry surface elevation measurements, as discussed throughout this chapter. Readers are referred to Edwards[25] for a more comprehensive review of these coordinate frames.

Due to project budget and time constraints, it was not possible to measure all the offsets and alignments between the sensor frames (laser, IMU, GPS, aircraft body), and most of them are not accounted for in the surface elevation computation. The exception is that the vertical offset between the GPS antenna and the laser sensor face was measured following the UAS integrations, and were found to be ∼15 cm for the Manta (MUSCOX) and ∼41 cm for the SIERRA (CASIE). Without the horizontal offset and alignment measurements, their values are set to zero for convenience, which implies perfect co-location and alignment between the frames. It is clearly not physically possible for the sensor and aircraft frames to be located at the same point in space, and the approach taken here does introduce errors into the surface elevation measurements due to the lever-arm offsets and sensor misalignments.

Given the available information, the east, north, and vertical (ENV) location of the laser footprint measurement point on the Earth's surface is computed using Equation 5.1. The yaw/heading is measured clockwise relative to true North, and the footprint (fp) elevation (V_{fp}) is relative to the WGS84 ellipsoid. Notice the the vertical separation between the GPS antenna and laser sensor face (Z_{gl}) is subtracted from the GPS altitude (V_{gps}) as a means to account for this offset and effectively locate the GPS antenna in the

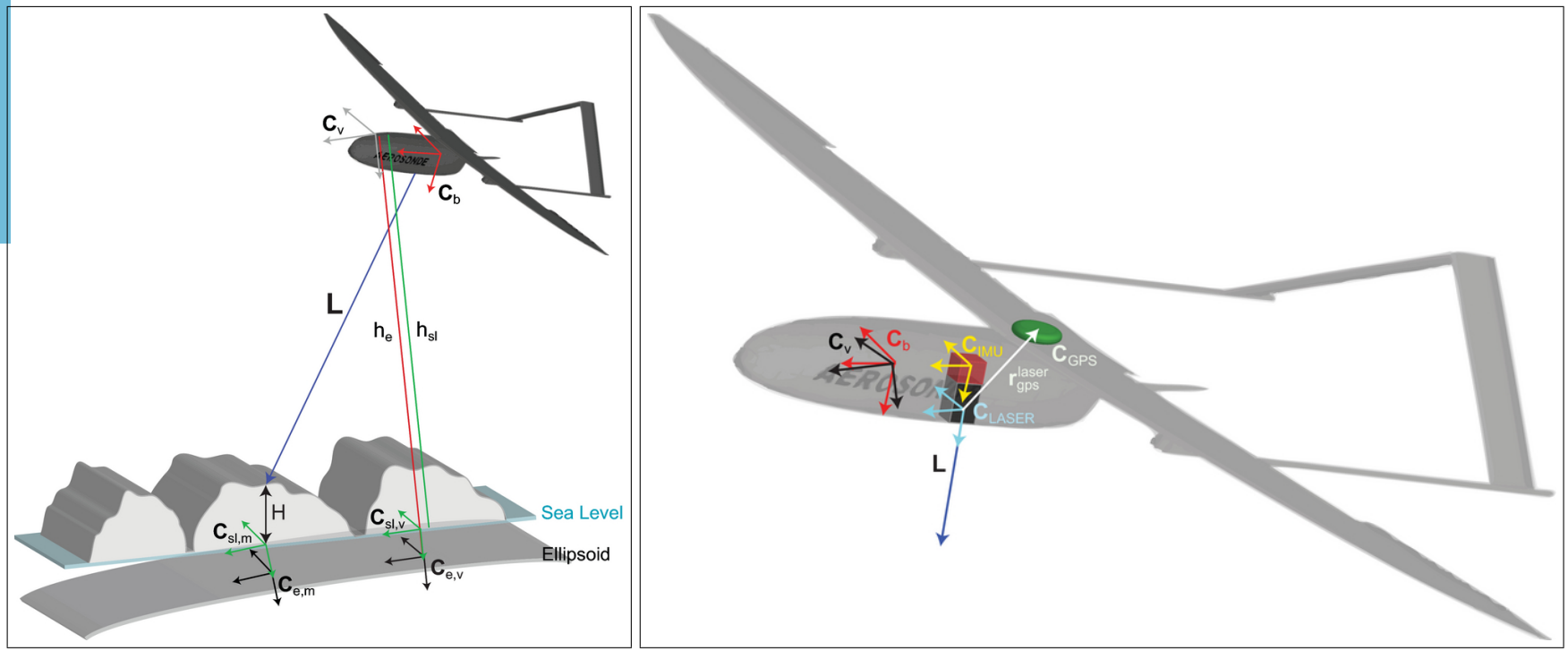

Figure 5.1: The relevant airborne laser altimetry coordinate frames. The frame orthonormal basis vectors are described as: $\mathbf{C}_{f,s}$. The subscript f indicates the frame: ellipsoidal (e), sea level (sl), vehicle (v), body (b), laser (l), IMU, (i), and GPS (g). The subscript s indicates the surface location: measurement point (m), or the vehicle point (v). The aircraft height above the ellipsoid (h_e) and above sea level (h_{sl}) are shown, along with the laser range measurement (L), and the lever-arm vector between the laser and GPS frames (r_g^l), which has an associated alignment rotation matrix (implied). The laser surface measurement location and ellipsoidal height are computed using Equation 5.1. The WGS84 ellipsoid is used throughout this research, unless otherwise noted. These figures were taken from Edwards[25].

same horizontal plane as the laser. However, any horizontal offset that may exist between the antenna and laser will translate into the vertical dimension as the aircraft attitude changes and the coordinate frames rotate accordingly. The elevation error introduced by this horizontal lever-arm effect is discussed further in Section 5.3.4. Future effort should be placed on measuring all the frame offsets and alignments, and the mathematics for deriving the laser footprint surface location (i.e. Equation 5.1) should be updated to account for them.

$$\begin{pmatrix} E_{fp} \\ N_{fp} \\ V_{fp} \end{pmatrix} = R_{yaw} \cdot R_{roll} \cdot R_{pitch} \cdot \begin{pmatrix} E_{gps} \\ N_{gps} \\ V_{gps} - Z_{gl} - L \end{pmatrix} \tag{5.1}$$

where...

$$R_{roll} = \begin{pmatrix} \cos(\phi) & 0 & \sin(\phi) \\ 0 & 1 & 0 \\ -\sin(\phi) & 0 & \cos(\phi) \end{pmatrix}$$

$$R_{pitch} = \begin{pmatrix} 1 & 0 & 0 \\ 0 & \cos(\theta) & -\sin(\theta) \\ 0 & \sin(\theta) & \cos(\theta) \end{pmatrix}$$

$$R_{yaw} = \begin{pmatrix} \cos(\psi) & -\sin(\psi) & 0 \\ \sin(\psi) & \cos(\psi) & 0 \\ 0 & 0 & 1 \end{pmatrix}$$

Z_{gl} = vertical offset between the GPS antenna and laser sensor face

L = laser range measurement

ϕ = roll

θ = pitch

ψ = yaw/heading

(5.2)

As described above, CULPIS surface elevation measurements are derived directly from the laser range data, the IMU pointing data, and the GPS position data. The IMU and GPS data are interpolated to the laser sample times to generate a synchronous dataset, and Equation 5.1 is used to compute the east, north, and vertical coordinates of the laser footprint location relative to the WGS84 ellipsoid. This is the means by which surface elevation is derived from the CULPIS sensor data throughout this study. The measurement error inherent to each individual sensor will translate into errors in the derived surface elevations. Accordingly, the assessment presented in this chapter begins by examining the error affiliated with each sensor, which includes a more detailed discussion of the sensor alignment and offset errors, and finishes with an analyses of the full-system operational performance and its practical surface profiling capabilities.

The GPS vertical positioning inaccuracies contribute substantially to the CULPIS elevation measurement error budget, and thus garners a considerable amount of attention in Section 5.3.3. Appendix I provides a review of basic GPS positioning methodology, mathematical formulation, and inherent metrics which are used to assess the solution quality. The primary goal of the GPS assessment is to quantify the vertical error of the position solutions computed using the NovAtel Waypoint 8.10 GrafNav GPS processing software. This software package serves as a black-box post-processing tool utilized to perform kinematic, L1 carrier phase, differential positioning of the CULPIS GPS data. While this software provides substantial positioning capabilities and a certain level of convenience, there is minimal description of its proprietary processing algorithms. As such, it was necessary to become familiar with its functionality and to explore its capabilities in order to achieve the best-possible GPS positions. Furthermore, the accuracy of dGPS is known to degrade over long baseline distances, so it is important to establish the positioning capabilities for the baselines encountered in Arctic campaigns.

The strategy implemented to assess the operational quality of CULPIS altimetry measurements is based on first performing a ground-based GPS survey of the airport runway at the deployment location in order to generate a "truth" reference surface using local-baseline dGPS ("local" implies a very-short baseline distance, <300 m). The survey data are also used to assess the vertical error of dGPS position solutions computed using a wide range of baseline distances. CULPIS data are then collected during repeat flights over the runways, and the derived surface elevations are compared to the "truth" reference surface to evaluate

the operational quality of the CULPIS measurements. This method is outlined as follows:

(1) Generate a "ground-truth" reference surface by surveying the airport runway.

- Collect repeat, ground-based GPS elevation data along the central transect of the runway.
- Compute the L1-carrier, local-baseline, dGPS position solutions for the runway transect data.
- Compute the mean transect elevation profile and use this as the "truth" reference surface.

(2) Evaluate the vertical position quality of the local-baseline runway transect dGPS solutions.

- Compute differences between local-baseline dGPS transect data and the reference surface.
- Compute mean, standard deviation, root-mean-square (RMS), and variogram error statistics.
- This represents the highest-quality dGPS positioning capabilities.

(3) Evaluate the runway transect dGPS quality of solutions computed using a range of baselines.

- Compute L1 dGPS runway transects using all available reference stations within 1000 km.
- Compute differences between all the baseline dGPS transects and the reference surface.
- Compute mean, standard deviation, RMS, and variogram error statistics.
- This represents the CULPIS dGPS positioning quality over a range of baselines.

(4) Evaluate the CULPIS operational system performance.

(a) Compare runway elevation profile data collected during flight to the runway reference surface.

- Compute differences between the runway profile data and the reference surface.
- Compute mean, standard deviation, RMS, and variogram error statistics.
- This represents the CULPIS measurement quality achieved during MUSCOX and CASIE.

(b) Compare co-located data collected at the intersections of MUSCOX crossover flight-lines.

- Compute the elevation difference mean, standard deviation, and RMS error statistics.
- Additional characterization of the CULPIS measurement quality during MUSCOX.

(c) Investigate the sea ice surface profiling capabilities using data collected during CASIE.

- Discuss considerations for profiling sea ice freeboard, roughness, and ridging.

5.2 Prior Error Analysis

Before delving into the operational error analysis of the CULPIS, it is relevant to review past analyses conducted by Smith[107] and Edwards[25] during the development of the system. Their efforts led to the current system's hardware and software architecture that is described in Chapter 2, and provides a foundation for the analysis presented in the following sections.

Smith[107] began investigating the potential for a small UAS altimeter by simulating the systematic performance that could be expected onboard an Aerosonde UAS, and by identifying the surface elevation measurement error sources. He focused primarily on evaluating the error of two IMU sensors that were property of the research group, the Microstrain 3DM and the 3DM-G. Laboratory static testing revealed that these two IMUs have similar performance, with roll and pitch error standard deviations of $\sim 0.05^\circ$, and a higher yaw error standard deviation of $\sim 0.18^\circ$. Both units were found to have minimal systematic drift. Dynamic testing revealed that the angular determination error increased significantly up to 10° at angular rates $>100^\circ/s$, which is well beyond the rate expected during nominal UAS flight.

Data collected during CASIE reveal that typical aircraft attitude dynamics are on the order of $1^\circ/s$ (see Section 5.3.2). At a slightly more conservative rate of $2^\circ/s$, Smith's tests indicate that the IMU measurement error would be $\sim 1^\circ$. The manufacturer states a pointing error of $\pm 2^\circ$ in dynamic environments; however, it is likely that this error level is valid for angular rates higher than those expected during typical UAS flight, and thus, the measured error of $\sim 1^\circ$ is quite reasonable. Smith used the empirical error statistics to parameterize an IMU sensor model, and then simulated elevation measurements collected over a flat surface. The simulations showed that the IMU angular determination error introduced an error of ± 1 cm to the elevation measurements during low-dynamic, near-level flight at 100 m AGL. It was also found that the simulated GPS altitude error contributed the most error to the elevation measurements.

Edwards[25] built upon Smith's work with a primary objective to evaluate "the operational and instrumental considerations for a high-accuracy laser profiling system mounted on a small UAS measuring the topography and thickness of freeboard sea ice in the Arctic." He began by quantifying the ULS laser measurement error, and found that it has a precision (error standard deviation) of 1.34 cm when operated at

500 Hz without averaging consecutive pulses. He then put effort into evaluating GPS processing methodologies and characterizing the static positioning performance. The IMU, laser, and GPS empirical error values were used to develop improved sensor simulations, and a full system model was implemented to quantify the elevation measurement error over an artificial sea ice surface. Using the knowledge gained from the system simulations, Edwards concluded by developing the basic hardware and software that serves as the CULPIS payload computer to provide accurate measurement timing.

Static testing of the CULPIS NovAtel SSII GPS receiver in Boulder, CO drew attention to a number of pertinent issues. In general, GPS vertical positioning is 2-3 times less precise than horizontal positioning due to the inherent geometry of the GPS satellite constellation. Satellites are not located below the measurement point, which leads to a relatively high vertical dilution of precision (VDOP) and correspondingly poor vertical positioning [90]. Additionally, code phase processing based on pseudorange measurements yields a RMS error of 2-5 m, and as such, carrier phase differential processing is needed to achieve the performance required for ice surface profiling. While dual-frequency differential positioning provides higher-quality solutions than single-frequency positioning, dual-frequency receivers start out around $4000, which was beyond the project budget constraints during the developmental phase. As such, the single-frequency SSII receiver, which costs ~$350, was chosen for CULPIS.

In kinematic dGPS positioning, the observations from a roving receiver are differenced against those from a reference ground station to resolve carrier ambiguities and remove common ranging errors. The ability to accurately resolve the carrier phase is critical when one considers that one carrier cycle offset corresponds to 19 cm of error. With short baseline distances between the rover and reference stations, ranging inaccuracies stemming from satellite clock, ephemeris errors, multipath, and ionospheric and tropospheric refraction are relatively equal, and are thus removed in the difference. As the baseline distance grows, the GPS signals received at the two receivers will have traveled through different regions of the atmosphere, and their errors will not fully cancel in the difference. The remaining error level is dependent upon the atmospheric activity, but in general, as baseline distance increases the propagation errors become larger and dGPS position solutions become less accurate. Examples of this are shown in Figure 5.2, which generally shows decreasing accuracy and precision with increasing distance. The left panel depicts the vertical accuracy for various

GPS positioning methods, and the right panel shows the vertical precision (standard deviation) for single and dual frequency static positioning. The remaining atmospheric and multipath propagation errors cause a positioning error that slowly varies on the order of 1-4 hours with the changing satellite geometry.

Static tests of the CULPIS GPS receiver showed that for a 1 km baseline the carrier solution was two orders of magnitude better than code solution; however, for baselines >20 km the kinematic ambiguity resolution (KAR) algorithm could not fix an integer ambiguity using the L1 carrier alone, and a less-accurate floating point ambiguity was resolved. The L1 dGPS error was found to be ±1 m with a standard deviation on order of 50 cm for a 500 km baseline. The tests also showed that vertical positioning in Barrow is expected to be 15% less precise than in Boulder based simply on the ratio of the VDOP values in those locations.

Edwards implemented a full system model to evaluate the expected measurement error, sensor misalignment error, and measurement latency error. Misalignment is the error in determining the orientation of one instrument frame with respect to another, and latency is the inability to correctly determine the measurement time, specifically, the timing error between when the sensor took the measurement and its associated time stamp. The simulations showed that a 2500 μs latency introduces an error standard deviation of ∼3 cm. With a latency of 500 μs the error standard deviation is reduced to ∼0.5 cm. A sensor misalignment of 5° introduces an error equal to 1% of the flight altitude AGL at a 5° off-nadir pointing angle. For example, with a 5° pointing angle at 100 m AGL, a misalignment of 5° introduces a 1 m error. Additionally, the simulations indicated that interpolating the GPS and IMU data to the laser measurement times introduces a 0.1 mm error. In the best-case senario with dual frequency carrier dGPS and no latency or misalignment, the simulations showed a total surface measurement error standard deviation of 3.5-5.5 cm for 100-1000 m AGL flight altitude.

The simulation results indicated that the latency be kept to less than 500 μs and the alignment be known to within 0.2° to achieve the desired performance. In practice, it was able to implement a system architecture that limits the latency to <200 μs. Unfortunately, highly-accurate sensor alignment was not achieved during the UAS integrations discussed herein, and is assumed to be ±1°. As such, sensor misalignment is expected to introduce a decent amount of error to the CULPIS elevation measurements.

The material presented in the following sections reviews the laser, IMU, and GPS measurement error

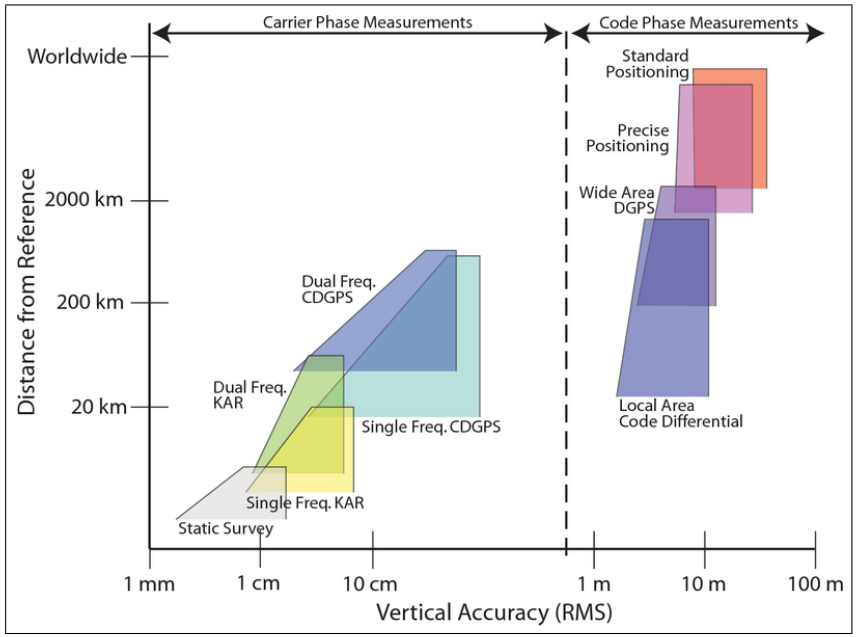

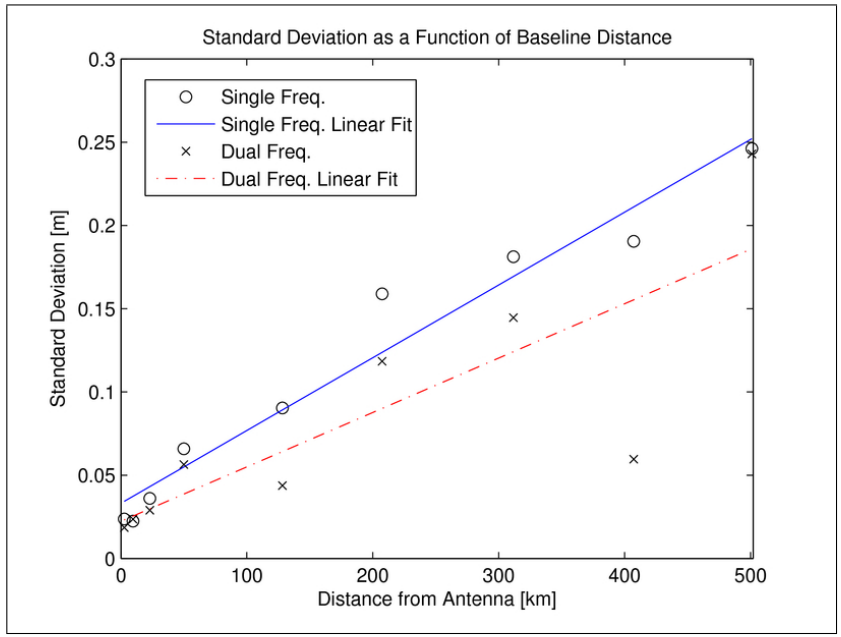

Figure 5.2: The quality of dGPS processing methods over a range of baseline distances based on the current literature. Accuracy (RMS) and precision (standard deviation) are shown to decreases with distance. Both figures were taken from Edwards [25]. The plot on left was adapted from horizontal comparisons in [96] with experimental results and quoted accuracies in data sheets and publications [83, 90, 93]. The plot on right was generated from experimental static measurement data collected by Edwards [25]. Note the axes are reversed on the two plots.

in greater depth, and then focuses on assessing the operational performance of the CULPIS. Considerable emphasis is placed on evaluating the kinematic dGPS positioning error at the high latitudes of the deployment locations and as baselines increases to large distances on the order of 500 km, and greater. This is an appropriate follow-on study to those carried out by Edwards as he characterized the static dGPS performance in Boulder, CO for baselines less than 500 km.

5.3 Sensor Error Analysis

5.3.1 Laser Error

A fraction of the CULPIS measurement error can be attributed to the intrinsic error of the ULS laser. The manufacturer indicates a range error of ±2 cm, and although it is not specifically indicated, this likely represents the mean absolute accuracy. Edwards[25] tested the ULS measurement precision with a 500 Hz pulse repetition frequency (PRF) and no sample averaging, and found that the measurement residuals were bound to a range of ±6 cm with a standard deviation (precision) of 1.34 cm. Implementing a higher pulse rate and averaging consecutive samples reduces the measurement noise, and as such, different ULS settings are implemented for campaign operations than were tested by Edwards. Specifically, the PRF is set to 4000 Hz, 10 consecutive measurement pulses are averaged, and a minimum of 4 of these 10 pulses must return valid range measurements. This provides an operational measurement rate of 400 Hz.

The full list of ULS settings used for campaign operations are provided in Table 5.2, and the measurement noise affiliated with the operational settings are represented by Figure 5.3. The residual error is bound to a range of ±5 cm and has a standard deviation (precision) of 0.6 cm. As shown by the residual histogram, nearly all of the error is within ±2 cm, with only a few outliers beyond this range. Accordingly, 2 cm is taken to be the laser measurement error, which agrees with manufacturers specification. These results illustrate the improved precision achieved by averaging consecutive samples.

Along with the discussion of laser ranging error, it is important to note that the aircraft flight altitude and speed have a direct impact on the measurement spatial resolution. The laser footprint is proportional to the measurement height AGL, and as such, it is possible to resolve smaller-scale features at lower altitudes.

Table 5.2: The CULPIS ULS laser operational settings used during campaign deployment. All other settings are left to their default value or unspecified/unchecked unless indicated below.

parameter	setting
Units	Meters
Short, Long, & Check Gate	☐
Offset Distance	0
Laser Power Level	High
Cooperative Target	☐
Intensity Rejection	Min=0, Max=6000
RS485 Termination	☑
Mode	Averaging
PRF	4000 Hz
Pulses/Measure	10
Dithering	☐
Minimum Good Pulses	4
Output Processing	off
Output Setup Port	RS232 Configuration Port
Continuous Autostart	☑
ULS Autostart	☑

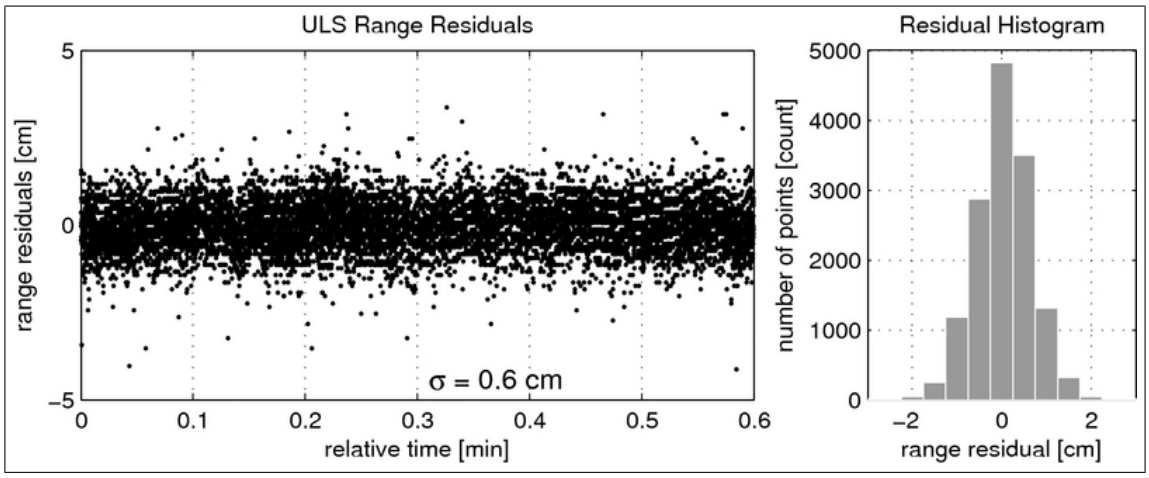

Figure 5.3: The ULS laser range residual error has a standard deviation of 0.6 cm. These data were collected using the operational settings specified in Table 5.2 at a range of ∼29 m from a static target during the ULS interference testing described in Appendix F. The histogram indicates that nearly all of the residuals are within ±2 cm, which is taken to be the measurement accuracy.

For example, with the ULS beam divergence of 3 milliradian, the laser footprint diameter is 30 cm from 100 m AGL, and 60 cm from 200 m AGL, etc. Additionally, the laser measurement rate of 400 Hz is equivalent to one measurement every 2.5 ms. Assuming a nominal ground speed of 30 m/s, the along-track separation of the footprint center point is 7.5 cm. Substantial overlap exists between consecutive measurements, which facilitates continuous sampling of the ground surface.

5.3.2 IMU Error

The IMU pointing angle measurement error, or angle determination error, can introduce a considerable level of error to the CULPIS surface elevation measurements, especially at high flight altitudes and at high attitude angles (roll and pitch). The surface height measurement error stemming from the IMU angular determination uncertainty is described by Equation 5.3, which is dependent upon the laser range (directly related to the aircraft altitude AGL), the true laser pointing angle off vertical, and the intrinsic IMU measurement error. This equation is generalized for a single pointing angle off nadir and does not decompose the angle into the roll and pitch components. Smith[107] performed dynamical testing of the CULPIS IMU that indicated the angle determination error is $\sim 1^{\circ}$ for typical UAS attitude rates of $\sim 2^{\circ}/s$.

$$\boxed{\epsilon_L = \ L\left[cos\left(\theta\right) - cos\left(\theta + \epsilon_\theta\right)\right]} \tag{5.3}$$

where...

ϵ_L = height error from the intrinsic IMU error

L = laser range measurement

θ = laser true off-nadir pointing angle

ϵ_θ = IMU pointing angle determination error

The behavior of Equation 5.3 is shown graphically in Figure 5.4. Since this error is dependent on three variables, it is presented as a function of IMU error and pointing angle at a constant range of 100 m (Figure 5.4 top panel), and as a function of range and pointing angle for a constant IMU measurement error of 1° (Figure 5.4 bottom panel). It is clear that the height errors are quite substantial (order meters) for large ranges, pointing angles, and IMU angular errors. At a range of 100 m with an off-nadir pointing

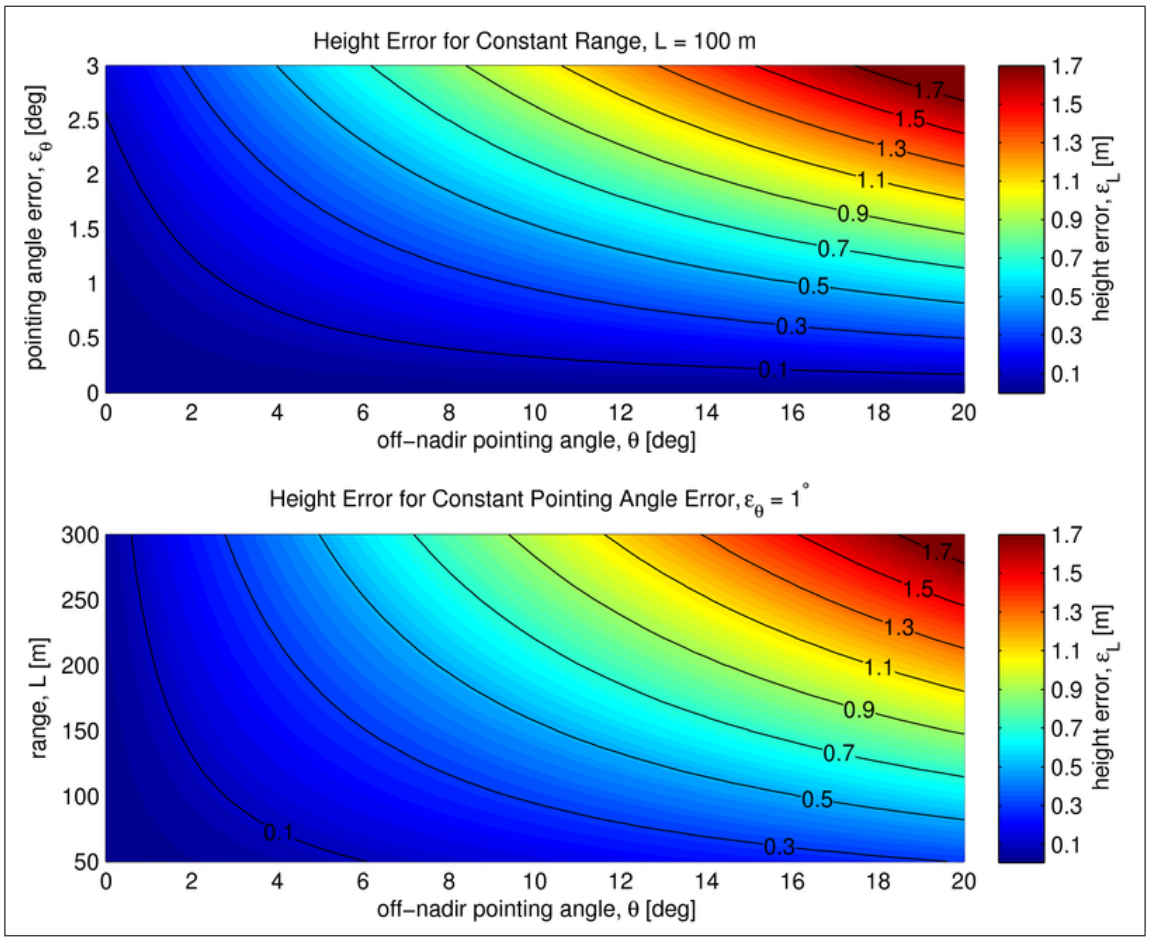

Figure 5.4: The CULPIS elevation error resulting from the intrinsic IMU angular measurement error as described by Equation 5.3. The top plot shows the elevation error at a constant laser range of 100 m as a function of the IMU measurement error and the pointing angle, and the bottom plot shows the elevation error for a constant IMU measurement error of 1° as a function of the laser range and pointing angle.

angle of 5° and an angular determination error of 1°, the surface elevation measurement error is ∼17 cm. The highest quality data is obtained at low altitude with near-nadir, well known pointing. For this reason, surface elevation data collected while the UAS is performing a turning maneuver are assumed to be of poor quality, and are not used for geophysical analysis.

Examples of roll and pitch measurements collected during CASIE flight 8 from three different IMUs onboard the SIERRA UAS are shown in Figure 5.5. The C-Migits is a high-grade IMU with 10 Hz sampling that was flown onboard the SIERRA, but was not flown onboard the Manta UAS during MUSCOX. The Piccolo IMU is part of the Cloud Cap Piccolo autopilot that was utilized for both the SIERRA and Manta UAS. The Piccolo IMU data are transmitted as part of the aircraft telemetry data stream, which occurs once every three seconds via Iridium link. It is clear that the C-Migits and Piccolo IMUs depict very similar aircraft attitude behavior. The 75 Hz Microstrain 3DM-GX1 shows dramatically different, sporadic behavior with a long stabilization period following the large turns, and apparent cross-coupling of the roll and pitch measurements. The source of these errors is unknown and should be investigated in the future. Based on this analysis and additional visual inspection of the Microstrain IMU data not presented here, it was decided that these data are not of sufficient quality for deriving surface elevations. As such, C-Migits IMU data were used to derive CASIE surface elevations, and Piccolo IMU data were used to derive MUSCOX surface elevations.

Figure 5.5 also shows that the aircraft flies with a continual rolling and pitching motion, which is likely a result of the autopilot attempting to maintain constant airspeed. During straight and level flight, the roll angle oscillates between ±3° and the pitch angle between $1-7°$. Data collected outside these bounds are not used for geophysical analysis to limit the impact of the IMU angular determination error. The C-Migits FFT shows that the dominant aircraft attitude motion has a periodicity of ∼200 meters/cycle, which corresponds to a frequency of ∼0.15 Hz at 30 m/s flight speed. This is in excellent agreement with results presented by Smith[107], who found that the Aerosonde UAS has a natural flight frequency of 0.16 Hz. With one oscillation corresponding to 6° of angular rotation (e.g. ±3° of roll), the nominal angular rate is 0.9°/s.

As a final note regarding the IMU measurements, it is important to recall that Smith[107] found the Microstrain IMU yaw measurements to be less precise than those for roll and pitch. Although the Microstrain

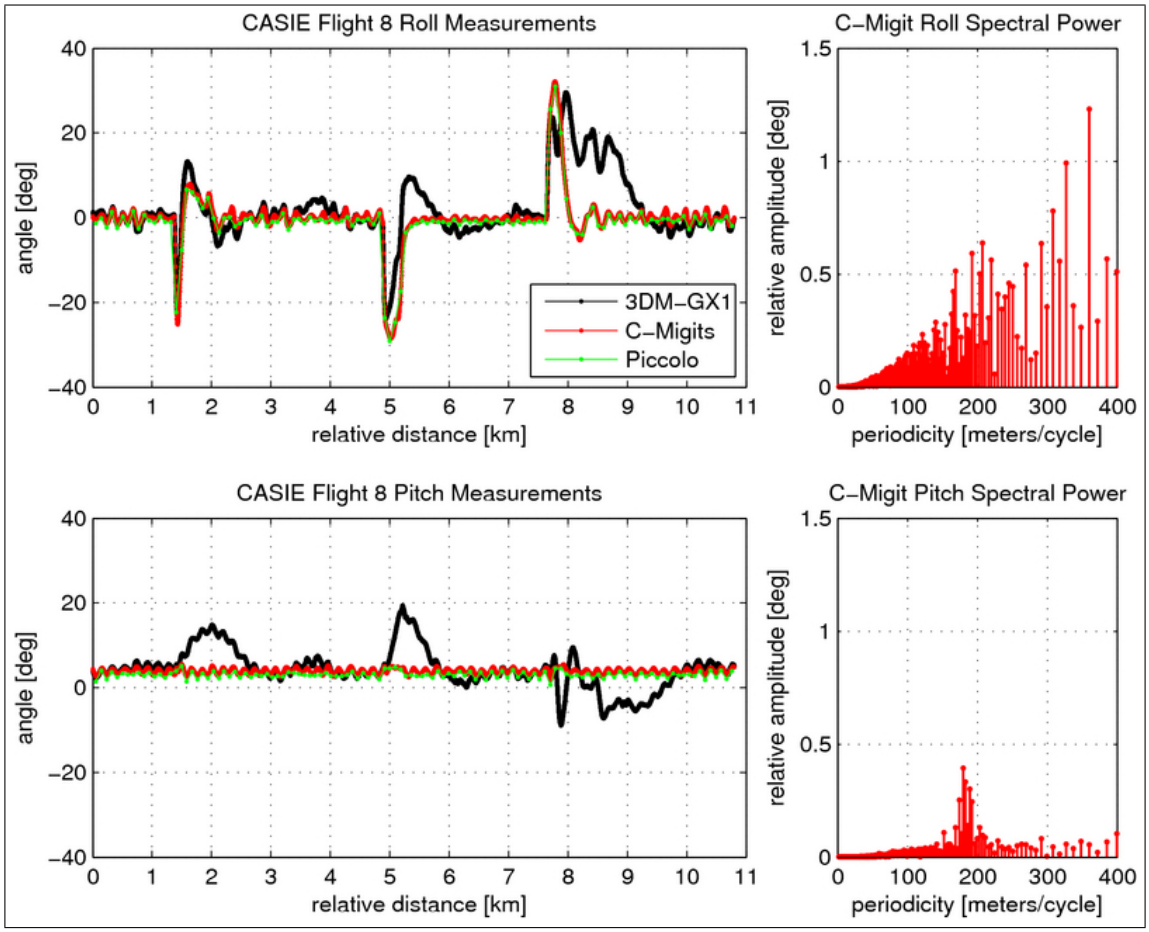

Figure 5.5: CASIE flight 8 example UAS roll and pitch attitude, and their spectral power, for Microstrain 3DM-GX1, C-Migit, and Piccolo IMU measurements. The C-Migits (10 Hz measurement rate) and Piccolo (3-second measurement rate) observations agree quite well, whereas the Microstrain (75 Hz measurement rate) observations have considerable error during and following turns. The C-Migits FFT spectra shows a dominant aircraft attitude periodicity of ∼200 meters/cycle.

IMU data were not used to derive surface elevations, it is assumed that the C-Migits and Piccolo yaw data are also less precise than their roll and pitch data. Additionally, Edwards[25] showed the importance of highly-accurate sensor alignment knowledge. Unfortunately, the sensor alignment was not accurately measured during the CULPIS UAS integration, and as such, misalignment may contribute significantly to the derived surface measurement error. For these two reasons, it was decided that the CULPIS GPS course over ground (COG) data that are output from the Waypoint software would be used for the yaw/heading direction in the elevation computation performed using Equation 5.1. Using the GPS COG direction will avoid imprecision associated with the IMU yaw measurements, and will limit the impact of the IMU misalignment. However, the COG direction describes the flight track direction, not the aircraft heading direction, and therefore, using the COG direction ignores the aircraft crab angle (angle between the heading and track angles) that may be associated with flight in a cross-wind.

5.3.3 GPS Error

The CULPIS GPS is used to determine the geographic position of the system during flight, and with knowledge of the surface range from the laser and the aircraft attitude from the IMU, surface elevations are computed using Equation 5.1, as previously discussed. A basic review of GPS fundamentals and mathematical formulations are presented in Appendix I, and a general understanding of that material is assumed throughout this discussion. As a brief overview, GPS computes positions in the WGS84 ellipsoid inertial reference frame, and thus, the derived CULPIS elevation measurements are also relative to the ellipsoid. While GPS offers an easy means for computing geographic position, its measurements are afflicted by orbit errors, receiver and satellite clock errors, atmospheric propagation errors as the GPS signals travels through the ionosphere and troposphere, multipath error, and additional unmodeled error. If these errors are unaccounted for they will reduce the accuracy and precision of the GPS position solutions.

Standard GPS (sGPS) positions are computed by tracking the course-acquisition (C/A) code transmitted on the L1 (link 1) carrier frequency. The positioning resolution offered by sGPS code solutions is relatively course, and improved performance can be achieved by tracking the carrier phase. The carrier phase multipath errors are typically at centimeter level, whereas code multipath error is at meter level;

however, the carrier phase measurements are ambiguous in whole cycles. This ambiguity must be resolved, and is done so using a method known as kinematic ambiguity resolution (KAR). Furthermore, by tracking the L1 and L2 (link 2) carrier phases it is possible to essentially eliminate the ionospheric error due to the known dispersive propagation at these two frequencies. Differential GPS is a method for further reducing atmospheric propagation errors. This method is based on the understanding that for receivers located within close proximity to one another (i.e. tens to possibly hundreds of kilometers, or less) these errors are highly correlated, and can be removed by differencing their time-matched measurements. However, as the baseline distance increases between the receivers, the errors become uncorrelated and are not fully removed in the differencing method. The magnitude of the remaining error is primarily dependent upon the difference in atmospheric conditions along the signal path.

Airborne laser altimetry systems typically utilize relatively long-baseline L1/L2 dGPS to accurately position the aircraft. During the CULPIS design phase the decision was made to use a L1-only GPS receiver to reduce the costs from ∼$4000 to ∼$350. A fair amount of literature has been published discussing the long-range performance of L1/L2 dGPS as utilized for airborne laser altimetry, and they have shown accuracies on the order of 10-15 cm, with primary error contributions being multipath (∼2 cm), tropospheric propagation (∼5 cm), and the reference station positioning error (∼4 cm) [17, 68, 70, 105, 130]. It is fairly well understood that long-range L1 dGPS has relatively poor quality since the L1/L2 combination required for the ionospheric correction cannot be made, and as such, there is minimal reporting of L1 dGPS vertical accuracy. For this reason, and to characterize the practical CULPIS elevation measurement error, it is important to establish the CULPIS L1 dGPS positioning capabilities for the operational scenarios encountered during MUSCOX and CASIE (i.e. baseline distances of 50-500+ km, latitude >65° N).

The work done by Edwards[25] serves as a reference point for the GPS capabilities that can be expected for the CULPIS system. As shown in Figure 5.2, long-baseline (e.g. ∼500 km) L1 dGPS nominally provides vertical positioning accuracy and precision of $\gtrsim$25 cm, or worse. The assessment presented in this section is carried out, in part, to verify these expectations and to evaluate the operational kinematic L1 dGPS positioning error as a function of the reference station baseline distance. Additionally, it was necessary to evaluate the capabilities of the NovAtel Waypoint software which was utilized to perform the L1 dGPS

positioning. It should be noted that the precise orbits and ephemerids were used for all processing.

To accomplish the task at hand, ground-based runway survey data were collected at the local airports during the MUSCOX and CASIE deployments, and all the available permanent GPS stations within 1000 km are used to differentially position the runway survey data using NovAtel Waypoint 8.10 GrafNav. The permanent GPS station data were acquired from the UNAVCO, Inc.[2] geodetic GPS monument archive at their native 30-second data rate. As will be discussed, local-baseline (i.e. close-range, <300 m) dGPS positioning of the runway survey data is used to generate a "truth" reference surface, which is in turn used to gauge the quality of the longer-baseline dGPS survey data. In this manner, it will be possible to quantify the dGPS performance over a range of baseline distances, and subsequent analysis of flight-based laser profile data collected over the runway will shed light on instrumentation and aircraft integration error sources for the purpose of characterizing the practical CULPIS operational performance.

During the MUSCOX and CASIE deployments temporary GPS reference stations ILCU and NYCU were established in close vicinity (<300 m) to the runways at Ilulissat, Greenland and Ny-Ålesund, Svalbard. These stations were operated by CU personnel throughout the duration of the campaigns and were equipped with dual-frequency Trimble R7 survey-grade receivers provided courtesy of UNAVCO. They were operated with the same measurement rate as the CULPIS GPS receivers (5 Hz during MUSCOX, 10 Hz during CASIE), and they serve as the local-baseline reference stations used to perform dGPS positioning of the ground runway survey data used to generate the "truth" reference surface. Accurate knowledge of the reference stations is critical in dGPS positioning because error in the reference station position translates directly into error (bias) in the rover position. The method used to determine the precise position of the temporary stations is described in Appendix H, and it is shown that these positions have a precision of <1 cm. The absolute accuracy is not known, but is assumed to be ∼2 cm, which is in line with the value cited by Krabill et al.[70].

The long-distance monument GPS stations used to position the runway data are shown in Figure 5.6, with the stations used for MUSCOX processing shown in green and the stations used for CASIE processing shown in blue. These permanent stations record L1/L2 carrier data at a 30-second rate, and their positions

[2] UNAVCO, Inc.: http://www.unavco.org/

were computed using the Jet Propulsion Laboratory (JPL) online Automatic Precise Positioning Service[3] (APPS) using several hours of data collected around the period of the runway surveys (4 hours of data for MUSCOX stations, 6 hours of data for CASIE stations). The two temporary CU reference stations, ILCU and NYCU, are shown in red. A full list of the reference stations, and their baseline distance relative to ILCU and NYCU, that are used to evaluate the MUSCOX and CASIE runway survey GPS positioning is provided in Table 5.3.

The Manta and SIERRA UAS were pulled back-and-forth along the runways at Ilulissat and Ny-Ålesund in order to survey the surface elevation and generate the "truth" reference surface. The Manta was towed with a cord by a person who walked across the runway two times (down-and-back), and the SIERRA was placed on a trailer which was pulled by a truck back-and-forth across the runway four times (down-and-back twice). The trailer height was measured with a ruler to be 53 cm, with an estimated uncertainty of ± 2 cm. The two survey dates and times are provided in Table 5.4. During both surveys the CULPIS recorded L1 GPS phase data (at 5 Hz during MUSCOX, and 10 Hz during CASIE), and dGPS post-processing was performed using NovAtel Waypoint.

Due to the fact that the Waypoint software is proprietary and serves as a black-box processing tool, it was necessary to determine the processing methodology and input parameters (primarily the *a priori* covariance weights) that provide the most accurate and precise positions. To accomplish this, educated trial and error dGPS processing was carried out on the MUSCOX runway survey data using ILCU and SRMP as exploratory reference stations in a case-study analysis. The runway survey data were processed using each reference station individually, and using both stations simultaneously. Additionally, the survey data and station data were interpolated to various sampling times to investigate the dependence on measurement cadence, and also the Waypoint *a priori* covariance weights were adjusted to determine the most suitable values. Though the results of this study are not presented in detail, it was found that single-station dGPS processing with the reference station measurements interpolated to the roving receiver sampling rate (5 Hz for MUSCOX, 10 Hz for CASIE) provide the best results.

A similar investigation study was carried our using the CASIE runway survey data. The findings from

[3] JPL Automatic Precise Positioning Service: http://apps.gdgps.net/index.php)

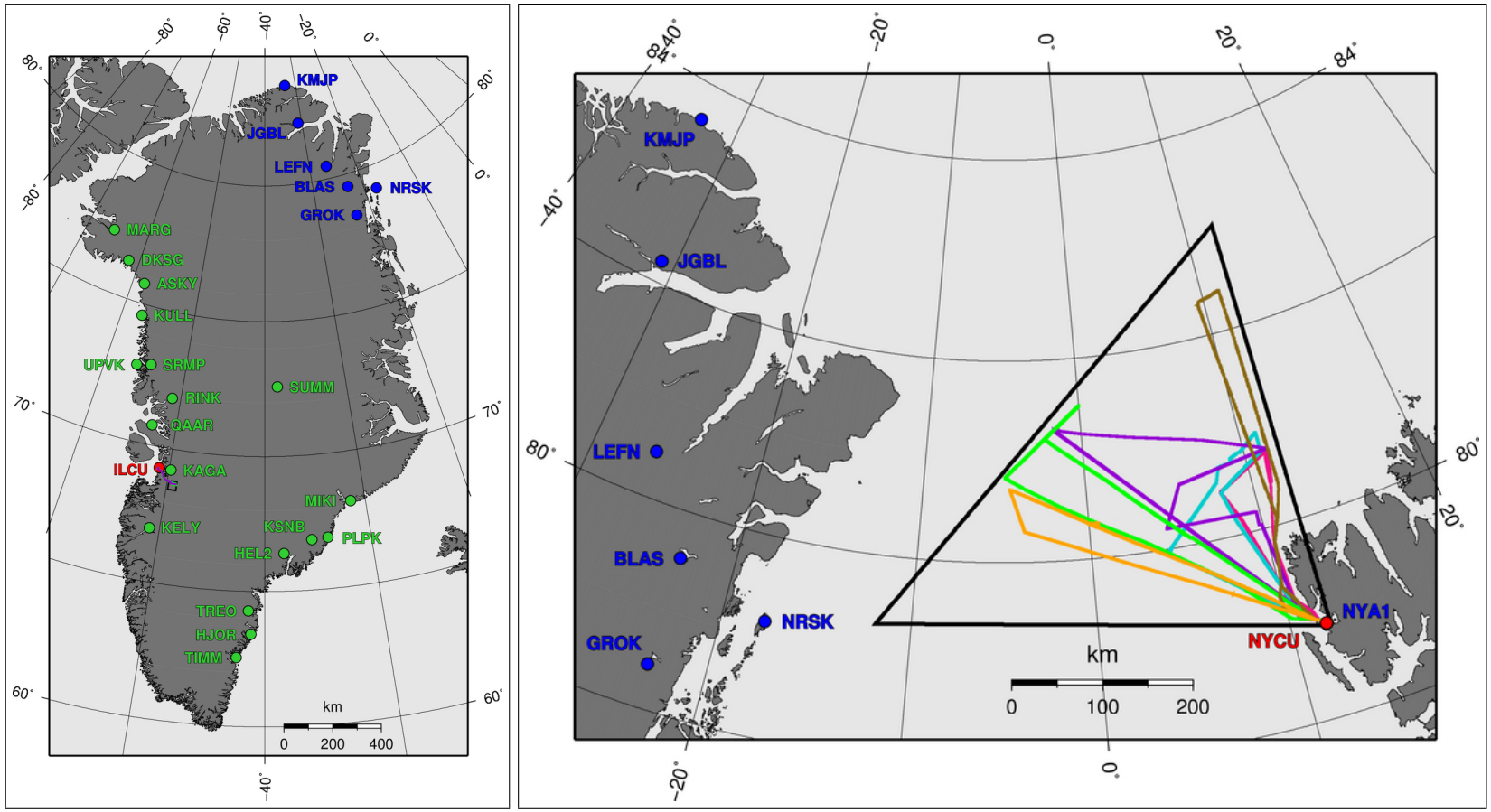

Figure 5.6: The GPS reference stations used to assess the quality of MUSCOX and CASIE dGPS post-processing. Stations shown in green are used to differentially position MUSCOX CULPIS GPS data and stations shown in blue are used to position CASIE data. Reference stations shown in red are the temporary stations established by CU personnel while on deployment.

Table 5.3: MUSCOX and CASIE differential GPS reference stations, and their baseline distances relative to ILCU (for MUSCOX stations) and NYCU (for CASIE stations). ILCU and NYCU were located within 300 m of the local runways.

campaign	station ID	baseline distance [km]
MUSCOX	ILCU	0.0
	KAGA	49.4
	QAAR	178.3
	KELY	251.4
	RINK	290.7
	SRMP	426.5
	UPVK	435.9
	SUMM	590.3
	HEL2	626.1
	KULL	631.9
	KSNB	697.1
	TREO	697.7
	PLPK	755.0
	ASKY	761.4
	HJOR	785.3
	MIKI	803.3
	TIMM	846.6
	DKSG	864.2
	MARG	997.9
CASIE	NYCU	0.0
	NYA1	0.3
	NRSK	622.1
	BLAS	719.4
	GROK	753.1
	LEFN	766.6
	JGBL	839.6
	KMJP	890.8

Table 5.4: The MUSCOX and CASIE runway ground-survey and flight-profile data collection times.

campaign	ground survey date	time period [UTC]	duration [min]
MUSCOX	16 July 2008	21:55:02 - 22:17:52	22.8
CASIE	12 July 2009	07:56:08 - 08:06:39	10.5

campaign	flight profile date	time period [UTC]	duration [hrs]
MUSCOX	9 July 2008	01:54:31 - 06:43:04	4.81
CASIE	14 July 2009	15:00:50 - 17:49:05	2.80

Table 5.5: The *a priori* covariance weights used for NovAtel Waypoint differential processing of CULPIS GPS data. For all processing the "distance effect" parameter was set to "low", which adds an additional 0.8 parts-per-million (PPM) of the baseline distance to the weights.

tracking signal	C/A Code [m]	L1 Carrier [cm]
short-baseline (<1 km)	4.0	2
long-baseline (>1 km)	2.5	5

this study were similar to those for the MUSCOX study; however, dual-station dGPS processing using both NYCU and NYA1 provided slightly more precise results that single-station processing with either NYCU or NYA1 alone for the local-baseline positioning. As was found for MUSCOX, CASIE single-station processing provided the most precise long-baseline dGPS positions. The short- and long-baseline covariance weights that provided the most precise vertical elevations for the MUSCOX and CASIE runway survey data are presented in Table 5.5.

The MUSCOX "truth" reference surface was computed in the following manner. First, Waypoint was used to differentially position the runway survey data relative to the local station ILCU, and two meters of data on either end of the runway survey were removed to eliminate data collected while turning in order to minimize sampling of the runway lateral elevation change. Then, the GPS data were interpolated to every 1 mm to mitigate velocity affects (data bunching) on the running mean. The running mean was then computed using a 5 meter window size, and the GPS antenna height above the ground surface (34.3 cm as mounted in the Manta UAS) was removed from the running mean to provide the final MUSCOX runway reference surface.

The CASIE reference surface was computed in a similar manner except the data were positioned relative to the local stations NYCU & NYA1 simultaneously, 50 meters of data were removed from either end of the runway survey to eliminate the turns (the truck/trailer used to pull the SIERRA had a much larger turning radius than the person walking the Manta), and a 10 meter window size was used to compute the running mean. The trailer floor height above the runway surface (53 cm) and the GPS height above the trailer floor (77.2 cm as mounted in the SIERRA) were removed from the running mean to provide the final CASIE runway reference surface.

As previously mentioned, all the GPS stations shown in Figure 5.6 and Table 5.3 were used to differen-

tially position the MUSCOX and CASIE runway survey data, but three of the survey datasets are examined in particular detail (i.e. focus datasets) to illustrate the varying levels of performance. These three datasets are the real-time C/A pseudorange sGPS solutions, the data positioned relative to the local-baseline reference stations (ILCU for CASIE and dual-station NYCU & NYA1 for CASIE), and data positioned relative to select long-baseline monument sites (SRMP for MUSCOX, KMJP for CASIE). The SRMP station was chosen because its 427 km baseline is roughly equal to the longest baseline encountered during CASIE (considerably longer than those encountered during MUSCOX), and KMJP was chosen because its 891 km baseline is representative of potential future UAS missions that could extend farther north into the Arctic Ocean.

Before examining the runway survey elevations, it is useful to evaluate a variety of GPS solution metrics. These metrics provide insight to the position quality based on the satellite geometry and the least-squares covariance matrix. Figure 5.7 shows GPS metrics reported by the Waypoint software for the MUSCOX and CASIE local-baseline (ILCU, NYCU & NYA1) dGPS solutions, and the two select long-baseline (SRMP, KMJP) dGPS solutions. The metrics are not available for the sGPS positions that are recorded in real-time by the CULPIS GPS receiver. Waypoint processes data in the forward and reverse time directions separately, and then uses a variance-weighted combination of the forward and reverse solutions to form the final position solution. The separation distances plotted at the top of Figure 5.7 are the differences between the forward and reverse solutions, and provide an overall estimate of the solution accuracy. The second row of plots shows the drift of the L1 KAR float solution, which indicates the degree to which the software was able to resolve and maintain lock on the carrier phase. The L1 RMS and standard deviations, shown in the bottom two plots, are derived from the covariance matrix, as shown on page 165.

Other than the vertical component of the KMJP solution, the separations between the forward and reverse solutions are not dramatically different for the short- and long-distance dGPS positioning. However, the long-distance (SRMP, KMJP) ambiguity drift, L1 RMS, and covariance standard deviations are considerably higher than those for the short-distance baselines (ILCU, NYCU & NYA1). This suggests that the increased differences in the ionospheric and atmospheric conditions along the signal transmission path between the long baselines introduces increased propagation error, rendering it more difficult to resolve the carrier ambiguity and increasing the overall position error. The ambiguity drift introduces approximately 1-4

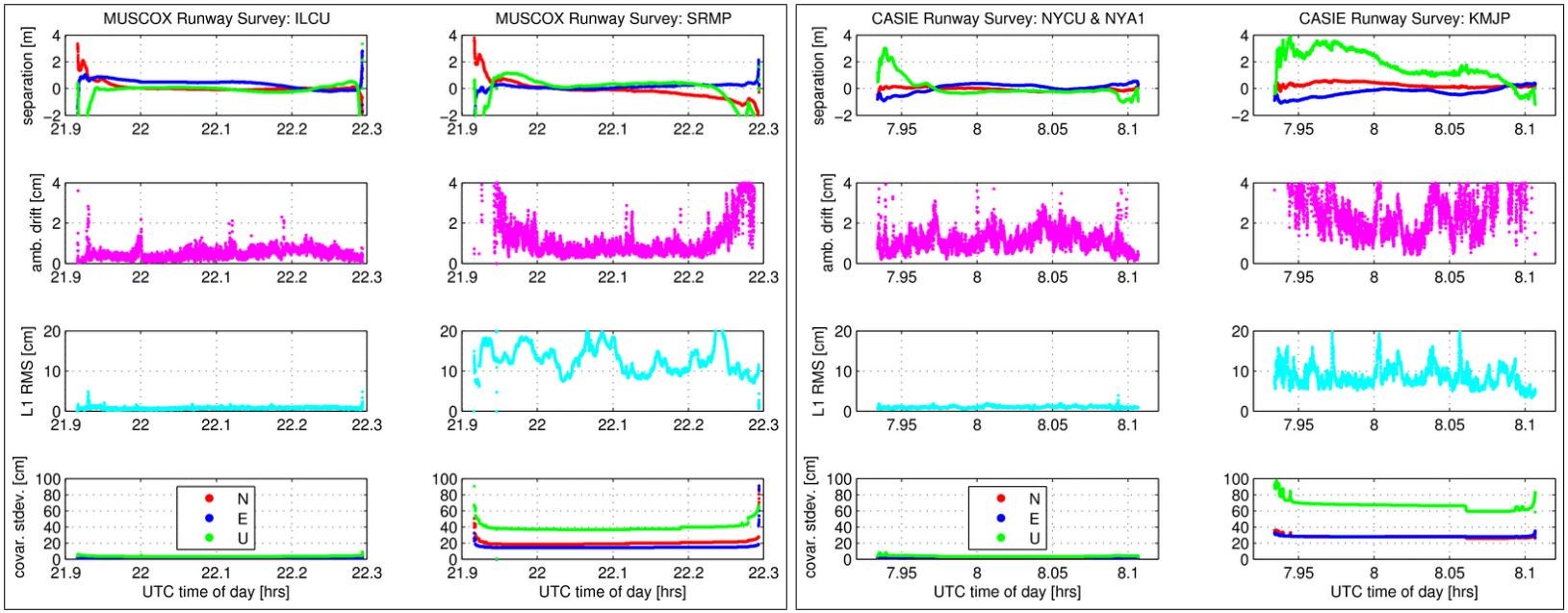

Figure 5.7: The MUSCOX (left panel) and CASIE (right panel) GPS runway survey NovAtel Waypoint solution quality metrics for short-distance (left columns: ILCU and NYCU & NYA1) and long-distance (right-columns: SRMP and KMJP) dGPS post-processing. Separation is the distance between the position solutions processed in the forward and reverse time directions. The ambiguity drift is the drift of the KAR float solution. The L1 RMS and covariance standard deviations are derived from the least-squares covariance matrix for the north, east, and up (NEU) position components. The metrics presented here are described further in Appendix I.

Table 5.6: MUSCOX and CASIE GPS runway survey elevation error statistics relative to the "truth" reference surface. The ILCU and NYCU & NYA1 statistics represent the quality of short-baseline dGPS positioning solutions, SRMP and KMJP represent long-baseline solutions, and sGPS represents the real-time pseudorange code solutions. The nugget is the variogram standard deviation value at a lag of 1 second, and the sill is the maximum variogram standard deviation value at time lags less than 15 minutes. See Equation 5.5 for the variogram formulation.

campaign	station	mean [cm]	stdev [cm]	RMS [cm]	nugget, $\gamma_{1\text{-sec}}$ [cm]	sill, $\gamma_{15\text{-min}}$ [cm]
MUSCOX	ILCU	0.0	1.7	1.7	0.4	2.6
	SRMP	-15.1	35.9	39.0	0.9	48.7
	sGPS	0.7	103.9	103.8	0.9	143.8
CASIE	NYCU & NYA1	0.1	5.4	5.4	0.7	7.3
	KMJP	103.8	66.1	123.1	3.8	120.7
	sGPS	326.3	107.6	343.6	2.1	176.8

cm of error to the long-baseline dGPS solution, and the covariance standard deviation indicates an overall vertical precision of approximately 40-70 cm.

The number of visible satellites and the dilution of precision (DOP) parameters are shown in Figure J.2 on page 168, and are essentially the same for all the reference stations. In general, there is a high number of visible satellites, which is favorable for a quality solution. However, the low-horizon geometry of the satellites is not favorable for a high-quality vertical solution, as made evident by the relatively high VDOP and position DOP (PDOP) values. It is also evident that the solutions are poorest toward the beginning and end of the time series where the KAR algorithm, as run in the forward and reverse directions, is initializing and waiting for satellite lock and a sufficient change in satellite geometry to be able to resolve the carrier ambiguity.

The MUSCOX and CASIE runway survey elevation profiles for the three focus datasets (sGPS, local-baseline dGPS, and long-baseline dGPS) are shown in Figure 5.8, along with their difference error relative to the "truth" reference surface. The runway surfaces are relatively smooth such that the vertical variability in the survey data represents imprecision in the solutions. The mean, standard deviation, and RMS error statistics for the focus datasets are provided in Table 5.6. The runway survey error statistics, presented as a function of baseline distance for all the reference station position solutions, are shown in Figure 5.10, and generally do not show a strong correlation with distance.

For clarification, it is important to note that that the RMS error discussed here, and throughout this

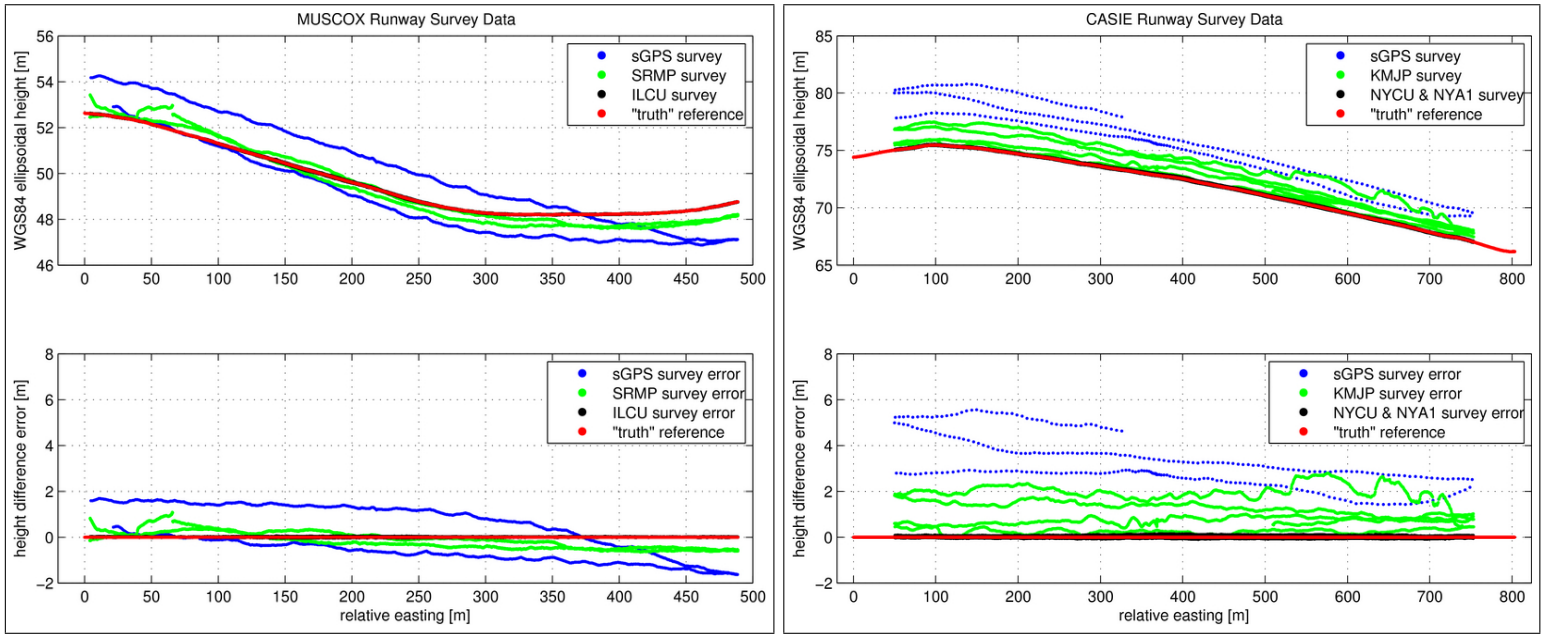

Figure 5.8: MUSCOX and CASIE runway elevation surveys for three different GPS positioning solutions, and their error relative to the reference "truth" survey. The sGPS surveys, shown in blue, are the pseudorange code solutions computed in real-time by the CULPIS GPS receiver. The surveys shown in green are solutions from long-baseline dGPS post-processing, and surveys shown in black are solutions from short-baseline dGPS post-processing. The "truth" reference surfaces, shown in red, are the spatial running average of the short-baseline solutions. The error statistics for each survey are presented in Table 5.6.

document, is computed using Equation 5.4. In this computation, the mean error bias is not removed from the observed data, and as such, the RMS incorporates both the bias and standard deviation of the error. In this manner, if the observation are unbiased, the RMS is equal to the standard deviation.

$$\boxed{\text{RMS} = \sqrt{\frac{\sum_{i=1}^{n} (x_{1,i} - x_{2,i})^2}{n}}} \tag{5.4}$$

where...

RMS = root-mean-square error

$x_{1,i}$ = observed data

$x_{2,i}$ = "truth" reference data

n = number of data points

As expected, local-baseline dGPS processing provides the most precise overall runway survey position solutions, with RMS errors of 1.7 cm and 5.4 cm for MUSCOX and CASIE, respectively. This finding confirms that it was indeed appropriate to compute the "truth" reference surfaces from these data. It is also clear that the sGPS solutions provide the least precise overall positions, with MUSCOX and CASIE RMS errors of approximately 1.04 m and 3.44 m. The long-baseline dGPS solutions (SRMP and KMJP) provide intermediate overall precisions, with RMS errors of 39.0 cm and 1.24 m. It is important to note that some of the variability within and between the dGPS runway survey transect data is introduced by lateral changes in the location of the Manta and SIERRA as they were towed back-and-forth along the runway. It is expected that there is decimeter-level lateral variability in the runway surfaces (verified by visual inspection of the runways during the MUSCOX and CASIE deployments). Additionally, it is likely that elevation variability was introduced by the vertical vibration of the UAS as they were pulled along the runway.

It is important to recognize that the error mean, standard deviation, and RMS of the entire runway survey dataset presented in Table 5.6, represent the accuracy and precision (relative to the "truth" survey) of the CULPIS GPS measurements over the full time period of the surveys (∼22 minutes for MUSCOX, ∼10 minutes for CASIE). An important performance metric that is particularly relevant to sea ice topography measurements is the relative point-to-point measurement precision over shorter time periods, which is

relevant for computing ice surface roughness and ridging characteristics.

Geostatistical analysis methods can be implemented to assess the spatial behavior of a geophysical variable. As discussed in Herzfeld[38], the underlying concept of geostatistics is that of the regionalized variable. A regionalized variable is a spatial or temporal variable, such as surface elevation or GPS position, with a transitional behavior between deterministic and random states. In general, regionalized variables are deterministic (i.e. predictable) over shorter time or space scales, and transition to a more random (i.e. unpredictable) state or behavior at longer scales. Taking the example of surface elevation, the elevation at two points that are located close to each other are likely to have a similar elevation. As one moves farther away from a point with a measured elevation, one is less likely able to predict the elevation that will be measured at another site, until a distance is reached beyond which prediction from the first measurement site is no longer possible. This distance is known as the range.

It is important to recognize that while surface elevation, and other geophysical variables, share the general transitional behavior of regionalized variables, their spatial or temporal properties are different and dependent on the specific nature of the variables. For instance, in a mountain range, topography varies over short distances (hundreds of meters to kilometers), whereas the gravity field only changes over much larger distances (tens of kilometers). As such, topography (elevation) generally has a smaller range than gravity (gravity anomaly) [38]. In the case of GPS position, the temporal behavior is dependent primarily on the changing satellite constellation geometry and the signal propagation environment.

In geostatistical analysis, a variogram reflects the behavior of a geophysical variable which is spatially correlated at a certain space or time scale and which is not correlated for large distances (i.e. beyond the range). In other words, variograms show the variability, or decorrelation, of data as a function of distance or time lag. Variograms can be characterized by the parameters sill, range, and nugget [38]. The sill corresponds to the total variance of the dataset. The nugget is the residual variance of repeated sampling in the same location, or of samples spaced closer than the resolution of the data. As mentioned, the concept of a regionalized variable involves the notion that samples spaced closer together are related more than samples spaced farther apart, which results in a variogram with low values for short scales, and values increasing to the sill value, which is indicative of the random nature of the variable, for samples exceeding a certain scale.

This scale is termed the range. Beyond the range the regionalized variable behaves like a random variable.

Herzfeld[39] has done extensive geophysical morphology analysis and classification using variograms as a means to extract information on complex spatial variability signatures. Applications of variograms are wide ranging, but have proven useful in topics such as mapping of marine-geologic provinces from bathymetric data (e.g. [35, 40, 43]), characterization of sea ice and snow surface properties (e.g. [36, 37, 45, 46]), and the analysis of glacial deformation (e.g. [41, 42, 44]). For the purposes herein, variograms are used to evaluate the GPS and CULPIS error variability and magnitude as a function of lag.

It is intuitive to think of the kinematic GPS error as a regionalized variable that transitions from deterministic behavior at short time scales to a random behavior at longer time scales based on the changing satellite geometry and signal propagation conditions. The error variogram will essentially show the short-lag, point-to-point error (i.e. high-frequency noise), how rapidly the error grows, and the maximum error of the GPS solutions. The longer-scale random behavior of GPS solutions is well recognized and is attributed primarily to changes in the atmospheric propagation and multipath error, which slowly vary with changes in satellite geometry (e.g. [3, 9, 33, 90, 110]). Over short periods of time the GPS positions are relatively precise. Over longer time periods, or lags, the satellite geometry changes significantly, the error grows, and the positions become more uncorrelated. The error variograms are a method for examining the error growth and the associated position solution decorrelation.

The variogram (variability as a function of time lag), is computed using Equation 5.5 [39]. In practice, a lag bin size, h, is specified along with a bin tolerance. For the variograms computed in this section, a bin size of 1 second with a tolerance of ± 0.5 seconds about bin center was used to evaluate the GPS point-to-point precision. The choice of a 1-second bin size was driven by the fact that the sGPS data has a measurement rate of 1 Hz, so it is not possible to use a smaller bin size. Runway survey elevation error variograms for L1 dGPS positions relative to the ILCU, SRMP, NYCU & NYA1, and KMJP reference stations, and the sGPS pseudorange positions are shown in Figure 5.9. Even with the prescribed bin size, aliasing artifacts are evident in the sGPS variograms. The runway survey elevation error variograms for GPS data positioned

relative to all the reference stations are shown in Figure J.3 on page 169.

$$\boxed{\gamma^2(h) = \frac{1}{2\,|N(h)|} \sum_{(i,j)\in N(h)} [z(x_i) - z(x_j)]^2} \tag{5.5}$$

where...

x = time or location

h = time or distance lag = $|x_i - x_j|$

z = surface elevation error relative to the "truth" reference

γ^2 = elevation error variance over the time or distance lag h

γ = elevation error standard deviation over the time or distance lag h

$N(h)$ = the set of pairs of observations i, j

$|N(h)|$ = number of i, j pairs in the set $N(h)$

A number of variogram characteristics are useful for assessing the vertical GPS positioning precision and the error behavior. The variogram value in the first lag bin, referred to here as the nugget, represents the error that can be expected over the short time (distance) period of 1 second (30 m when flying at 30 m/s), which essentially represents the point-to-point, high-frequency measurement precision. The variogram slope and curvature at short lags illustrates how quickly the error grows, and the peak variogram value, referred to as the sill, indicates the expected error over a longer time (distance) lag. The variogram nugget (variogram value at 1-second lag), and the variogram sill (maximum variogram value for lags less than 15-minutes) are presented in Table 5.6.

It is important to note that this GPS elevation error variogram analysis is inherently limited by the time period of the runway surveys (presented in Table 5.4). As such, the sill values presented here are only representative of the total GPS error variability over the relatively short time period of the runway surveys. It is recognized that the GPS satellite geometry and atmospheric conditions vary over much longer scales (i.e. days and longer), and therefore the GPS elevation error sill values for datasets collected over a longer time period would likely be larger than those presented here. Furthermore, repeat GPS measurements were not made at the exact same locations along the runway, and therefore the variogram nugget could not be

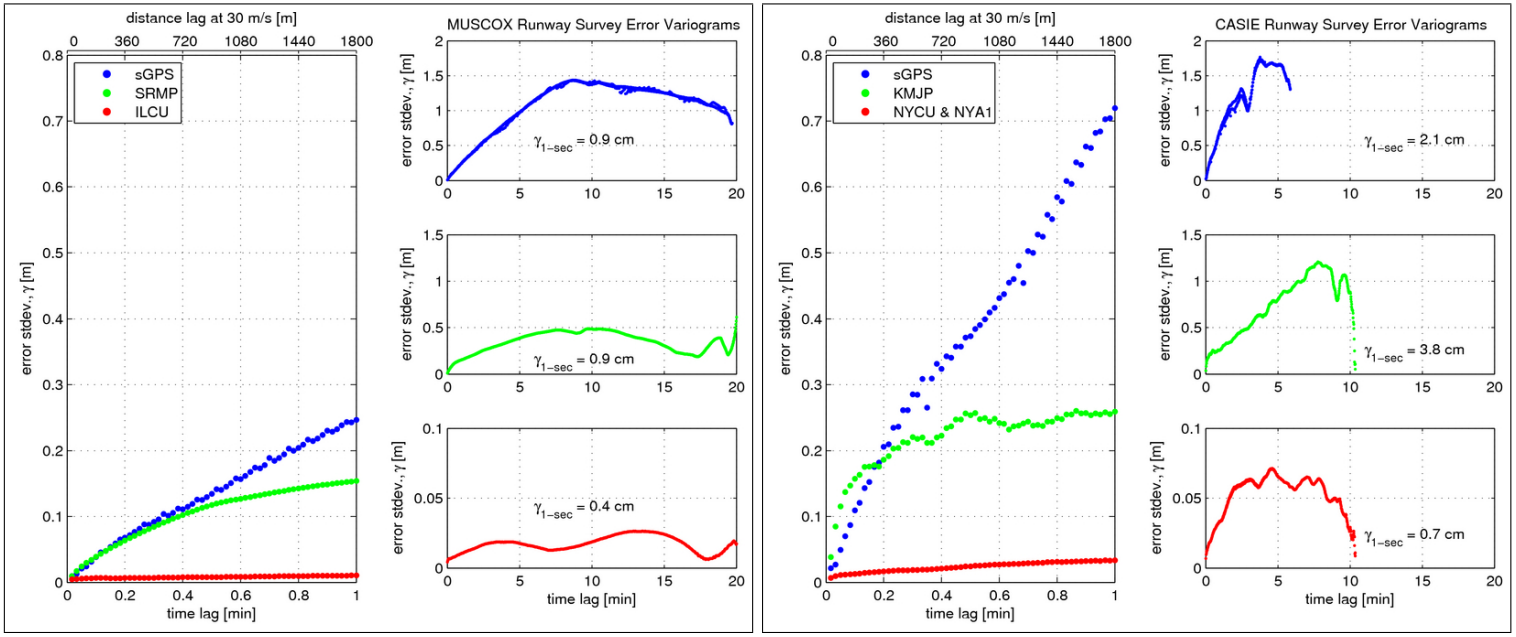

Figure 5.9: MUSCOX (left panel) and CASIE (right panel) GPS runway survey elevation error variograms for real-time pseudorange code positioning (sGPS, shown in blue), long-baseline dGPS positioning (SRMP and KMJP, shown in green), and short-baseline dGPS positioning (ILCU and NYCU & NYA1, shown in red). See Equation 5.5 for the variogram formulation. The plotted values are the variogram elevation error standard deviations, γ, as a function of time lag, h. The taller plots in the left column of each panel are closeup views spanning a 1-minute time lag, and the three smaller plots in the right column of each panel are the same data, but span 20 minutes to show the error variability over a longer time period. The top x-axis of the taller plots show the equivalent distance lag for a hypothetical situation where the GPS receiver were traveling at a flight speed of 30 m/s. The nugget is the variogram value at 1 second lag, and the sill is the maximum variogram value at lags less than 15 minutes. The variogram nugget and sill values for each survey are presented in Table 5.6.

computed according to its true definition (the residual variance of repeated sampling in the same location, or of samples spaced closer than the resolution of the data). The variogram value within the first lag bin (1-second lag) is taken to be a close approximation of the nugget.

For both the MUSCOX and CASIE runway surveys, the sGPS positions generally exhibit the most rapid error growth (although the KMJP growth-rate is faster at times <0.1 minute), and the highest overall error, as indicated by the large standard deviation, RMS, and sill values. The short-baseline dGPS solutions provide the best positioning with the smallest error mean, standard deviation, RMS, nugget, sill, and slowest error growth. It is insightful to note that the long-baseline dGPS positions exhibit considerably less error than sGPS positions at time lags greater than 0.4 minutes (720 m at 30 m/s). One interesting finding is that the variogram nugget shows a strong correlation with baseline distance, as shown by Figure 5.11; however, the overall error statistics (mean, stdev, rms, sill) are weakly correlated with distance (see Figure 5.10).

Based on the anomalous behavior exhibited by MUSCOX data positioned relative to KAGA in Figure 5.11, it was determined that the KAGA station was not reliable. As such, the closest reference station examined (other than the very short ILCU, NYCU, and NYA1 stations) is QAAR, which falls just shy of 200 km from the MUSCOX runway. It is evident from Figures 5.10 and 5.11 that for CULPIS L1 dGPS positioning at high latitudes, beyond a baseline of 200 km the overall vertical position error is not significantly influenced by increasing the distance further. However, the point-to-point error noise continues to increase with baseline distance. In other words, once the baseline exceeds ~200 km, the GPS overall accuracy has reached it's maximum error (i.e. an error "saturation point"), yet the point-to-point measurement precision continues to degrade as the baseline increases.

It appears that for baselines >200 km, the total atmospheric propagation delay between the two GPS receiver locations has essentially reached a peak value and has leveled-off, but increasing baselines continue to afflict the carrier phase, making it increasingly difficult for the KAR algorithm to maintain a stable fix on the phase, thereby introducing high-frequency noise. This phenomenon is supported by work that has shown that the tropospheric and ionospheric propagation error decorrelation scales are in the range of 50-200 km (e.g. [78, 110]). More specifically, Stoew and Elgered[110] found that for spatial scales smaller than 200 km the zenith tropospheric delay error correlations become significant, and for larger scales the error correlations

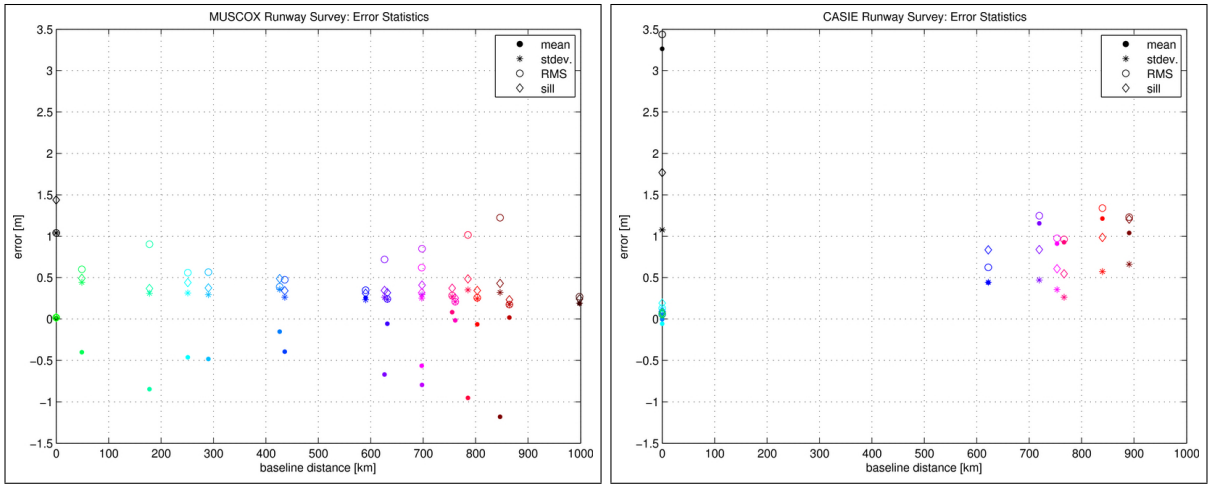

Figure 5.10: MUSCOX and CASIE runway survey elevation error statistics for sGPS and dGPS positioning relative to the reference stations shown in Figure 5.6 and Table 5.3. The colors correspond to the reference station legend in Figure 5.11. The sill is the maximum variogram value at time lags less than 15 minutes. There is not a strong correlation between baseline distance and any of the statistics presented here.

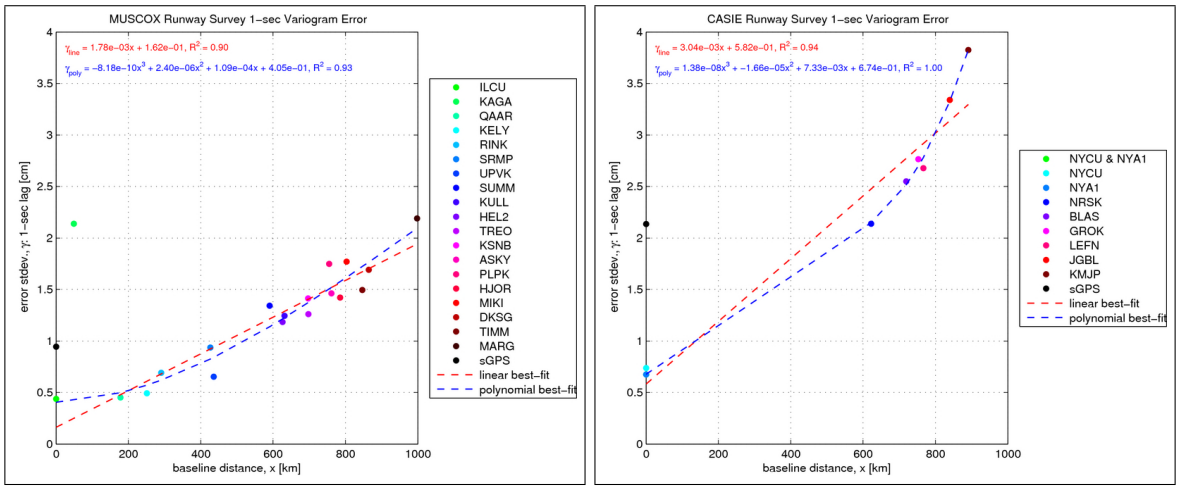

Figure 5.11: MUSCOX and CASIE GPS runway survey elevation error variogram nugget v. baseline distance. This plot shows the point-to-point decorrelation of dGPS position solutions as a function of baseline distance. Equations for the linear and polynomial best fit curves, along with the associated R^2 value, are shown in their corresponding colors.

are small and slowly decreasing with distance. A plot taken from their paper is shown as Figure J.1 on page J.1, and illustrates the ∼200 km tropospheric delay decorrelation scale. Additionally, Lee et al.[78] show that ionospheric delay increases drastically for scales (i.e. spatial separation distances) up to ∼50 km, and then continues to slowly increase.

Again, it is important to recognize that the mean error corresponds to error in the absolute position accuracy, whereas the error standard deviation correspond to relative position precision. As such, positions with a high mean error will not provide reliable absolute elevations, as desirable for total ice mass computations. However, precise positions, with a low point-to-point relative error, are useful for ice topography computations even if they have poor accuracy.

5.3.4 Alignment and Offset Error

It is important to recall that the computation of surface elevation using Equation 5.1 represents the idealized case where all the sensor reference frames are collocated and aligned with the vehicle body frame. In practice, when the sensors are integrated into the UAS, there are three-dimensional (3D) lever-arm offsets and pointing misalignments between all the reference frames. Other than the vertical offset between the GPS antenna and the laser sensor face, the lever-arms and alignments between the other sensor frames were not accurately measured during the CULPIS UAS integrations. In a static environment, the offsets and misalignments will introduce a constant error bias to the derived surface measurements; however, this error will continually change with the dynamics of aircraft flight, thereby introducing variable error to the elevation measurements. For example, a horizontal offset between the GPS antenna and the laser will translate into the vertical dimension as the aircraft attitude changes.

The magnitude of the vertical error introduced by the horizontal offset between the GPS antenna and laser is described by Equation 5.6. The error magnitude is dependent upon the horizontal offset distance and the aircraft off-horizontal attitude angle, and the nature of this error is illustrated by Figure 5.12. The horizontal offset between the antenna and laser is constrained by the size of the UAS and the relative location of those two sensors on the aircraft. For both the Manta and SIERRA integrations, these two sensors were located in close proximity, with a horizontal separation assumed to be less than 20 cm. Given a 20 cm offset

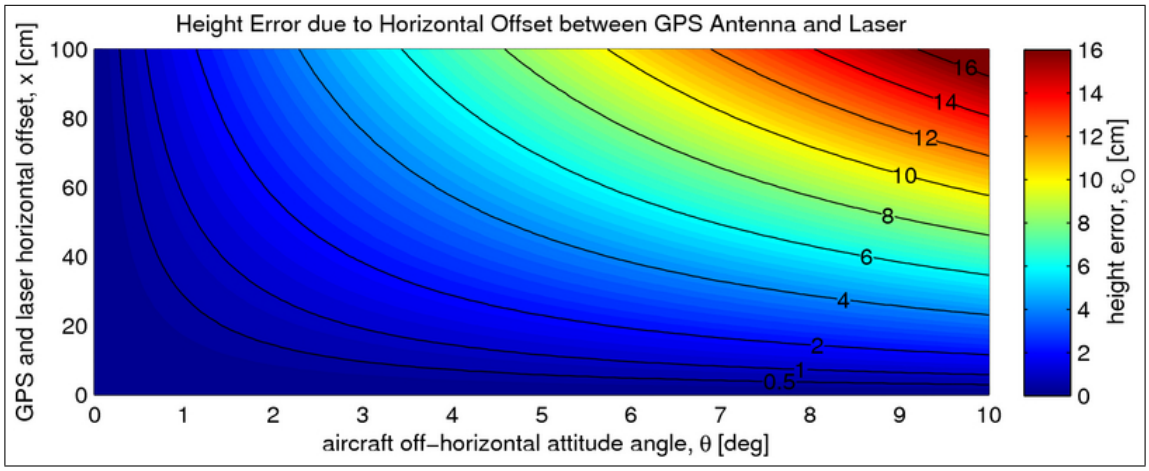

Figure 5.12: The CULPIS profile elevation error resulting from the horizontal lever-arm offset between the GPS antenna and the laser sensor head. This assumes that the GPS antenna is located at the aircraft center of mass (i.e. the rotation center). As the aircraft attitude deviates from horizontal, the relative vertical offset between the laser and GPS antenna will change, thereby introducing error into the derived elevation profile data. This error is described by Equation 5.3.

and a 5° off-horizontal attitude angle, the vertical error is ∼2 cm. This assumes that the GPS antenna is located at the aircraft center of rotation (i.e. center of mass). Deviation from the center of rotation will introduce additional error not modeled by Equation 5.6.

$$\boxed{\epsilon_O = \ x \cdot \sin(\theta)} \tag{5.6}$$

where...

ϵ_O = height error due to the GPS antenna and laser horizontal offset

x = horizontal distance offset between the GPS antenna and laser

θ = aircraft off-horizontal attitude angle

In addition to the lever-arm offset error, misalignment between the IMU, laser, and aircraft body frames will also introduce error. The angular misalignment can be thought of as contributing to the IMU angle determination error. In other words, the sensor frame misalignment is synonymous with inaccuracies in the IMU angular measurements, and is therefore described by Equation 5.3. A moderate amount of care was taken to align the sensor reference frames during the CULPIS UAS integrations, and it is assumed that they are within ±1° of each other. This degree of misalignment will introduce a ∼17 cm vertical error for

data collected at an off-nadir attitude angle of 5° from 100 m AGL.

It is recognized that the unknown lever-arm offsets and misalignments between the sensor frames introduce error into the CULPIS surface elevation measurements. In order to improve the CULPIS elevation accuracy, future effort should be placed on measuring the offsets and alignments, and enhancing the mathematics of Equation 5.1 to account for them appropriately.

5.4 Operational System Error Analysis

5.4.1 Runway Profiling Error

Section 5.3.3 focused on assessing the CULPIS GPS vertical positioning capabilities by performing ground-based surveys of the runways at Ilulissat and Ny-Ålesund and examining the dGPS solution quality for a range of baselines. This section, and the two that follow, focus on assessing the fully-integrated CULPIS system performance by examining elevation data collected in-flight during the MUSCOX and CASIE campaigns. One of the very first operational tests that was carried out was to fly over a van that was parked in the middle of the Ilulissat runway during MUSCOX and simply verify that the van profile could be identified in the CULPIS surface height data. The results of this test are illustrated in Figure K.1 on page 171, and show that it was indeed possible to identify the van's signature.

To assess the in-flight operational performance in a more quantitative sense, the "truth" reference surfaces were repeatedly overflown by the Manta and SIERRA UAS and profiled with the CULPIS during the MUSCOX and CASIE deployments. The runway profiling flight dates and times are listed in Table 5.4 on page 60. The CULPIS surface elevation measurements collected during these overpasses are compared to the "truth" runway survey to gauge the quality of the flight data. This analysis is focused on evaluating the vertical accuracy of the CULPIS topography data by quantifying the error between the flight-based runway elevation profiles and the ground-based "truth" runway survey. As previously mentioned, collecting measurements over a surveyed reference surface to assess the quality of flight-based measurements is a fairly standard method which has been exercised for both the NASA and the Technical University of Denmark airborne laser altimeter systems (e.g. [68, 131]), among others.

The MUSCOX and CASIE runway overflight ground tracks are shown in Figure 5.13, along with the profile data used to assess the CULPIS performance, the local GPS reference stations, and the truth runway surveys. As discussed in Section 5.3.2, the CULPIS Microstrain IMU data were determined to be of poor-quality data; however, 1 Hz aircraft attitude measurements were collected by the Manta and SIERRA Piccolo autopilots during these line-of-sight flights. Due to the proprietary nature of this system, the exact capabilities of its IMU are not known, but it is a microelectromechanical sensor (MEMS) with 3-axis gyroscopes and accelerometers functional up to 300°/s . The Piccolo and CULPIS IMU specifications are comparable, but the CULPIS IMU samples at 100 Hz whereas the Piccolo provides 1 Hz measurements. The slower measurement rate will will introduce minor interpolation errors into the elevation data. The SIERRA C-Migits IMU was not functional during the runway overflights.

The CULPIS laser and GPS data, and the Piccolo IMU data are used in Equation 5.1 to compute the ENV coordinates of the laser footprint measurement locations in the WGS84 ellipsoid. As was done with the ground-based runway survey analysis, sGPS and short- and long-distance baseline dGPS data were used to generate three sets of runway profile data to highlight the GPS positioning effects on the derived elevation data. The GPS positioning parameters as reported by the Waypoint software are presented in Figure K.2 on page 172. In general, they show similar performance as found for the runway survey data presented in Figure 5.7 on page 63; however, there appear to be several loss-of-lock incidents where lock on the carrier phase is lost and then gradually recovered. This occurrence leads to intermittent periods of poor positioning.

To facilitate a comparison between the in-flight runway profile data and the "truth" runway survey data, the CULPIS elevations were filtered to retain quality data in close vicinity to the reference survey. Data collected with the aircraft roll ranging between -3° and +3°, pitch between +1° and +7°, and footprints within 3 m horizontally of the reference surveys were deemed "quality" runway profile data suitable for comparison with the reference surveys. Both the Manta and SIERRA UAS nominally fly with a slight upward pitch angle, which accounts for the skew in the chosen pitch range. The runway profile data were then divided into two different groups, data collected at altitudes below 200 m AGL, and data collected at altitudes greater than 200 m AGL but less than 400 m AGL. This division of the data will highlight the impact of altitude on the IMU pointing error and the resulting elevation measurement quality. Throughout

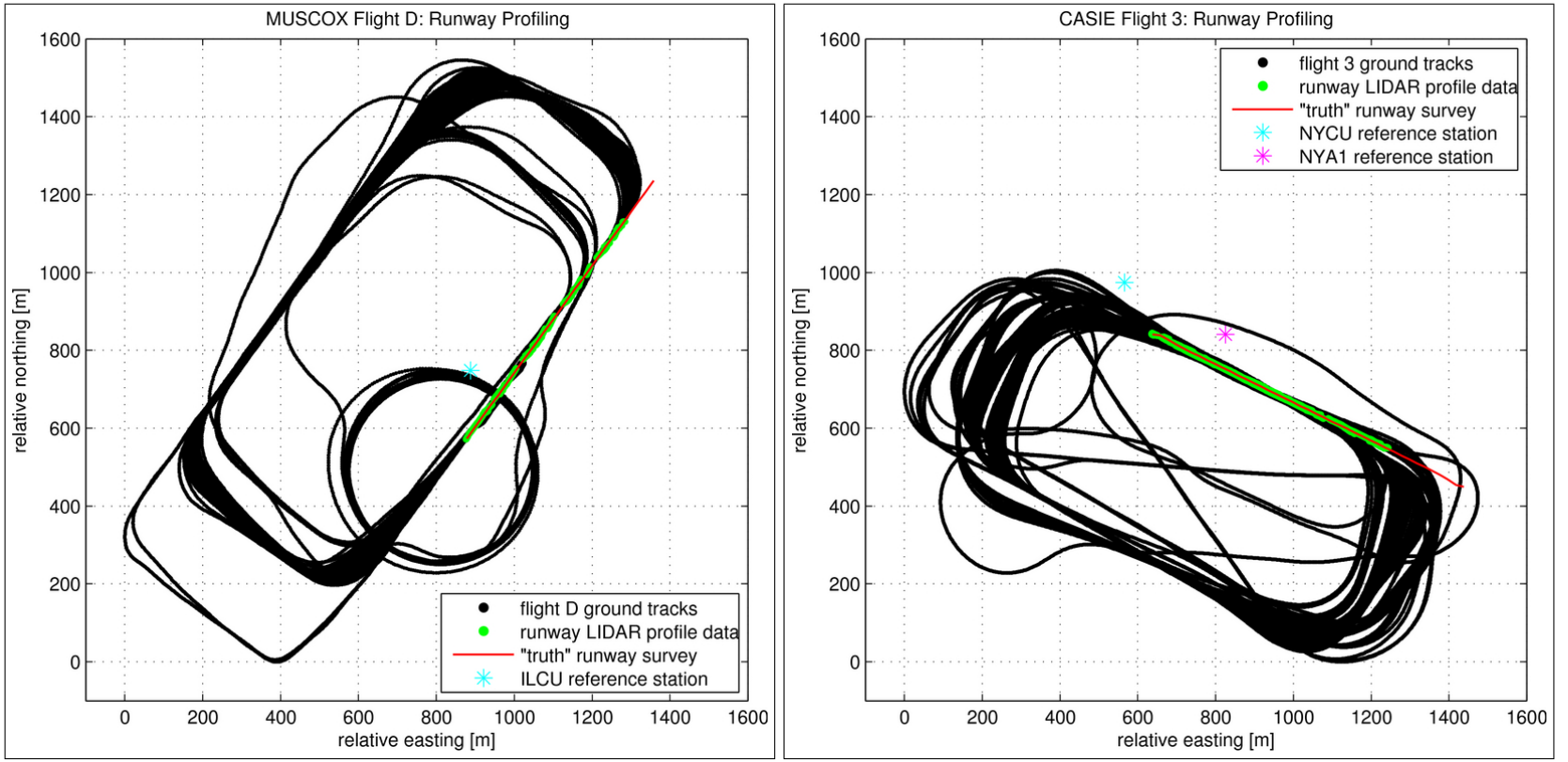

Figure 5.13: The MUSCOX and CASIE runway profiling flight tracks are shown in black. The CULPIS-derived runway elevation profile data (shown in green) are compared to the "truth" reference surveys (shown in red) to evaluate the CULPIS measurement accuracy and precision. The location of the reference stations used for dGPS positioning are indicated by asterisks.

this comparison it is important to recognize that the laser measurements are not exactly spatially coincident with the truth runway survey measurements, and as such, there will be some disagreement between these two due to lateral variations in the runway surface topography not captured by the ground-based runway survey.

The three sets of runway profiles derived from data collected below 200 m AGL, along with the truth runway survey, are shown in the top plots of Figure 5.14. The difference error between the profile data and the truth survey is shown in the bottom plots, along with the error mean (μ), standard deviation (σ), and RMS. The elevation error is the difference between a profile measurement and the"truth" reference height at the same location (i.e. same easting). The overall accuracy throughout the flight period is described by the error mean (μ), and the overall precision (spread) is described by the error standard deviation (σ). The RMS error is a single metric which encapsulates both the mean and standard deviation.

The measurement error statistics for data collected below and above 200 m AGL are presented in Table 5.7. It is evident that, as expected, both the MUSCOX and CASIE sGPS data have the least agreement with the reference surveys, and the two dGPS datasets have considerably better agreement. The sGPS data describes the worst case scenario where dGPS processing is not possible, and thus, represents the upper bound for CULPIS surface height measurement quality. Furthermore, the data collected at altitudes <200 m AGL is more accurate and precise than data collected at higher altitude. The low-altitude, short-baseline dGPS measurements have an accuracy (mean error) within 3 cm and a precision (error standard deviation) of less than 20 cm. These values increase somewhat dramatically to an accuracy within 55 cm and precision of less than 40 cm for the high-altitude data. The long-baseline data shows accuracies between approximately 60-80 cm, with precisions between 25-45 cm for low-altitude data, and 50-80 cm precisions for high-altitudes. The sGPS data have accuracies of 50-200 cm and precisions of 150-260 cm.

As previously mentioned, the error mean, standard deviation, and RMS statistics of the full runway profile dataset, as reported in Table 5.7, describe the CULPIS performance over the full period of the profile flights, capturing both the short and long time-scale variability within this period. For applications such as measuring sea ice freeboard (using local water surface tie-points) and roughness characteristics, knowledge of the absolute ice surface elevation is not critically important. Rather, the ice elevations within small isolated

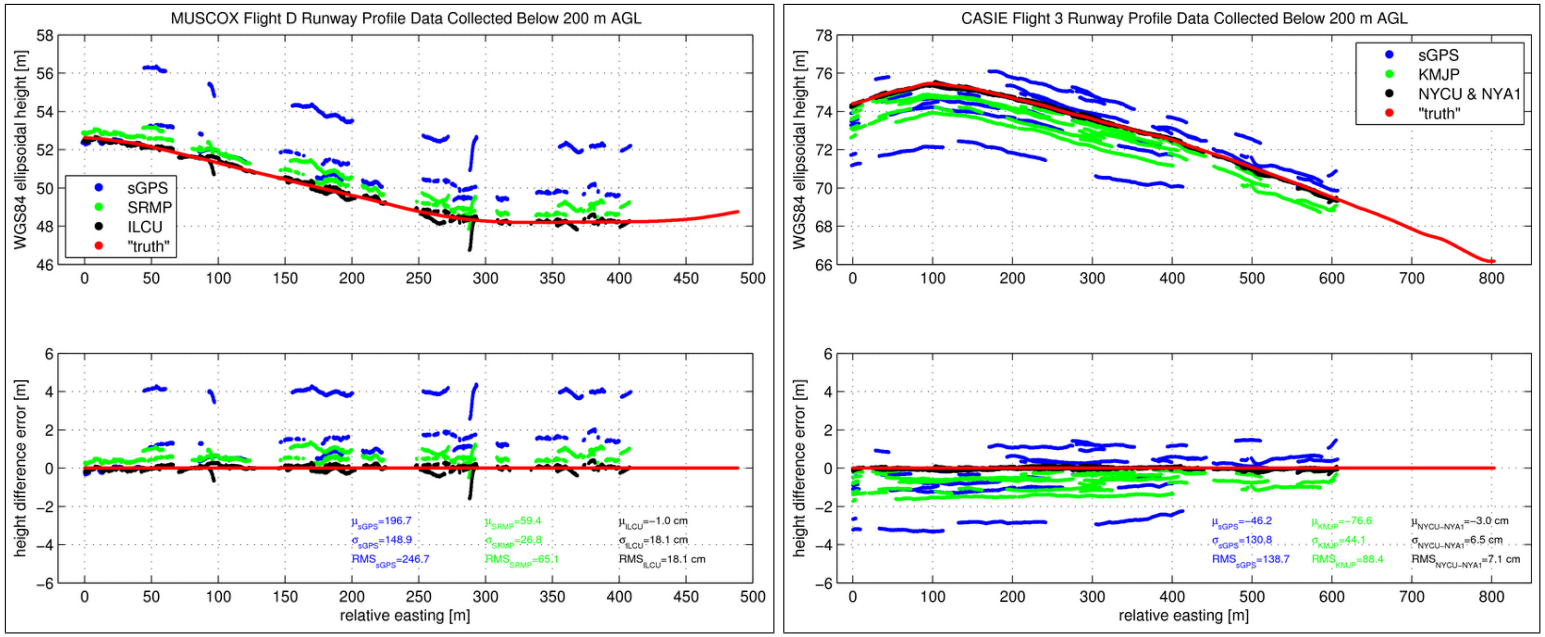

Figure 5.14: MUSCOX and CASIE runway profiles derived from CULPIS data collected during flight using three different GPS positioning solutions, and their error relative to the "truth" reference survey, shown in red. The sGPS profiles, shown in blue, were generated using the pseudorange code solutions computed in real-time by the CULPIS GPS receiver. The profiles shown in green were generated using long-baseline dGPS post-processing solutions, and profiles shown in black were generated using short-baseline dGPS post-processing solutions. All profiles presented here were generated from CULPIS data collected below 200 m AGL. The error statistics for each profile are shown in their corresponding colors, and are also presented in Table 5.7.

Table 5.7: MUSCOX and CASIE runway profile elevation error statistics relative to the "truth" reference survey for CULPIS data collected below 200 m AGL, and data collected above 200 m AGL but below 400 m AGL. The ILCU and NYCU & NYA1 statistics represent the quality of profiles generated using short-baseline dGPS positioning solutions, SRMP and KMJP represent profiles generated using long-baseline solutions, and sGPS represents profiles generated using the real-time pseudorange code solutions.

	reference	mean [cm]		st. dev. [cm]		RMS [cm]	
campaign	station	(<200 m)	(>200 m)	(<200 m)	(>200 m)	(<200 m)	(>200 m)
MUSCOX	ILCU	-1.0	-28.5	18.1	37.7	18.1	47.2
	SRMP	59.4	-1.5	26.8	77.8	65.1	77.9
	sGPS	196.7	177.4	148.9	257.0	246.7	312.3
CASIE	NYCU/A1	-3.0	-54.6	6.5	24.9	7.1	60.0
	KMJP	-76.6	-81.0	44.1	49.5	88.4	94.9
	sGPS	-46.2	68.9	130.8	210.6	138.7	221.6

regions can be computed and compared in a relative sense to one another. For example, surface roughness can be described by the elevation standard deviation over a given distance. If this distance scale is chosen to be 1 km, one can compute the surface standard deviation over 1 km regions, and compare the relative variability amongst these regions without knowledge of the absolute heights. Given this logic, it is important to identify the scale at which low-frequency, high-amplitude GPS variability does not dramatically affect the surface measurements.

As was done in Section 5.3.3, the measurement variability over a range of time/space scales can be described by the error variogram (Equation 5.5). To assess the in-flight operational performance of the CULPIS measurements over a range of scales, a single, representative runway overpass was identified, and its error variogram was computed. The single runway profile elevation errors are shown in Figure 5.15, and the error variograms are shown in Figure 5.16.

Due to the relatively short runway length, the variograms only extend to a maximum lag of approximately 100 m. However, within this distance the error quickly grows and levels-off at a sill value of ∼30 cm for the MUSCOX data, and ∼5 cm for the CASIE data at a lag near 50 m (3 seconds when flying at 30 m/s). As shown by Figure 5.9 in the previous section, the GPS error variability at a lag of 3 seconds is less than 2 cm. As such, the error variogram sill presented here in Figure 5.16, represents the CULPIS measurement error, excluding GPS errors, which arises primarily from aircraft attitude and altitude impact on IMU inaccuracies and sensor misalignments, the unknown lever-arm offset errors, the laser residual noise, and errors

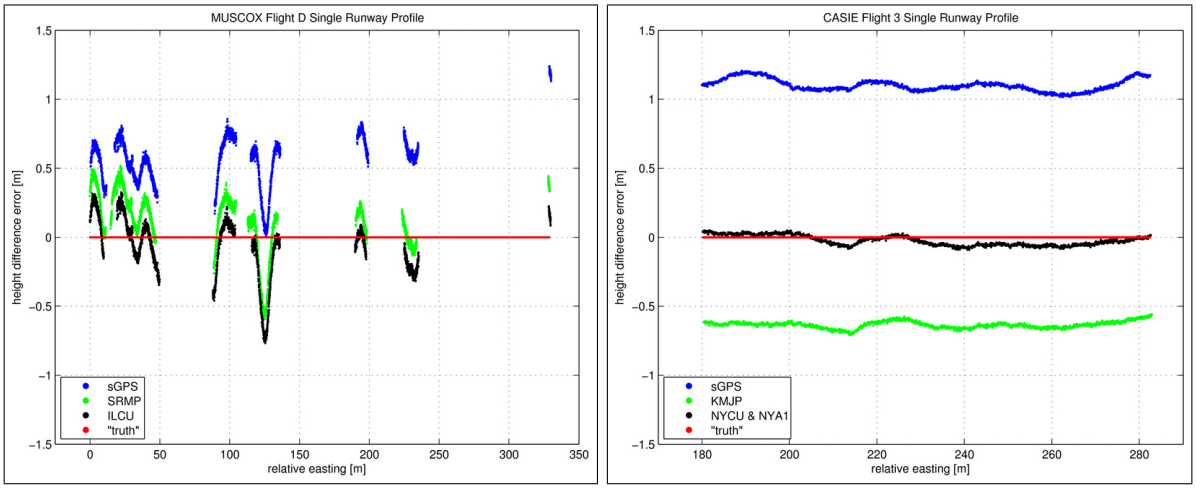

Figure 5.15: MUSCOX and CASIE single runway overpass elevation error relative to the "truth" reference survey. The sGPS profiles, shown in blue, were generated using the pseudorange code solutions computed in real-time by the CULPIS GPS receiver. The profiles shown in green were generated using long-baseline dGPS post-processing solutions, and profiles shown in black were generated using short-baseline dGPS post-processing solutions. The MUSCOX data were collected at an altitude of ∼155 m AGL and the CASIE data were collected at an altitude of ∼70 m AGL.

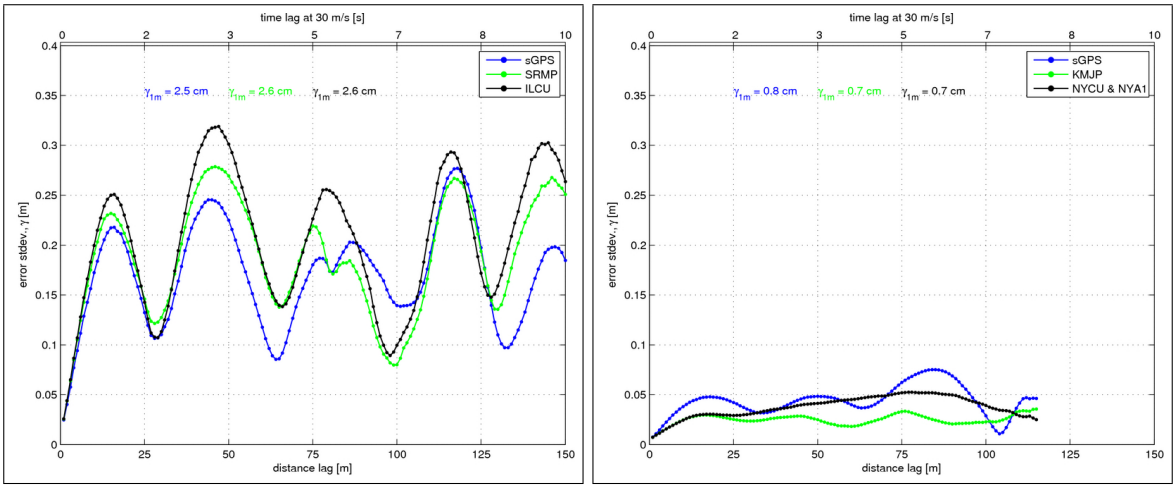

Figure 5.16: MUSCOX and CASIE single runway overpass elevation profiling error variograms as a function of distance. The sGPS variograms, shown in blue, depict the error variability of profiles generated using the pseudorange code solutions. The variograms shown in green depict the error variability of profiles generated using long-baseline dGPS post-processing solutions, and variograms shown in black depict the error variability of profiles generated using short-baseline dGPS post-processing solutions. The top x-axis shows the equivalent time lag assuming a nominal flight speed of 30 m/s. The nugget is chosen to be the variogram value at a lag of 1 meter, and is presented for each processing method in the corresponding color. These variograms are derived from the profiles presented in Figure 5.15.

associated with interpolating the GPS (5 Hz MUSCOX, 10 Hz CASIE) and IMU (1 Hz) data to the laser sample times (400 Hz). This is supported by the fact that all three profile variograms computed using the different GPS positioning methods exhibit similar behavior, which suggests these data are independent of GPS errors over the short distance scale of 100 m.

The cause of the dramatically higher variogram values for the MUSCOX data, as compared to the CASIE data, is somewhat unknown, but potentially stems from a combination of sources. First of all, the CULPIS software that was used during MUSCOX to read and record the instrument data contained flaws that resulted in considerable amounts of data being sporadically "lost" (i.e. not recorded) throughout the entire campaign. Because of this, the MUSCOX data contains intermittent gaps, which lead to increased errors in the interpolated GPS and IMU data. This flaw was corrected prior to the CASIE mission. Additionally, the smaller size of the Manta UAS, as compared to the SIERRA UAS, may lead to more unstable flight characteristics with increased attitude motion. The effect of aircraft attitude and IMU inaccuracies is discussed below, along with an investigation of the UAS attitude variability.

To investigate the Manta and SIERRA flight characteristics, 15 minutes of roll and pitch measurements collected during the runway profile flights are examined to evaluate the attitude variability. The roll and pitch time series and corresponding fast Fourier transform (FFT) spectral power are presented in Figure 5.17. The wind speed and variability statistics presented in Table 5.8 suggest similar conditions during the two flights; however, the spectral signatures are quite different. The CASIE roll spectrum shows two distinct peaks at approximately 10 and 40 seconds/cycle, whereas the MUSCOX roll spectrum shows peak near 20 seconds/cycle, and a peak centered near 70 seconds/cycle. The smaller size of the CASIE runway and available flight space lead to smaller-radius flight tracks with tighter turns, thereby resulting in lower-periodicity (higher frequency) spectral characteristics. As shown in Table 5.8, the total roll power is nearly the same for both campaigns. The nearly equivalent total roll power suggest similar overall roll behavior.

The pitch spectral characteristics are fairly dissimilar for the two campaigns, with CASIE showing a more well defined periodicity peaking near 15 seconds/cycle, whereas the MUSCOX spectral power is more uniformly distributed over higher period (lower frequency) cycles. These long period cycles are likely associated with a consistent up-and-down pitching of the Manta UAS, a flight characteristic which is evident

Table 5.8: The UAS roll and pitch FFT total spectral power and wind conditions for a subset of the MUSCOX and CASIE runway profiling flights. These values are associated with data presented in Figure 5.17.

parameter	MUSCOX	CASIE
roll total spectral power	207.9	230.1
pitch total spectral power	103.0	56.9
wind speed mean (m/s)	3.8	3.2
wind speed stdev (m/s)	1.6	1.6

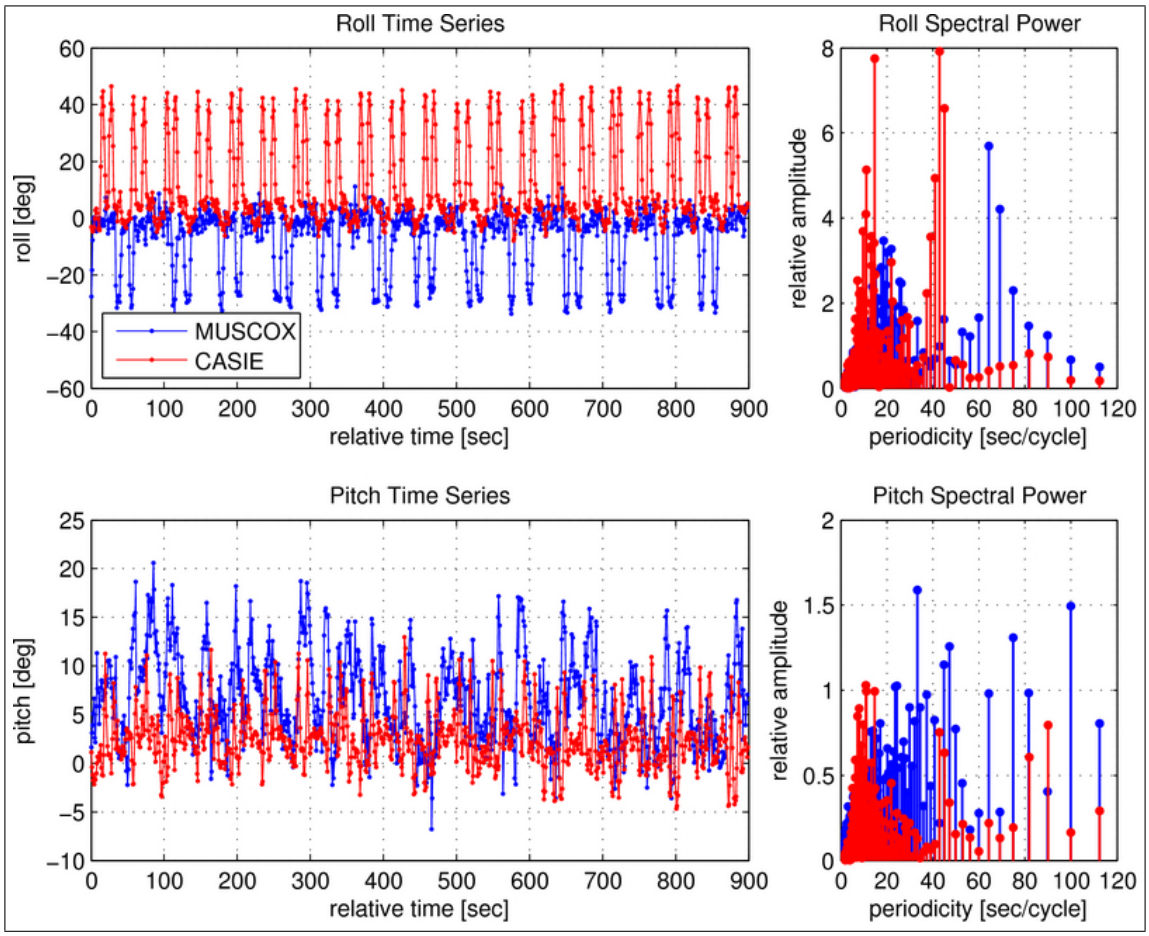

Figure 5.17: The UAS roll and pitch, and corresponding FFT spectra, for a subset of the MUSCOX and CASIE runway profiling flights. The total spectral power and wind speed means and standard deviations associated with these data are presented in Table 5.8.

in the CULPIS video data (data not presented here). The pitch total spectral power is almost twice as high for the MUSCOX campaign, which suggests that the Manta flies with higher attitude variability. As presented in Figure 5.4, larger attitude angles combined with IMU uncertainty lead to increased measurement error, as evident in the MUSCOX data.

5.4.2 Ice Sheet Crossover Error

As an additional investigation to the operational performance of the CULPIS elevation measurements, a crossover point analysis was carried out using data collected within the MUSCOX study region to assess the consistency of repeat surface observations. Crossover data are defined as data collected at intersecting transects within 5 m of each other. The data within the 5 m radius of the intersection point are averaged together to provide a mean surface elevation at the crossover point for each intersecting transect. The radius of 5 meters was chosen to smooth out small scale surface variability and measurement error to achieve a measurement representative of the crossover point surface elevation. A total of 271 intersection points were identified and are shown in the top panel of Figure 5.18. The histogram of differences between the transect crossover elevations is shown in the bottom panel of Figure 5.18, along with the difference mean, standard deviation, and RMS error.

The difference histogram somewhat resembles a normal distribution with an error mean of 40.3 cm, a standard deviation of 128.1 cm, and an RMS of 134.1 cm. These data were collected over a 6 day period in late July. During this period it is expected that the ice surface may have melted and or moved to some extent; however, this change is likely negligible relative to the CULPIS measurement difference error found during this time. These data were collected at relatively high altitude above the surface (>200 m AGL), and as such the IMU measurement uncertainty and sensor misalignments are magnified. Additionally, relatively long time periods between repeat overpasses (on the order of hours to days) implies that these errors encapsulate both the lower-frequency GPS positioning variability and higher-frequency instrument and aircraft attitude error variability. Furthermore, the overall performance of the CULPIS was compromised during MUSCOX due to the software architecture which led to considerable amounts of lost data.

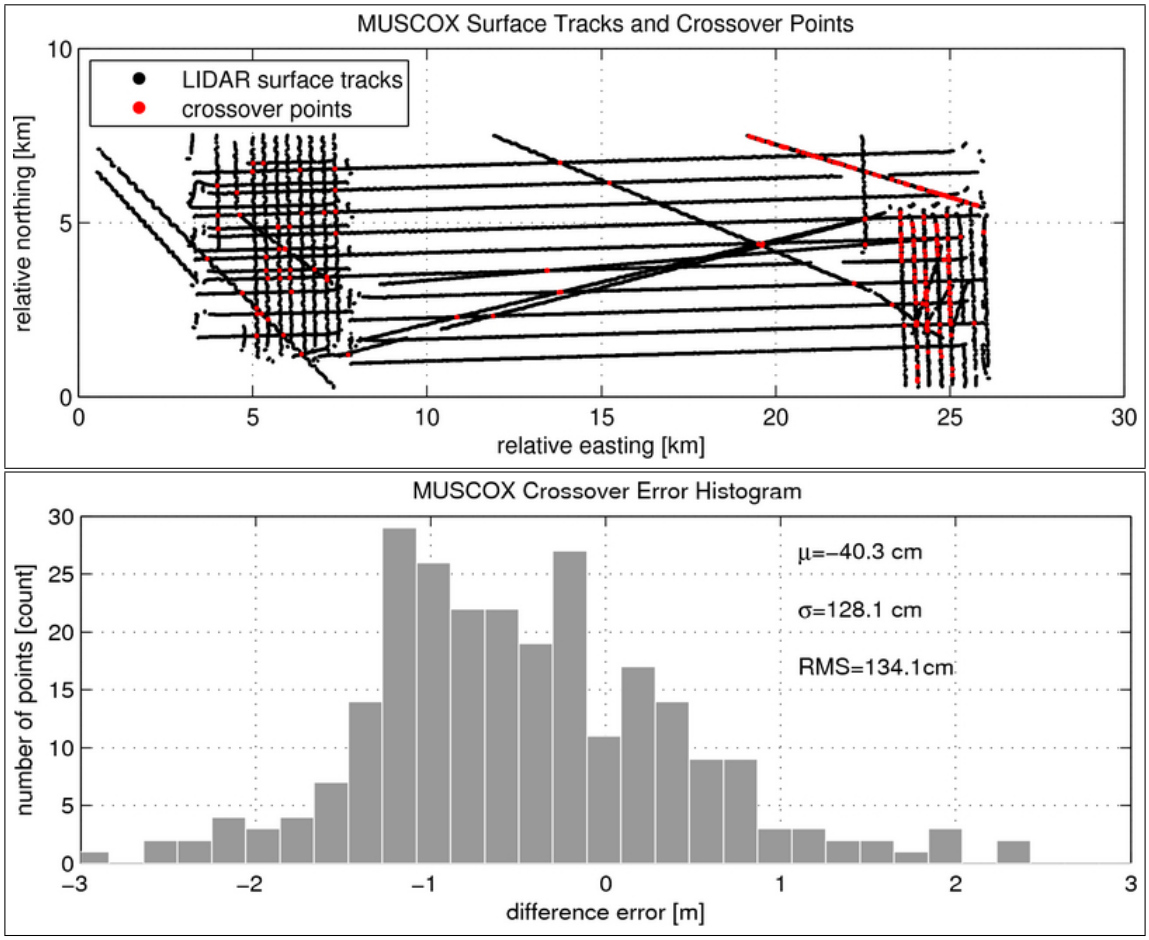

Figure 5.18: The top panel shows the MUSCOX ground tracks within the study region and the crossover locations. The bottom panel shows the difference error histogram for surface elevations collected at the crossover locations, along with the error mean, μ, standard deviation, σ, and RMS statistics.

5.4.3 Sea Ice Profiling Error

Up to this point the error analysis has focused primarily on relatively short segments of GPS and CULPIS altimetric data collected over the runways at Ilulissat and Ny-Ålesund, and the MUSCOX crossover error analysis characterized the system performance in 2008 over the Greenland ice sheet; however, the full elevation profiles collected during this campaign were not thoroughly examined. In order to better evaluate the long-term CULPIS systematic performance, the CASIE flight 9 data are examined in more detail. Preliminary investigation of the flight 9 data showed several relatively large elevation discontinuities where the surface height varied over a wide range during a short period of time. This variability was beyond that expected for sea ice topography, which provided motivation for further investigation into the source of this anomalous elevation data. It was found that the GPS covariance height standard deviation was dramatically elevated during these times. The exact cause of this is unknown, but it is speculated that, for some reason, the CULPIS GPS receiver temporarily lost lock on the L1 carrier phase of one, or several satellites at these times, which led to a instantaneous and dramatic change in the apparent satellite visibility and geometry, which in turn manifested itself as a abrupt change in the GPS position solution. Regardless of the cause, its occurrence can be identified by large "spikes" in the height standard deviation.

The GPS height standard deviation is a parameter that is reported by the NovAtel Waypoint software. The Waypoint users manual defines it as the "estimated up position standard deviation in the local level frame." This definition is somewhat ambiguous, which makes it difficult to determine mathematically what this parameter represents and how it is calculated and related to the GPS least squares solution. It is assumed to be the product $\sigma_a \cdot \sigma_v$ derived from the covariance matrix, C_l, shown on page 165. The point being made is that the derivation of the height standard deviation parameter is not entirely clear, which highlights a limitation of using commercial software packages. Regardless, this parameter has been found to be a good indicator of unreliable dGPS position solutions, and therefore continues to be used. Since it is assumed to derive from the covariance matrix, it is also referred to as the height covariance standard deviation or the height uncertainty. These expressions are all synonymous.

The GPS solution height uncertainty for CASIE flight 9 is shown in the top plot of Figure 5.19. The

corresponding CULPIS surface elevation profile is shown in the bottom plot. Dramatic peaks in the GPS height uncertainty are apparent throughout the dataset, and these peaks suggest that the position solution is of relatively poor quality at these times. In comparison with surface elevation profile, it is evident that several of the uncertainty peaks are affiliated with anomalous elevations. Based on this correspondence it is concluded that the GPS and elevation values are not valid during these times and should be removed from the dataset. The anomalous data is automatically identified by computing the standard deviation of the height uncertainty in 200 m windows stepped along the time series, and flagging data where the standard deviation is $\geq$0.5 mm. These data are a shown in red in Figure 5.19 and are not used for subsequent sea ice geophysical analysis. The data shown in black are considered valid, and serve as the final surface elevation data which are used for geophysical analysis. Plots of the height uncertainty and surface elevation for CASIE flights 4, 7, 8, and 11 are presented in Figures M.3-M.6 on pages 180-183.

As an initial demonstration of the CULPIS's capabilities for sea ice topography profiling, the ellipsoidal surface elevation measurements collected during CASIE flight 8 over two different regions of sea ice are shown in Figure 5.20, along with the coincident visible imagery. The images have not been orthorectified so the exact locations of the laser ground tracks through the images are not known; however, they do depict the general ice surface characteristics within in the two regions. Region A consists of relatively smooth ice with extensive melting and a few distinct ridge features approximately one meter high. The nominal ice surface has an ellipsoidal elevation of roughly 35 m. Region B consists of broken ice floes and open water leads. In general the surface is more rough than that of region A and lacks prominent ridge features. Much of the roughness is affiliated with the small, broken ice floes. As evident in the visible imagery, these floes often have rough, ridged edges that are likely created by impact and compression with the surrounding ice. This is a common feature that is seen throughout the CASIE image dataset. Laser returns from the open water at a relative northing distance between 430-500 m indicate that the local water level has an ellipsoidal surface elevation of $\sim$32.6 m, as shown by the blue line.

There are a number of important points to discuss regarding the sea ice profiles from regions A and B. To begin, the nominal ice surface ellipsoidal elevation is approximately two meters higher in region A than in region B. This is most likely due to large-scale ocean surface fluctuations resulting from the spatial variability

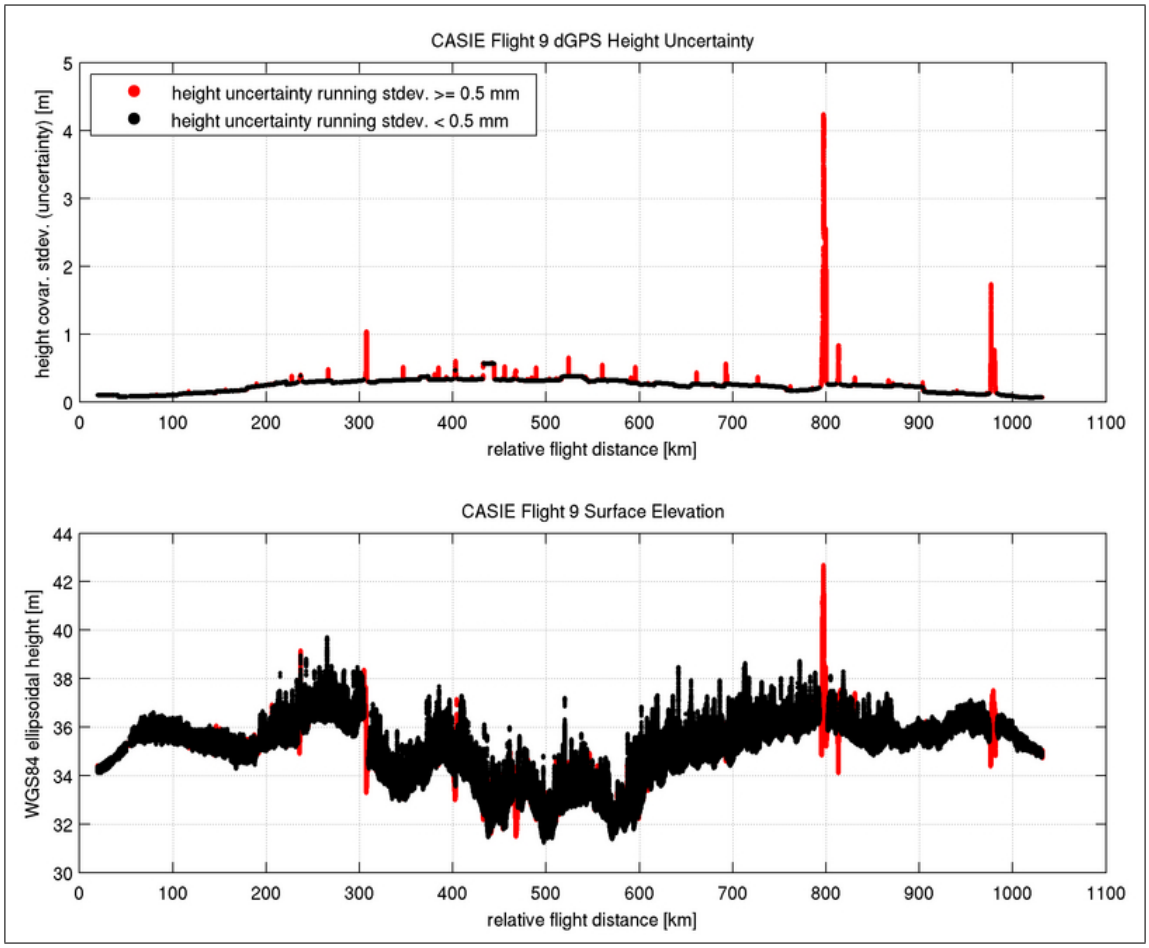

Figure 5.19: CASIE flight 9 dGPS height uncertainty and surface elevation profiles. The dGPS height uncertainty is the covariance standard deviation described by Equation I.16 on page 165. All data are rejected where the running standard deviation of the height uncertainty within a 200 m window is $\geq$0.5 mm. These data are shown in red. Plots of the height uncertainty and surface elevation for CASIE flights 4, 7, 8, and 11 are provided in Appendix M.

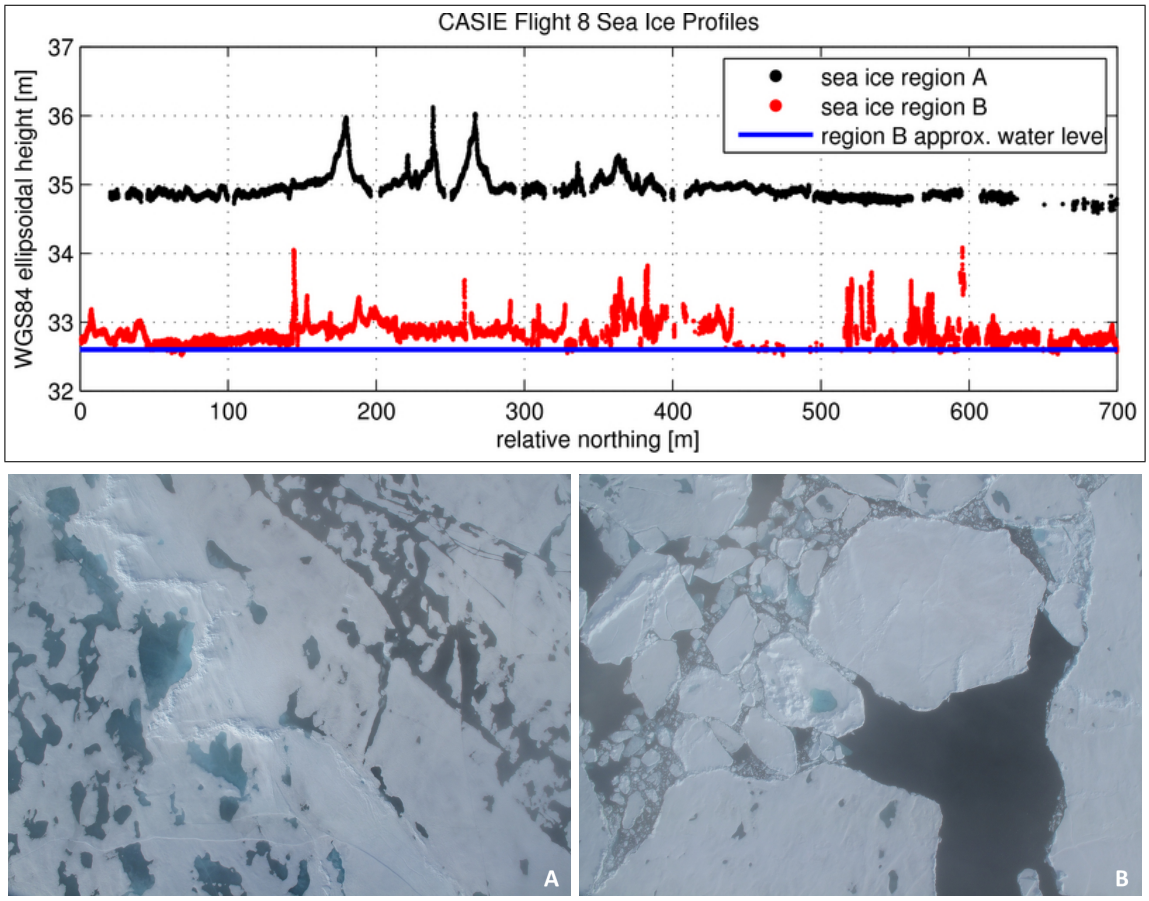

Figure 5.20: The surface profiles for two regions of sea ice overflown during CASIE flight 8. These surface profiles were generated with data collected at ∼165 m AGL and processed using long-baseline dGPS position solutions relative to reference stations NYCU & NYA1. The sea ice in region A (black profile, left image) is relatively smooth with a large ridging structure, extensive melting, and no open-water leads. The sea ice in region B (red profile, right image) is rougher, and is comprised of angular floes and leads. CULPIS data collected over the large lead in region B serves as a tie point that is used to approximate the local water level (shown as the blue line). The sea ice freeboard can then be determined relative to this level. The large height bias between sea ice in region A and B is predominantly due to geoid and ocean dynamic topography differences at these two locations. With the absence of open-water leads in region A, it is not possible to directly measure the local water. However, the lowest ice elevations, typically located on either side of ridge features, are a close approximation of the water level, and thus, these minimum elevations can be used to estimate the freeboard [48].

of the geoid, dynamic ocean topography, tides, and atmospheric pressure loading. These phenomenon will cause the ocean surface elevation level to vary by several meters over distances of hundreds of kilometers, and considerable effort is placed on accurately measuring their magnitude to aid in the analysis of Arctic sea ice satellite altimetry data (e.g. [27, 29]). The broad-scale sea level fluctuations of 1-5 meters are clearly evident in the CASIE flight 9 elevation profile shown in the bottom plot of Figure 5.19.

The large-scale ocean surface variability makes it challenging to determine the ice freeboard from the profile data because the local water elevation is not directly known, such as region A. In other locations, such as region B, leads in the ice are present, and laser returns from open water make it possible to determine the local water level (represented by the blue line in Figure 5.20), which can then be subtracted from the profile ellipsoidal elevation to give the freeboard height. In region A this is not possible because open water is not present. However, as discussed by Weeks et al.[128] and Hibler et al.[48], the minimum ice elevations located on either side of pressure ridges are close to, or slightly below, the local water level. As such, the minimum profile elevation for a given region, whether it be derived from laser returns over open water or ice, is a valid approximation for the local water level. Of course the sample region must be large enough to capture the ice ridging features, but not so large that it entrains the large-scale ocean surface and instrumentation error variability. From the quantitative and qualitative analysis presented in this chapter, it is determined that a region 200 m in distance is suitable for computing the minimum elevation to estimate the local water level. This is justified in the following section.

5.5 Error Analysis Summary

The performance assessment presented in this chapter was carried out in order to quantify the CULPIS elevation measurement error sources and to characterize its capabilities for sea ice and ice sheet surface profiling. This objective was accomplished by taking a number of steps. First, the CULPIS kinematic dGPS positioning error was evaluated by comparing ground-based runway survey measurements to a "truth" runway reference surface. Then, the CULPIS full-system altimetry error was evaluated by comparing flight-based runway profile measurements to the runway reference surface, and by examining the error between ice sheet measurement crossover data collected during MUSCOX. Finally, sea ice elevation profiles were

examined to highlight issues associated with measuring ice freeboard, roughness, and ridging.

In general, the CULPIS elevation measurement accuracy is critically affected by GPS positioning uncertainties, which are dominated by ionospheric and tropospheric propagation error. Since the CULPIS utilizes a single-frequency receiver (to minimize cost), atmospheric corrections cannot be made. During science mission flights dGPS baselines range from tens to hundreds of kilometers, and thus ionospheric and atmospheric signal propagation effects are substantial. The IMU angle determination error and sensor misalignment error also contribute a relatively large amount of error, Furthermore, the horizontal lever-arm offset between the GPS antenna and laser were not measured following the UAS CULPIS integration, and thus this error is not accounted for.

Figure 5.21 summarizes the CULPIS measurement error characteristics and its short-lag, relative positioning capabilities. The data plotted in black and red are the ellipsoidal surface elevation variograms of the profile data collected in sea ice regions A and B corresponding to Figure 5.20. These surface profiles were derived using CULPIS GPS data which were positioned using long-baseline (>200 km and <500 km) dGPS processing relative to the NYCU & NYA1 reference stations. The ice surface standard deviation grows rapidly to 15 cm over a short lag distance of approximately 20 m, and then continues to grow slowly to reach the maximum variogram sill standard deviation of approximately 18-23 cm at lags greater than 200 m. The variogram sill represents the nominal ice surface roughness, and agrees well with ice roughness computations presented in the following chapter.

The data plotted in green and cyan are the variograms of the ground-based MUSCOX GPS runway survey error and the flight-based CASIE runway profile error, respectively. The MUSCOX runway survey GPS data (affiliated with the green variogram) were positioned using long-baseline dGPS processing relative to to the SRMP reference station (baseline distance of 426.5 km). This is the same variogram plotted in green in the left panel of Figure 5.9, and it depicts the GPS error over the first 500 m of lag. The CASIE runway profile GPS data (used to derive the elevation data affiliated with the cyan variogram) were positioned using long-baseline dGPS processing relative to the KMJP reference station (baseline distance of 890.8 km). The variogram shown here in cyan is the same variogram shown in green in the right panel of Figure 5.16, and it depicts the full system profiling error of the CULPIS over a relative short distance lag of ∼100 m (roughly

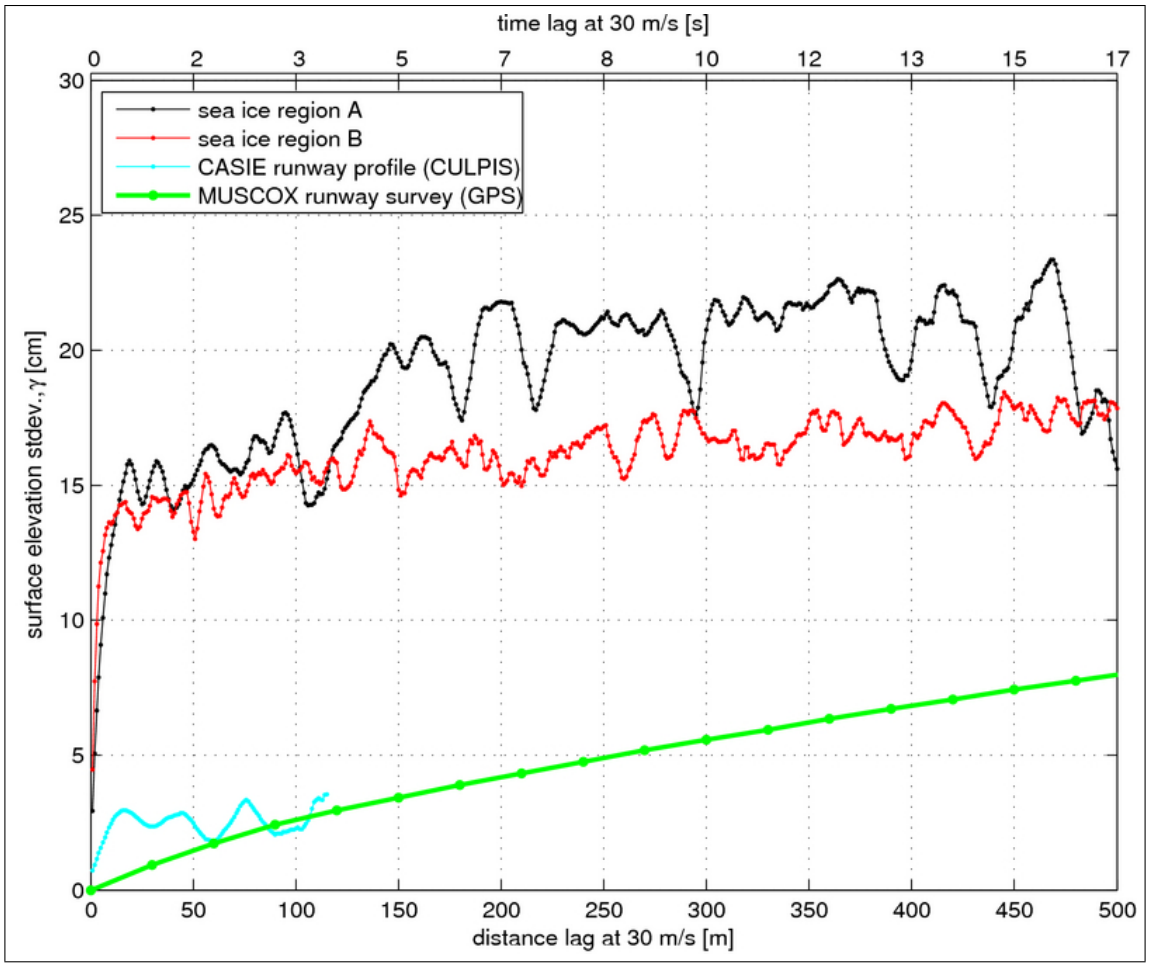

Figure 5.21: Sea ice surface and CULPIS instrumentation error variograms. The variograms plotted in black and red depict the sea ice surface elevation variability (elevation standard deviation as a function of lag) collected in regions A and B discussed in Figure 5.20. These surface profiles were generated with data collected at ∼165 m AGL and processed using long-baseline dGPS position solutions relative to reference stations NYCU & NYA1. The variogram plotted in green depicts the surface elevation error variability of the MUSCOX long-distance dGPS runway survey processed relative to the SRMP reference station. This is the same data that is plotted in green in the left panel of Figure 5.9. The variogram plotted in cyan depicts the surface elevation error variability of the CASIE runway profile generated with CULPIS data collected at ∼70 m AGL and processed using dGPS solutions relative to long-distance reference station KMJP. This is the same data that are plotted in green in the right panel of Figure 5.16. The variograms shown here in green and cyan represent the systematic error variability of the CULPIS components as a function of time or distance, assuming a flight speed of 30 m/s. The systematic variability is considerably less than the ice surface variability, shown in black and red, over these lags. This figure indicates that the CULPIS can be used to precisely measure relative changes in ice surface elevation over short distance lags less than 200 m with systematic error less than 10 cm.

half the distance of the runway profile which was used to generate the variogram).

Figure 5.21 shows that the GPS altitude error grows relatively slowly, whereas the full system profiling error grows relatively fast, reaching its peak standard deviation of ∼3 cm at a lag of only ∼20 m. The full system error includes the error contribution from the GPS, but it is evident that the GPS error does not dominate the system error until a lag of ∼100 m. This suggests that at lags less than 100 m the system error is dominated by the laser, IMU, lever-arm, and sensor misalignment errors, which have a combined error standard deviation of ∼3 cm.

The GPS error continues to grow with lag, and thus it is important to choose a lag distance over which relative surface elevation measurements can be computed to minimize the instrumentation error to an acceptable level. At a lag of 200 m the GPS error is ∼4 cm, and as stated above, the remaining systematic error is ∼3 cm. Therefore, for distance lags of 200 m the full system error will be ∼7 cm, which meets the goal measurement precision (point-to-point error) requirement of 10 cm. Based on this error analysis, the subsequent geophysical analysis utilizes relative surface heights computed within 200 m sections of data to evaluate sea ice roughness and ridging characteristics. This method eliminates the large-scale ocean surface variability and minimizes the CULPIS systematic error to an acceptable level less than 10 cm.

The CULPIS error budget is summarized in Table 5.9 and is broken into two sections. The top section characterizes the CULPIS absolute measurement error and represents the vertical accuracy of individual elevation measurements collected over all time and distance scales. These are conservative values that represent the high-end error bounds. The bottom section specifies the relative error for measurements collected over short time and distance scales. In other words, the absolute error specifies the accuracy to which ellipsoidal elevation measurements are known, and the relative error specifies the precision to which elevation measurements are known over relatively short scales. The absolute accuracy is relevant to applications such as ice sheet elevation mapping where measurements are collected over relatively long time and distance scales (i.e. $\geq$ minutes, $\geq$ decimeters) and the absolute elevation is critical for estimating mass loss and gain. On the other hand, the precision is relevant to applications which are focused on relative changes in surface elevation over relatively short time and distance scales (i.e. $\leq$ minutes, $\leq$ decimeters), such as investigations of sea ice freeboard, roughness, and ridging characteristics. The conservative estimate

Table 5.9: The CULPIS measurement error budget. The top section shows the error source and the absolute error value for each source. These are conservative error bounds distilled from the analysis presented in this chapter that represent the absolute measurement accuracy over long scales (i.e. $\geq$ minutes, $\geq$ decimeters). The typical absolute error values may be lower for sources that are dependent on the pointing angle, GPS baseline distance, height AGL, or sensor alignments and offsets. The lowest error that can reasonably be expected with the current CULPIS instrumentation is $\sim$50 cm, based on more liberal assumptions than those reported in this table. Reducing the absolute error to $<$20 cm may be achieved by upgrading to a dual-frequency GPS receiver, implementing a more precise IMU, and by accounting for sensor alignments and offsets. The bottom section shows the lag-dependent, relative measurement error. This represents the measurement precision over short scales (i.e. $\leq$ minutes, $\leq$ decimeters). These values are based on the variogram analysis summarized by Figure 5.21. The CULPIS error of 3 cm at a lag of 20 m is dominated by the laser, IMU, lever-arm, and sensor misalignment errors. The GPS error is relatively small at a lag of 20 m, but grows to 4 cm at a lag of 200 m. As such, the full systematic error is 7 cm at a lag of 200 m.

error source	absolute error (i.e. accuracy) [cm]
timing latency	1
data interpolation	1
laser range	2
GPS reference station	2
sensor lever-arm offsets	5[a]
sensor misalignment	17[b]
IMU angle	17[c]
GPS altitude	50 ± 25[b]
CULPIS total	$\boxed{95 \pm 25}$

lag-dependent variogram error	relative error (i.e. precision) [cm]
CULPIS 200 m lag	3[e]
GPS altitude 200 m lag	4
CULPIS 200 m lag total	$\boxed{7}$

[a] Value for 50 cm horizontal offset, 5° off-horizontal attitude angle.
[b] Value for 1° misalignment, 5° off-nadir pointing angle, 100 m AGL range.
[c] Value for 1° angle determination error, 5° off-nadir pointing angle, 100 m AGL range.
[d] Value for long-baseline (order 500 km) L1 carrier phase dGPS positioning.
[e] Value based on data collected from $\sim$70 m AGL during straight and level flight.

of the CULPIS absolute measurement error is 95±25 cm, and the relative error over a 200 m lag is 7 cm.

The CULPIS measurement timing latency and the measurement interpolation to the laser sample times are reported by Edwards[25] to introduce an error of ∼0.5 cm and ∼0.1 mm, respectively. Conservative values of 1 cm are reported in Table 5.9. The laser range error of 2 cm encapsulates most of the residuals shown in Figure 5.3, and is the same value reported by the manufacturer. An error of 2 cm is also attributed to the position of the dGPS reference stations ILCU and NYCU. An error of 5 cm is attributed to the GPS antenna and laser horizontal lever-arm offset, which is the height difference between these two sensors given a 50 cm horizontal offset and a 5° aircraft off-horizontal attitude angle. That error will be <1 cm if the horizontal offset is less than 10 cm, which typically has been the case. With a 1° IMU angle determination error, the corresponding elevation error is 17 cm for data collected at a 5° off-nadir pointing angle from 100 m AGL. Sensor misalignment manifests itself as IMU uncertainty error, and introduces an additional 17 cm of error for data collected at a 5° pointing angle from 100 m AGL with a 1° misalignment. Both of these errors are reduced to ∼10 cm for a 3° pointing angle, which is a more liberal estimate of the nominal flight conditions. The GPS altitude error of 50±25 cm is representative of the long-baseline L1 dGPS error observed during the MUSCOX runway survey. The GPS error may be larger over longer time periods (i.e. measurements made over periods of hours, or longer), and may vary with changes in geographic location and solar activity. Based on the cited accuracy of NASA airborne laser systems, it is speculated that implementing L1/L2 dGPS processing could reduce the error to ∼10 cm.

In summary, the CULPIS absolute error is 95±25 cm, and is dominated by L1 dGPS altitude errors stemming from atmospheric propagation delay. The lowest error that can reasonably be expected with the current CULPIS instrumentation is ∼50 cm. Reducing the absolute error to <20 cm for future campaigns will require upgrading to a dual-frequency GPS receiver, a more precise IMU, and highly-accurate measurements of sensor alignments and offsets.

Based on the information learned from this error analysis, the processing steps taken to compute high-quality surface elevation data suitable for scientific geophysical analysis are outlined below. It is worth noting that each individual step has been automated such that no manual user intervention, interpretation, or quality control is required.

- Differentially position the temporary GPS reference station relative to the closest permanent GPS monument (KAGA during MUSOCX, NYA1 during CASIE) using NovAtel Waypoint, and use the RSS method (see Appendix H) to accurately compute its true position. Alternatively, use the JPL online APPS to compute its position.
- Differentially position the CULPIS GPS flight data relative to the temporary GPS reference station. May use multiple reference stations if there are several in close vicinity. This was done for CASIE data where NYCU & NYA1 were both used simultaneously to position the CULPIS GPS data.
- Remove non-valid laser data, which is indicated by a range value equal to 5 mm.
- Linearly interpolate the dGPS altitude, roll, pitch, and COG data to the laser measurement times.
- Use range, dGPS, roll, pitch, and COG data to geolocate the measurement using Equation 5.1.
- Remove data contaminated by clouds, which is indicated by an ellipsoidal surface elevation $\geq$45 m.
- Remove data collected at high aircraft attitude angles, where |roll| is $\geq 3^\circ$ and pitch is $\leq 1^\circ$ and $\geq 7^\circ$.
- Compute the running standard deviation of the dGPS covariance height uncertainty using a 200 m window, and remove data where the standard deviation is $\geq$0.5 mm.
- Compute relative surface elevations within 200 m windows for further geophysical analysis.

Chapter 6

Sea Ice Topography Profiling

6.1 Sea Ice Profiling Overview

The purpose of this chapter is to evaluate and demonstrate the capabilities of CULPIS to measure the basic topographic properties of sea ice, such as ice freeboard, roughness, and ridging. To begin, two examples are presented that illustrate the general nature of the CULPIS elevation data and the usefulness of coincident imagery to help interpret and validate the data. In Section 6.2 the CASIE data is examined in more detail. Proxy freeboard elevation is derived and used to calculate surface roughness, and ridge height and ridge separation distributions. These topography characteristics represent the 2009 summertime sea ice conditions found in Fram Strait. The observed ridge distributions are compared to theoretical distributions as a means to verify the CULPIS measurements. To finish, in Section 6.3 the proxy freeboard data are used to simulate measurements that would be made by altimeters with a larger ground footprint in order to demonstrate that fine-resolution spatial sampling is needed in order to properly observe the ridging distributions.

An initial example of CULPIS of sea ice topography measurements is presented as Figure 6.1, which shows the surface elevation profile along a 2 km stretch of sea ice collected during CASIE flight 9. These data were collected along the red lines that transect the two underlying images. The red lines are purely notional as the exact laser footprint locations within the scenes are not known because the imagery has only undergone center-point geolocation and has not been orthorectified. The top image is a true-color mosaic of 11 consecutive still camera digital photographs. Open leads, ice floes, ridges, smooth ice, and melt ponds are all visible. The bottom image shows the microwave backscatter collected by the microASAR

instrument over the same region ∼15 minutes prior, and it uniquely identifies similar features. The surface heights span approximately 4 m and depict a dynamic topography with regions of low and high variability and ice floes of varying thickness. There are clearly two distinct ice floe types within the scene; those with smooth ice and no ponding, and those with rough ice and extensive ponding. These characteristics may be related to the ice thickness and age, and provide insight to the overall stability of the ice pack [88]. The surface features captured by these three datasets have high correspondence with one another and illustrate the complimentary nature of these UAS measurements.

As a second example, elevation profiles generated from data collected during two passes at different altitude over an ice ridge complex are presented in Figure 6.2. Each overpass represents about 10 seconds of data. The black and red lines on the image indicate the approximate locations of the transects. The still image is timestamped and geolocated, but the exact locations of the transects within the scene are not precisely known because the image itself is not orthorectified, and the transects were collected roughly 50 minutes apart. The latter is a factor since the sea ice pack is in motion. The second overflight was therefore shifted to help compensate for ice drift, which was estimated from the local wind data provided in real-time by the SIERRA's telemetry data; however, some mismatch is unavoidable when using this basic dead-reckoning approach. In general, the data collected at the two altitudes depict similar features. There are two prominent ridge peaks approximately 1 m high with small ridges and depressions evident throughout the profiles. The smaller features are not as evident in the data collected at the higher altitude since the size of the laser footprint on the ground is larger, leading to a more integrated and smoothed surface signal.

The ability to resolve fine-scale relative height variability, as shown here, allows for the estimation of surface roughness and sea ice freeboard (ice & snow), without the need for absolute height referencing, by using the range to open leads as reference "tie-points" of the local water level (e.g. [48, 51]). This of course requires that laser returns be obtained from open water in the leads, a necessity that is not always met. When the open water is very calm, as was the case for the flight tracks shown in Figure 6.1, the surface behaves as a specular reflector, similar to a mirror. In that figure, data is missing over the leads because the laser pulses were reflected off the water surface away from the laser receive optics. The return pulse was never detected and a measurement was not reported. To address this limitation, the surface elevation measurements can be

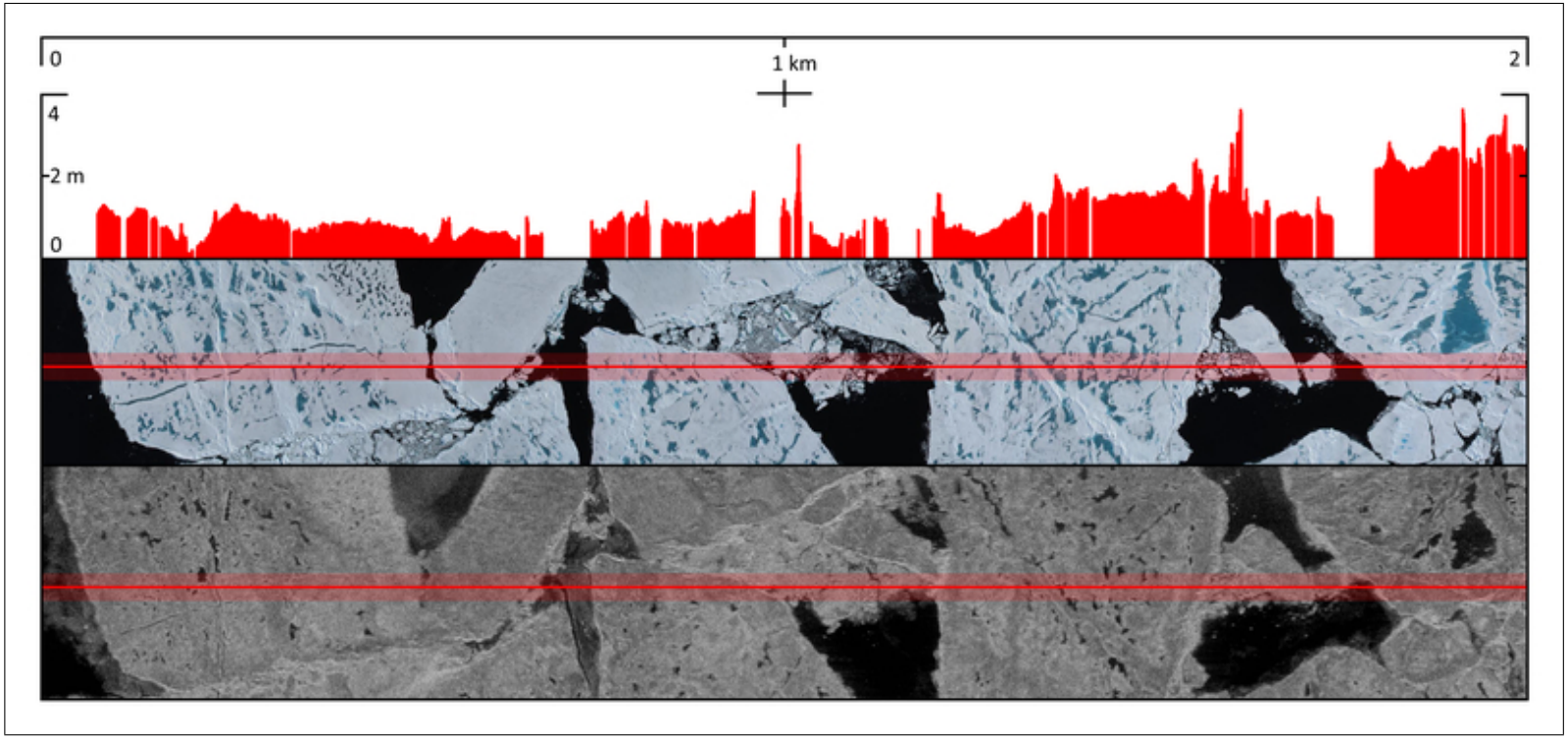

Figure 6.1: A surface elevation profile spanning 2 km generated from CULPIS data collected during CASIE flight 9 from ∼355 m AGL, and coincident imagery. The top panel depicts the surface profile along the red lines shown in the two underlying images. The images have not been orthorectified, so the depicted profile locations are somewhat notional and are not exact. The top image (center panel) is a true-color photo mosaic, and the bottom image is the microwave backscatter measured by the Artemis, Inc. microASAR. Spatially-coincident ice ridges, valleys, and open-water leads are evident in all three datasets.

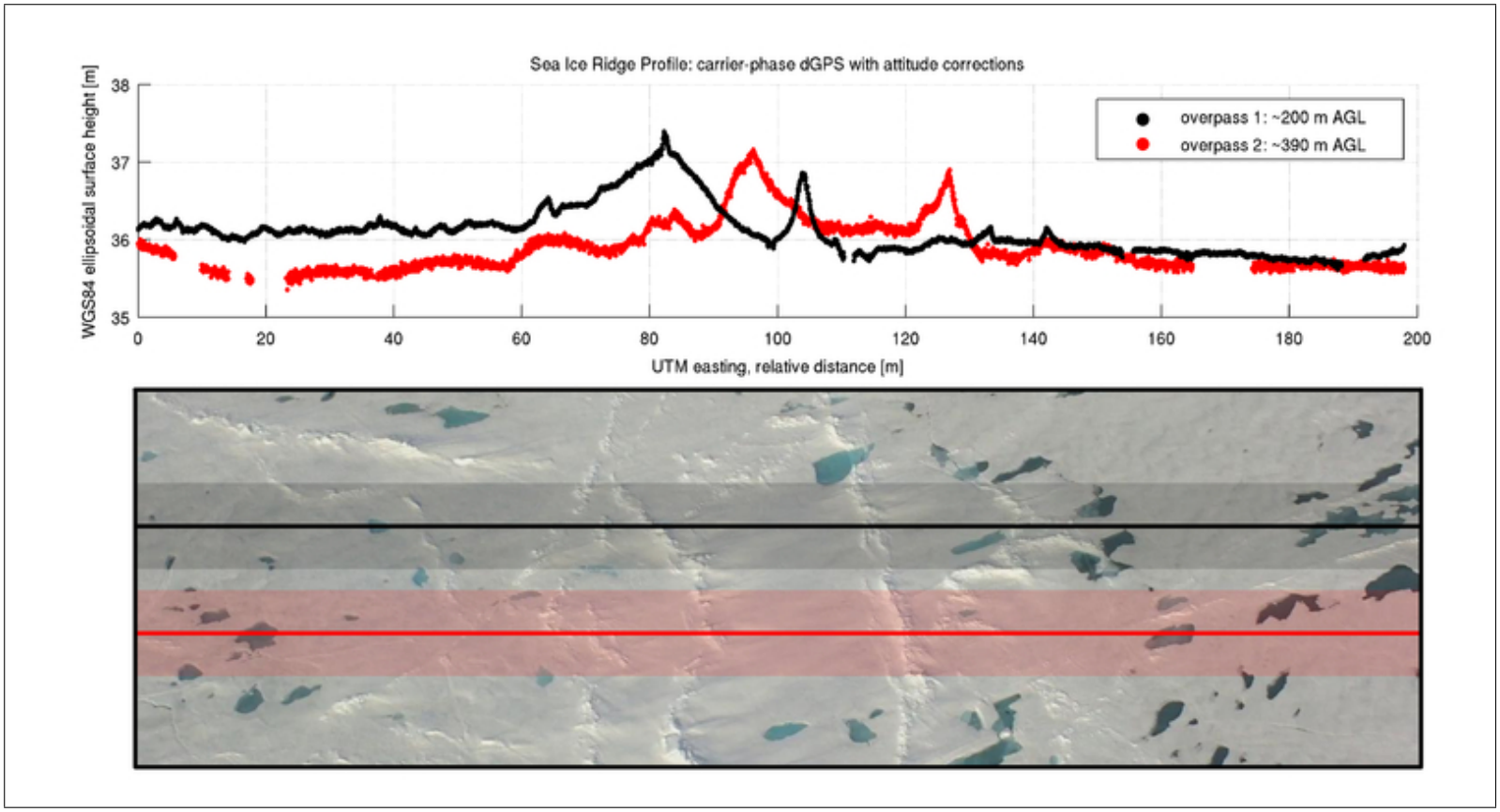

Figure 6.2: Sea ice ridges identified in CASIE surface elevation data. The top plot shows elevation profiles generated from CULPIS data collected at ∼200 m and ∼400 m AGL during two flight passes over an ice ridge complex. The bottom panel shows the approximate locations of the two profiles within a digital video frame. The image has not been orthorectified, so the depicted profile locations are somewhat notional and are not exact. Differences between the two elevation profiles are due primarily to spatial and temporal offsets of the data.

corrected for the local geoid, tides, and ocean dynamic topography, and then expressed as absolute height relative to the local sea level in order to provide a direct measure of freeboard (e.g., [27, 28]). That process is beyond the scope of this research. As was previously mentioned, the lowest-elevation within a specified region is assumed to represent the local water level. This lowest-elevation level is computed along the entire flight track and then removed from the native ellipsoidal heights to generate a proxy freeboard.

As a means to verify the ridge heights measured by the CULPIS altimetry data, and to demonstrate an additional method for computing ridge heights, a CULPIS still photo was used to compute the height of ridge features based on the sun elevation angle and the shadow lengths. The ridge height calculations and results are presented in Appendix M (see Equation M.1 and Figure M.1). In general, the ridge heights calculated from the shadow lengths are of similar magnitude to the ridge heights identified in Figure 6.2 from CULPIS elevation profile data, which adds validity to the CULPIS altimetry measurements. It also demonstrates that ridge heights can be computed from the CULPIS imagery, independent of the altimetry data. Using stereo-pair photography it may be possible to compute ridge heights across the swath covered by the still imagery, thereby achieving 2-dimensional (2D) spatial coverage such as that provided by a scanning laser system. An additional example of the still photography utility is shown in Appendix M where an image has been classified to determine the fractional coverage of different sea ice surface types (see Figure M.2 and Table M.1). Finally, coincident microASAR and CULPIS video images are presented in Appendix M to illustrate their complimentary nature (see Figures M.8-M.10). These examples elude to the wealth of information contained within the CASIE dataset and the potential for future studies to exploit these data.

6.2 Arctic Sea Ice Profiles

One of the overarching objectives of the CASIE campaign is to identify distinguishable morphological characteristics of sea ice in Fram Strait, and to investigate the correspondence between these characteristics and the age and originating location of the ice. The Arctic sea ice age in July 2009 during the CASIE deployment is shown in Figure 6.3. During this time, the study region (indicated by the black triangle) contained predominantly one and two year old ice. The black ice drift tracks in Figure 6.3 show the motion of select ice parcels located within the CASIE study region in July 2009 over a two year period prior to

the deployment (motion from July 2007 through July 2009). These tracks were derived using an ice motion tracking algorithm developed by Dr. Charles Fowler at the University of Colorado at Boulder, which has proven valuable for tracking individual ice parcels and their characteristics as they advect through the Arctic Ocean [115]. It is evident that the ice within the CASIE study region originated near the East Siberian Sea and traversed across the central Arctic via the Transpolar Drift. Since the ice within the study region is all of similar age and evolved along similar drift tracks, it is expected that the observations collected during CASIE will show similar morphological characteristics throughout the region.

The primary ice surface morphological features investigated here are ice freeboard, roughness, and ridging characteristics. As previously mentioned, without manual identification of open-water leads, it is challenging to remove the large-scale elevation variability associated with the geoid, dynamic ocean topography, tides, and atmospheric pressure loading. As such, a proxy-freeboard is computed from which surface roughness and ridging characteristics are further derived.

The proxy-freeboard (referred to simply as freeboard from here onward) and roughness measurements for CASIE flight 9 are illustrated by Figure 6.4. The CULPIS surface elevation measurements are shown in the top plot. Data have been removed where the laser return was not valid (i.e. the laser returns an error value of 5 mm for the range), where the IMU attitude data were outside of the specified bounds (i.e. roll outside of $\pm 3^{\circ}$, pitch outside of 1-7°), and where the GPS height uncertainty was large. The running minimum elevation, shown in red, is used as a proxy for the local water level. This is the minimum elevation within a 400 m window stepped at 200 m increments. The assumption here is that within the 400 m window, the minimum elevation is associated with an open-water lead and thus represents the local water level. While extensive manual validation of this assumption was not carried out, it is certainly possible that open water was not measured every 400 m throughout the dataset. However, as discussed in Hibler et al.[48] and first noted by Weeks et al.[128], the minimum elevation points located on either side of ridging features are often depressed slightly below water level. Through this reasoning, it is assumed that the minimum elevation computed here is a suitable estimate of the local water level.

The ice freeboard, shown in the center plot of Figure 6.4 for CASIE Flight 9, is computed by subtracting the running minimum elevation from the native ellipsoidal elevation profile. This is essentially the same

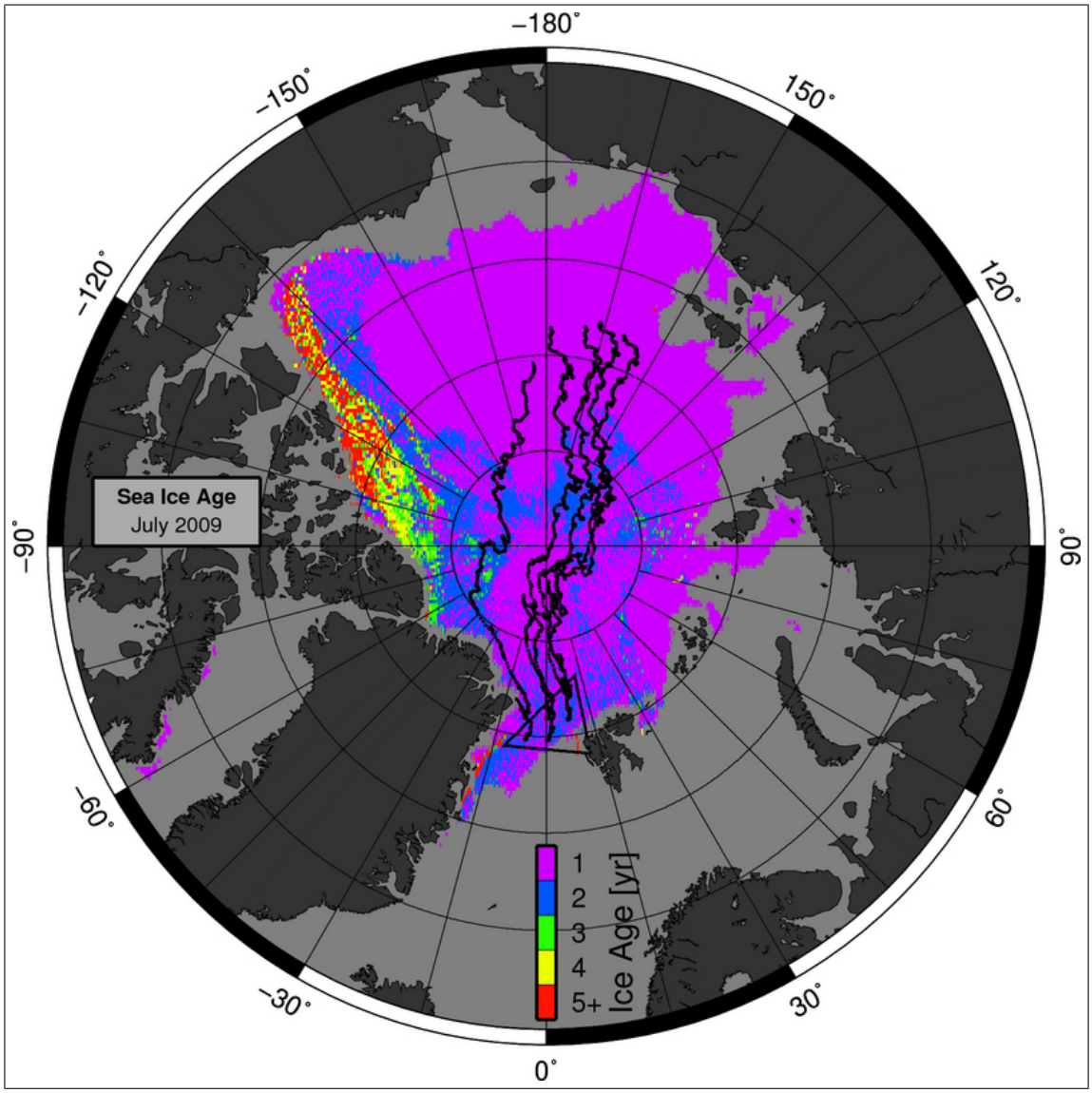

Figure 6.3: The age of Arctic sea ice in July 2009 during the CASIE deployment, and 2-year ice drift tracks for sea ice located within the CASIE study domain. The sea ice found within the CASIE domain (shown by black triangle) during the deployment period was predominantly 1-year and 2-year old ice. The drift tracks that extend across the Arctic Basin show the motion of this ice over a 2 year period prior to the deployment. This figure suggests that the ice within the CASIE domain originated in the same general region and experienced similar drift motion. The ice age data and ice motion algorithm were provided by Dr. Charles Fowler at University of Colorado.

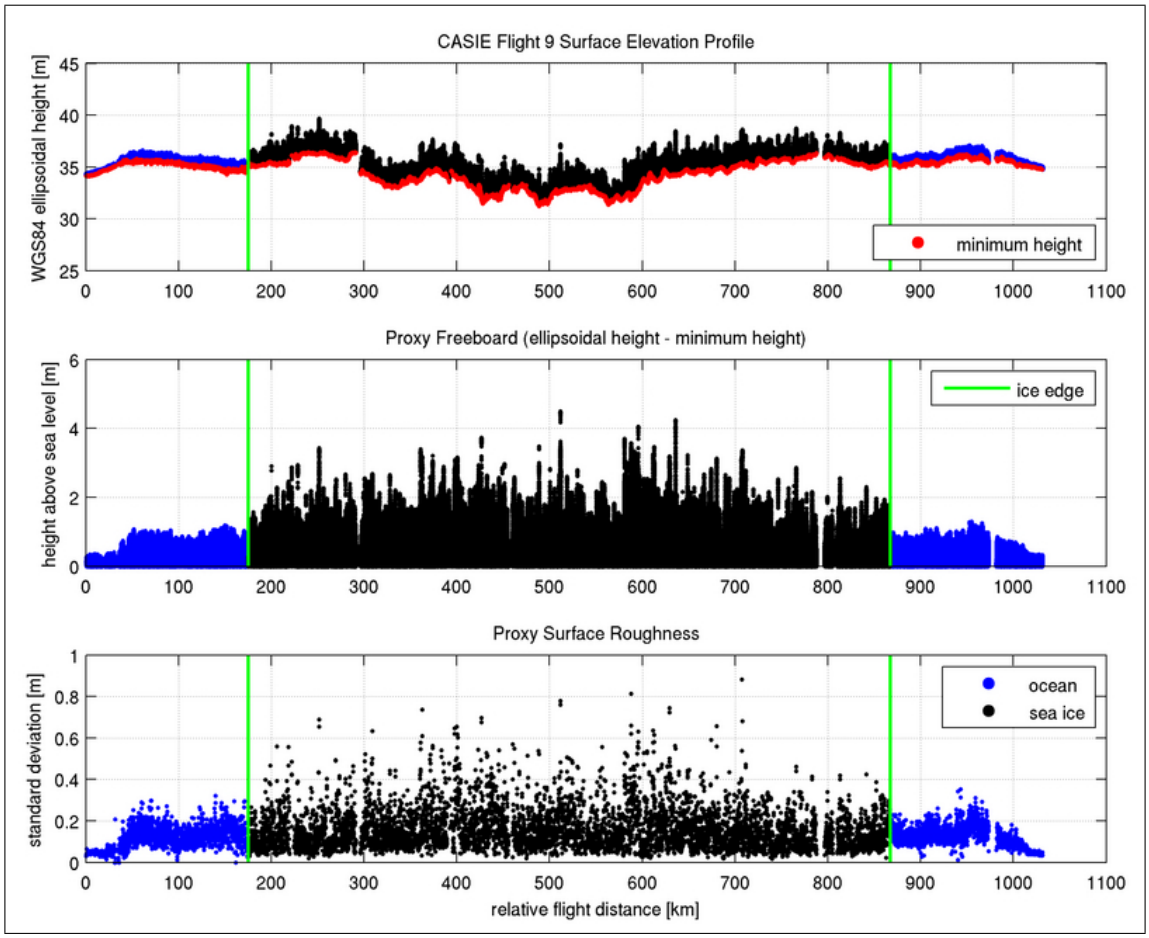

Figure 6.4: CASIE flight 9 surface elevation profile (top), freeboard (middle), and roughness (bottom). Data collected over open-water are shown in blue and data collected over the ice pack are shown in black. The location of the ice pack edge is shown by the green lines. The running minimum elevation (shown in red at top) was computed within a 400 m window stepped at 200 m increments, and serves as a proxy for the local water level. The ice freeboard is then equal to the ellipsoidal surface elevation minus the running minimum elevation. The freeboard for open-water data represents the ocean wave height amplitude. The surface roughness is the freeboard standard deviation within a 200 m box stepped at 100 m increments. The surface freeboard and roughness are noticeably higher over sea ice. The surface elevation, freeboard, and roughness plots for CASIE flights 4, 7, 8, and 10 are shown as Figures M.3-M.6 on pages 180-183.

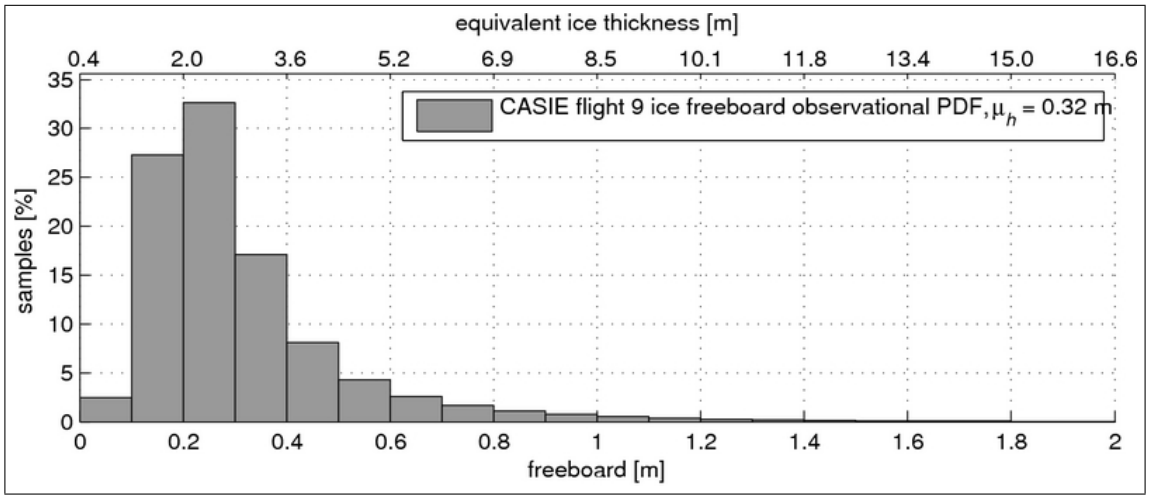

Figure 6.5: CASIE flight 9 observed sea ice freeboard PDF. The mean freeboard hight, μ_h, is 0.32 m. The freeboard median and mode values are 0.26 m and 0.19 m. The top x-axis shows the equivalent ice thickness (freeboard plus draft) based on Equation 6.1.

method employed by Hibler et al.[48] to remove aircraft altitude variations from laser profiles of sea ice in order to estimate freeboard and further derive pressure ridge characteristics. The ice freeboard distribution for CASIE flight 9 is shown in Figure 6.5. The freeboard distribution is asymmetric with mean, median, and mode values of 0.32 m, 0.26 m, and 0.19 m. The mean ice freeboard of 0.32 m corresponds to an ice thickness of 2.97 m based on Equation 6.1, which was empirically derived by Alexandrov et al.[2] by fitting a linear regression to freeboard and thickness observations. Since the CULPIS data were collected toward the end of the summer melt period, it is assumed that the snow cover has melted away, and therefore does not need to be accounted for in the conversion from freeboard to total ice thickness.

$$\boxed{H_i = \ 8.13 \ F_i + 0.37} \tag{6.1}$$

where...

H_i = ice thickness

F_i = ice freeboard

The CULPIS sea ice freeboard and corresponding thickness values agree well with thickness observations made in early April 2009 (approximately 3.5 months prior to the CASIE deployment) using an airborne electromagnetic induction sounding instrument, which showed mean ice thicknesses of approximately 2-3 me-

ters along flight tracks over Fram Strait [34]. This high level of correspondence between these two datasets further validates the CULPIS measurements.

Using the ice freeboard data is is possible to compute a general surface roughness parameter that is independent of the water level variability. The general surface roughness is defined here as the elevation standard deviation within a 200 m section of data, and is shown for CASIE Flight 9 in the bottom plot of Figure 6.4. The 200 m distance was chosen in accordance with the CULPIS error analysis study, summarized in Section 5.5, which indicates the accumulated instrument error is less than 10 cm over this distance.

The surface elevation roughness along all CASIE science mission flight tracks is shown in Figure 6.6. The color-coded flight tracks corresponding to Figure 4.3 on page 34 are visible where surface roughness data does not exist. Missing roughness data is predominantly due to cloud cover obstructing the laser signal. Again, the open-ocean freeboard height represents the wave height amplitude. Within the sea ice pack there are regions of relatively low and high surface roughness, but there is is no clearly dominant spatial pattern or arrangement to the surface roughness. This agrees with the expectations since the ice pack within the CASIE study region is comprised mainly of one and two year old ice that originated in similar locations and followed similar drift tracks. It does, however, appear that the ice toward the north that lies along the horizontal track of flight 8 is relatively smooth, whereas the ice to the west and south is more rough.

There is a region of high roughness in the open ocean between the northern coast of Svalbard and the edge of the ice pack. CULPIS laser data and camera imagery indicate that large waves were present in this section of the ocean during the flight overpass which accounts for the high surface roughness. This indicates that the CULPIS is able to measure ocean wave amplitude, which presents another application for this instrument package. An example of open ocean wave detection is presented as Figure M.7 on page 184.

Sea ice ridge peaks are identified in the freeboard data, and the ridge height and ridge separation distributions are compared to the theoretical distributions derived by Hibler et al.[50] to evaluate the validity of the CULPIS sea ice topography measurements. Several steps are taken to identify ridge peaks in the CULPIS elevation data. First, ice freeboard is computed by removing the running minimum elevation as previously described. Then, every elevation point is averaged with the surrounding ± 5 points to generate a running mean freeboard elevation profile in order to smooth the noise inherent to the laser measurements.

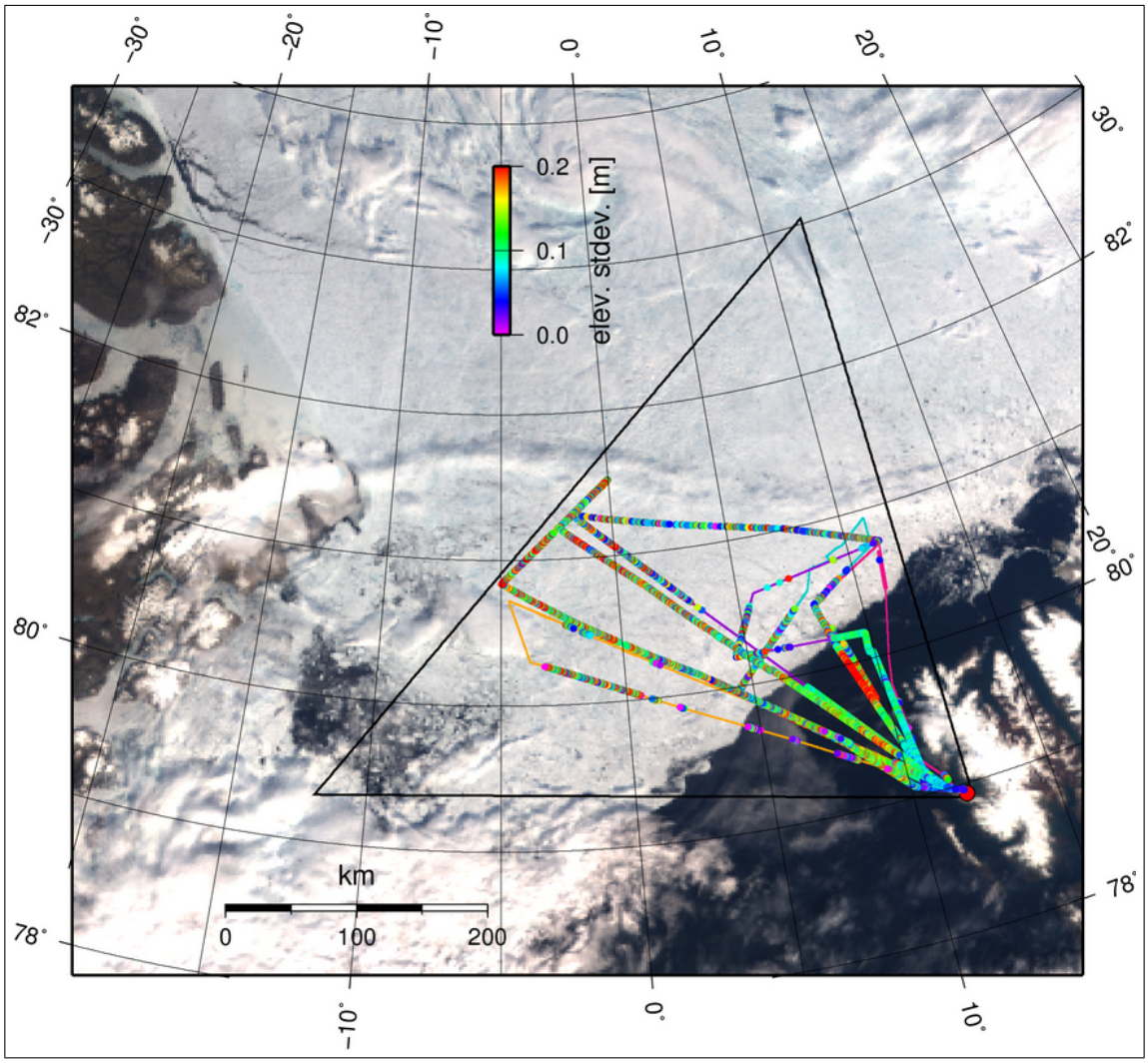

Figure 6.6: Sea ice surface roughness along all CASIE flight tracks. The surface roughness is the standard deviation of the freeboard height within a 200 m window stepped at 100 m increments. Missing data is predominantly due to cloud cover obstructing the laser signal. In general, the ice surface is rougher than the ocean surface at the scale of 200 m, except for a section of high roughness (red in color) located between the northern coast of Svalbard and the sea ice edge. CULPIS laser data and still and video camera imagery indicate that large waves were present in this section of the ocean during the flight overpass. Regions of both high and low surface roughness exist throughout the ice pack, and the observations suggest higher surface roughness in the central and southern regions.

Computing the running mean using the neighboring ±5 data points is computationally much faster than performing a spatial running average based on relative distance; however, it has a caveat associated with it. The neighboring running mean method that was used is the same as a spatial running mean only if the data are uniformly spaced throughout the dataset. Due to variations in flight speed, aircraft attitude motion, and missing data, this is not the case. As such, the neighbor running mean introduces non-linear errors in the spatial dimension. Fortunately, the elevation data are relatively uniformly spaced during CASIE flight 9 and these errors are relatively small. The spacing was found to be ∼10 cm between consecutive measurements. As such, the 11-point running mean that was implemented (each data measurement ±5 measurements) corresponds to a ∼110 cm running average.

The final step taken to identify ridge peaks is to find local maxima in the smoothed freeboard data which are greater than 60 cm high (a specification also used by Hibler et al.[50]) and separated by more than 350 measurement points. With the ∼10 cm measurement spacing, this corresponds to a minimum allowable ridge separation of 35 m. Once again, the same spatial non-linearity issue is associated with this ridge spacing requirement. The ridge separation requirement of 350 measurement points was determined by visual inspection. Requiring that the ridge peaks be separated by 350 points is implemented to limit the number of false-positive ridge peak detections and to identify only the prominent peaks within the complex ridging structures. The ridge detection methodology is illustrated in Figure 6.7 for a 500 m section of data. The freeboard surface elevation is shown in black, the smoothed freeboard is shown in green, and the detected ridge peaks are shown in red.

The ridge detection methodology has a couple drawbacks beyond the spatial non-linearity issue. Taking the 11-point running average slightly suppresses the ridge peak heights. Notice that the red dots in Figure 6.7 fall several centimeters below the actual ridge peak shown by the black freeboard data. Also, requiring the 350-point peak separation ignores closely separated peaks. As such, the peak located at a relative distance of ∼400.75 m in Figure 6.7 is not identified. As will be shown below, the ridge height and ridge separation distributions agree very well with the theoretical distributions presented by Hibler et al.[50], which suggests that the ridge detection methodology implemented here is quite satisfactory. However, future effort should be taken to improve the ridge detection method.

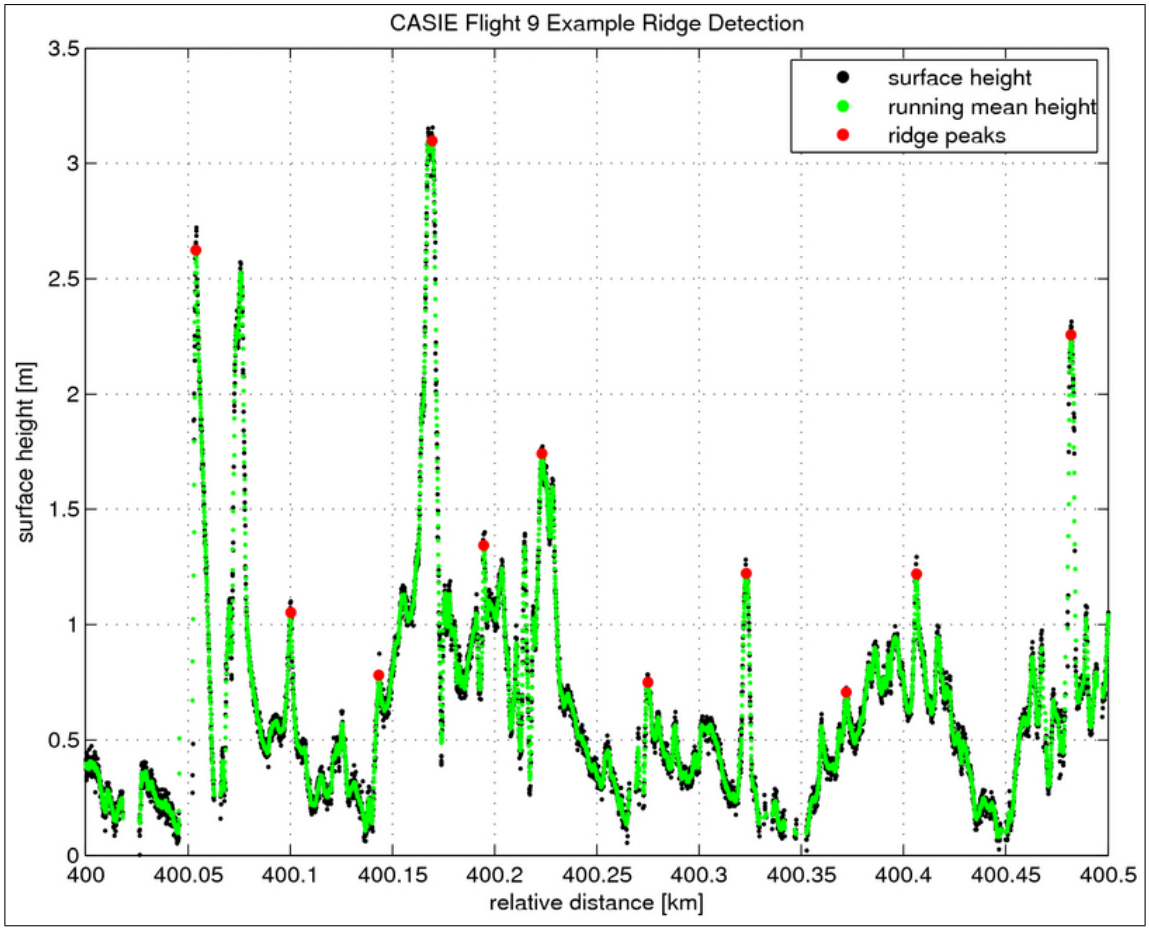

Figure 6.7: A section of CASIE flight 9 elevation profile data illustrating the sea ice ridge peak detection methodology. Ridge peaks are identified in the following manner: (1) The running minimum elevation is removed from the native CULPIS surface profile data to generate the proxy freeboard surface height measurements, shown in black. (2) An 11-point running average, stepped every point, is computed from the freeboard data to smooth the laser measurement noise. This running average is shown in green. (3) Ridge peaks, shown in red, are then identified as local maxima surface heights >0.6 m that are separated by more than 350 points.

The theoretical normalized sea ice ridge height PDF as derived by Hibler et al.[50] is shown as Equation 6.2. This distribution assumes that the ridges are randomly oriented linear features which are geometrically congruent in cross section (i.e. have a cross-sectional area proportional to the square of their relief). A variational calculation then yields the most likely distribution of ridge heights that will produce a given volume of deformed ice per unit area [50, 122]. More specifically, for a given sea ice elevation dataset with a mean ridge height of $\langle h \rangle$, this equation specifies the probability that a ridge will have a height greater than h_0 and between h and $h + dh$, where h_0 is the minimum allowable ridge height and dh is the ridge height distribution bin size.

$$\boxed{P(h)dh = \ 2\lambda\langle h\rangle e^{\lambda h_0^2} e^{-\lambda h^2} dh} \tag{6.2}$$

where...

$P(h)dh$ = probability that a ridge will have a height between h and $h + dh$

λ = parameter determined from average ridge height (Figure 3 in Hibler et al.[50])

h = ridge height

$\langle h \rangle$ = mean ridge height

h_0 = minimum ridge cutoff height

dh = ridge height bin size

In practice, Hibler et al.[50] specified a minimum ridge height of 60 cm, which is the same value utilized in the current ridge detection methodology described above, and they specified a ridge height bin size of 30 cm, as utilized here. It is important to note that the mean ridge height, $\langle h \rangle$, is the only empirically-derived value that is required to compute the PDF. The calculation does require the parameter λ, but this is also dependent upon the mean ridge height and can be determined from Figure 3 in Hibler et al.[50]. As such, it is evident that the ridge height distribution for any sea ice elevation dataset is only dependent on the mean ridge height.

The normalized theoretical PDF for the distance separation between adjacent sea ice ridges follows a negative exponential described by Equation 6.3 [50, 91]. This equation specifies the probability that adjacent

ridges will be separated by a distance x given a mean separation distance of $\langle x \rangle$ and a distance bin size of dx. In practice, Hibler et al.[50] specified a separation bin size of 60 m and only investigated the separation of ridges who's height was greater than 60 cm (as was done with the ridge height PDF). Similar to the ridge height PDF, the ridge separation PDF is based on only one empirically calculated value, the mean ridge separation in this case.

$$\boxed{P(x)dx = \ \mu e^{-\mu x} dx} \tag{6.3}$$

where...

$P(x)dx$ = probability that adjacent ridges will be separated by a distance x

x = ridge separation distance

$\langle x \rangle$ = mean ridge separation distance

μ = population parameter estimated by $\dfrac{1}{\langle x \rangle}$

dx = ridge separation bin size

The CASIE flight 9 mean ridge height and mean ridge separation were calculated to be 1.05 m and 166.3 m, respectively. The ridge heights were binned using a minimum height of 60 cm and a bin size of 30 cm, and the ridge separations were binned using a bin size of 50 m to generate the observed ridge height and ridge separation PDFs, which are shown in Figure 6.8, along with the theoretical distributions and the difference between the observations and the theory. It is evident that the observations show a greater probability of smaller ridges (0.6-0.9 m ridge heights) and shorter separations (0-100 m ridge separations), and a smaller probability of larger ridges (0.9-1.8 m ridge heights) and larger separations (>100 m ridge separations) than indicated by the theory. However, the observations and theory generally agree to within 5% of each other for all bins, which strongly validates the CULPIS elevation measurements and the ridge peak detection methodology. The red and green theoretical ridge height curves are the same as those presented in Figure 8 of Hibler et al.[50], and illustrate how the distribution shifts to a greater probability of higher ridge hights for sea ice with a higher mean ridge height.

To investigate the relationship between ridge height and ridge separation, the separations between

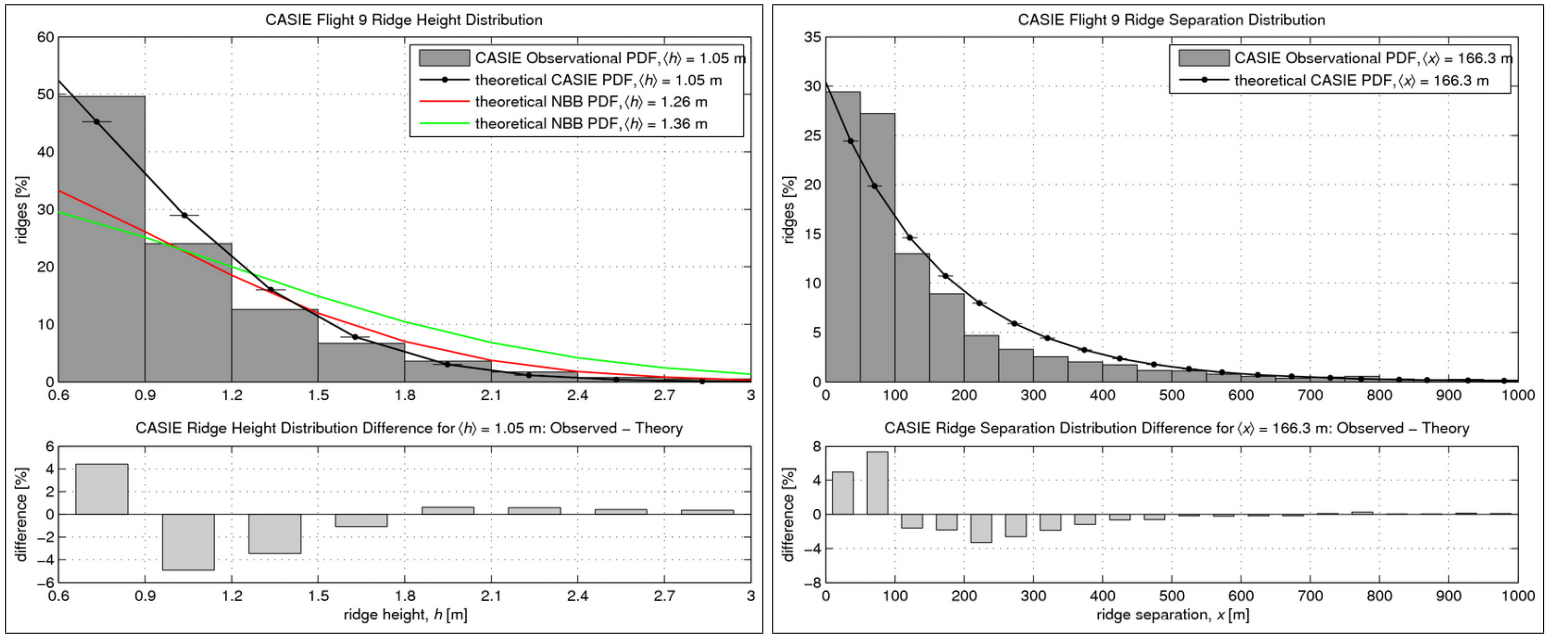

Figure 6.8: CASIE flight 9 observed and theoretical sea ice ridge height (left panel) and ridge separation (right panel) normalized PDFs, and their differences. The mean observed ridge height is 1.05 m, and the mean observed ridge separation is 166.3 m. The theoretical PDFs based on these means, as described by Equations 6.2 and 6.3, are shown by the black curves. The difference between the observations and theory are shown by the lower bar plots. The red and green curves at left were presented in Hibler et al.[50], and illustrate how the distribution changes to favor a greater probability of higher peaks for sea ice with a larger mean peak height.

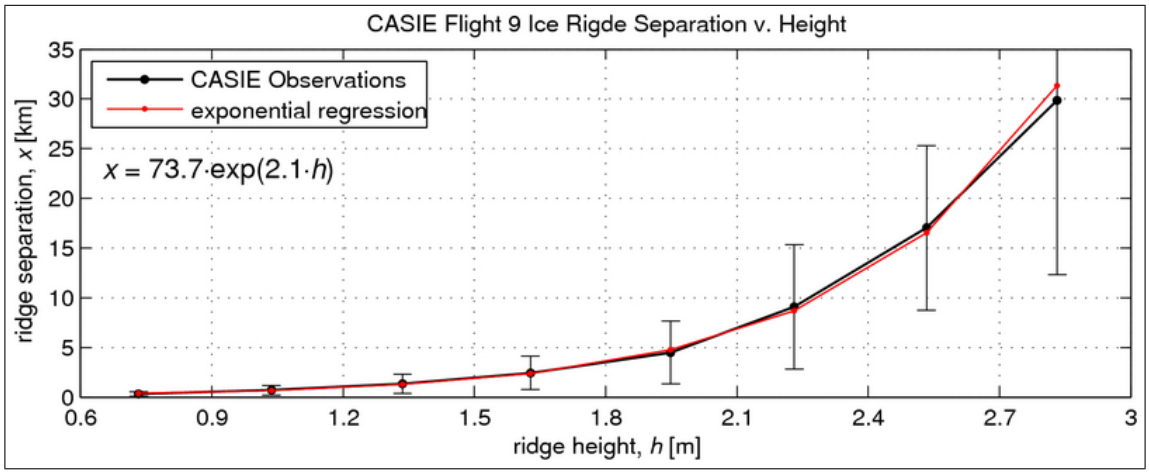

Figure 6.9: CASIE flight 9 observed sea ice ridge separation as a function of ridge height (shown in black), and the exponential best-fit regression (shown in red, Equation 6.4). The 1σ error bars are also plotted, and illustrate the wide separation distribution and few number of the largest ridges.

ridges contained within each height bin of Figure 6.8 were computed. The mean ridge separation for each hight bin is shown in Figure 6.9, along with the 1σ separation standard deviation error bars. This figure suggests that smaller ridges are spaced closer together, which is to be expected since they occur more frequently. The large error bars for the highest ridges indicates that there are relatively few large ridges and their separations are quite variable. Nonetheless, the empirical relationship between sea ice ridge height and ridge separation is described by Equation 6.4.

$$\boxed{x = \ 73.7e^{2.1h}} \tag{6.4}$$

where...

x = ridge separation distance

h = ridge height

The mean sea ice ridge height and the ridge frequency in one kilometer sections of data along all CASIE science mission flight tracks are shown in Figure 6.10. Again, the color-coded flight tracks corresponding to Figure 4.3 on page 34 are visible where these data do not exist. To be clear, ridge frequency is defined as the number of ridges per kilometer. As previously discussed, the mean ridge height is an important parameter that can be used to describe the ridge height distribution within a given region. Additionally, the ridge

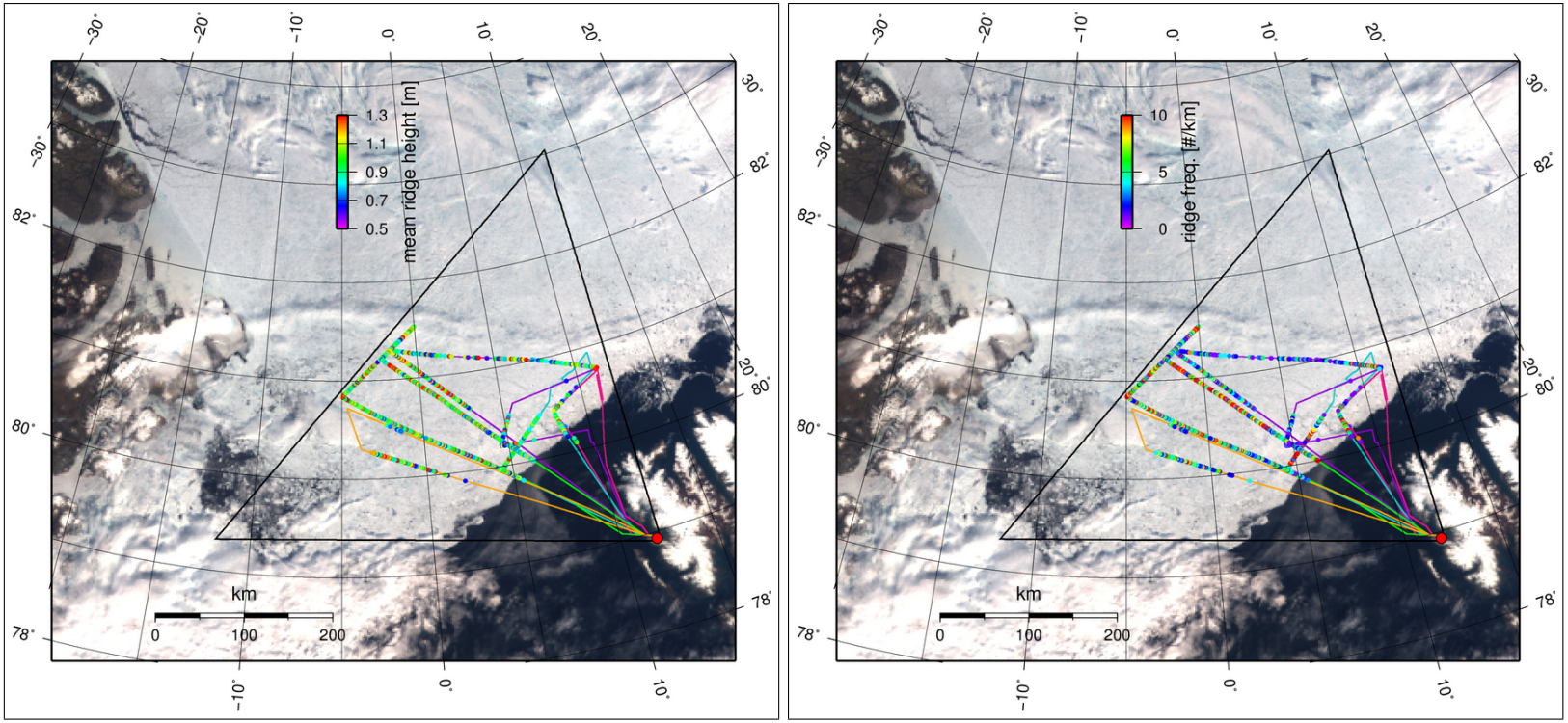

Figure 6.10: The sea ice mean ridge height along all CASIE flight tracks is shown in the left panel, and the ridge frequency is shown in the right panel. These parameters were computed over 1 km segments of data. The ridge frequency is the number of ridges per 1 km. Missing data is predominantly due to cloud cover obstructing the laser signal. Regions of both high and low mean ridge height exist throughout the ice pack, with values being somewhat elevated in the central and southern regions.

frequency is an empirical value that describes the ridging intensity, which can be used to further describe sea ice characteristics and its variability [51]. Similar to the ice surface roughness, the mean ridge height and ridge frequency do not show any predominant spatial pattern within the ice pack. However, as noted by Hibler et al.[51], "annual variation in new ice production due to ridging is sufficiently large to suggest that ridging plays an important role in the overall mass balance of the Arctic Basin," which highlights the importance of monitoring these sea ice characteristics.

6.3 Simulated Sea Ice Profiles

The scientific community places a considerable amount of effort into estimating the total ice mass balance within the Arctic Basin; however, satellite radar and laser altimetry systems with relatively large footprint sizes are the primary instruments utilized to make such measurements on a basin-wide scale. In the most basic sense, the range measurement detected by an altimeter system is equal to the true surface height structure within the footprint convolved with the sensor impulse response function. This provides a single elevation measurement that, in effect, is the mean (or weighted mean) surface elevation within the measurement footprint. As such, large footprints are unable to resolve fine-scale ridging features, and therefore may not properly represent the true thickness or ridging characteristics of the the sea ice.

To investigate the affect that the measurement footprint size has on the ability to accurately detect the sea ice ridging characteristics, the fine-resolution CULPIS surface profile data from CASIE flight 9 are averaged over a range of scales to simulate the spatial smoothing that occurs for measurement footprints with diameters ranging from 10-70 m at an increment of 10 m, and then the ridge height and separation PDFs are computed for the simulated elevation data. This range of footprints was chosen because 70 m is the footprint diameter of ICESat[1] and 10 m is the footprint diameter of ICESat-2[2] . While this investigation is not meant to simulate the ICESat and ICESat-2 measurements, the chosen range of diameters will provide a certain level of insight to both the legacy and next-generation instrumentation capabilities, and will demonstrate the utility of fine-resolution measurements that can be provided by small UAS.

To simulate the elevation that would be detected by different footprint sizes, each CULPIS freeboard

[1] ICESat footprint diameter taken from Zwally et al.[132].
[2] ICESat-2 footprint diameter taken from http://icesat.gsfc.nasa.gov/icesat2/instrument.php

data point is averaged with a specified number of surrounding points to create a smoothed, running-average freeboard elevation profile. For example, to simulate a 10 m footprint, each elevation point is averaged with the surrounding 100 points (±50 points). With the nominal 10 cm spacing, averaging 100 points is equivalent to averaging over a distance of 10 m. In this fashion, a 70 m footprint is simulated by averaging each data point with the surrounding 700 points (±350 points), and so on.

The running-average simulation method was utilized because it is relatively simple to implement and computationally fast, but it does have several implications worth noting. First of all, in order to generate the desired spatial average (e.g. 10 m footprint) this method assumes that adjacent elevation data points have exactly 10 cm horizontal spacing. As was previously discussed, the data point spacing is not exactly 10 cm, nor is it perfectly uniform throughout the dataset. Secondly, the simulation averaging method retains the CULPIS along-track measurement spacing of approximately 10 cm, which may not be representative of altimeter systems with larger footprints. For example, ICESat has an along-track measurement spacing of 170 m (see Table 5.1), from which it is not possible to resolve continuous or individual ridge profiles. However, Kowk[74] had done promising work using ICESat waveform signatures to identify ice roughness prior to its failure in 2009. The third point worth noting is that the spatial averaging is only done in one dimension, along the CULPIS profile ground track. In reality, a larger footprint would average over a 2D surface area that would not have a radially-symmetric height distribution. Finally, throughout these simulations, the CULPIS freeboard elevation profile is taken to be the "true" surface height, which is not exactly the case since the "true" surface has been convolved with the CULPIS footprint and its own impulse response function. Despite these limitations, it is believed that the simulations are a useful method to illustrate the affect that larger measurement footprints have on measuring Arctic sea ice ridging characteristics. Although the methodology could be improved, the material in this section provides considerable insight and offers potential for further development and investigative studies.

The simulated surface elevation profiles for 10 m and 70 m measurement footprint diameters are presented in Figure 6.11. This is the same section of data from CASIE flight 9 that is shown in Figure 6.7. The data shown in black are the native CULPIS freeboard heights, the data in green are the spatially-averaged, simulated heights, and the red points show the detected ridge peaks. As previously discussed,

the ridge detection methodology has its own limitations, but has been found to work sufficiently well (i.e. capable of detecting ridge height and ridge separation distributions that agree to within 5% of the theoretical distributions). The simulation was also carried out for footprints with a diameter of 20, 30, 40, 50, and 60 m, but the elevation profiles are not presented here. Notice that larger footprints provide measurements that indicate an overall smoother surface with considerably smaller ridge heights.

The CASIE flight 9 ridge height and ridge separation PDFs for the 10 m and 70 m simulated footprint measurements are shown in Figure 6.12, along with the theoretical distributions (described by Equations 6.2 and 6.3) for the "true" mean ridge height of 1.05 m and the mean ridge separation of 166.3 m that were observed by the CULPIS. The difference between the simulated ridge heights and separations and the theoretical "true" ridge heights and separations (simulation value minus theoretical value) for all the simulated footprint sizes are shown in Figure 6.13. Within each height and separation bin, the gray-scale colors correspond to the simulated footprint size.

Figures 6.12 and 6.13 clearly indicate that larger footprints bias the ridge observations toward smaller, farther spaced ridges. The simulated footprint sizes overestimate the percentage of ridges with heights ranging from 0.6-0.9 m by approximately 25-40%, and underestimate the percentage of ridges with heights greater than 0.9 m by as much as nearly 15%. Additionally, the simulated footprints underestimate the percentage of ridges with separations less than 400 m by upwards of 10% for the shortest separation bins, and the simulations overestimate the percentage of ridges by 1-2% for almost all separation bins greater than 400 m.

Not only does the measurement footprint size modify the ridge height and separation PDFs, but it reduces the total number of ridges detected. As shown in Table 6.1, 4145 ridges were detected in the native CULPIS freeboard elevation data collected during CASIE flight 9. In the simulated elevation data that represents a footprint diameter of 10 m, 2422 ridges were detected, which is a 41.6% reduction relative to the "true" number of ridges detected in the native CULPIS data. Furthermore, only 661 ridges were detected in the 70 m footprint simulated elevation data, which is a 84.1% reduction relative to the actual number of ridges in the dataset. It is clearly evident that larger measurement footprints have a dramatic effect on the ability to detect sea ice ridge characteristics; however, the running average simulation method implemented here does not alter the overall observed mean ice thickness.

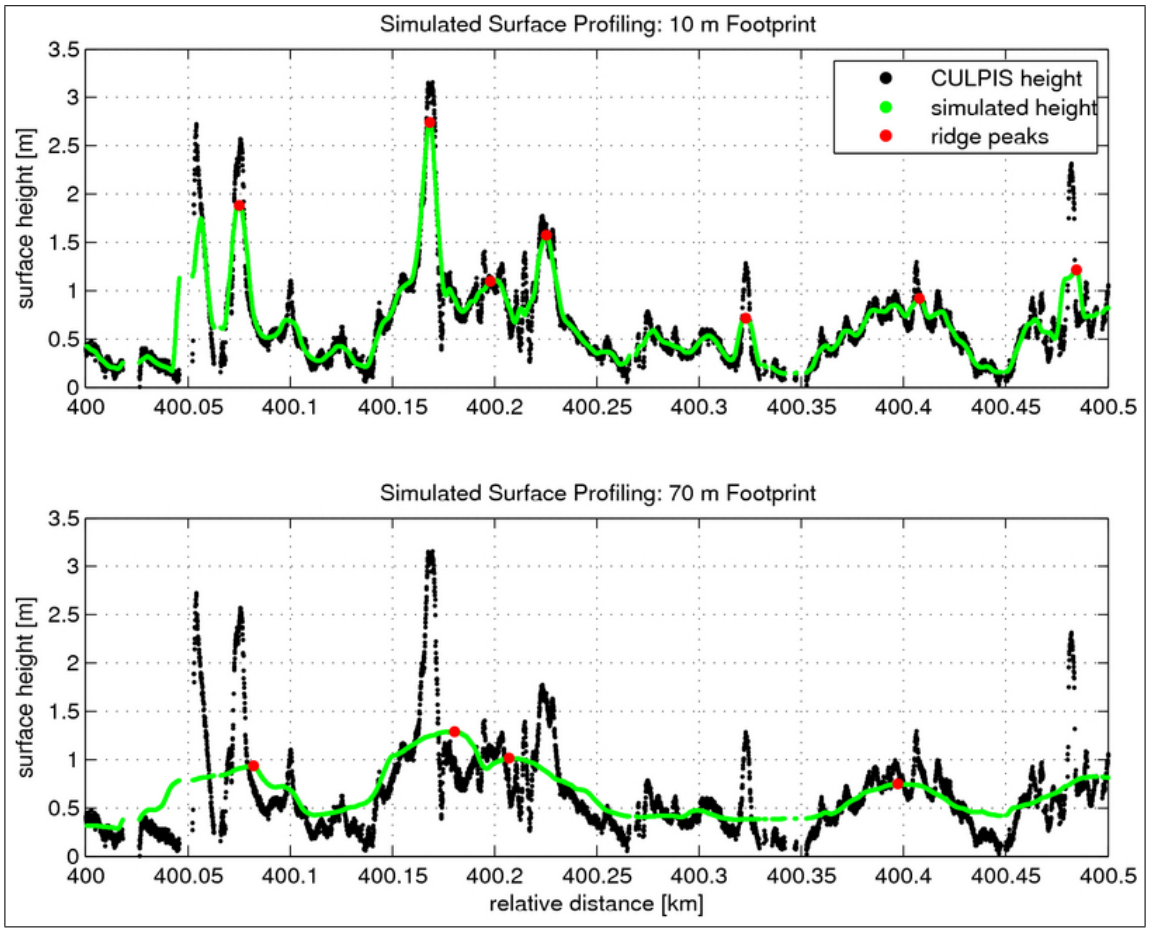

Figure 6.11: A section of CASIE flight 9 freeboard surface height data (shown in black), the simulated elevation profiles that would be observed from two altimeter systems with larger footprints (shown in green), and the resulting ridge peak detection (shown in red). This is the same section of data presented in Figure 6.7. The native CULPIS freeboard surface height data are smoothed using continuous 10 m (top plot) and 70 m (bottom plot) window-size running averages.

Table 6.1: The total number of sea ice ridges detected in CASIE flight simulated freeboard elevation data representing various footprint measurement sizes, along with the percent reduction in the number of detected ridges relative to the "true" number of ridges detected in the native CULPIS data, which is 4145 ridges.

footprint diameter [m]	ridges count [#]	percent reduction [%]
10	2422	41.6
20	1654	60.1
30	1261	69.6
40	1001	75.9
50	837	79.8
60	749	81.9
70	661	84.1

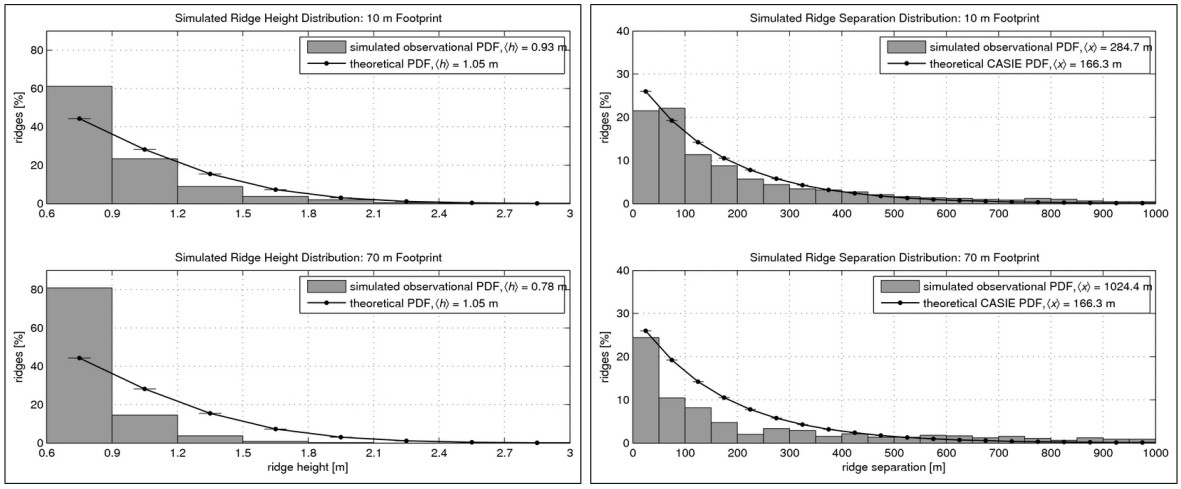

Figure 6.12: CASIE flight 9 sea ice ridge height and ridge separation distributions for simulated surface profile data representing 10 m and 70 m laser footprints. The simulated mean ridge heights are 0.93 m and 0.78 m, and the mean ridge separations are 284.7 m and 1024.4 m. The "true" mean ridge height and separation are 1.05 m and 166.3 m, where the CULPIS observations presented in Figure 6.8 are taken to be truth. The black curves shown here depict the theoretical distributions, described by Equations 6.2 and 6.3, for the "true" mean height and separation.

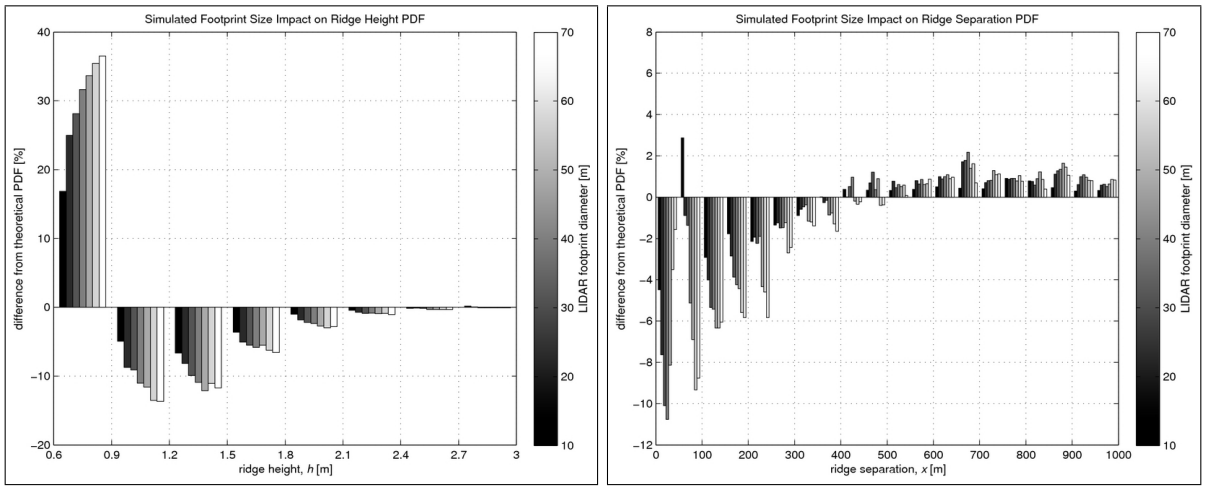

Figure 6.13: CASIE flight 9 sea ice ridge height and ridge separation distribution error relative to the theoretical distributions that represent the "true" CULPIS observations for simulated surface profile data of 10, 20, 30, 40, 50, 60, and 70 m laser footprints. The theoretical distributions are described by Equations 6.2 and 6.3, and are presented in Figure 6.8 for the "true" mean ridge height and separation of 1.05 m and 166.3 m, as measured by the CULPIS. It is evident that larger laser footprint sizes bias the distribution toward smaller, further spaced ridges.

A final method for examining the observational limitations imposed by larger measurement footprints is through a FFT analysis, which by its nature highlights the impact on the detected surface structure frequency, or periodicity in this case, where periodicity is equal to the inverse of frequency. To investigate this impact, a 10 km section of CASIE flight 9 freeboard elevation data was randomly chosen and used to simulate 10 m and 70 m footprint measurements. The surface structure periodicity was then computed using a FFT for the native CULPIS elevation data and the two simulated elevation datasets. Finally, the simulated surface periodicity spectra were subtracted from the native "true" surface spectra show the difference imposed by the larger measurement footprints. The results of this investigation are shown in Figure 6.14. The top plot shows the native and the two simulated freeboard elevation profiles. The middle plot shows the corresponding surface periodicity that is resolved by the three profile datasets. The bottom plot shows the difference between the "true" and the two simulated periodicity spectra.

As shown in the bottom plot of Figure 6.14, the simulated surface spectra have lesser amplitude (i.e. highest difference) at shorter periodicities than the spectra of the native CULPIS surface profile. The 10 m footprint spectra shows large difference errors for periodicities less than 50 meters/cycle (i.e. for elevation features with 50 m spacing), and the 70 m footprint spectra shows large difference errors for periodicities less than 200 meters/cycle (i.e. for elevation features with 200 m spacing). In effect, these values indicate the surface structure length-scales which are not accurately resolved by larger measurement footprints.

It is important to note that the FFT analysis is somewhat different than the ridge separation analysis in that it utilizes the full freeboard elevation dataset, which includes the fine-scale structure as well as the large ridge structure. It is evident that the dominant elevation features have spatial separations ranging between approximately 150-200 meters, as indicated by the high spectral power at these periodicities in the center plot of Figure 6.14. This agrees well with the mean ridge spacing of 166.3 m. It also should be noted that the sea ice surface FFT spectra shown in Figure 6.14 have high power at shorter periodicities (<150 meters/cycle), whereas the aircraft attitude FFT computed using data representative of nominal science mission flights (i.e. mostly straight and level flight, see Figure 5.5) was shown to have high power at relatively long periodicities (>150 meters/cycle). This supports the notion that the IMU measurement error adds minimal error to the CULPIS surface elevation measurements over relatively short distances.

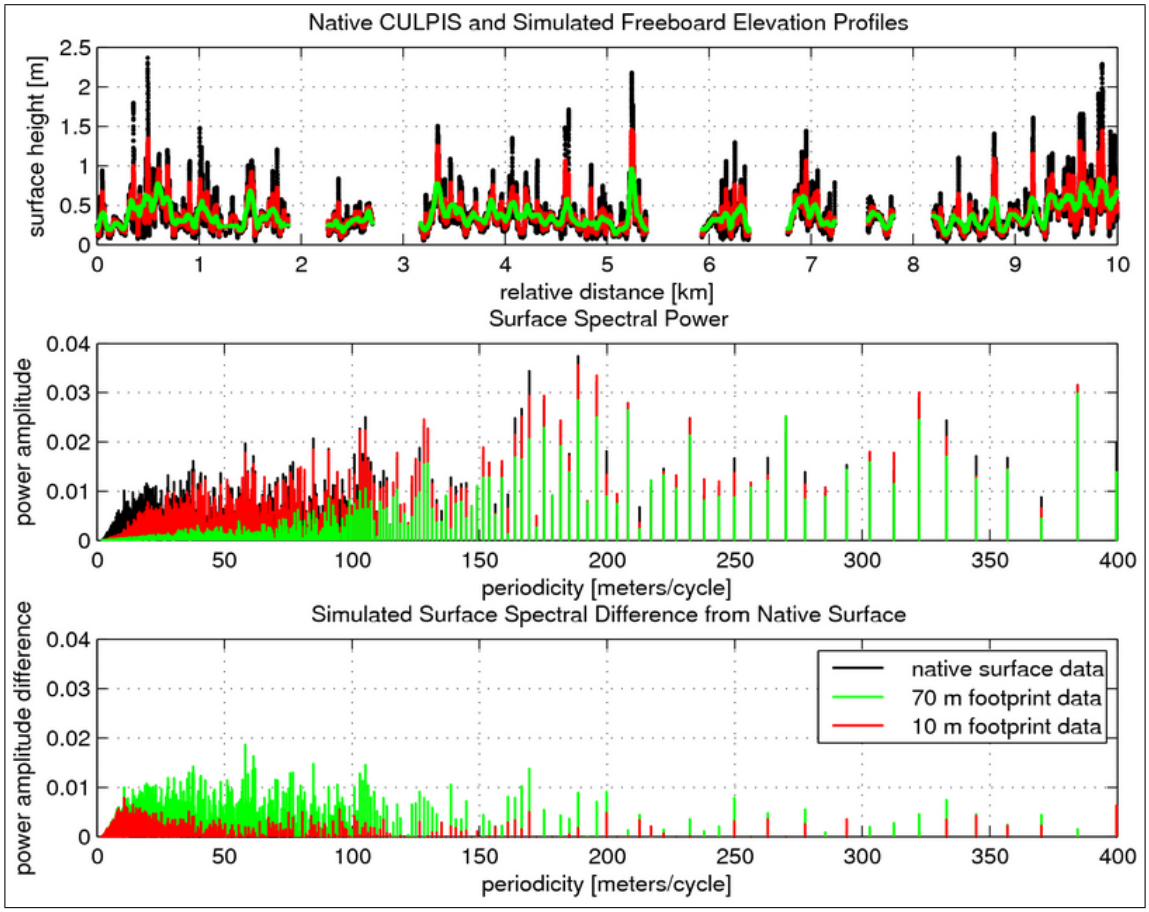

Figure 6.14: CASIE flight 9 surface FFT spectral power and error for simulated profile data. The top plot shows the native CULPIS surface profile data (black), and simulated profile data for 10 m (red) and 70 m (green) laser footprints. The center plot shows the FFT spectra of these three profile datasets. The bottom plot shows the difference between the simulated FTT spectra and the "true" CULPIS FFT spectra ("truth" minus simulation). The different plot indicates that a 10 m footprint will have considerable error observing elevation features with a periodicity (i.e. spacing) less than 50 m, and a 70 m footprint will have error observing elevation features with a periodicity less than 200 m.

Chapter 7

Summary

In recent years, the Arctic has experienced a dramatic reduction in the overall extent of summertime sea ice, and the remaining ice is transitioning from a thick perennial ice pack with a large fraction of old multiyear ice, to a thinner seasonal ice pack consisting primarily of first- and second-year ice. These dramatic changes not only have implications for the persistence and survivability of sea ice and feedback mechanisms affecting climate change, but also have implications for socially relevant issues, such as international commerce and resource exploration [15, 60].

The changes occurring to the Arctic sea ice manifest themselves in the physical characteristic of the ice. As the ice becomes younger and thinner, there are changes in ice thickness, roughness and ridging features. This research has focused on assessing the ability of the CULPIS laser altimetry system to collect quality ice topography data from UAS, and demonstrates that UAS remote sensing technologies can improve our capabilities to monitor the state and evolution of the Arctic sea ice.

The CULPIS is as a robust, lightweight, inexpensive instrument package that was developed to collect land ice and sea ice surface elevation and imagery from small UAS [20, 25, 107]. The primary components are a laser, IMU, GPS module, still and video cameras, and power regulation and C&DH systems. The C&DH system controls the various instruments and accurately timestamps the data to yield synchronized co-located topography and imagery data. It is a 12W system with a mass and volume of roughly 1.7 kg and 2560 cm^3, and which costs approximately $5100 USD. When flown at 30 m/s and 100 m AGL, it provides surface elevation measurements with an along-track spacing of 7.5 cm and a 30 cm diameter ground footprint. From this altitude the cameras provide imagery with sub-decimeter-level resolution. With its accurate time

stamping and laser profiling capabilities, it is considered to be an advancement over past UAS cryospheric observation payloads, such as that discussed in Inoue et al.[58], which consisted primarily of a still cameras and meteorological sensors.

The CULPIS has been integrated into four UAS platforms; the BAE Systems Manta, the NASA SIERRA, the AAI Aerosonde, and the University of Alaska's Insitu ScanEagle. Three of these UAS have been deployed operationally to make land and sea ice observations. In July 2008 the Manta was flown out of Ilulissat, Greenland to measure ice sheet surface characteristics in the vicinity of supraglacial melt lakes as part of the NOAA MUSCOX project. Data collected during this campaign were used to generate a fine-resolution DEM of the ice surface. In July 2009 the SIERRA was flown out of Ny-Ålesund, Svalbard to measure sea ice properties in Fram Strait as part of the NASA CASIE project. The observations collected during CASIE are the primary focus of this research. Finally, in September and October 2009 the CULPIS was flown onboard the Aerosonde to map sea ice topography and wave heights in the Southern Ocean between McMurdo and Terra Nova Bay, Antarctica as part of the NSF TNB UAS project [13]. The CULPIS has also been integrated into the ScanEagle UAS and is currently available for scientific investigations.

The wide array of UAS into which the CULPIS has been integrated over a relatively short period of time, and the campaigns which have been completed, demonstrates the systems versatility and reproducibility, as well as the utility of UAS to provide coincident, synchronized, multi-sensor measurements in polar environments. Rapid availability, ease of instrument integration, and the potential for relatively minimal logistical requirements are additional features that make UAS an attractive method for collecting geophysical data. Additionally, UAS are well suited for surface topography mapping since they generally have slower flight speeds than manned aircraft, and it is justifiable to take greater risk with UAS. As such, they can be flown at lower altitude, thereby reducing the measurement error and yielding finer spatial resolution. These capabilities highlight the potential for UAS to provide widely distributed polar elevation observations which may be leveraged to augment manned-aircraft and spaceborne efforts to monitor the variability and evolution of land ice and sea ice.

The operational performance of the CULPIS was assessed by comparing flight-based elevation profiles to "truth" ground-based runway surveys. The absolute measurement error was determined to be 95±25

cm, and the measurement precision was determined to be 7 cm for short segments of data less than 200 m in length. The absolute accuracy is primarily limited by relatively low-frequency L1 dGPS positioning uncertainties stemming from ionospheric and tropospheric signal propagation errors, which are on the order of 50±25 cm. This error can likely be reduced to ∼15 cm by implementing a L1/L2 GPS receiver that will make it possible to eliminate the ionospheric error. By modeling the tropospheric error it may be possible to reduce the total GPS error to <10 cm. The IMU angular determination and sensor misalignment uncertainties of 1° each contribute 17 cm of error given a 5° off-horizontal attitude angle and a 100 m AGL flight altitude. The error introduced by the horizontal lever-arm offset between the GPS antenna and laser is ∼5 cm given a 20 cm offset and 5° attitude angle. The IMU, misalignment, and lever-arm errors can be reduced considerably (i.e. combined total of $\lesssim$10 cm) by implementing a higher-quality IMU, by flying lower, and by accurately measuring the senor alignments and offsets. Errors stemming from the GPS reference station positioning, the laser range measurement, data interpolation, and timing latency contribute the least amount of error, with a combined total of ∼5 cm. Currently, the CULPIS is not suited for measuring ice sheet elevation change; however, it is expected that by performing the suggested improvements, the total absolute measurement error can be reduced to $\lesssim$20 cm, which will lend itself for ice sheet change detection.

With the current implementation the CULPIS does provide high-precision measurements over short distances. A variogram analysis of the error suggests that over a distance of 200 m the total system precision is <10 cm, with the GPS precision being ∼4 cm, and the remaining sensor error being ∼3 cm. As such, relative height differences can be computed with high precision over short distances, which is needed for measurements of sea ice freeboard, roughness, and ridging. Given the high measurement precision, it was possible to derive ridge height and ridge separation distributions that are within 5% of the theoretical distributions. Finally, the necessity of fine-resolution topography measurements was demonstrated by simulating observations that would be collected with larger altimeter footprint sizes. Footprint diameters of 10-70 m reduced the total number of ridges detected by 40-85% and biased the ridge distributions toward smaller, further spaced ridges. The number of ridges with heights ranging from 0.6-0.9 meters were overestimated by up to almost 45%, and ridges with a separation less than 400 m were underestimated by up to 10%. Furthermore, surfaec roughness features with a periodicity less than 50 m/cycle are substantially unresolved by 10 m footprints, and roughness

features with a periodicity less than 200 m/cycle are substantially unresolved by 70 m footprints.

This research has shown an integration between science and technology by demonstrating the ability to observe geophysical phenomena which are of great interest to the scientific community and commercial industries by synthesizing new and improved technologies. Measurements of ice freeboard, roughness, and ridging have been made for the first time using a laser altimeter system flown on small UAS. The measurements are fine-resolution and high-quality, which make them suitable for calibrating and validating satellite observations and sea ice models. Additionally, the CULPIS and UAS are ideal for collecting timely observations of sea ice conditions to facilitate safe shipping and resource exploration operations in the Arctic. In conclusion, it has been shown that a relatively inexpensive laser altimeter system can be flown on UAS over broad regions in polar environments to collect fine-resolution surface elevation data which are pertinent for assessing the state of sea ice conditions, and which have sufficient quality to meet the requirements of the scientific community. These systems have the ability to augment current airborne and spaceborne observations and have the potential to provide widely-distributed, multi-sensor, synchronized measurements to enhance future investigations of Arctic sea ice.

Bibliography

[1] J.J. Adler. Assessing supraglacial water volume and the changing dynamics of the surface topography near the Jakobshavn Glacier, Greenland. PhD thesis, University of Colorado at Boulder, 2010.

[2] V. Alexandrov, S. Sandven, J. Wahlin, and O.M. Johannessen. The relation between sea ice thickness and freeboard in the Arctic. Cryosphere, 4(3):373–380, 2010.

[3] A.R. Amiri-Simkooei, C. Tiberius, and P.J.G. Teunissen. Assessment of noise in gps coordinate time series: Methodology and results. Journal of Geophysical Research, 112(B7):B07413, 2007.

[4] O. Babko, D.A. Rothrock, and G.A. Maykut. Role of rafting in the mechanical redistribution of sea ice thickness. Journal of Geophysical Research, 107(C8):3113, 2002. ISSN 0148-0227.

[5] F.I. Badgley. Heat balance at the surface of the arctic ocean. US-IGY Drifting Station Alpha Arctic Ocean 1957-1958, page 69, 1965.

[6] E.P. Baltsavias. Airborne laser scanning: Existing systems and firms and other resources. ISPRS Journal of Photogrammetry and Remote Sensing, 54(2):164–198, 1999.

[7] D.G. Barnett. A long-range ice forecasting method for the north coast of alaska. Sea Ice Processes and Models, pages 402–409, 1980.

[8] J.B. Blair, D.L. Rabine, and M.A. Hofton. The Laser Vegetation Imaging Sensor: A medium-altitude, digitisation-only, airborne laser altimeter for mapping vegetation and topography. ISPRS Journal of Photogrammetry and Remote Sensing, 54(2):115–122, 1999.

[9] G. Blewitt. Basics of the GPS technique: Observation equations. Geodetic Applications of GPS, pages 10–54, 1997.

[10] R.H. Bourke and R.P. Garrett. Sea ice thickness distribution in the arctic ocean. Cold Regions Science and Technology, 13(3):259–280, 1987.

[11] A.C. Brenner, J.P. DiMarzio, and H.J. Zwally. Precision and accuracy of satellite radar and laser altimeter data over the continental ice sheets. Transactions on Geoscience and Remote Sensing, 45(2): 321–331, 2007.

[12] J.C. Brock, C.W. Wright, A.H. Sallenger, W.B. Krabill, and R.N. Swift. Basis and methods of NASA airborne topographic mapper lidar surveys for coastal studies. Journal of Coastal Research, 18(1): 1–13, 2002.

[13] J.J. Cassano, J.A. Maslanik, C.J. Zappa, A.L. Gordon, R.I. Cullather, and S.L. Knuth. Observations of Antarctic polynya with unmanned aircraft systems. Eos Trans. AGU, 91:28, 2010.

[14] D.J. Cavalieri and H.J. Zwally. Satellite observations of sea ice. Advances in Space Research, 5(6): 247–255, 1985.

[15] C. Chivers. Russia plants underwater flag at North Pole. The New York Times. New York, 2007.

[16] O.L. Colombo and A.G. Evans. Testing decimeter-level, kinematic, differential gps over great distances at sea and on land. In ION GPS-98, pages 1257–1264, 1998.

[17] O.L. Colombo, A. Sutter, and A.G. Evans. Evaluation of real-time, long-range, precise, differential, kinematic gps using broadcast orbits. Proceedings ION GNSS-2003, Portland, Oregon, 2003.

[18] J.C. Comiso, P. Wadhams, W.B. Krabill, R.N. Swift, J.P. Crawford, and W.B. Tucker III. Top/bottom multisensor remote sensing of arctic sea ice. Journal of Geophysical Research, 96(C2):2693–2709, 1991.

[19] L.N. Connor, S.W. Laxon, A.L. Ridout, W.B. Krabill, and D.C. McAdoo. Comparison of envisat radar and airborne laser altimeter measurements over arctic sea ice. Remote Sensing of Environment, 113 (3):563–570, 2009.

[20] R.I. Crocker, J.A. Maslanik, S.E. Palo, C. Fowler, J. Adler, U.C. Herzfeld, M.M. Fladeland, E.C. Weatherhead, and M. Angier. Performance assessment of a small LIDAR altimeter deployed on unmanned aircraft for glacier and sea ice surface topography profiling. In AGU Fall Meeting Abstracts, volume 1, page 0511, 2009.

[21] R.I. Crocker, J.A. Maslanik, J.J. Adler, S.E. Palo, U.C. Herzfeld, and W.J. Emery. A sensor package for ice surface observations using small unmanned aircraft systems. Transactions on Geoscience and Remote Sensing, 50(4):1033–1047, 2012.

[22] J.A. Curry, J.L. Schramm, and E.E. Ebert. Sea ice-albedo climate feedback mechanism. J, 1151(8): 240–247, 1995.

[23] J.A. Curry, J. Maslanik, G. Holland, and J. Pinto. Applications of Aerosondes in the Arctic. Bulletin of the American Meteorological Society, 85(12):1855–1861, 2004.

[24] M. Edwards, D. Madsen, C. Stringham, A. Margulis, B. Wicks, and D.G. Long. MicroASAR: A Small, robust LFM-CW SAR for operation on UAVs and small aircraft. In Geoscience and Remote Sensing Symposium, 2008. IGARSS 2008. IEEE International, volume 5. IEEE, 2009.

[25] M.W.M. Edwards. Comprehensive error analysis and integration of an airborne laser profiling system for Arctic sea ice freeboard measurements. Master's thesis, University of Colorado at Boulder, 2008.

[26] M.M. Fladeland, R. Berthold, L. Monforton, R. Kolyer, B. Lobitz, and M. Sumich. The NASA SIERRA UAV: A new unmanned aircraft for earth science investigations. In AGU Fall Meeting Abstracts, volume 1, page 0365, 2008.

[27] R. Forsberg and H. Skourup. Arctic Ocean gravity, geoid and sea-ice freeboard heights from ICESat and GRACE. Geophysical Research Letters, 32(21), 2005.

[28] R. Forsberg, K. Keller, and S.M. Jacobsen. Laser monitoring of ice elevations and sea-ice thickness in Greenland. International Archives OF Photogrammetry Remote Sensing and Spatial Information Sciences, 34(3/W4):163–168, 2001.

[29] R. Forsberg, H. Skourup, O. Andersen, S. Laxon, A. Ridout, A. Braun, J. Johannessen, F. Siegismund, C.C. Tscherning, and P. Knudsen. Combination of spaceborne, airborne and surface gravity in support of arctic ocean sea-ice and mdt mapping. European Space Agency,(Special Publication) ESA SP, SP-627:21–26, 2007.

[30] C. Fowler, W.J. Emery, and J. Maslanik. Satellite-derived evolution of Arctic sea ice age: October 1978 to March 2003. Geoscience and Remote Sensing Letters, 1(2):71–74, 2004. ISSN 1545-598X.

[31] K.A. Giles, S.W. Laxon, D.J. Wingham, D.W. Wallis, W.B. Krabill, C.J. Leuschen, D. McAdoo, S.S. Manizade, and R.K. Raney. Combined airborne laser and radar altimeter measurements over the fram strait in may 2002. Remote Sensing of Environment, 111(2):182–194, 2007.

[32] S. Goebell. Comparison of coincident snow-freeboard and sea ice thickness profiles derived from helicopter-borne laser altimetry and electromagnetic induction sounding. Journal of Geophysical Research, 116(C8):C08018, 2011.

[33] T. Gregorius and G. Blewitt. The effect of weather fronts on gps measurements. GPS World, 9(5): 53–60, 1998.

[34] C. Haas, S. Hendricks, H. Eicken, and A. Herber. Synoptic airborne thickness surveys reveal state of arctic sea ice cover. Geophysical Research Letters, 37(L09501):1–5, 2010.

[35] U.C. Herzfeld. A method for seafloor classification using directional variograms, demonstrated for data from the western flank of the mid-atlantic ridge. Mathematical Geology, 25(7):901–924, 1993.

[36] UC Herzfeld. Geostatistical interpolation and classification of remote sensing data from ice surfaces. International Journal of Remote Sensing, 20(2):307–327, 1999.

[37] U.C. Herzfeld. Vario functions of higher order–definition and application to characterization of snow surface roughness. Computers & geosciences, 28(5):641–660, 2002.

[38] U.C. Herzfeld. Atlas of Antarctica: Topographic maps from geostatistical analysis of satellite radar altimeter data, volume 1. Springer Verlag, 2004.

[39] U.C. Herzfeld. Master of the obscure–automated geostatistical classification in presence of complex geophysical processes. Mathematical Geosciences, 40(5):587–618, 2008.

[40] U.C. Herzfeld and C.A. Higginson. Automated geostatistical seafloor classification–principles, parameters, feature vectors, and discrimination criteria. Computers & Geosciences, 22(1):35–41, 1996.

[41] U.C. Herzfeld and H. Mayer. Surge of bering glacier and bagley ice field, alaska: An update to august 1995 and an interpretation of brittle-deformation patterns. Journal of Glaciology, 43(145):427–434, 1997.

[42] U.C. Herzfeld and H. Mayer. Seasonal comparison of ice-surface structures in the ablation area of jakobshavn isbræ drainage system, west greenland. Annals of Glaciology, 37(1):199–206, 2003.

[43] U.C. Herzfeld and C. Overbeck. Analysis and simulation of scale-dependent fractal surfaces with application to seafloor morphology. Computers & Geosciences, 25(9):979–1007, 1999.

[44] U.C. Herzfeld, M. Stauber, and N. Stahl. Geostatistical characterization of ice surfaces from ers-1 and ers-2 sar data, jakobshavn isbræ, greenland. Annals of Glaciology, 30(1):224–234, 2000.

[45] U.C. Herzfeld, H. Mayer, N. Caine, M. Losleben, and T. Erbrecht. Morphogenesis of typical winter and summer snow surface patterns in a continental alpine environment. Hydrological Processes, 17(3): 619–649, 2003.

[46] U.C. Herzfeld, J.A. Maslanik, and M. Sturm. Geostatistical characterization of snow-depth structures on sea ice near point barrow, alaska–a contribution to the amsr-ice03 field validation campaign. Geoscience and Remote Sensing, IEEE Transactions on, 44(11):3038–3056, 2006.

[47] WD Hibler. A dynamic thermodynamic sea ice model. Journal of Physical Oceanography, 9:815–846, 1979.

[48] W.D. Hibler III. Removal of aircraft attitude variation from laser profiles of the Arctic ice pack. Journal of Geophysical Research, 77(36):7190–7915, 1972.

[49] W.D. Hibler III and L.A. LeSchack. Power spectrum analysis of undersea and surface sea-ice profiles. Journal of Glaciology, 11(63), 1972.

[50] W.D. Hibler III, W.F. Weeks, and S.J. Mock. Statistical aspects of sea-ice ridge distributions. Journal of Geophysical Research, 77(30):5954–5970, 1972.

[51] W.D. Hibler III, S.J. Mock, and W.B. Tucker III. Classification and variation of sea ice ridging in the western Arctic Basin. Journal of Geophysical Research, 79(18):2735–2743, 1974.

[52] M.A. Hofton and J.B. Blair. Laser altimeter return pulse correlation: A method for detecting surface topographic change. Journal of Geodynamics, 34(3):477–489, 2002.

[53] M.A. Hofton, E. Malavassi, and J.B. Blair. Quantifying recent pyroclastic and lava flows at Arenal Volcano, Costa Rica, using medium-footprint lidar. Geophysical Research Letters, 33(21):L21306, 2006. ISSN 0094-8276.

[54] M.M. Holland, C.M. Bitz, E.C. Hunke, W.H. Lipscomb, and J.L. Schramm. Influence of the sea ice thickness distribution on polar climate in ccsm3. Journal of Climate, 19(11):2398–2414, 2006.

[55] M.M. Holland, D.A. Bailey, and S. Vavrus. Inherent sea ice predictability in the rapidly changing arctic environment of the community climate system model, version 3. Climate Dynamics, 36(7):1239–1253, 2011.

[56] G. Holloway and T. Sou. Has arctic sea ice rapidly thinned? Journal of Climate, 15(13):1691–1701, 2002. ISSN 1520-0442.

[57] S.M. Hvidegaard and R. Forsberg. Sea-ice thickness from airborne laser altimetry over the arctic ocean north of greenland. Geophysical Research Letters, 29(20):1952, 2002.

[58] J. Inoue, J.A. Curry, and J.A. Maslanik. Application of Aerosondes to melt-pond observations over Arctic sea ice. Journal of Atmospheric and Oceanic Technology, 25(2):327–334, 2008.

[59] O.M. Johannessen, E.V. Shalina, and M.W. Miles. Satellite evidence for an arctic sea ice cover in transformation. Science, 286(5446):1937, 1999.

[60] R.A. Kerr. A warmer Arctic means change for all. Science, 297(5586):1490, 2002.

[61] R.D. Ketchum Jr. Airborne laser profiling of the arctic pack ice. Remote Sensing of Environment, 2: 41–52, 1971.

[62] L. Koenig, S. Martin, M. Studinger, and J. Sonntag. Polar airborne observations fill gap in satellite data. Eos, Transactions American Geophysical Union, 91(38):333, 2010.

[63] W. Krabill, E. Frederick, S. Manizade, C. Martin, J. Sonntag, R. Swift, R. Thomas, W. Wright, and J. Yungel. Rapid thinning of parts of the southern greenland ice sheet. Science, 283(5407):1522–1524, 1999.

[64] W. Krabill, W. Abdalati, E. Frederick, S. Manizade, C. Martin, J. Sonntag, R. Swift, R. Thomas, W. Wright, and J. Yungel. Greenland ice sheet: High-elevation balance and peripheral thinning. Science, 289(5478):428, 2000.

[65] W.B. Krabill. Airborne laser topographic mapping results from Initial Joint NASA/US Army Corps of Engineers experiment. NASA, 1980.

[66] W.B. Krabill and C.F. Martin. Aircraft positioning using global positioning system carrier phase data. Navigation, 34(1):1–21, 1987.

[67] W.B. Krabill and R.N. Swift. Airborne lidar experiments at the savannah river plant, june 1985. Technical report, NASA, Washington, DC USA. Scientific and Technical Information Div., 1987.

[68] W.B. Krabill, R.H. Thomas, C.F. Martin, R.N. Swift, and E.B. Frederick. Accuracy of airborne laser altimetry over the Greenland ice sheet. International Journal of Remote Sensing, 16(7):1211–1222, 1995.

[69] W.B. Krabill, C.W. Wright, R.N. Swift, E.B. Frederick, S.S. Manizade, J.K. Yungel, C.F. Martin, J.G. Sonntag, M. Duffy, W. Huislander, and J.C. Brock. Airborne laser mapping of Assateague National Seashore beach. Photogrammetric Engineering and Remote Sensing, 66(1):65–71, 2000. ISSN 0099-1112.

[70] W.B. Krabill, W. Abdalati, E.B. Frederick, S.S. Manizade, C.F. Martin, J.G. Sonntag, R.N. Swift, R.H. Thomas, and J.G. Yungel. Aircraft laser altimetry measurement of elevation changes of the Greenland ice sheet: Technique and accuracy assessment. Journal of Geodynamics, 34(3-4):357–376, 2002.

[71] R. Kwok. Near zero replenishment of the arctic multiyear sea ice cover at the end of 2005 summer. Geophysical Research Letters, 34(5):5501, 2007.

[72] R. Kwok and D.A. Rothrock. Decline in arctic sea ice thickness from submarine and icesat records: 1958–2008. Geophysical Research Letters, 36(15):L15501, 2009.

[73] R. Kwok, H.J. Zwally, and D. Yi. ICESat observations of Arctic sea ice: A first look. Geophysical Research Letters, 31(16):L16401, 2004. ISSN 0094-8276.

[74] R. Kwok, G.F. Cunningham, H.J. Zwally, and D. Yi. Icesat over arctic sea ice: Interpretation of altimetric and reflectivity profiles. Journal of Geophysical Research, 111(C6):C06006, 2006.

[75] R. Kwok, G.F. Cunningham, H.J. Zwally, and D. Yi. Ice, Cloud, and land Elevation Satellite (ICESat) over Arctic sea ice: Retrieval of freeboard. Journal of Geophysical Research, 112(C12):C12013, 2007. ISSN 0148-0227.

[76] R. Kwok, GF Cunningham, M. Wensnahan, I. Rigor, HJ Zwally, D. Yi, et al. Thinning and volume loss of the arctic ocean sea ice cover: 2003–2008. Journal of Geophysical Research, 114(C7):C07, 2009.

[77] S. Laxon, N. Peacock, and D. Smith. High interannual variability of sea ice thickness in the Arctic region. Nature, 425(6961):947–950, 2003. ISSN 0028-0836.

[78] J. Lee, S. Pullen, S. Datta-Barua, and P. Enge. Assessment of nominal ionosphere spatial decorrelation for lass. In Proceedings of Position, Location and Navigation Symposium (PLANS). IEEE, 2006.

[79] K.E. Lilly and J. Stewart. Arctic alaska north slope resupply operations. Mariners Weather Log, 21: 8–12, 1977.

[80] R.W. Lindsay and J. Zhang. The thinning of arctic sea ice, 1988-2003: Have we passed a tipping point? Journal of Climate, 18(22):4879–4894, 2005.

[81] L.E. Link, W.B. Krabill, and R.N. Swift. A prospectus on airborne laser mapping systems. Advances in Space Research, 3(2):309–322, 1983.

[82] W.H. Lipscomb. Remapping the thickness distribution in sea ice models. Journal of Geophysical Research, 106(C7):13, 2001.

[83] J. Liu, M.E. Cannon, P. Alves, M.G. Petovello, G. Lachapelle, G. MacGougan, and L. DeGroot. A performance comparison of single and dual frequency GPS ambiguity resolution strategies. GPS Solutions, 7(2):87–100, 2003. ISSN 1080-5370.

[84] J. Maslanik, S. Drobot, C. Fowler, W. Emery, and R. Barry. On the arctic climate paradox and the continuing role of atmospheric circulation in affecting sea ice conditions. Geophysical Research Letters, 34(3):L03711, 2007.

[85] J. Maslanik, J. Stroeve, C. Fowler, and W. Emery. Distribution and trends in arctic sea ice age through spring 2011. Geophysical Research Letters, 38(13):L13502, 2011.

[86] J.A. Maslanik, M.C. Serreze, and R.G. Barry. Recent decreases in arctic summer ice cover and linkages to atmospheric circulation anomalies. Geophysical Research Letters, 23(13):1677–1680, 1996.

[87] J.A. Maslanik, M. Sturm, M.B. Rivas, A.J. Gasiewski, J.F. Heinrichs, U.C. Herzfeld, J. Holmgren, M. Klein, T. Markus, D.K. Perovich, J.G Sonntag, J.C. Stroeve, and K. Tape. Spatial variability of Barrow-area shore-fast sea ice and its relationships to passive microwave emissivity. Transactions on Geoscience and Remote Sensing, 44(11):3021–3031, 2006. ISSN 0196-2892.

[88] J.A. Maslanik, C. Fowler, J. Stroeve, S. Drobot, J. Zwally, D. Yi, and W. Emery. A younger, thinner Arctic ice cover: Increased potential for rapid, extensive sea-ice loss. Geophysical Research Letters, 34 (24):L24501, 2007. ISSN 0094-8276.

[89] J.A. Maslanik, R.I. Crocker, K. Wegrzyn, C. Fowler, U.C. Herzfeld, D. Long, R. Kwok, M.M. Fladeland, and P. Bui. Characterization of Fram Strait sea ice Conditions using the NASA SIERRA unmanned aircraft system. In AGU Fall Meeting Abstracts, volume 1, page 06, 2009.

[90] P. Misra and P. Enge. Global Positioning System: Signals, measurements and performance second edition. Lincoln, MA: Ganga-Jamuna Press, 2006.

[91] S.J. Mock, A.D. Hartwell, and W.D. Hibler III. Spatial aspects of pressure ridge statistics. Journal of Geophysical Research, 77(30):5945–5953, 1972.

[92] R. Nelson, W. Krabill, and J. Tonelli. Estimating forest biomass and volume using airborne laser data. Remote Sensing of Environment, 24(2):247–267, 1988.

[93] Inc. NovAtel. OEM4 family of receivers, user manual, 2008.

[94] J.E. Overland and M. Wang. Large-scale atmospheric circulation changes are associated with the recent loss of arctic sea ice. Tellus A, 62(1):1–9, 2010.

[95] J.T. Overpeck, M. Sturm, J.A. Francis, D.K. Perovich, M.C. Serreze, R. Benner, E.C. Carmack, F.S. Chapin III, S.C. Gerlach, L.C. Hamilton, L.D. Hinzman, M. Holland, H.P. Huntington, J.R. Key, A.H. Lloyd, G.M. MacDonald, J. McFadden, D. Noone, T.D. Prowse, P. Schlosser, and C. Vorosmarty. Arctic system on trajectory to new, seasonally ice-free state. Eos, 86(34):309–316, 2005.

[96] B.W. Parkinson and J.J. Spilker. The global positioning system: Theory and applications. AIAA, 1996. ISBN 1563471078.

[97] R.R. Parmerter and M.D. Coon. Model of pressure ridge formation in sea ice. Journal of Geophysical Research, 77(33):6565–6575, 1972.

[98] M.C.L. Patterson, A. Brescia, and Advanced Ceramics Research Tuscon AZ. Integrated sensor systems for UAS. In 24^{th} Bristol UAV Systems Conference, 2008.

[99] M.C.L. Patterson, J. Morris, and Advanced Ceramics Research Tuscon AZ. Small UAS imaging capabilities. In 24^{th} Bristol UAV Systems Conference, 2009.

[100] D.K. Perovich, W.B. Tucker III, and K.A. Ligett. Aerial observations of the evolution of ice surface conditions during summer. Journal of Geophysical Research, 107(C10):8048, 2002. ISSN 0148-0227.

[101] R.J. Reed and W.J. Campbell. The equilibrium drift of ice station alpha. Journal of Geophysical Research, 67(1):281–297, 1962.

[102] G.Q. Robin, D.J. Drewry, V.A. Squire, and A.S. Laughton. Satellite observations of polar ice fields [and discussion]. Philosophical Transactions of the Royal Society of London. Series A, Mathematical and Physical Sciences, 309(1508):447–461, 1983.

[103] D.A. Rothrock and J. Zhang. Arctic ocean sea ice volume: What explains its recent depletion? Journal of Geophysical Research, 110(C1):C01002, 2005.

[104] D.A. Rothrock, Y. Yu, and G.A. Maykut. Thinning of the Arctic sea-ice cover. Geophysical Research Letters, 26(23):3469–3472, 1999. ISSN 0094-8276.

[105] A.H. Sallenger Jr, W.B. Krabill, R.N. Swift, J. Brock, J. List, M. Hansen, R.A. Holman, S. Manizade, J. Sontag, A. Meredith, K. Morgan, J.K. Yunkel, E.B. Frederick, and Stockdon H. Evaluation of airborne topographic lidar for quantifying beach changes. Journal of Coastal Research, 19(1):125–133, 2003.

[106] W. Schwarzacher. Pack ice studies in the arctic ocean. Journal of Geophysical Research, 64(12): 2357–2367, 1959.

[107] L.A. Smith. System model of a UAV and sensor package for the measurement of sea ice freeboard, roughness, and topography. Master's thesis, University of Colorado at Boulder, 2007.

[108] K. Steffen, A.E. Behar, D. McGrath, W.T. Colgan, T.P. Phillips, and J. Adler. Monitoring Greenland ice sheet's climate and exploring moulins (Invited). In AGU Fall Meeting Abstracts, volume 1, page 07, 2009.

[109] N. Steiner, M. Harder, and P. Lemke. Sea-ice roughness and drag coefficients in a dynamic-thermodynamic sea-ice model for the Arctic. Tellus A, 51(5):964–978, 1999. ISSN 0280-6495.

[110] B. Stoew and G. Elgered. Spatial and temporal correlations of the gps estimation errors. TOUGH report, 2005.

[111] J. Stroeve, M.M. Holland, W. Meier, T. Scambos, and M. Serreze. Arctic sea ice decline: Faster than forecast. Geophysical Research Letters, 34(9):L09501, 2007. ISSN 0094-8276.

[112] J.C. Stroeve, M.C. Serreze, F. Fetterer, T. Arbetter, W. Meier, J. Maslanik, and K. Knowles. Tracking the Arctic's shrinking ice cover: Another extreme September minimum in 2004. Geophysical Research Letters, 32(4):L04501, 2005. ISSN 0094-8276.

[113] A.S. Thorndike, D.A. Rothrock, G.A. Maykut, and R. Colony. The thickness distribution of sea ice. Journal of Geophysical Research, 80(33):4501–4513, 1975.

[114] G.W. Timco and R.P. Burden. An analysis of the shapes of sea ice ridges. Cold Regions Science and Technology, 25(1):65–77, 1997.

[115] M. Tschudi, C. Fowler, J. Maslanik, and J. Stroeve. Tracking the movement and changing surface characteristics of arctic sea ice. Selected Topics in Applied Earth Observations and Remote Sensing, 3(4):536–540, 2010.

[116] M.A. Tschudi, J.A. Curry, and J.A. Maslanik. Airborne observations of summertime surface features and their effect on surface albedo during FIRE/SHEBA. Journal of Geophysical Research, 106(D14): 15335, 2001. ISSN 0148-0227.

[117] W.B. Tucker III, W.F. Weeks, and M. Frank. Sea ice ridging over the alaskan continental shelf. Journal of Geophysical Research, 84(C8):4885–4897, 1979.

[118] W.B. Tucker III, A.J. Gow, and W.F. Weeks. Physical properties of summer sea ice in the fram strait. Journal of Geophysical Research, 92(C7):6787–6803, 1987.

[119] N. Untersteiner. On the mass and heat budget of arctic sea ice. Meteorology and Atmospheric Physics, 12(2):151–182, 1961.

[120] N. Untersteiner. Remarks on the cooling power in polar regions. US-IGY Drifting Station Alpha Arctic Ocean 1957-1958, 13(3/4):81, 1965.

[121] N. Untersteiner and F.I. Badgley. The roughness parameters of sea ice. Journal of Geophysical Research, 70(18):4573–4577, 1965.

[122] P. Wadhams. Sea-ice topography of the arctic ocean in the region 70 degrees w to 25 degrees e. Philosophical Transactions of the Royal Society of London. Series A, Mathematical and Physical Sciences, 302(1464):45–85, 1981.

[123] P. Wadhams. Evidence for thinning of the arctic ice cover north of greenland. Nature, 345(6278): 795–797, 1990.

[124] P. Wadhams and J.C. Comiso. The ice thickness distribution inferred using remote sensing techniques. Microwave remote sensing of sea ice, 68:375–383, 1992.

[125] P. Wadhams and N.R. Davis. Further evidence of ice thinning in the arctic ocean. Geophysical Research Letters, 27(24):3973–3975, 2000.

[126] P. Wadhams and N.R. Davis. Arctic sea-ice morphological characteristics in summer 1996. Annals of Glaciology, 33(1):165–170, 2001.

[127] P. Wadhams, W.B. Tucker III, W.B. Krabill, R.N. Swift, J.C. Comiso, and N.R. Davis. Relationship between sea ice freeboard and draft in the arctic basin, and implications for ice thickness monitoring. Journal of Geophysical Research, 97(C12):20325–20, 1992.

[128] W.F. Weeks, A. Kovacs, and W.D. Hibler III. Pressure ridge characteristics in the arctic coastal environment. In First International Conference on Port and Ocean Engineering under Arctic Conditions, volume 1, pages 152–183, 1971.

[129] E. Zaugg, D. Long, M. Edwards, M. Fladeland, R. Kolyer, I. Crocker, J. Maslanik, U. Herzfeld, and B. Wallin. Using the MicroASAR on the NASA SIERRA UAS in the Characterization of Arctic Sea Ice Experiment. In Radar Conference, 2010 IEEE, pages 271–276. IEEE, 2010.

[130] X. Zhang. Precise point positioning: Evaluation and airborne lidar calibration. Technical report, Danish National Space Center 4, 2006.

[131] X. Zhang and R. Forsberg. Assessment of long-range kinematic GPS positioning errors by comparison with airborne laser altimetry and satellite altimetry. Journal of Geodesy, 81(3):201–211, 2007.

[132] H.J. Zwally, B. Schutz, W. Abdalati, J. Abshire, C. Bentley, A. Brenner, J. Bufton, J. Dezio, D. Hancock, D. Harding, T. Herring, B. Minster, K. Quinn, S. Palm, J. Spinhirne, and R. Thomas. ICESat's laser measurements of polar ice, atmosphere, ocean, and land. Journal of Geodynamics, 34(3-4): 405–445, 2002.

Appendix A

Acronyms

2D	Two Dimensional
3D	Three Dimensional
AES	Aerospace Engineering Sciences
AGL	Above Ground Level
AMAP	Arctic Monitoring and Assessment Programme
AOL	Airborne Oceanographic Lidar
AON	Arctic Observing Network
APPS	Automatic Precise Positioning Service
ATM	Airborne Topographic Mapper
BT	Brightness Temperature
C/A	Course/Acquisition
CASIE	Characterization of Arctic Sea Ice Experiment
C&DH	Command and Data Handling
CDP	Carrier-phase Differential Positioning
COG	Course Over Ground
COTS	Commercial Off-The-Shelf
CU	University of Colorado at Boulder
CULPIS	CU Laser Profilometer and Imaging System
DEM	Digital Elevation Model

dGPS	differential GPS
DOP	Dilution Of Precision
ECEF	Earth Centered, Earth Fixed
ENV	East, North, Vertical
ESA	European Space Agency
FFT	Fast Fourier Transform
GCS	Ground Control Station
GLAS	Geoscience Laser Altimeter System
GNSS	Global Navigation Satellite System
GPS	Global Positioning System
HDOP	Horizontal Dilution of Precision
IGS	International GNSS Service
IMU	Inertial Measurement Unit
JPL	Jet Propulsion Laboratory
KAR	Kinematic Ambiguity Resolution
L1	Link 1
L2	Link 2
LALE	Low Altitude, Long Endurance
LIDAR	LIght Detecting and Ranging
LVIS	Land, Vegetation, and Ice Sensor
MEMS	MicroElectroMechanical Sensor
MODIS	Moderate Resolution Imaging Spectroradiometer
MUSCOX	MUlti-Sensor Cryospheric Observation eXperiment
NASA	National Aeronautics and Space Administration
NAVOCEANO	Naval Oceanographic Office
NEU	North, East, Up (same as ENV)
NOAA	National Oceanic and Atmospheric Administration

NSF	National Science Foundation
NSIDC	National Snow and Ice Data Center
PCB	Printed Circuit Board
PDF	Probability Density Function
PDOP	Position Dilution of Precision
PPM	Parts Per Million
PPP	Precise Point Positioning
PRF	Pulse Repetition Frequency
RECUV	Research and Engineering Center for Unmanned Vehicles
RMS	Root-Mean-Square
RS	Reference Stations
RSS	Root Sum of the Squares
SAR	Synthetic Aperture Radar
sGPS	standard GPS
SIERRA	Science Instrumentation Environmental Remote Research Aircraft
SSII	Superstar II
TEC	Total Electron Content
TNB	Terra Nova Bay
UAS	Unmanned Aircraft Systems
ULS	Universal Laser System
USD	United States Dollar
UTC	Coordinated Universal Time
VDOP	Vertical Dilution of Precision

Appendix B

CULPIS Component Specifications

All specification based on data gathered in spring 2010

Refer to Table 2.1 for power, mass, volume, and cost specifications

Laser Rangefinder (LIDAR Unit)

Function: Measures the distance from the laser optics processing head to the ground surface and the laser pulse return power.
Manufacturer: Laser Technology, Inc.
Model: Universal Laser System (ULS)
Wavelength: 905 nm (IR)
Beam Divergence: 3 mrad (∼30 cm diameter footprint at 100 m range)
Pulse Rate: 10-5000 Hz, configurable
Measurement Rate: 400 Hz nominal, 2000 Hz maximum, configurable measurement modes
Data Rate: 16.6 MB/h
Maximum Range: 500 m (over nominal ice targets)
Output Power: 100, 200, or 400 nJ per pulse, configureable
Eye Safety: Class 1, 7 mm eye safe (FDA, CFR21)
Accuracy: ±2 cm
Resolution: 1 mm
Dimensions: 14.3 x 12 x 6.3 cm

Inertial Measurement Unit (IMU)

Function: Measures the aircraft attitude (roll, pitch, and yaw) to correct the laser range and surface measurement location for off-nadir pointing.
Manufacturer: Microstrain, Inc.
Model: 3DM-GX1 (alternate models include the 3DM and 3DM-G, specifications not provided here)
Sensor Overview: A MEMS system that combines three angular rate gyroscopes with three orthogonal accelerometers and magnetometers.
Measurement Rate: 100 Hz
Data Rate: 13.2 MB/h
Gyro Rate: 300°/s
Accuracy: 0.5° (static), 2° (dynamic)
Dimensions: 9 x 6.5 x 2.5 cm

GPS Receiver

Function: Measures the aircraft horizontal and vertical position in the WGS84 ellipsoid.
Manufacturer: NovAtel, Inc.
Model: Superstar II (SSII; no longer in production)
Measurement Type: single frequency C/A code pseudorange and L1 carrier-phase
Measurement Rate: 1-10 Hz
Data Rate: 5.5 MB/h (for 10 Hz measurement rate)
Measurement Precision: 1 cm RMS (L1 carrier-phase)
Interface: The GPS receiver is connected to the C&DH PCB via a custom communications PCB that was developed by the University of Colorado, AES.
Dimensions: 9 x 4.6 x 1.5 cm

GPS Antenna

Manufacturer: Antcom Corporation
Model: 3G15A-XT-1
Frequency: L1
Low Noise Amplifier Gain: 33 dB
Dimensions: 1.8 cm (height) x 8.9 cm (diameter)

Digital Still Camera

Function: Provide continuous fine-resolution imagery coincident with the laser elevation measurements.
Manufacturer: Canon
Model: PowerShot G10 (alternate models include the PowerShot SX100 IS and SX110 IS, specifications not provided here)
Resolution: 14.7 megapixels, 4416 x 3312 pixels
Field of View: 65° x 50°
Shutter Controller: The timing of the shutter trigger is controlled by the URBI Camera Control manufactured by Blip, It Pty Ltd.
Data Rate: 2.6 GB/h when photos are taken at 5 second intervals.
Data Storage: Still photos are stored on the camera's SD card. A 32 GB SD card will provide enough storage for ∼12 hours worth of photos taken at 5 second intervals, which is sufficient to provide continual ground coverage at 200 m AGL and 30 m/s.
Voltage: The camera is supplied 7.4V by passing 12V from the power regulation PCB through an adjustable voltage regulator manufactured by Blip.
Camera Dimensions: 11 x 7 x 5 cm
URBI Dimensions: 4 x 5.5x 1.2 cm

Digital Video Camera

Function: Provide fine-resolution HD video coincident with the laser elevation measurements.
Manufacturer: Aiptek
Model: A-HD+ 1080P (alternate models include the A-HD 720P, specifications not provided here)
Resolution: 1440 x 1080 pixels at 30 f/s (1080P) or 1280 x 720 pixels at 60 f/s (720P)
Data Rate: 3 GB/h for 1080P HD video data.
Data Storage: Video files are stored on the camera's SD card. A 32 GB SD card will provide enough storage for ∼10.6 hours worth of 1080P video data.
Dimensions: 12 x 7.5 x 3.5 cm

Command and Data Handling (C&DH) PCB

Function: Control, timestamp, and log the laser, IMU, and GPS data. Trigger the still camera and record the trigger time.
Manufacturer: University of Colorado, AES
Data Storage: The data is logged and stored on a microSD card using a Gumstix Pro XM4 linux microcomputer. A 1 GB microSD card will provide enough storage for approximately 20 hours worth of data.
Additional Functionality: Records temperature and barometric pressure data, available digital and analog communications ports for interfacing with additional peripheral devices.
Dimensions: 14 x 7.7 x 2 cm

Power Regulation PCB

Function: Supply conditioned power to the various instruments at their required voltage from a single input power source.
Manufacturer: University of Colorado, AES
Input Voltage: 8-40V DC (12V nominal)
Output Voltage: 3.3V, 5V, 9V, and 12V DC
Power Efficiency: $\eta = 93\%$
Dimensions: 14 x 7.7 x 2 cm

Appendix C

Still Camera Shutter Trigger Timing Derivation

The derivation presented here yields Equation C.5, which specifies the time separation that is required to achieve a desired overlap between consecutive pictures.

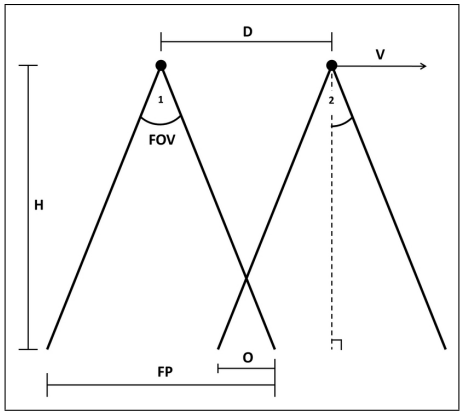

Figure C.1: Parameters relevant to the still camera trigger timing derivation.

D = along-track distance between origin of consecutive photos, [m]

V = aircraft velocity (speed), [m/s]

t = still camera shutter trigger timing separation, [s]

FP = along-track photo footprint extent, [m]

H = height above ground surface, [m]

FOV = camera along-track field-of-view, [deg]

O = consecutive photo overlap, [m]

OP = consecutive photo overlap percentage, [1-100%]

$$D = V^{*}t \tag{C.1}$$

$$\frac{FP}{2H} = \tan\left(\frac{FOV}{2}\right)$$
$$FP = 2H\tan\left(\frac{FOV}{2}\right) \tag{C.2}$$

$$O = FP^{*}OP \tag{C.3}$$

$$\begin{aligned} D &= \frac{FP}{2} + \frac{FP}{2} - O \\ &= FP - O \\ &= FP - FP^{*}OP \text{ (from C.3)} \\ &= FP\,(1 - OP) \end{aligned}$$
$$\begin{aligned} FP &= \frac{D}{1 - OP} \\ &= \frac{V^{*}t}{1 - OP} \text{ (from C.1)} \end{aligned} \tag{C.4}$$

$$\frac{V^{*}t}{1 - OP} = 2H\tan\left(\frac{FOV}{2}\right) \text{ (from C.2 \& C.4)}$$
$$\boxed{t = \frac{[1 - OP]\left[2H\tan\left(\frac{FOV}{2}\right)\right]}{V}} \text{ (same as Equation 2.1 in §2.3)} \tag{C.5}$$

Appendix D

CULPIS Derivative Configurations: CULPIS-X and Moulin Probe

The CULPIS-X and the moulin probe, shown in Figure D.1, are two instrument packages that are derived from the CULPIS components. The CULPIS-X consists of all the CULPIS instrumentation, with the addition of a pyrometer and spectrometer. It has been configured to slide into the flare tube of a US Coast Guard C-130 manned aircraft. An upgraded version of the one pictured here will be operated during flights-of-opportunity in support of NASA's IceBridge program to make land and sea ice surface topography measurements. The moulin probe is a cylindrical package that is lowered into the depths of moulins on the Greenland ice sheet. The probe is rotated as it is lowered, and the ULS and IMU are used to measure the pointing angle and the range to the moulin wall. From these data it is possible to reconstruct the 3D inner structure of the moulin and monitor its changes over time [108].

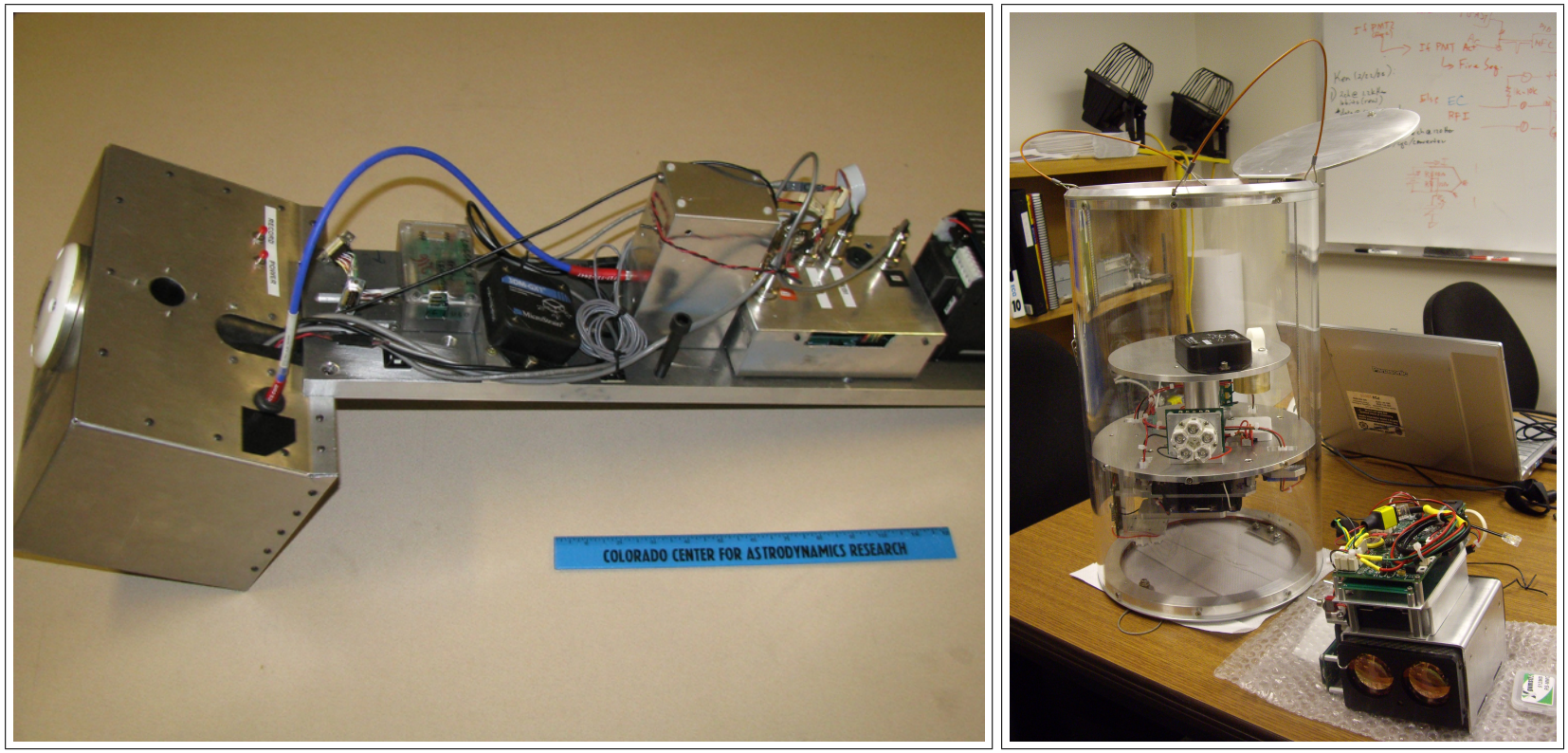

Figure D.1: The US Coast Guard C-130 payload, known as CULPIS-X (left), and the moulin probe (right) are two instrument packages derived from the CULPIS components. An upgraded version of the CULPIS-X that is shown here will be flown on future Coast Guard Arctic Domain Awareness flights in support of NASA's IceBridge program. The moulin probe has been used to map the 3D structure of moulins in the Greenland ice sheet [108].

Appendix E

MUSCOX Example Hyperspectral Imagery

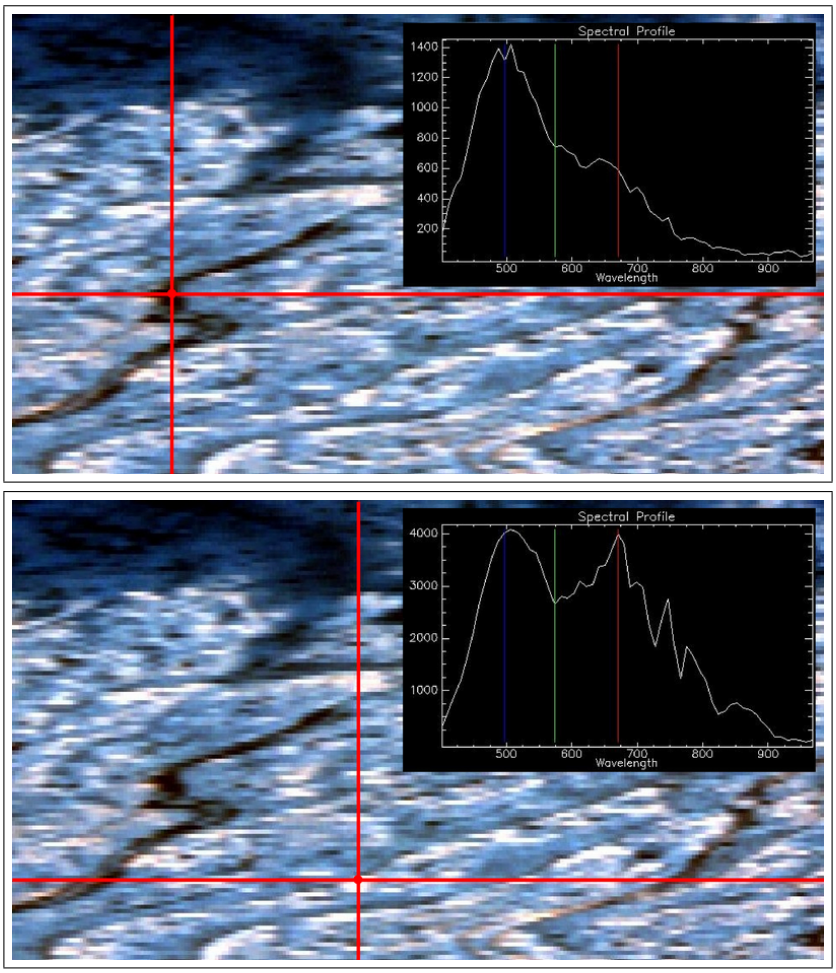

Figure E.1: Greenland ice surface spectra collected during MUSCOX with the Resonon hyperspectral camera. The spectra shown are taken at the intersection of the red lines. The bottom spectra, taken over bright ice, has a high peak in the red band, unlike the top spectra taken over dark ice. These data are peripheral to this dissertation research, but were investigated as part of Francesca Lettang's Masters thesis, and are presented to further illustrate the types of data that can be collected from UAS.

Appendix F

CULPIS Laser Interference Testing

With the desire to have two ULS units operating simultaneously for the CASIE mission it was imperative to assess the potential of interference. Since the two ULS operate at the same wavelength, it is possible for one unit to detect the pulse transmitted by another unit. This acts as a false-positive signal at an incorrect time, and results in an inaccurate, erroneous range measurement. To test for interference and characterize its signal, two ULS were pointed toward a wall ∼29 m away and aligned to desired angular offsets using a pair of protractors printed onto paper. The protractor alignment paper and the dual ULS testing setup are pictured in Figure F.1. Data was collected for approximately 3 minutes during each test, during which time I walked back-and-forth in front of the wall one time to act as a ranging signal.

Range measurements collected during two tests done with different offset angles are shown in Figure F.2. The data on left were collected with a 0° offset (parallel alignment) and the data on right were collected with a 3° offset. As shown in the top left panel, erroneous range measurements are detected by ULS 1 when the two units are aligned nearly parallel, whereas the range data are a clean and consistent ∼29 m for the 3° offset test (top right panel). The two bottom panels of Figure F.2 show closeup views of the data as I walked in front of the target wall. During the 0° test my range signal is detected by both ULS at nearly the same time, confirming their parallel alignment, and interference noise is evident for ULS 1. During the 3° test my range signal is detected by both ULS at different times due to their angular offset, and interference noise is not present. These tests confirmed that interference would likely not occur during CASIE, where a 15° offset was desired, and if interference did occur it would be possible to recognize its signature in the range data.

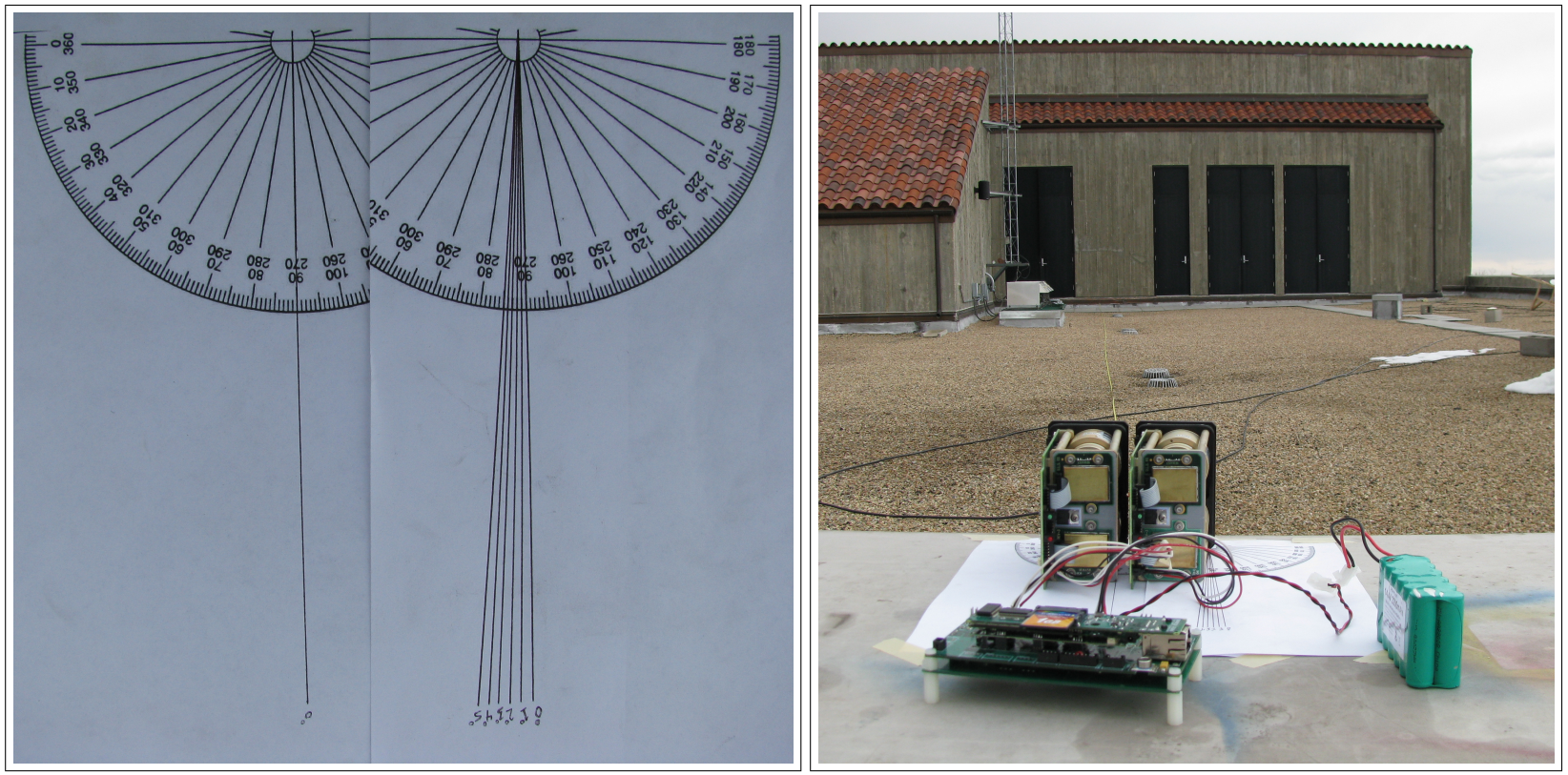

Figure F.1: The setup used to test and characterize the interference between two ULS laser units, operating simultaneously, in preparation for integration into the SIERRA UAS for the CASIE campaign. The left image shows two sheets of paper with protractors printed on each, and drawn lines that were used to align the two ULS with a desired offset angle. The right image shows the testing setup in which the two ULS were aligned facing a wall ∼29 m away. Range measurements were recorded for roughly 3 minutes, during which time I walked back-and-forth along the wall one time acting as a detection signal.

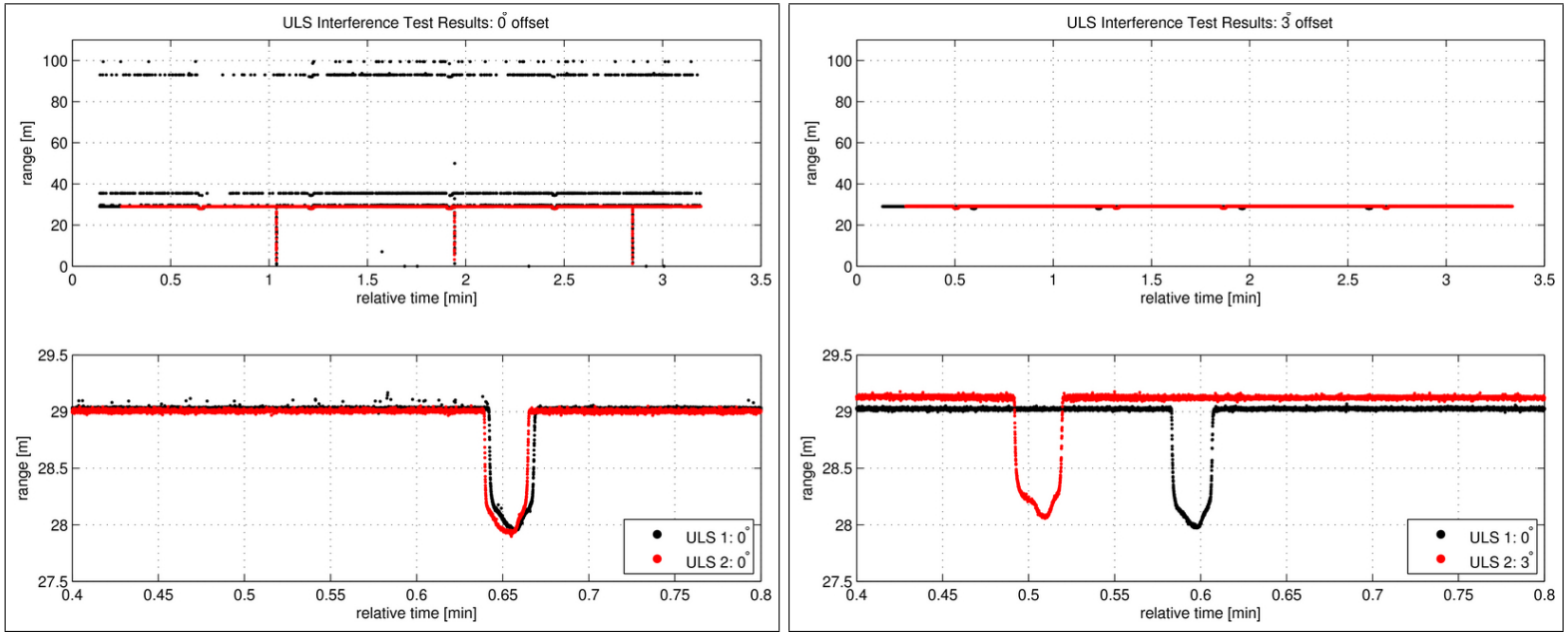

Figure F.2: The dual ULS interference testing results. The plot on top left shows considerable interference between the two laser units when aligned parallel with a 0° offset. Erroneous range values (>29 m) persist throughout the testing period, and transient spikes of decreased range exist near 1, 2, and 3 minutes. The plot on bottom right is a closeup view showing the range signal as I walked in front of the target wall. My signal was detected at almost the exact same time by the two ULS units, confirming their near-parallel alignment. The plot on top right shows no interference between the two laser units when aligned with a 3° offset. The closeup view of the range measurement as I walked in front of the wall shows considerable temporal offset and illustrates that the range signal was accurately detected by both laser units. The range measurements from ULS 2 are slightly larger since it was angled outward with a longer path length to the wall.

Appendix G

CULPIS ScanEagle Launch Testing

To ensure the CULPIS is able to withstand the 8+ G acceleration forces associated with the pneumatic launch [communication with Greg Walker], the payload underwent extensive testing at Hood Technology, Inc. on 8 April 2009. These testing efforts were a collaboration between the University of Colorado, the University of Alaska, American Aerospace Engineering, based out of White Salmon, Washington, and Hood Technology, Inc. located in Hood River, Oregon. Thanks are extended to Greg Walker, Mike Bartlett, Ben Cryder, Bill Bradley, Cory Roeseler, Mark Napier, and James Kreiser for their involvement with the CULPIS ScanEagle launch testing. The test unit consisted of a the CULPIS payload bay attached to a ScanEagle fuselage with the wings removed. To simulate normal payload operation, a battery pack was used to provide 12V of power to the CULPIS unit. The launcher was a newly-manufactured Hood Technology Soft-Start Superwedge. The test unit was mounted to an overhead assembly riding on an angled steel cable with cinch straps. At a distance from the launcher, a collar and strap system were used to slow the overhead assembly and test unit post launch. The testing launch assembly setup is shown in Figure G.1 and the results of each test are provided in Table G.1.

The maximum expected launch speed of a ScanEagle with a Superwedge launcher is 30 m/s [communication with Cory Roeseler]. Numerous zip line tests exceeded that launch speed (maximum tested launch speed was 34 m/s) and the CULPIS payload unit remained structurally intact and continued to function during and after the testing periods. However, during a few of the tests the payload lost power and ceased operation because the battery was drained. There was not sufficient time to recharge the battery after each testing period, so two of the test were done without powering on the payload and were focused on assessing

Figure G.1: The ScanEagle zip line testing setup and equipment. The ScanEagle CULPIS instrument package, shown on top left, is mounted in a mock ScanEagle fuselage and hung from a taught cable, shown on top right, and launched using a pneumatic catapult, shown in the bottom figure.

Table G.1: The ScanEagle zip line testing results, provided here, indicate that the CULPIS payload is structurally able to withstand the ScanEagle launch forces.

Test	Launch Time [local]	Launch Pressure [psi]	Launch Speed [m/s]	Notes
1	10:41	31	19.6	all systems functioning
2	11:11	40	23.0	all systems functioning
3	11:26	47	25.0	see Notes A & B
4	12:56	56	28.6	all systems functioning
5	13:15	64	30.3	all systems functioning
6	13:35	70	N/A	see Note C
7	13:44	70	31.6	see Note A
8	14:46	75	33.0	see Note A
9	14:58	80	33.8	see Note D
10	15:11	79	34.0	see Note D
11	15:21	80	33.9	all systems functioning

Note A: Power loss from drained battery.
Note B: Still camera power cord became disconnected.
Note C: Disconnected launcher circuitry, no speed displayed.
Note D: Structural test only, CULPIS not powered on.

the payload's structural durability. During normal operation the payload will receive power directly from the aircraft generator, and thus the power loss from the drained battery was determined to be an issue of no concern.

The zip-line test results validated the ability of the CULPIS ScanEagle payload to survive the launch acceleration forces, but also highlighted a few other issues that required attention. During one of the tests the still camera power cable became disconnected, identifying the need to securely adhere all wiring harness and instrument connections. Discussion also led to the realization that the payload power supply from the ScanEagle generator could potentially glitch and drop below the 12V operating voltage, which would terminate the functionality of the cameras for the remainder of the flight. Additionally, upon aircraft recovery with the tether-line capture method, the aircraft is immediately powered off, thus killing power to the payload. When this occurs the video camera is not properly cycled through its power-down routine and the video data file is not closed properly, leading to a corrupt file and loss of all video data.

To prevent these two power-failure situations from occurring, the primary UAS payload power supply (aircraft generator) and a 12V standby battery are passed through silicon diodes and then connected in parallel to create a switchover circuit. In this manner, if the primary power is interrupted, the payload will draw power from the standby battery for the time being. Finally, vibration-dampening clips will replace the standard connectors used to attach the payload bay to the fuselage, and a padding material will be placed between the payload bay and the fuselage bulkheads to dampen vibration in order to minimize image blur and long-term structural fatigue.

Appendix H

GPS Reference Station Positioning

The CASIE CU GPS reference station (RS), NYCU, and its environmental surroundings are shown in Figure H.1. The main visibility obstructions and multipath sources are large mountains on one side, and several buildings and a gravel roadway that saw limited traffic on the opposing side. Several methods for accurately positioning NYCU were examined, and the results of those tests are summarized in Table H.1 and Figure H.2. The best positioning results (lowest vertical and horizontal standard deviations) are obtained by carrier phase differential positioning with one RS using a 30 second measurement rate, and filtering the data based on the root sum of the position offsets squared (RRS, Equation H.1).

$$\boxed{RSS = \left[(E - E_{mean})^2 + (N - N_{mean})^2 + (V - V_{mean})^2\right]^{1/2}} \tag{H.1}$$

The final method used to position NYCU is outlined below, and the position variability is summarized by Table H.2 and Figure H.3. The same method was used to position the ILCU station, and similar positioning statistics were achieved.

Table H.1: The CASIE NYCU GPS positioning statistics for various processing methodologies. Precise point positioning (PPP) and carrier phase differential positioning (CDP) using various data rates and reference stations were analyzed. The best results are provided by 30 sec CDP with one RS.

dataset corresponding to Figure H.2	stdev E [cm]	stdev N [cm]	stdev V [cm]
PPP 30 sec, 0 RS (green)*	0.07	0.04	0.08
CDP 30 sec, 2 RS (blue)*	8.38	3.63	8.12
CDP 30 sec, 1 RS (red)	0.02	0.02	0.02
CDP 0.1 sec, 1 RS (black)	1.97	3.19	13.64
CDP 10 sec, 1 RS (cyan)	0.76	0.91	2.71

*horizontal (E and N) positions not shown in Figure H.2.

Figure H.1: The CASIE NYCU temporary GPS reference station environmental surroundings. The GPS station was located in the vicinity of large mountains, several buildings, and a gravel roadway that saw limited traffic.

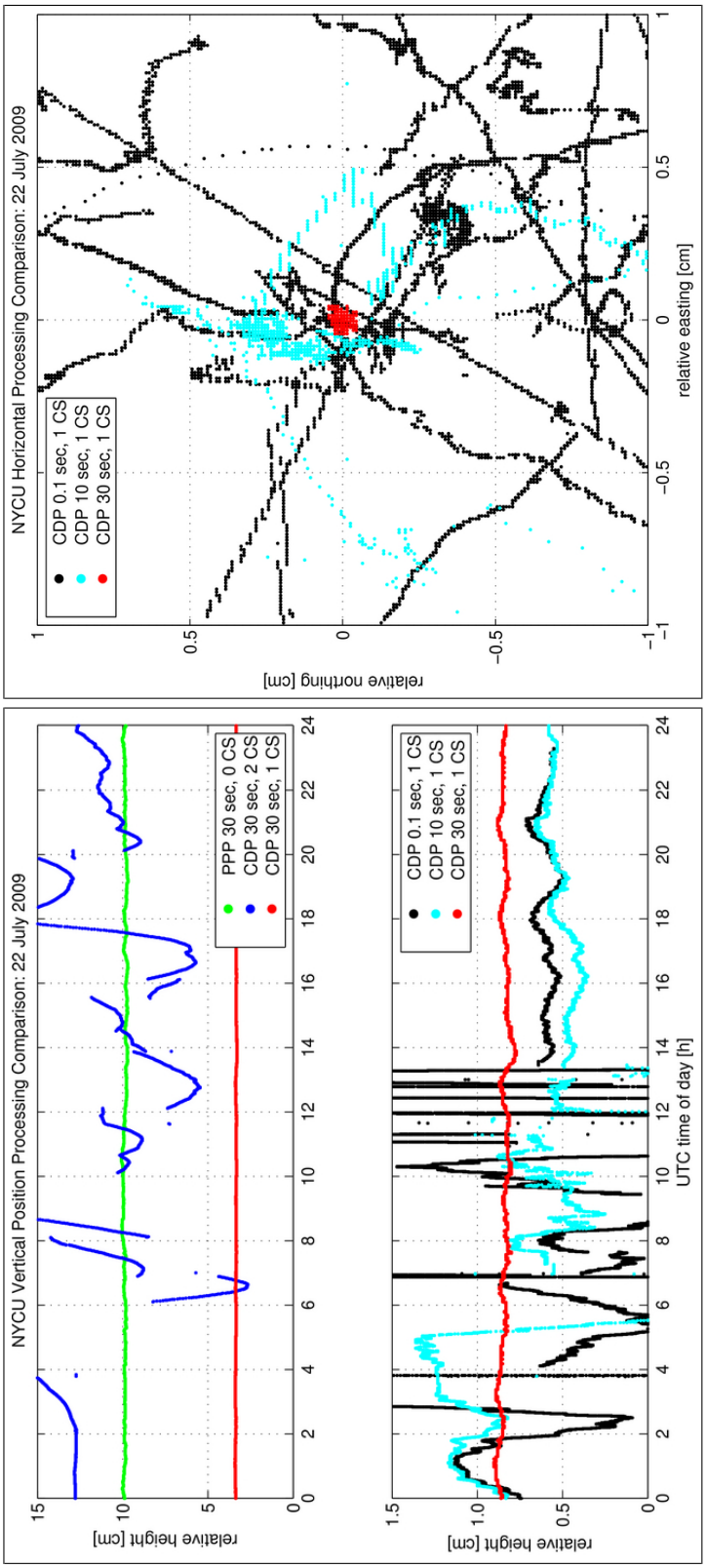

Figure H.2: The NYCU GPS reference station positioning methodology analysis figures. The left panel shows the relative height of the NYCU station over 24 hours for five different processing methods. The right panel shows the horizontal position of NYCU over 24 hours for the three CDP methods analyzed. Positioning using 30 sec CDP with one reference station exhibits the least variability, as indicated by Table H.1.

Table H.2: The CASIE NYCU GPS reference station final positioning statistics for 11-31 July 2009. The data retained after the first and second filters (shown in red) was used to compute the final position of the NYCU station.

dataset corresponding to Figure H.3	% of total data	stdev E [mm]	stdev N [mm]	stdev V [mm]
all data (black, cyan, red)	100	1.5	2.1	3.5
data retained after 1^{st} filter (cyan, red)	87	0.5	0.8	1.2
data retained after 2^{nd} filter (red)*	63	0.5	0.3	0.7

*Mean (Final) Position
latitude: 78.930852949 N
longitude: 11.853503732 E
WGS84 ellipsoidal height: 73.085 m

The Final method used to position the ILCU and NYCU GPS reference stations:

- Accumulate all data collected throughout deployment

  MUSCOX: 6-24 July 2008

  CASIE: 11-31 July 2009

- Subsample the data to a 30 second measuremnt rate
- Perform dual frequency, carrier phase, differential positioning using a single permanent reference station[1] (no tropospheric corrections)

  MUSCOX: KAGA - 49.4 km from ILCU

  CASIE: NYA1 - 292 km from NYCU

- Compute east (E), north (N), and vertical (V) offsets from the mean position
- Compute the 3D RSS, as shown by Equation H.1
- Remove data outside of 1 RSS value (filter 1)
- Compute new RSS
- Remove data outside of 1 RSS value (filter 2)
- Compute the mean of the remaining data

Both the MUSCOX and CASIE final CU reference station positions were computed using RSS method with very-short baseline dGPS data collected throughout the full deployment periods. To determine the relative quality of this method, the CU station positions were also computed using the JPL online APPS with data collected during the runway survey times specified in Table 5.4 on page 60. The positions, and their differences, derived using these two methods are shown in Table H.3. The position differences range between approximately 5 cm and 180 cm, and show better agreement for the MUSCOX data. Due to the considerably

[1] The permanent monument GPS data were obtained from UNAVCO.

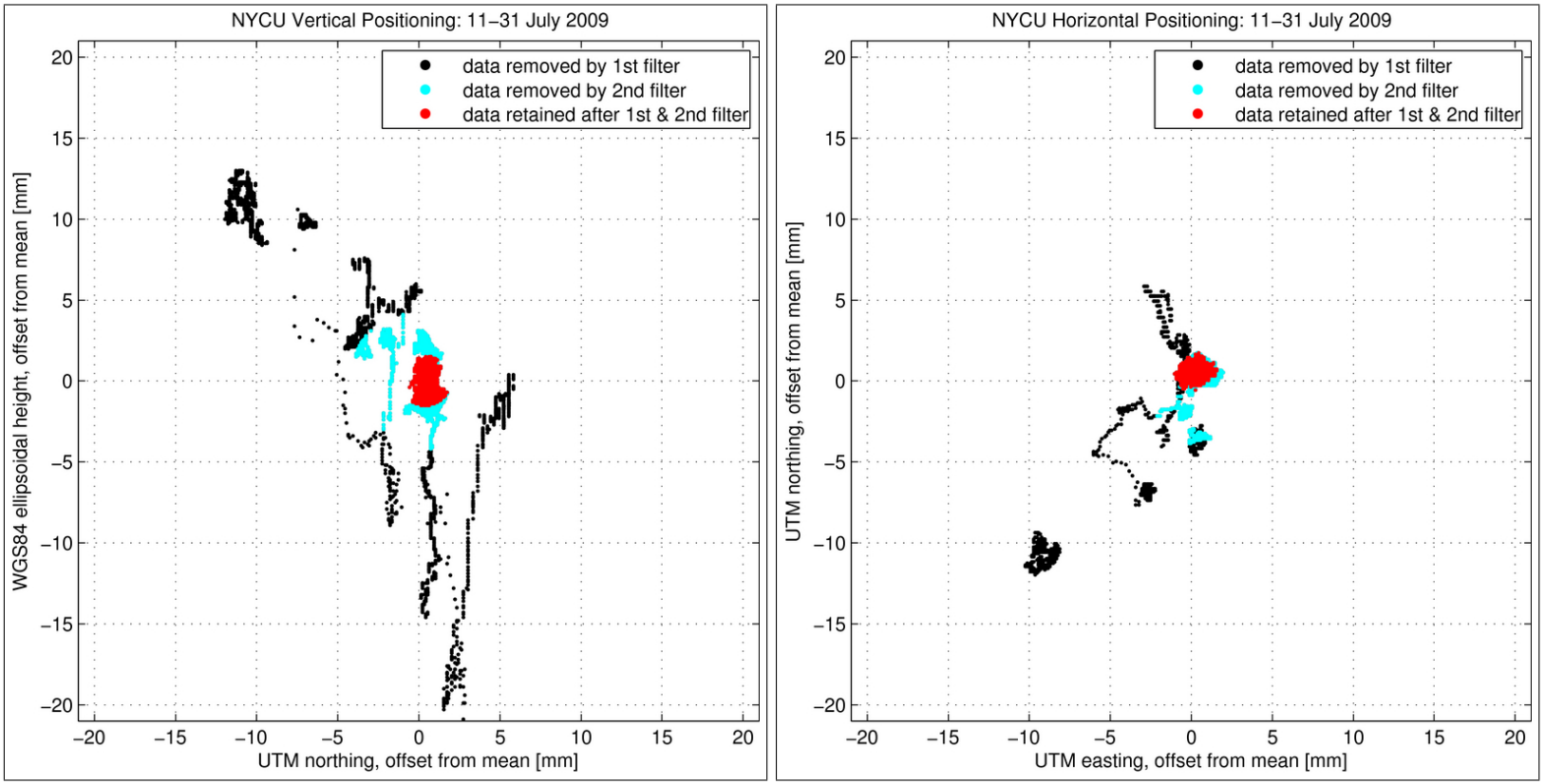

Figure H.3: The CASIE NYCU GPS reference station final vertical positioning for 11-31 July 2009. The data retained after the first and second filters (shown in red) were used to compute the final position of the NYCU station. The positioning statistics corresponding to these data are presented in Table H.2

Table H.3: CU reference station positioning comparison between the RSS and JPL online service processing results. Coordinates are reported in the ITRF05 reference frame.

station	direction	RSS method	JPL service	relative offset [cm]
ILCU	N	69° 14' 30.33413"	69° 14' 30.33593"	5.6
	E	-51° 03' 46.86773"	-51° 03' 46.88046"	13.9
	U	55.823 m	56.018 m	19.5
NYCU	N	78° 55' 51.07071"	78° 55' 51.08297"	37.9
	E	11° 51' 12.61335"	11° 51' 12.66181"	28.7
	U	73.102 m	71.302 m	180.0

longer data set used in the RSS computations versus the JPL computations (approximately 30 days of data versus 10 minutes of data), the RSS positions are considered to be more robust and were chosen as the final CU reference station positions used in all further dGPS processing of CULPIS data. Absolute error in the refrence station positions will translate directly to errors in the CULPIS dGPS positions; however, these absolute errors will not affect relative positions and the derived ice topography parameters.

Appendix I

GPS Fundamentals

The purpose of this appendix is to review GPS positioning fundamentals such that the reader is familiar with the basic methodology, terminology, and mathematics. This information is particularly relevant in the assessments of the CULPIS GPS error discussed in Section 5.3.3. The material and formulations presented here have been adapted from Blewitt[9] and Misra and Enge[90]. Readers are referred to those sources for a more comprehensive discussion.

GPS positioning is based on trilateration, which is the method of determining position by measuring distances to points at known coordinates. This is similar in concept to 2D triangulation, but is done in 3D space. Each GPS satellite transmits two encoded signal toward Earth, which consists of a carrier signal that is modulated with ranging codes and a navigation message. The two carrier signals, referred to as L1 and L2, are in the L-band, and have frequencies of:

$$\text{L1: } f_{L1} = 1575.42 \text{ MHZ}, \quad \text{and} \quad \text{L2: } f_{L2} = 1227.60 \text{ MHz}.$$

The L1 signal carries the C/A ranging code, an encrypted P(Y) ranging code, and the navigation message. The L2 signal carries only an encrypted P(Y) code. The decryption key for P(Y) codes is typically only available for military applications, and as such, these codes are not utilized by the general public, or within this research. The transmission time of the C/A code is encoded on the signal, and is based on an atomic clock onboard the satellite. The signal reception time is computed by the receiver, which typically use quartz-oscillator timing elements, and then the signal travel time (i.e. difference between transmit and receive times) can be used to calculate the range to the satellite. This range is referred to as pseudorange

because it includes clock errors (primarily receiver clock errors) and signal propagation errors, as discussed further below.

The navigation message contains, among other information, satellite atomic clock correction terms and orbital parameter terms, know as the broadcast ephemeris. These values are used in real-time by the receiver to correct the satellite clock error and to determine the (x, y, z) position of each satellite in the WGS84 earth-centered, earth-fixed (ECEF) coordinate frame. With the known reference positions of each satellite, the pseudoranges can then be used to trilaterate the receiver position and compute the clock bias using the formulations presented below. With four unknowns (receiver x,y,z and clock bias), four satellites must be visible to the receiver. It is important to note that improved, "precise" satellite clock corrections and orbit ephemerides are derived by institutions such as the International Global Navigation Satellite System (GNSS) Service (IGS) and the NASA JPL that are available at a somewhat delayed time for post-processing positioning. These precise ephemerides and clock corrections are implemented by the Waypoint software, and have been utilized in the processing of all GPS data collected as part of this research.

The pseudorange and carrier phase measurement models are shown as Equations I.1 & I.2. Each term is expressed in units of distance, typically meters, the superscript (k) indicates that the equation is formulated for all k number of visible satellites, and the subscripts ρ and ϕ indicate that these terms are frequency dependent and have differing behavior and magnitudes for the code and carrier measurements. The modeled pseudorange and carrier-range (the product $\lambda\phi$) are equal to the geometric range between the user's receiver and the satellite's transmitter, plus errors associated with signal timing and propagation through the space, atmosphere, and local environments. Carrier phase ranging is similar in theory to code ranging, but rather than tracking the C/A code, the phase of the received signal is tracked. Carrier tracking yields considerably higher ranging precision since the phase provides a much finner tracking scale than the code (L1 carrier wavelength of ~19 cm versus the C/A code chip length of 300 m). However, an increased complication arises because the phase measurement is ambiguous. The total number of cycles the wave has traveled before before being received is not known, which introduces an additional phase ambiguity variable, N, that must be solved for in Equation I.2.

$$\rho^{(k)} = r^{(k)} + c\left(\delta t_u - \delta t^{(k)}\right) + I_\rho^{(k)} + T_\rho^{(k)} + M_\rho^{(k)} + \varepsilon_\rho^{(k)} \tag{I.1}$$

$$\lambda\phi^{(k)} = r^{(k)} + c\left(\delta t_u - \delta t^{(k)}\right) - I_\phi^{(k)} + T_\phi^{(k)} + M_\phi^{(k)} + \lambda N^{(k)} + \varepsilon_\phi^{(k)} \tag{I.2}$$

where...

$\rho^{(k)}$ = pseudorange

λ = carrier wavelength

ϕ = carrier phase

$\lambda\phi$ = carrier-range

k = satellite ID

r = geometric range

c = free space light speed

δt_u = user receiver clock error

$\delta t^{(k)}$ = satellite clock error

I = ionosphere error

T = troposphere error

M = multipath error

N = carrier phase ambiguity

ε = unmodeled error

Signal timing errors arise from bias and drift of the satellite and receiver clocks relative to truth Coordinated Universal Time (UTC) time. The atomic clocks onboard each GPS satellite are quite stable and their behavior is well modeled; however, inexpensive quartz-oscillators typically used for receiver timing are relatively unstable, and thus dominate the clock error term.

Because the GPS signal does not travel through free space, transmission errors are introduced as the signal refracts through the ionosphere and troposphere. For GPS frequencies, the dispersive characteristics

of the ionosphere lead to a phenomenon referred to as code-carrier divergence in which the modulation code function is delayed while the carrier phase is advanced by an equal distance. The magnitude of the delay/advance, described by Equation I.3, is proportional to the ionosphere total electron content (TEC) along the signal path and, is also dependent upon the signal frequency. One TEC unit is equivalent to ∼16 cm of path delay. Total ionospheric path delay errors can range from centimeters to tens of meters, and are strongly dependent upon the ionospheric conditions.

$$I_\rho = \frac{40.3 \cdot TEC}{f^2} \tag{I.3}$$

$$= -I_\phi$$

where...

TEC = total electron content

f = carrier frequency

In practice, TEC can be estimated using ionospheric numerical model assimilations, or more accurately, the dispersive nature of the ionosphere can be exploited by using dual-frequency observations to compute the code delay and carrier advance, as shown in Equations I.4 and I.5. In this study, neither of these methods are applied because the Waypoint software was unable to ingest TEC data files, and single frequency receivers were used during field operations. However, this research does employ differential GPS, which, as discussed toward the end of this appendix, is another processing technique that can remove timing, orbit, and propagation errors common to multiple receivers. The primary limitation to this method is that as the distance increases between the various receivers used for differential positioning, the signal errors afflicting the different receiver sites becomes less similar, and thus are not fully removed by the differencing technique. As such, ranging errors stemming from the signal refraction through the ionosphere are not fully accounted for and will introduce error to the UAS GPS position, and subsequently the derived ice elevations.

$$P3 = a \cdot P1 - b \cdot P2 \tag{I.4}$$

$$L3 = a \cdot L1 - b \cdot L2 \tag{I.5}$$

where...

$P1$ = pseudorange on carrier 1

$P2$ = pseudorange on carrier 2

$P3$ = ionosphere-free pseudorange

$L1$ = carrier-range on carrier 1

$L2$ = carrier-range on carrier 2

$L3$ = ionosphere-free carrier-range

$$a = \frac{f_{L1}^2}{f_{L1}^2 - f_{L2}^2}$$

$$b = \frac{f_{L2}^2}{f_{L1}^2 - f_{L2}^2}$$

The troposphere is non-dispersive at the frequencies utilized by GPS, and as such, dual frequency measurements cannot be leveraged to estimate tropospheric error; it can only be modeled. The signal delay through the troposphere is dependent upon the air density along the transmission path, which can be estimated using formulations based on the partial pressure of the dry and wet (i.e. water vapor) atmospheric gas constituents, and the air temperature. Approximately 90% of the tropospheric delay is due to the dry atmosphere, which is fortunate as it is more predictable than the water vapor content. Tropospheric errors typically range from 2.3 - 2.6 meters at sea level, and down to around 2 meters at higher altitudes, such as in Boulder, Colorado. The Saastamoinen model is one commonly used algorithm for estimating the tropospheric delay. Unfortunately, the Waypoint software does not apply this, or any other tropospheric correction methodology.

Ranging errors are also introduced by multipath, which refers to the phenomenon of a signal reaching an antenna via two or more paths. As the signal travels through a user's local environment it will reflect off conductive surfaces (e.g. metal buildings, cars). The reflected signals will travel a longer distance than the direct signal, and thus are received at delayed times. The subsequent code and carrier phase measurements are for the sum of the received signal, and the resulting measurement error depends on the strength of the reflected signal and the delay between the direct and reflected signals. Typical multipath error in pseudorange measurements varies from 1-5 m, and errors in the phase measurements are typically two orders of magnitude

smaller (1-5 cm). Additional errors also exist which require further estimation, or are simply ignored and left unaccounted for. These include, but are not limited to, receiver noise, solid earth tides, and the remaining orbit, timing, and propagation errors which are not fully described by their models.

For further formulation, focus will be directed to the pseudorange model and the associated code positioning methodology. The carrier positioning mathematical formulation is essentially the same, but includes terms to account for the phase ambiguities. The modeled pseudorange equation (I.1) can be simplified by combining the user and satellite clock error to form a combined clock bias term, and by expressing the signal propagation error as a single accumulated error term, as shown in Equation I.6. The satellite positions are estimated with centimeter accuracy using the precise orbital ephemeris. If the error term ($\tilde{\varepsilon}_{\rho}^{(k)}$) is ignored, it is now clear that four variables must be solved for, the user's position (x_u, y_u, z_u), and the clock bias (δt).

$$\rho^{(k)} = r^{(k)} + c \cdot \delta t + \tilde{\varepsilon}_{\rho}^{(k)} \tag{I.6}$$

where...

$$r^{(k)} = \sqrt{\left(x^{(k)} - x_u\right)^2 + \left(y^{(k)} - y_u\right)^2 + \left(z^{(k)} - z_u\right)^2} \tag{I.7}$$

(x, y, z) = user & satellite ECEF coordinates

δt = combined clock bias

$\tilde{\varepsilon}_{\rho}$ = accumulated pseudorange error

With pseudorange measurements from four or more satellites it is possible to linearize the system of equations about an approximate user position, $\mathbf{x}_o$, using a Taylor series expansion, and then solve iteratively using the Newton-Raphson method. This formulation is outlined in Equations I.8-I.14. The least squares solution (Equation I.13) provides the position and time offsets from the initial guess ($\mathbf{x}_o$), and is iterated upon until the position offset elements of $\mathbf{x}$, $(\Delta x, \Delta y, \Delta z)$, are sufficiently small (e.g. < 1cm).

$$\Delta\rho^{(k)} = \rho_{observed}^{(k)} - \rho_{modeled}^{(k)} \tag{I.8}$$

$$= \begin{pmatrix} \frac{\partial \rho}{\partial x} & \frac{\partial \rho}{\partial y} & \frac{\partial \rho}{\partial z} & \frac{\partial \rho}{\partial t} \end{pmatrix} \begin{pmatrix} \Delta x \\ \Delta y \\ \Delta z \\ \Delta t \end{pmatrix} + \tilde{\varepsilon}_{\rho}^{(k)} \tag{I.9}$$

expanded to include all visible satellites:

$$\begin{pmatrix} \Delta\rho^1 \\ \Delta\rho^2 \\ \Delta\rho^3 \\ \vdots \\ \Delta\rho^{(k)} \end{pmatrix} = \begin{pmatrix} \frac{\partial \rho^1}{\partial x} & \frac{\partial \rho^1}{\partial y} & \frac{\partial \rho^1}{\partial z} & \frac{\partial \rho^1}{\partial t} \\ \frac{\partial \rho^2}{\partial x} & \frac{\partial \rho^2}{\partial y} & \frac{\partial \rho^2}{\partial z} & \frac{\partial \rho^2}{\partial t} \\ \frac{\partial \rho^3}{\partial x} & \frac{\partial \rho^3}{\partial y} & \frac{\partial \rho^3}{\partial z} & \frac{\partial \rho^3}{\partial t} \\ \vdots & \vdots & \vdots & \vdots \\ \frac{\partial \rho^{(k)}}{\partial x} & \frac{\partial \rho^{(k)}}{\partial y} & \frac{\partial \rho^{(k)}}{\partial z} & \frac{\partial \rho^{(k)}}{\partial t} \end{pmatrix} \begin{pmatrix} \Delta x \\ \Delta y \\ \Delta z \\ \Delta t \end{pmatrix} + \begin{pmatrix} \tilde{\varepsilon}_{\rho}^{1} \\ \tilde{\varepsilon}_{\rho}^{2} \\ \tilde{\varepsilon}_{\rho}^{3} \\ \vdots \\ \tilde{\varepsilon}_{\rho}^{(k)} \end{pmatrix} \tag{I.10}$$

in matrix notation:

$$\mathbf{b} = \mathbf{A}\mathbf{x} + \boldsymbol{\varepsilon} \tag{I.11}$$

where the design matrix...

$$\mathbf{A} = \begin{pmatrix} \frac{x_o - x^1}{r^1} & \frac{y_o - y^1}{r^1} & \frac{z_o - z^1}{r^1} & 1 \\ \frac{x_o - x^2}{r^2} & \frac{y_o - y^2}{r^2} & \frac{z_o - z^2}{r^2} & 1 \\ \frac{x_o - x^3}{r^3} & \frac{y_o - y^3}{r^3} & \frac{z_o - z^3}{r^3} & 1 \\ \vdots & \vdots & \vdots & \vdots \\ \frac{x_o - x^{(k)}}{r^{(k)}} & \frac{y_o - y^{(k)}}{r^{(k)}} & \frac{z_o - z^{(k)}}{r^{(k)}} & 1 \end{pmatrix} \tag{I.12}$$

and the solution is converged upon by iterating through...

$$\boxed{\mathbf{x} = \left(\mathbf{A}^T\mathbf{A}\right)^{-1}\mathbf{A}^T\mathbf{b}} \tag{I.13}$$

$$\boxed{\hat{\mathbf{x}} = \mathbf{x}_o + \mathbf{x}} \tag{I.14}$$

where...

$\mathbf{x}_o$ = approximate position and clock bias from initial guess or previous iteration

$\mathbf{x}$ = updated position and clock bias offsets from $\mathbf{x}_o$

$\hat{\mathbf{x}}$ = updated/final position and clock bias

The covariance matrix, $\mathbf{C}_l$, shown in Equation I.16, represents the visible satellite geometry and the expected measurement variance. The *a priori* covariance weight, σ_a, is somewhat subjective, but is typically set to the expected GPS positioning error standard deviation (e.g. code: 1 m, carrier: 1 cm are often used for simplicity). Various terms in the covariance matrix are used as metrics of the solution quality.

$$\mathbf{C} = \left(\mathbf{A}^T\mathbf{A}\right)^{-1} = \sigma_a^2 \begin{pmatrix} \sigma_x^2 & \sigma_{xy} & \sigma_{xz} & \sigma_{xt} \\ \sigma_{yx} & \sigma_y^2 & \sigma_{yz} & \sigma_{yt} \\ \sigma_{zx} & \sigma_{zy} & \sigma_z^2 & \sigma_{zt} \\ \sigma_{tx} & \sigma_{ty} & \sigma_{tz} & \sigma_t^2 \end{pmatrix} \tag{I.15}$$

and rotated to the local ENV coordinate frame...

$$\mathbf{C}_l = \mathbf{R}_l\mathbf{C}\mathbf{R}_l^T = \sigma_a^2 \begin{pmatrix} \sigma_e^2 & \sigma_{en} & \sigma_{ev} & \sigma_{et} \\ \sigma_{ne} & \sigma_n^2 & \sigma_{nv} & \sigma_{nt} \\ \sigma_{ve} & \sigma_{vn} & \sigma_v^2 & \sigma_{vt} \\ \sigma_{te} & \sigma_{tn} & \sigma_{tv} & \sigma_t^2 \end{pmatrix} \tag{I.16}$$

where...

σ_a = *a priori* covariance weight

$\mathbf{R}_l$ = rotation matrix from ECEF to ENV frames

The height standard deviation ($\sigma_a \cdot \sigma_v$), RMS, PDOP, VDOP, and horizontal DOP (HDOP) are solution quality metrics derived from the covariance matrix.

$$\text{height standard deviation} = \sigma_a \cdot \sigma_v \tag{I.17}$$

$$\text{RMS} = \sqrt{\sigma_x^2 + \sigma_y^2 + \sigma_z^2} \tag{I.18}$$

$$\text{VDOP} = \sigma_v \tag{I.19}$$

$$\text{HDOP} = \sqrt{\sigma_n^2 + \sigma_e^2} \tag{I.20}$$

$$\text{PDOP} = \sqrt{\sigma_n^2 + \sigma_e^2 + \sigma_v^2} \tag{I.21}$$

As previously mentioned, the carrier phase least-squares solution formulation is similar to that for pseudorange observations presented above; however, the design matrix, $\mathbf{A}$, contains terms for the phase ambi-

guity, N, of each visible satellite. The KAR method for determining the phase ambiguity is relatively complex and is beyond the scope of this review. The NovAtel Waypoint software implements proprietary KAR techniques, but in general, KAR is accomplished through differential GPS by forming "single differences" of the measurement equation (I.2) between multiple receivers and one satellite, and "double differences" between multiple receivers and multiple satellites in order to eliminate satellite clock biases and receiver clock biases. Following the removal of these biases, a linear system of equations can be formed and the ambiguities can be solved using least-squares.

It is important to note that KAR methodology requires changes in satellite geometry to initially lock on and track the carrier phase, and then relies on continual tracking of the carrier phase over time [90]. This has a few implications. First of all, satellite geometry changes fairly slowly relative to a static position on the ground, so it may take tens of minutes to initially resolve the phase [16, 17]. In kinematic applications, such as UAS flight, the motion of the receiver will change the geometry sufficiently such that this initialization time is considerably less. This occurrence is evident in plots of the ambiguity drift (e.g. Figure 5.7 on page 63), which show a high drift at the beginning and end of the time period (due to forward and reverse processing) when the KAR algorithm is initially resolving the phase. However, these periods of relatively high drift do not last longer than several seconds. Furthermore, phase cycle-slips and satellite loss-of-lock will inhibit the KAR solution and will require reinitialization of the algorithm [16].

Appendix J

Ancillary GPS Error Data

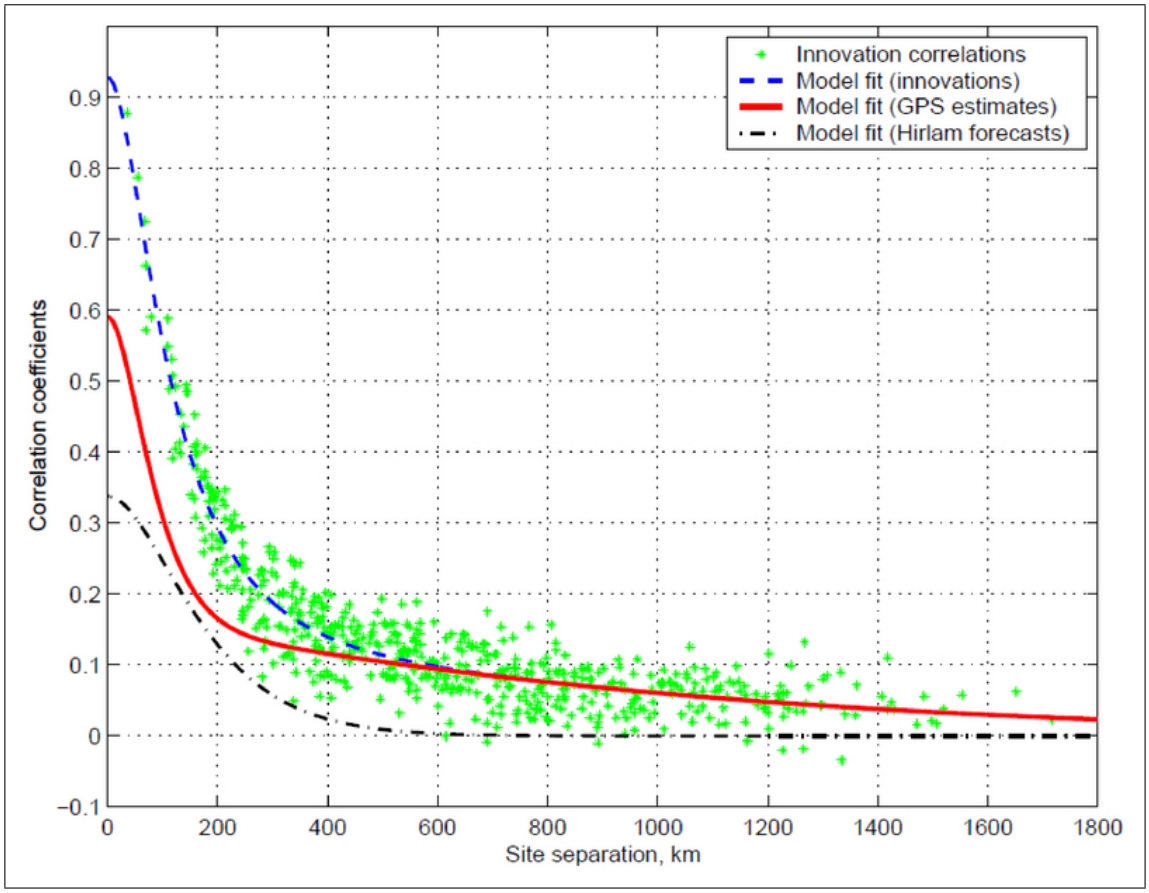

Figure J.1: The GPS tropospheric zenith delay spatial decorrelation. This figure was taken from Stoew and Elgered[110] and shows the horizontal correlations of the zenith tropospheric delay for a one year period for data collected throughout Sweden and Finland. The innovation correlations (green asterisks) are derived from radiosonde observations of tropospheric zenith delay, and three curves are various model estimates. This illustrates that the troposphere decorrelation scale is on the order of 200 km.

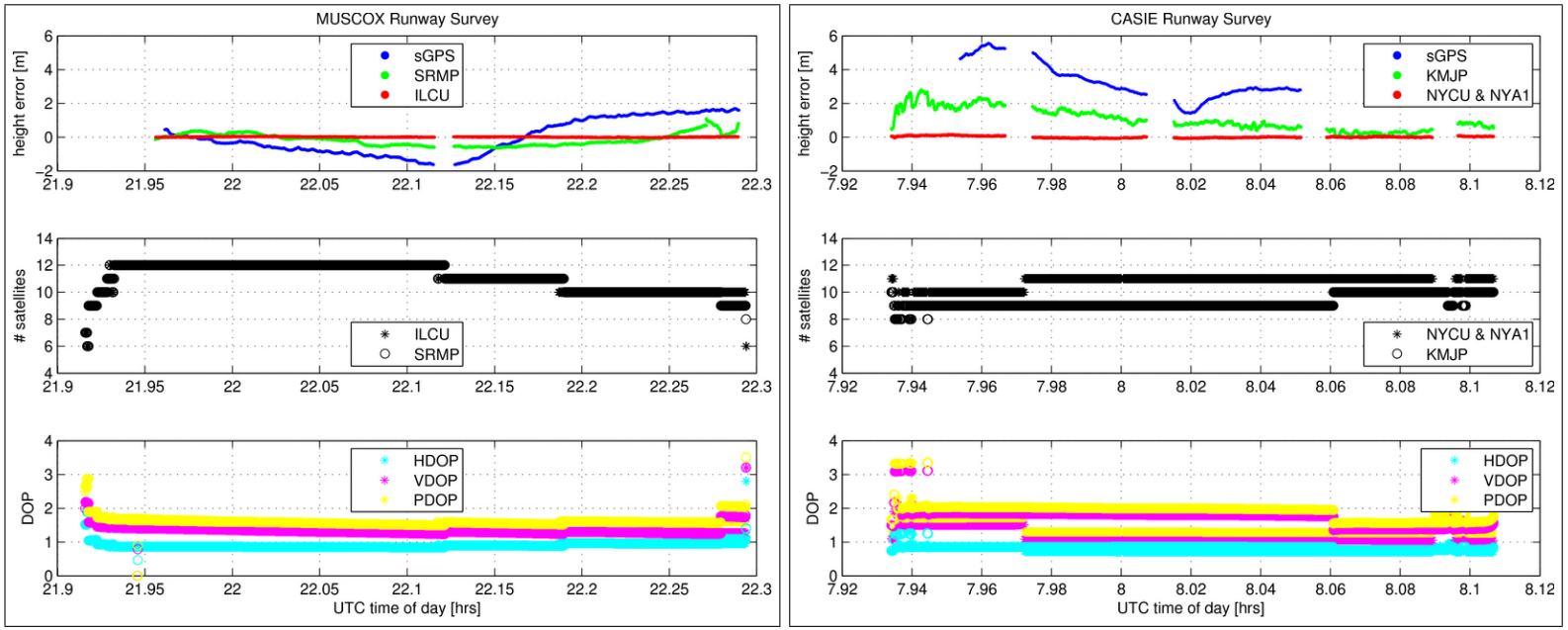

Figure J.2: MUSCOX and CASIE runway survey GPS visibility metrics. The top plots show the runway survey error relative to the "truth" reference surface for the real-time pseudorange code GPS solutions (sGPS), the long-baseline dGPS solutions (SRMP and KMJP), and the short-baseline dGPS solutions (ILCU and NYCU & NYA1). The middle plots show the number of visible satellites used to compute the solutions, and the bottom plot shows the horizontal, vertical, and position dilution of precision (HDOP, VDOP, PDOP) values over the survey time period. The number of satellites and DOP values are relatively constant over the survey period, which indicates the satellite geometry does not change significantly, and therefore will not introduce substantial error variability to the position solutions.

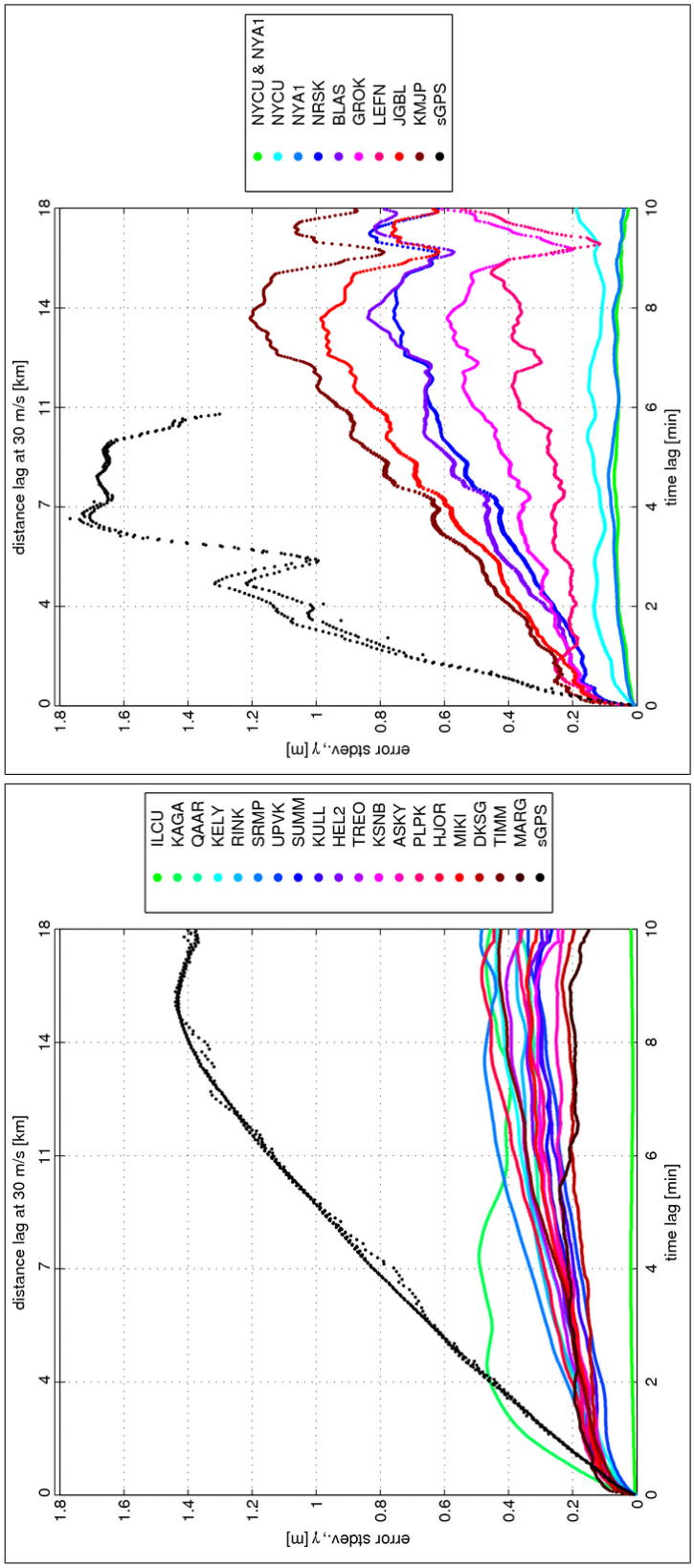

Figure J.3: MUSCOX (left panel) and CASIE (right panel) runway survey elevation error variograms for sGPS and dGPS positioning relative to the reference stations shown in Figure 5.6. The variogram formulation is presented in Equation 5.5 on page 69. The top x-axis show the equivalent distance lag assuming a flight speed of 30 m/s.

Appendix K

Ancillary Runway Profiling Data

An initial test carried out to gauge the capability of the CULPIS was to park a van in the middle of the Ilulissat runway and then fly over it with the Manta UAS to simply determine if it was possible to resolve the van profile. As illustrated by Figure K.1, it was indeed possible to resolve the van profile from CULPIS measurements. The data indicate a maximum van height of ∼5 ft, which is somewhat low relative to the on-site measurement of ∼6.5m ft. These data were not differentially positioned or corrected for off-nadir pointing, which introduce slight errors. The larger source of error likely results from the integrated spatial sampling that occurs as the ULS footprint passes over the surface. Overall, this simple test illustrates the basic ability of CULPIS to resolve meter-level surface variability.

The GPS positioning metrics as reported by the Waypoint software for the runway profile flights are presented in Figure K.2. Spikes in the ambiguity drift show times at which lock on the carrier ambiguity is lost and must be recovered. These times correspond to degraded positioning performance, as indicated by elevated separation and standard deviation statistics.

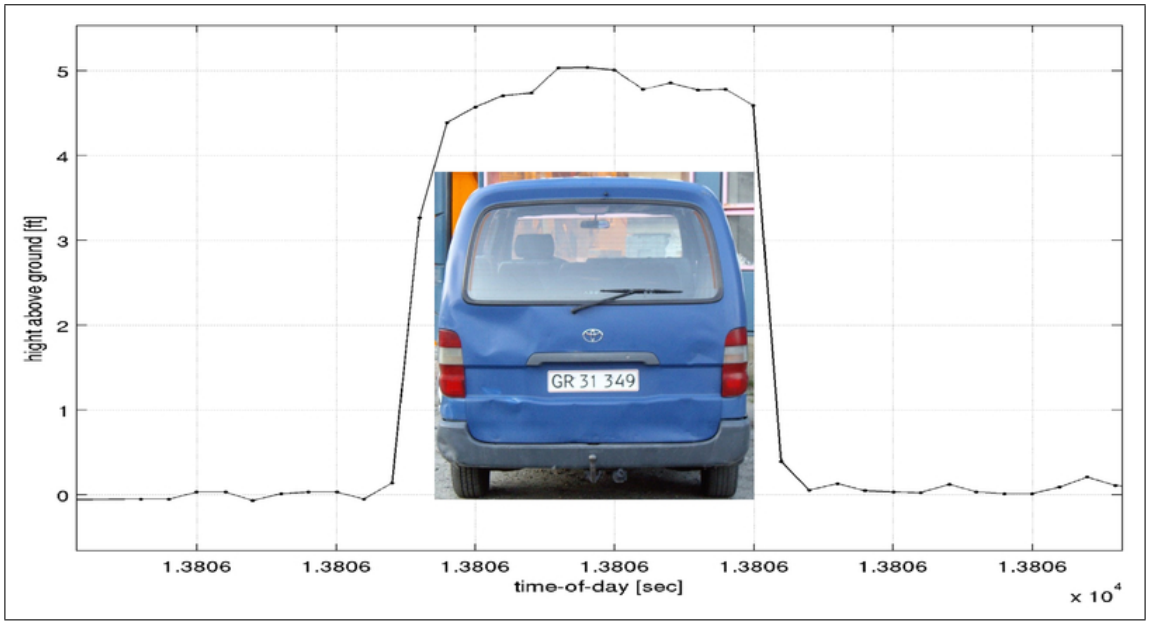

Figure K.1: A CULPIS-derived profile of the Hotel Arctic van. This data was collected during MUSCOX while the van was parked on the Ilulissat airport runway and the Manta UAS flew overhead. The GPS data have not been differentially positioned and the aircraft attitude data have not been used to geolocate the laser range measurements. This is an initial example that illustrates the ability of the CULPIS to resolve relatively fine (meter-level) surface variability.

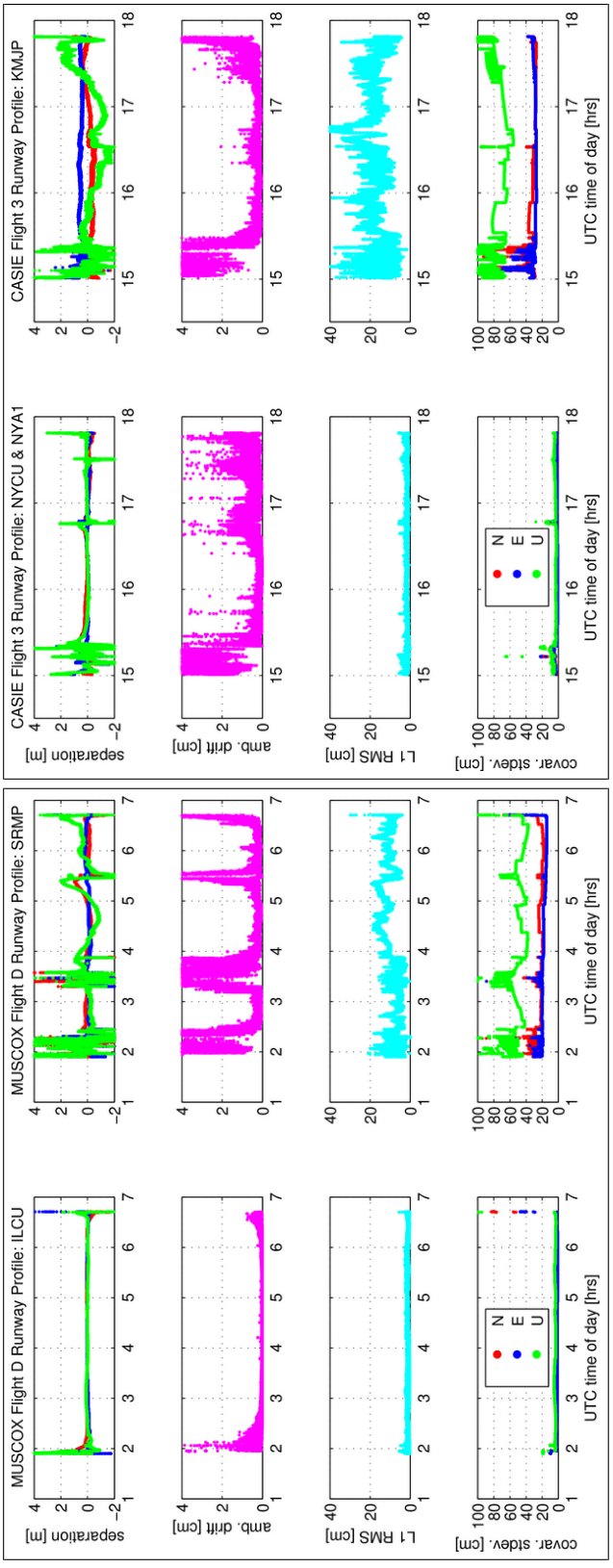

Figure K.2: The MUSCOX (left panel) and CASIE (right panel) runway profile NovAtel Waypoint solution quality metrics for short-distance (left columns: ILCU and NYCU & NYA1) and long-distance (right-columns: SRMP and KMJP) dGPS post-processing. Separation is the distance between the position solutions processed in the forward and reverse time directions. The ambiguity drift is the drift of the KAR float solution. The L1 RMS and covariance standard deviations are derived from the covariance matrix. The metrics presented here are described further in Appendix I.

Appendix L

Ancillary MUSCOX Ice Sheet Observations

To illustrate the capabilities of CULPIS for ice sheet topography mapping, exemplary MUSCOX data are presented. The CULPIS elevation data that were collected in the study region were spatially interpolated using ordinary kriging to generate a fine-resolution (500 m grid) surface DEM, shown in Figure L.1, which depicts the topography in the vicinity of the three melt lakes, labeled (1), (2), and (3). It should be noted that Lake 1 drained completely around 15 July 2008, prior to the MUSCOX UAS flights. Notice that the DEM depicts the location, shape, and size of the three lakes quite well amongst the undulating surface, as shown by the elevation contours at 960, 983, and 1205 m. The DEM identifies a depressed region to the south of Lake 1, which has potential to be the drainage basin. In addition to the fine-scale detail, the ice sheet is shown to have a broad ∼1% E-W downward slope within the 22x6 km observation region.

Select examples of different ice types that were identified in CULPIS still imagery collected during MUSCOX are shown in Figure L.2. Images (a)-(c) are still camera photos and image (d) is a frame from the video camera. Image (a) depicts the outlet glacier calving front and heavily crevassed central glacial stream. Image (b) shows a crevassed region of the outlet glacier further inland with a more linear, striated surface structure. Image (c) shows the relatively smooth inland ice and the edge of a melt lake, and image (d) shows the region of shattered and broken ice chunks in the location of drained lake 1. This ice was likely broken during the kinematic ice shift that caused the lake to drain. The CULPIS observations presented here depict the capabilities of CULPIS for mapping and imaging ice sheet surface topography with fine-resolution when flown on UAS.

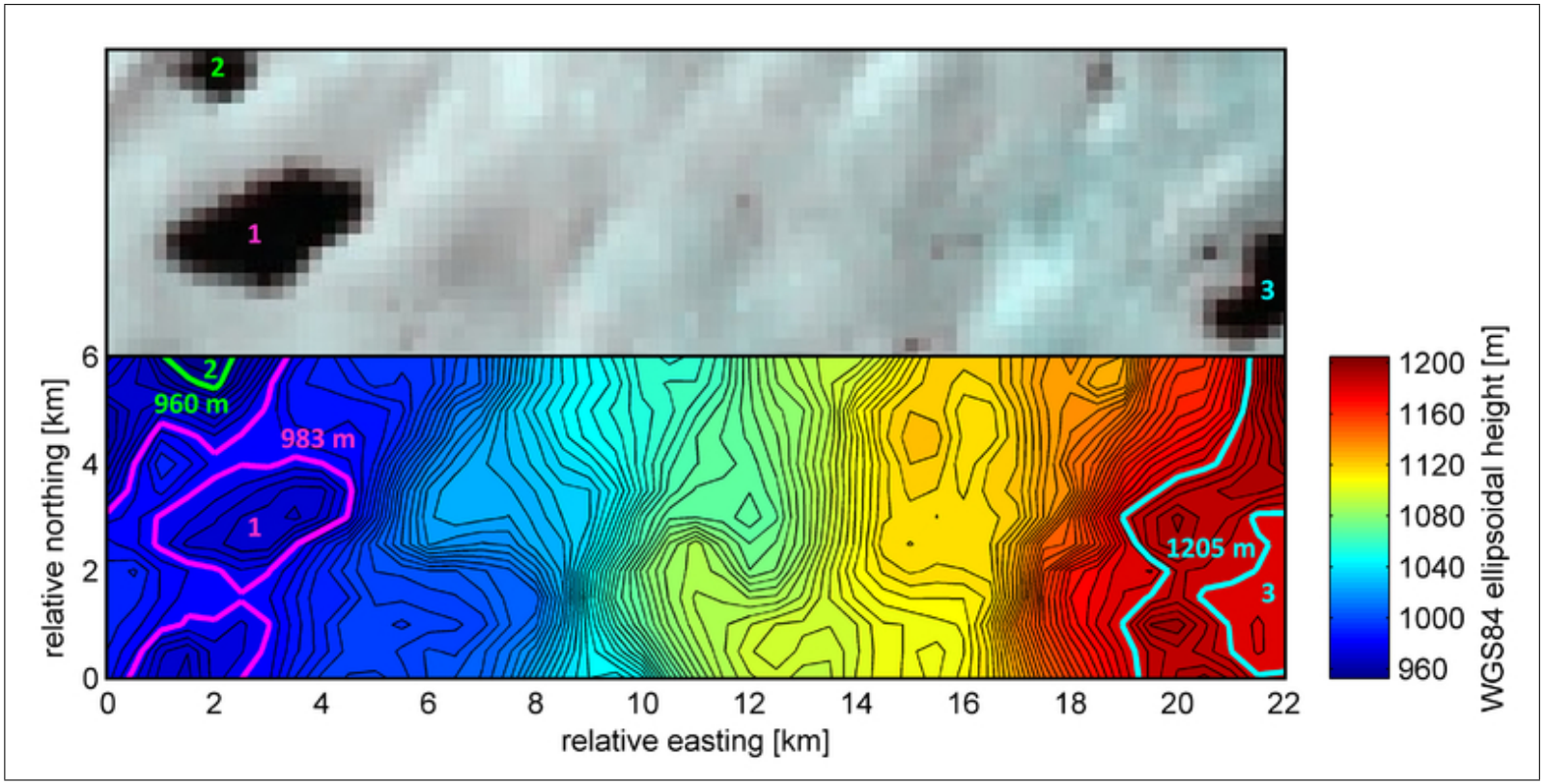

Figure L.1: A DEM generated by ordinary kriging of CULPIS data collected during MUSCOX from ∼200 m AGL. The top image is a 250 m pixel-size MODIS scene from 8 July 2008 which shows three melt lakes. The DEM shown below the image clearly depicts the shape and location of the lakes by the contours drawn at 960 m, 983 m, and 1205 m. Melt lake 1 drained after the satellite image was acquired and before the CULPIS data were collected. The depressed region to the south of lake 1 is potentially the drainage basin, which may have opened during a kinematic shift of the ice sheet, causing the lake to drain. See Figure L.2(d) for an image captured in this vicinity.

Figure L.2: Examples of four Greenland ice sheet surface structures captured in CULPIS still and video imagery collected during MUSCOX: (a) The outlet glacier calving front and heavily crevassed central glacial channel. (b) A strained and crevassed region of the outlet glacier central channel further upstream. (c) The relatively smooth inland ice and the edge of melt lake 3, as labeled in Figure L.1. (d) A region of broken ice chunks in the location of drained melt lake 1, as labeled in Figure L.1, which were likely created during a kinematic ice shift that caused the lake to drain.

Appendix M

Ancillary CASIE Sea Ice Observations

As a means to verify the ridge heights measured by the CULPIS altimetry data, and to demonstrate an additional method for computing ridge heights, a CULPIS still photo was used to compute the height of ridge features based on the sun elevation angle and the shadow lengths. The still photo and the four ridge features that were examined are shown in Figure M.1. The red dots show the approximate locations of the ridge peaks and shadows, and the black dot shows the level-ice reference surface height. These features are part of the same ridge complex shown in Figure 6.2 on page 100. The shadow associated with ridge feature 4 falls on noticeably elevated ground, such that the calculated height is likely smaller than the true peak height relative to the base of the ridge (indicated by the black dot). Ridge heights are computed from their shadow lengths and the solar elevation angle[1] using Equation M.1.

$$\boxed{H_r = d \cdot x \cdot \tan(\theta)} \tag{M.1}$$

where...

H_r = ridge height

d = ridge feature and corresponding shadow feature pixel separation

x = pixel size = $H_a \cdot 2.85e^{-4}$ (derivation not shown)

H_a = aircraft altitude AGL

θ = solar elevation angle[1]

[1] The solar elevation angle was acquired from the NOAA ESRL Solar Position Calculator online service.

The CULPIS still photos from a subset region of Figure 6.1 shown on page 99 were used to classify the surface using in-house thresholding methods developed by Dr. James Maslanik. Panel (a) of Figure M.2 is the true-color photo mosaic, and panel (b) shows the classified surface types, and illustrates the potential for inexpensive UAS camera systems to provide fine-resolution classification maps. The surface type areal coverage corresponding to Figure M.2 are presented in Table M.1.

With coincident ground coverage provided throughout CASIE by the CULPIS video data and microASAR imagery, it is possible to identify numerous sea ice types, or ice provinces, based on their differing surface structures. These unique features are representative of the environmental conditions and forces that the ice has experienced throughout its life history. As such, the visual appearance of the ice is quite beneficial for inferring its age, type, and discerning characteristics. Select examples of sea ice provinces identified in CASIE video and microASAR data are presented in Figures M.8 & M.9. With these complimentary datasets it possible to characterize the surface topography, roughness, and backscatter, along with the fraction of open water, melt ponds, ridges, and smooth ice, all of which are fundamental indicators of the ice type, age, and geophysical evolution.

The left image of Figure M.8 shows broken angular ice near the edge of the ice pack. It is likely that ocean surface waves propagating from the open ocean into the ice pack have fractured the ice. The larger smooth ice pieces have low microwave return and the smaller chunks of floating ice have a high return. The image on right shows a curvilinear feature that appears to be a lead that had previously frozen over and is now melting. The left image of Figure M.9 shows a lead between two large ice floes that is filled with smaller floes and jagged brash ice. The sharp edges of the brash ice suggest that the ice was recently fractured. The microwave backscatter is considerably higher from the brash ice that it is from the ice floes. The right image shows a heavily flooded region of ice adjacent to a meandering ridge. A considerable amount of snow has accumulated along the ridge in the form of snow drifts. The drifts are relatively smooth and have low backscatter, whereas the flooded ice has high backscatter. A final example of coincident microASAR and video imagery is shown in Figure M.10.

Figure M.1: Sea ice ridge heights calculated from the length of shadows in a photograph collected during CASIE. This ridge is part of the same ridge complex presented in Figure 6.2 on page 100. The ridge height calculation is described by Equation M.1. This image was collected from 200 m AGL at 15:26:43 UTC, and is located at 80°17'6" N, 4°27'57" E. Based on this time and location, the solar elevation angle, θ, was determined to be 24.98°. The numbered ridge features were found to have the following heights: (1) 1.01 m, (2) 0.69 m, (3) 1.57 m, (4) 1.06 m. The black dot is located at a point that appears to represent the nominal ice surface elevation.

Table M.1: Statistics for the surface classification of the CASIE still photograph presented in Figure M.2. This analysis was performed by Dr. James Maslanik.

surface class	areal coverage
pond fraction (blue)	16% of ice cover
rough ice fraction (red)	7% of ice cover
smooth ice fraction (green)	77% of ice cover
total ice fraction (blue, red, and green)	86% of total area
open-water fraction (black)	14% of total area

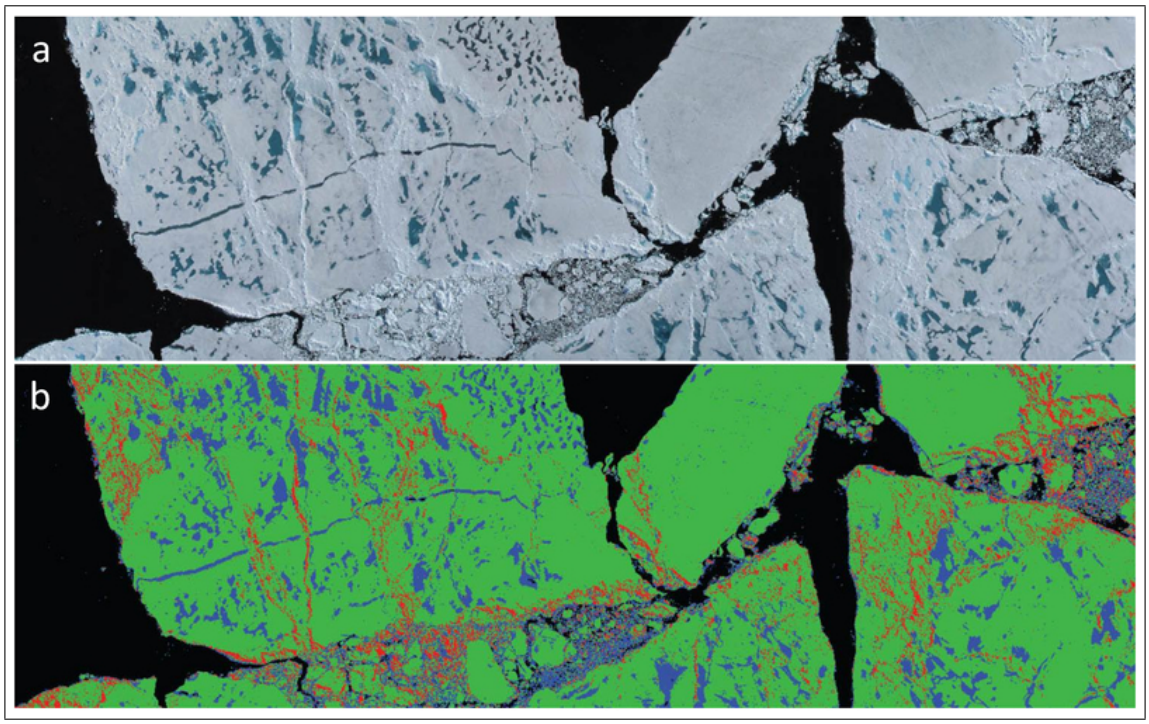

Figure M.2: A surface classification performed using a still photograph collected during CASIE: (a) True-color photo mosaic, which is a subset of the region shown in Figure 6.1 on page 99. (b) Surface classification of ponds and flooded ice (blue), rough and ridged ice (red), smooth ice (green), and open-water (black). The classification statistics corresponding to these images are presented in Table M.1. This analysis was performed by Dr. James Maslanik.

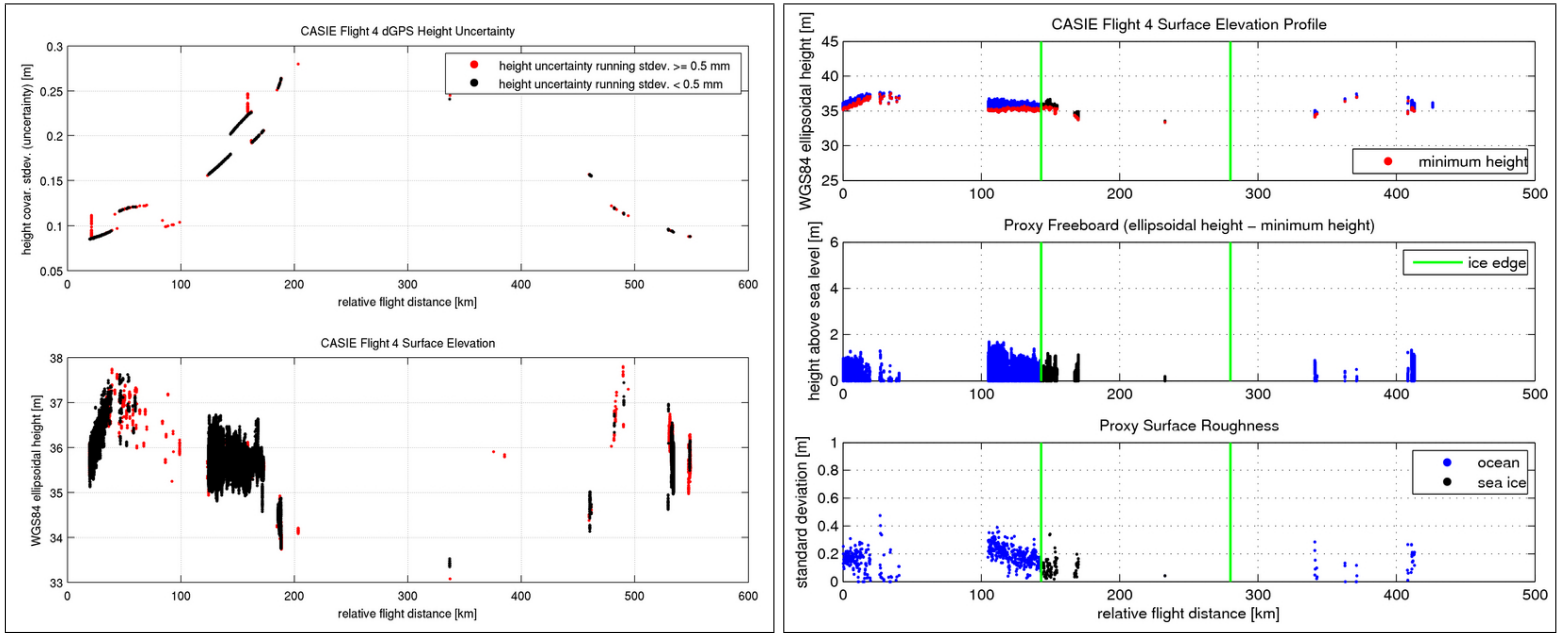

Figure M.3: The CASIE flight 4 dGPS height uncertainty and surface elevation profile are shown in the left panel. The dGPS height uncertainty is the covariance standard deviation (σ_v in Equation I.16 on page 165) from the least-squares covariance matrix. All data are rejected where the running standard deviation of the height uncertainty within a 200 m box is $\geq$0.5mm (shown in red). The surface elevation profile (top), freeboard (middle), and roughness (bottom) data are shown in the right panel. Data collected over open-water are shown in blue and data collected over the ice pack are shown in black. The location of the ice pack edge is shown by the green lines. The running minimum elevation (shown in red at top) was computed within a 400 m window stepped at 200 m increments, and serves as a proxy for the local water level. The ice freeboard is then equal to the surface elevation profile minus the running minimum elevation. The freeboard for open-water data represents the ocean wave height amplitude. The surface roughness is the freeboard standard deviation within a 200 m box stepped at 100 m increments.

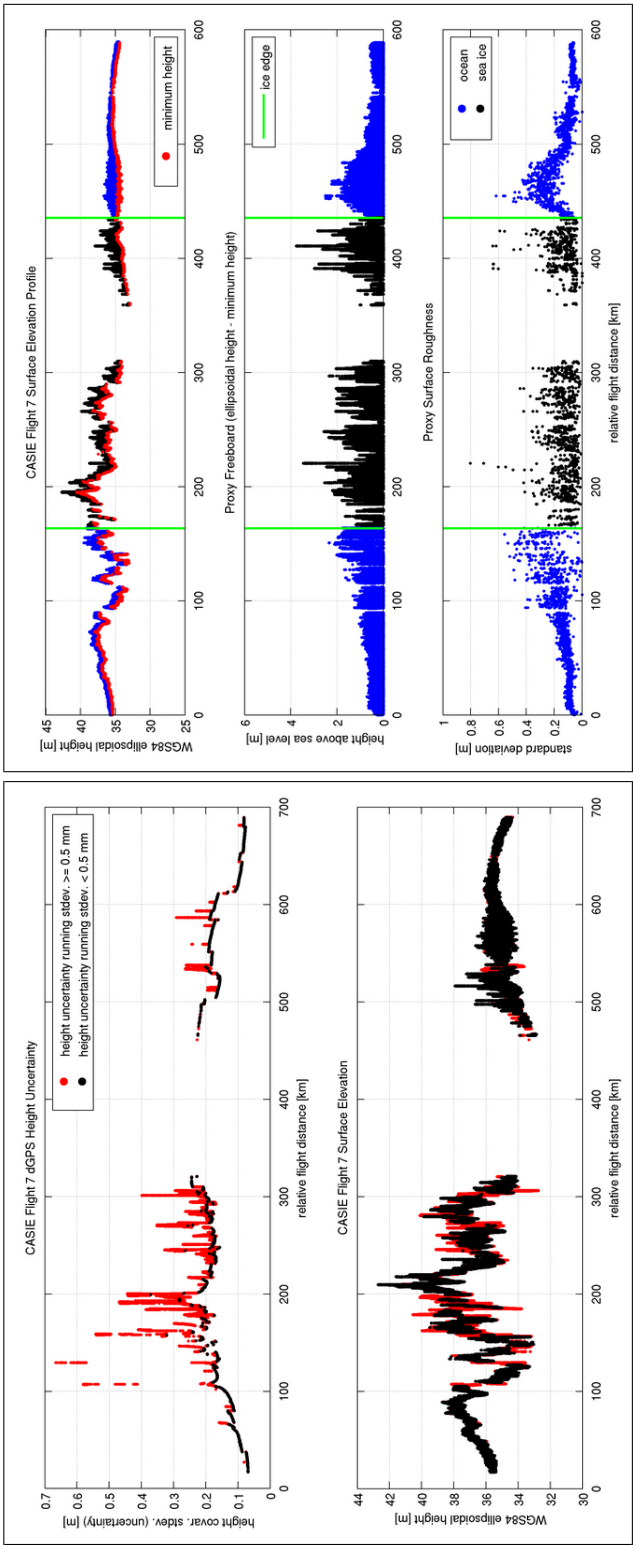

Figure M.4: The CASIE flight 7 dGPS height uncertainty and surface elevation profile are shown in the left panel. The surface elevation profile (top), freeboard (middle), and roughness (bottom) data are shown in the right panel. See Figure M.3 for further explanation.

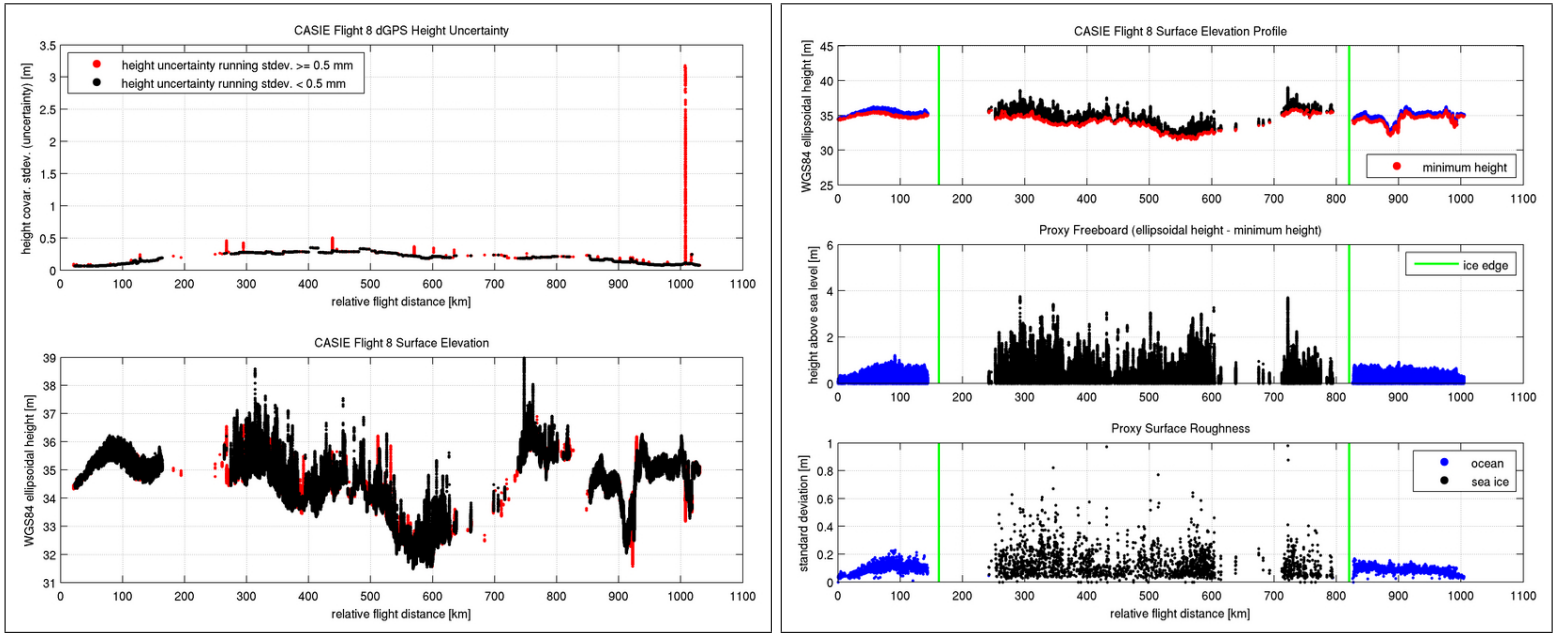

Figure M.5: The CASIE flight 8 dGPS height uncertainty and surface elevation profile are shown in the left panel. The surface elevation profile (top), freeboard (middle), and roughness (bottom) data are shown in the right panel. See Figure M.3 for further explanation.

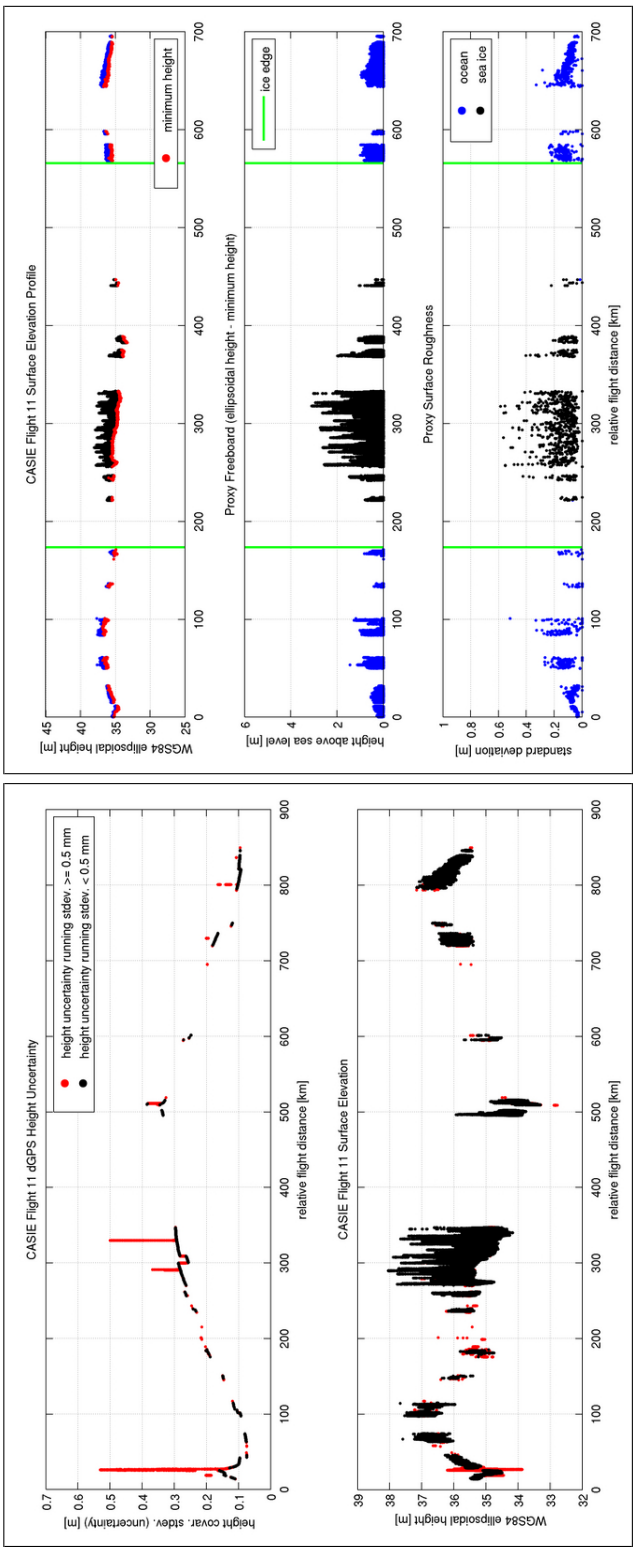

Figure M.6: The CASIE flight 11 dGPS height uncertainty and surface elevation profile are shown in the left panel. The surface elevation profile (top), freeboard (middle), and roughness (bottom) data are shown in the right panel. See Figure M.3 for further explanation.

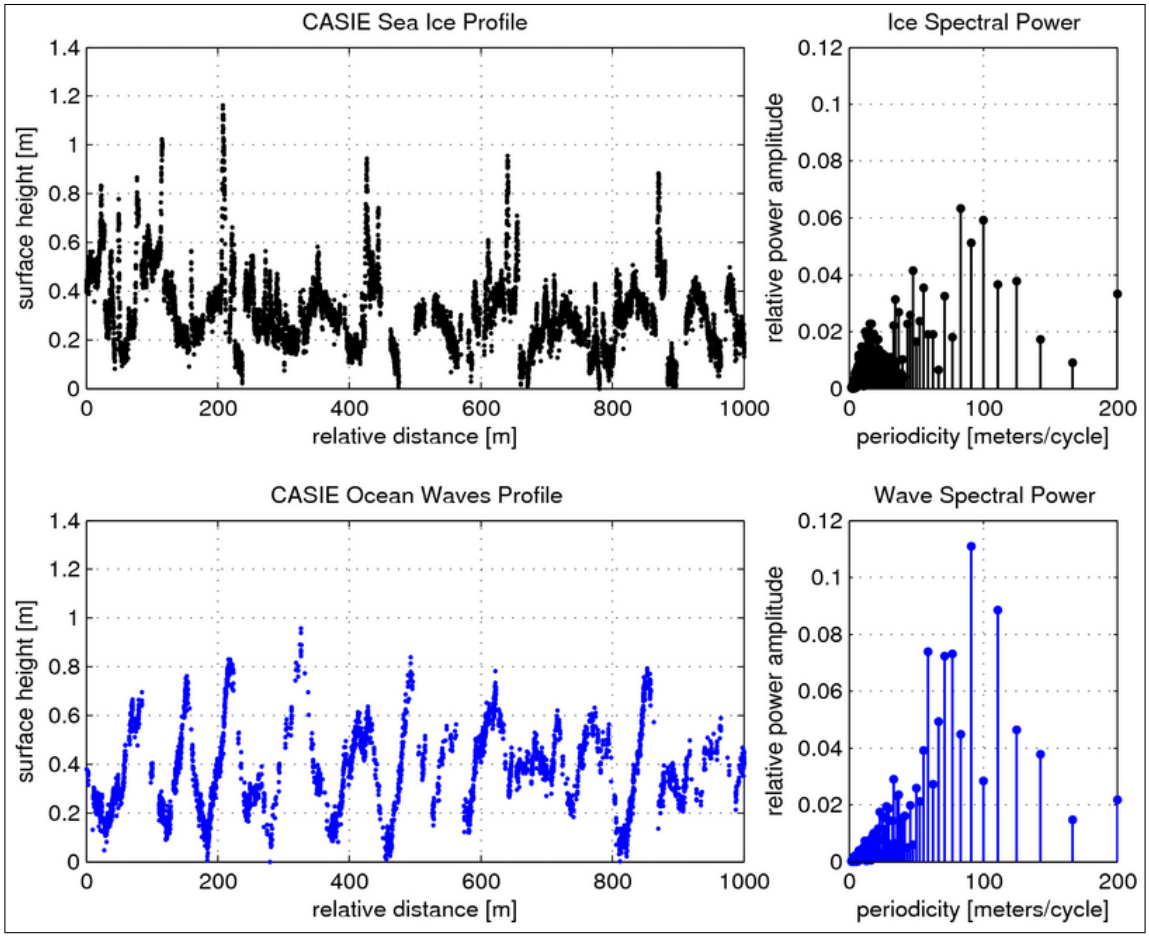

Figure M.7: CASIE flight 9 example sea ice and open-ocean wave profiles and FFTs. The sinusoidal nature of the open-ocean waves corresponds to a strong peak in the FFT spectral power near a periodicity (i.e. wavelength) of 100 m. The sea ice surface profile has a more uniform power distribution, which indicates a more random distribution of ice elevations.

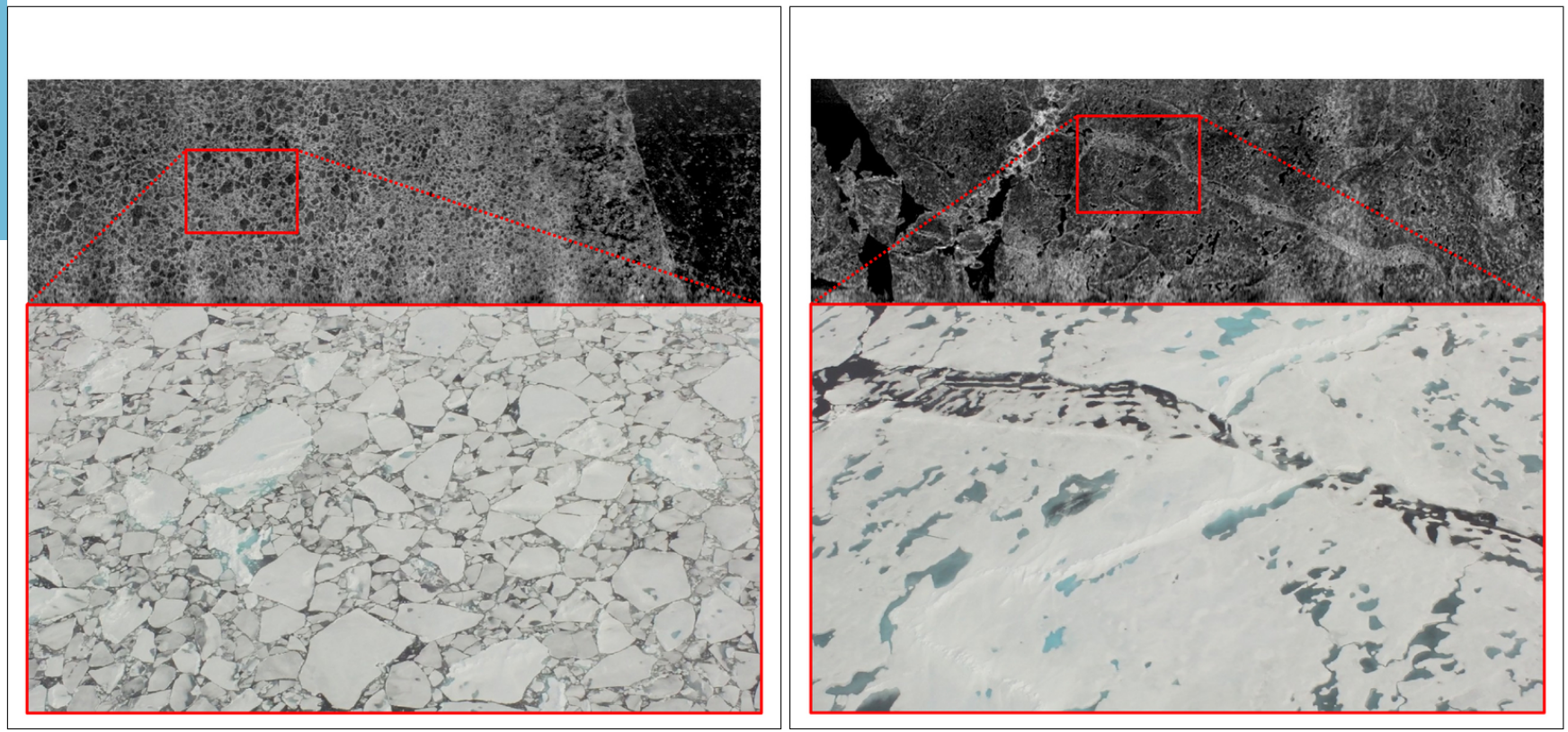

Figure M.8: Select sea ice types identified in CULPIS and microASAR imagery collected during CASIE flight 9. The top images are microASAR backscatter data and the bottom images are CULPIS video frames. The left panel depicts angular broken ice near the edge of the ice pack. The right panel depicts what appears to be a refrozen lead.

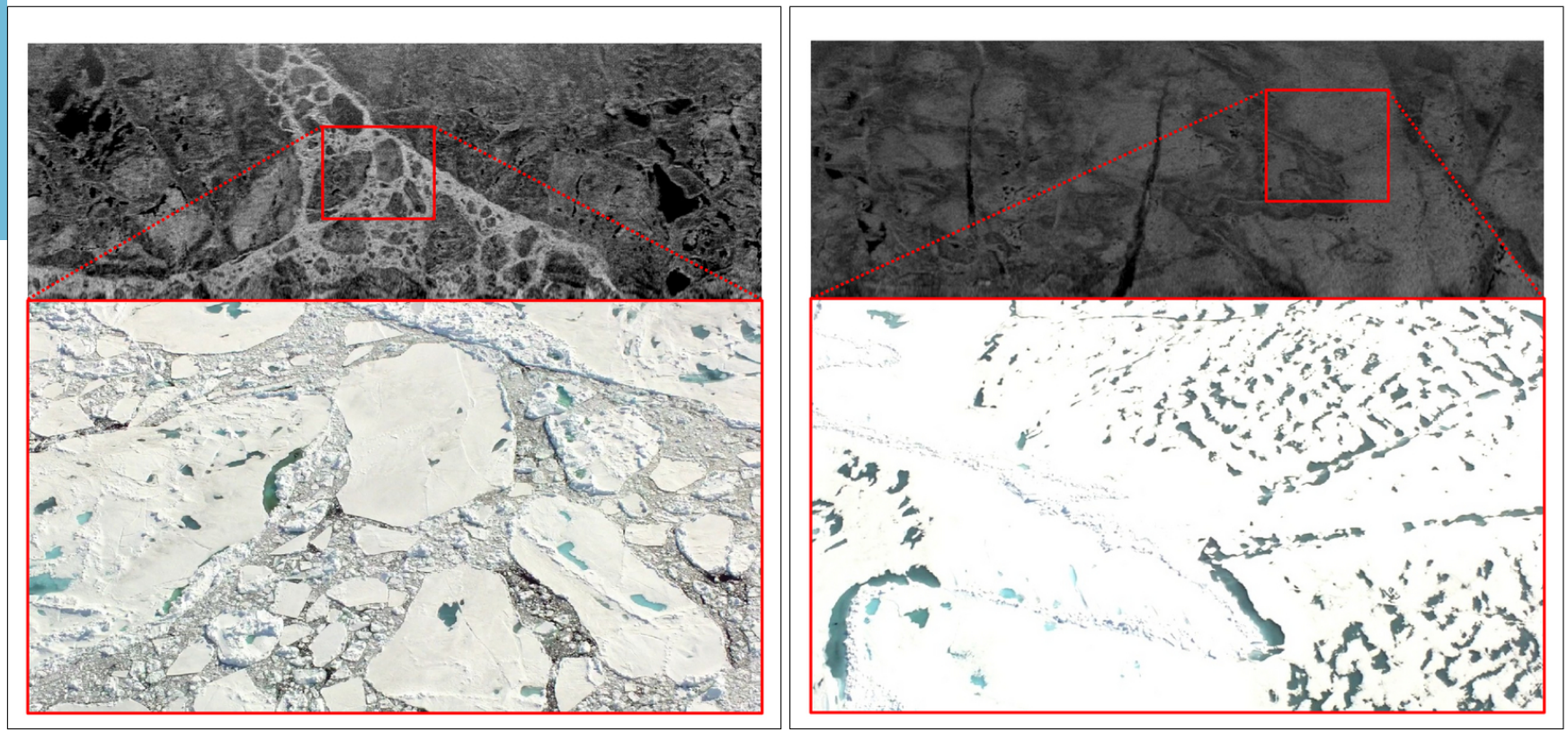

Figure M.9: Select sea ice types identified in CULPIS and microASAR imagery collected during CASIE flight 9. The top images are microASAR backscatter data and the bottom images are CULPIS video frames. The left panel depicts a lead with floes and brash ice. The right panel depicts a curving ridge feature adjacent to heavily flooded ice.

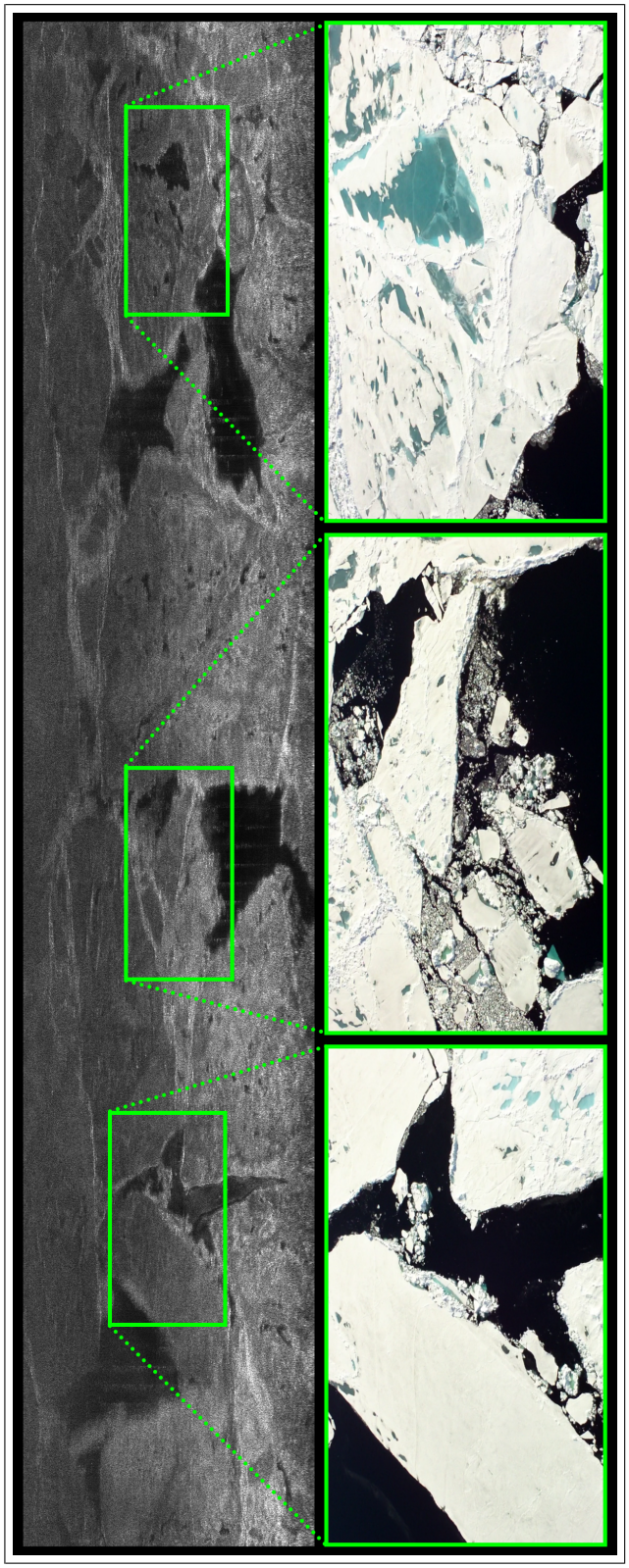

Figure M.10: Coincident microASAR backscatter and CULPIS video imagery collected over sea ice in July 2009. ❷